

# **Multi-photon processes in lanthanide-doped nanocrystals**

---

**Cover:** The star cloud consists of various nanocrystals synthesized in my PhD research. The front cover describes the downconversion process in which high-energy photons in blue are split into low-energy photons in red. As the reverse of downconversion, upconversion process, resulting in an emission of high-energy photons by adding the low-energy photons, is illustrated on the back cover. The universe symbolizes the infinite potential to explore the multi-photon processes and nanocrystals.

**IBSN:** 978-94-6380-204-8

**Printed by:** ProefschriftMaken || [www.proefschriftmaken.nl](http://www.proefschriftmaken.nl)

---

# **Multi-photon processes in lanthanide-doped nanocrystals**

Multi-foton processen in lanthanide gedoteerde nanokristallen  
(met een samenvatting in het Nederlands)

## **Proefschrift**

ter verkrijging van de graad van doctor aan de Universiteit Utrecht op gezag van de rector  
magnificus, prof.dr. H.R.B.M. Kummeling, ingevolge het besluit van het college voor promoties in  
het openbaar te verdedigen op maandag 21 januari 2019 des middags te 4.15 uur

door

**Zijun Wang**

geboren op 11 juni 1989 te Jiangxi, China

---

Promotor:  
Prof. dr. A. Meijerink

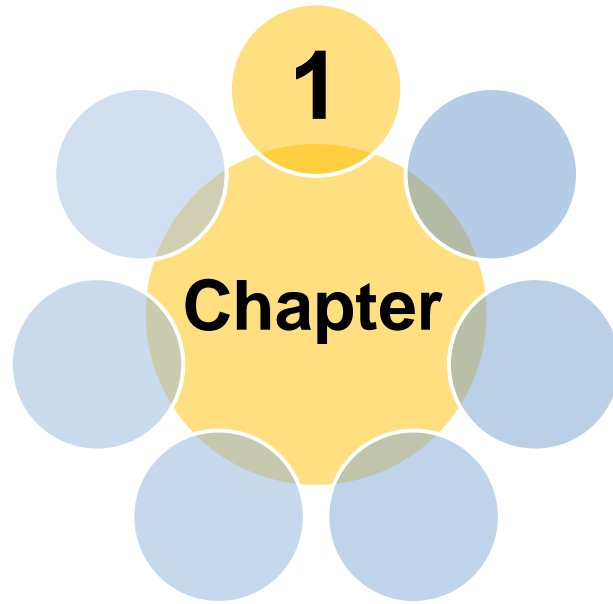
The research in this thesis was financially supported by the China  
Scholarship Council (No. 201506380101).

---

# Contents

<b>Chapter 1.</b> Introduction	1
<b>Chapter 2.</b> Photonic effects for magnetic dipole transitions	23
<b>Chapter 3.</b> Concentration quenching in upconversion nanocrystals	45
<b>Chapter 4.</b> Dye-sensitized downconversion	71
<b>Chapter 5.</b> One-step synthesis and luminescence properties of tetragonal double tungstates nanocrystals	85
<b>Chapter 6.</b> Thermal enhancement and quenching of upconversion emission in nanocrystals	99
<b>Chapter 7.</b> Summary & outlook	129
Samenvatting en vooruitblik	
List of publications	
List of conference contributions	
Acknowledgements	
About the author	



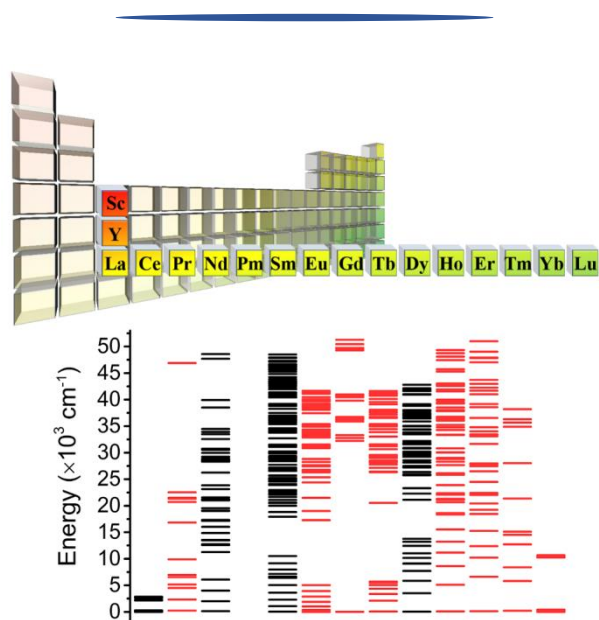


# Introduction

## 1.1 Lanthanide Ions

The lanthanides (Ln) are a series of elements from lanthanum to lutetium with atomic numbers from 57 to 71. In this series of elements, the inner 4f shell is filled with 0 to 14 electrons. Along with scandium and yttrium, the total 17 elements are known as rare earth (RE) elements and they are situated in the fourth, fifth and sixth rows of the periodic table (**Fig. 1.1**). Often the lanthanides are depicted at the bottom of the periodic table together with the actinides (Ac) and the 4f shell for the group of elements is partly filled with electrons. The lanthanides are mostly stable as trivalent ions with the electron configuration  $[\text{Xe}]4f^n5s^25p^6$  ( $n = 0-14$ ). The chemical properties of lanthanide ions are very similar because of the same valence electron configuration ( $5s^25p^6$ ). The  $\text{Ln}^{3+}$  ions do vary strongly in ionic radius: the ionic radius decreases across the series due to poor shielding of the increasing nuclear charge by the 4f electrons. This is known as the lanthanide contraction. The lanthanides are not widely known but the elements are indispensable for wide variety of optical, electric and magnetic applications.<sup>1</sup> Their unique optical and magnetic properties originate from the partly filled inner 4f<sup>n</sup> shell.

In this thesis, we focus on the optical properties of lanthanide ions. The optical properties are determined by the rich energy level structure of the 4f<sup>n</sup> configuration that arises from Coulomb interaction between the 4f electrons, spin-orbit coupling and crystal field splitting. The energy level structure was resolved for all lanthanides in the 1950s and 1960s, and collected in what is now



**Figure 1.1.** Lanthanides and their energy level structure. The location of rare earth ions (Sc, Y and the lanthanides) in the periodic table and the energy level structure (Dieke diagram) for trivalent lanthanide ions. The red color marks the  $\text{Ln}^{3+}$  ions studied in this thesis.

known as the Dieke diagram.<sup>2</sup> The Dieke diagram describing the  $4f^n$  energy levels for each trivalent ion is displayed in **Fig. 1.1**. The red-labelled ions correspond to lanthanides studied in this thesis. The wealth of energy levels in the infrared (IR), visible (VIS) and ultraviolet (UV) allows for transitions between different  $4f^n$  energy levels (f-f transitions) in absorption or emission spanning from IR to UV. The energy level structure is largely independent of the local environment of lanthanide ions because of the shielding effect by filled outer 5s and 5p orbitals. Note that no energy levels for  $\text{La}^{3+}$  and  $\text{Lu}^{3+}$  are included because the empty  $4f^0$  ( $\text{La}^{3+}$ ) and full  $4f^{14}$  ( $\text{Lu}^{3+}$ ) configuration cannot have different  $4f^n$  energy levels. The energy level scheme of  $\text{Pm}^{3+}$  is also missing as Pm is a radioactive element with no stable isotope. As a result of their unique energy level structure, lanthanide ions form a treasure for exploring luminescent materials. For instance,  $\text{Pr}^{3+}$ ,  $\text{Eu}^{3+}$ ,  $\text{Tb}^{3+}$  and  $\text{Nd}^{3+}$  ions are applied in commercial phosphors for X-ray imaging, white light sources and tunable lasers.

## 1.2 Optical Properties

The rich energy level structure of lanthanides is the basis for their unique optical properties. Transitions between different configurations within the  $4f^n$  shell are characterized by sharp absorption or emission lines and low oscillator strengths (weak absorption, long emission decay times). The sharpness of the lines is caused by the weak interaction with the environment (vibrations) as a result of the shielding of the inner  $4f^n$  configuration (where the optical transition takes place) from the surroundings by the filled  $5s^2$  and  $5p^6$  shells. The sharp electronic transitions in the optical spectra resemble atomic spectra that also show sharp purely electronic transitions. The low oscillator strengths stems from the parity forbidden character of the transitions. The transitions between different inner-shell  $4f^n$  states (in first approximation) give rise to no change in electric dipole (ED) moment and thus the transitions are forbidden as ED transitions. In this section, various aspects that determine the optical spectroscopy of lanthanide ions will be discussed.

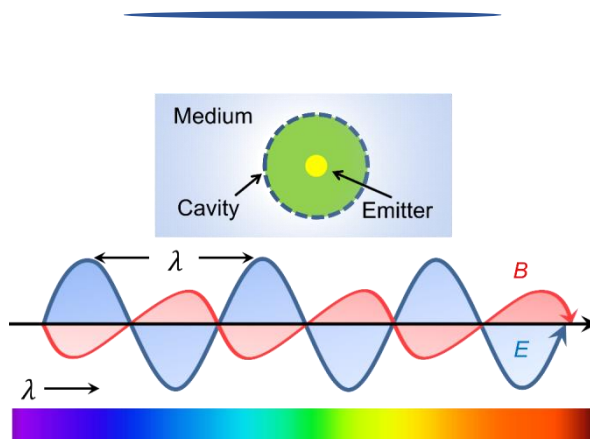
**Spontaneous Emission** Einstein performed pioneering work to provide insight in the interaction of matter and light.<sup>3</sup> Light is electromagnetic radiation, consisting of electric field  $E$  and magnetic field  $B$  (**Fig. 1.2**). The two oscillating components are perpendicular to each other and to the direction of propagation. Following absorption of a photon that brings a lanthanide ion to an excited state, depopulation to ground state or lower-energy state can occur in the form of emission of photons. The spontaneous rate of photon emission  $k$  follows the Fermi's golden rule:

$$k_r = \frac{2\pi}{\hbar} |M|^2 \rho \quad (1.1)$$

with  $\hbar$  the reduced Planck constant,  $M$  the matrix element that involves the dipole moment of the

optical transition and  $\rho$  the local density of states. The term  $M$  describes the strength of electronic transition in terms of transition dipole moments. For parity forbidden f-f transitions, the transition dipole moment is only non-zero because of admixture of opposite parity states into the  $4f^n$  states. This makes the formally parity forbidden f-f transition partly allowed as a forced ED transition. The admixture of opposite parity states is strongly connected with the quantum numbers  $SLJ$  ( $S$ : the total spin quantum number;  $L$ : the total orbital angular momentum quantum number;  $J$ : the total angular momentum quantum number). Selection rules that determine whether the transition is allowed as forced ED transition relate to the quantum numbers. An important selection rule governing the forced ED transitions in lanthanide ions is  $\Delta J = 0, 2, 4$  or  $6$  (not  $J = 0$  to  $J = 0$ ).<sup>4-6</sup>

The intensity of forced ED transition is typically 4-5 orders of magnitude lower compared with allowed ED transitions. Because of the ED forbidden character, the spontaneous emission rate for f-f emission is low, typically in the  $\text{ms}^{-1}$  range. This gives rise to long emission lifetimes. Forced ED transitions can occur in non-centrosymmetric systems as the odd-parity crystal field components can mix opposite parity states into the  $4f^n$  states to relax the parity selection rule. The degree of admixture scales inversely with the energy separation of  $4f^n$  and opposite parity (e.g.  $4f^{n-1}5d$ ) configurations, and strongly depends on the crystallographic environment around lanthanide ion. Often selection rules arising from the symmetry of crystal field levels involved in f-f transitions are overlooked. Symmetry rules are however equally important as the  $SLJ$  selection rule to determine the intensity of specific transitions.<sup>7</sup>



**Figure 1.2.** The interaction of light and matter. Light is electromagnetic radiation where both the oscillating electric field and the oscillating magnetic field can induce transition between energy levels of emitters such as lanthanide ions. The dielectric medium surrounding the emitter influences the transition probabilities through local field effects.

In addition to forced ED, f-f transitions in lanthanide ions can be induced by the oscillating magnetic vector in the electromagnetic wave. Magnetic dipole (MD) transitions are allowed in first-order but the oscillator strength is approximately  $10^{-6}$  times lower than that for allowed ED transitions. The selection rule for MD transitions is  $\Delta J = 0, \pm 1$  (again, not  $0 \rightarrow 0$ ). Although the pure MD transition is generally weak and is difficult to observe, tuning MD transition offers an alternative degree of freedom to engineer spontaneous emission. In this thesis, the  $\text{Gd}^{3+} {}^6\text{P}_{7/2} \rightarrow {}^8\text{S}_{7/2}$  transition (**Ch. 2**) is found to be 95% pure MD transition. This makes it possible to study the influence of the local surroundings on MD transition probabilities.

Lanthanide ions can also show interconfigurational  $4f^n \rightarrow 4f^{n-1}5d$  transitions. These transitions give rise to a change in dipole moment and are therefore allowed as ED transitions. The spontaneous emission rate is fast, typically in the  $\text{ns}^{-1}$  range. The energy of the excited  $4f^{n-1}5d$  state strongly depends on the local surroundings. A large crystal field splitting or a high degree of covalency shifts the 5d state from which emission is observed to lower energies. For example,  $\text{Ce}^{3+}$  emission originates from allowed d-f transitions and can be tuned from UV to visible region by variation of surrounding environment of  $\text{Ce}^{3+}$  ion. The emission lifetime is typically 20-70 ns.

The local density of states affects the spontaneous emission rate and depends on the photonic environment, such as the refractive index  $n$  of surrounding medium. As illustrated in **Fig. 1.2**, a model for local field effect comprises a microscopical lanthanide emitter and a surrounding cavity within a continuous medium. The local electric field  $E_{\text{loc}}$  acting on the emitter may differ from the macroscopic electric field  $E_0$  in the medium. Various models have been established to describe the relation between spontaneous emission rates of (forced) ED transitions and local field effects (**Chs. 2, 3, 5**). The spontaneous emission rate  $k_r$  is

$$k_r = \frac{4n\omega^3}{3\hbar c^3} \left(\frac{E_{\text{loc}}}{E_0}\right)^2 |\mu|^2 \quad (1.2)$$

where  $\omega$  is the emission frequency,  $c$  is the speed of light, and  $\mu$  is the transition dipole moment.<sup>8</sup> Besides the variation of  $k_r$  by embedding emitters in different media with finite range of possible refractive indices, there is a more powerful strategy to tune the spontaneous emission rate, discovered by Purcell in 1946. The spontaneous emission rate can be enhanced in a resonant cavity characterized by Purcell factor  $f$ :

$$f = \frac{3\lambda_c^3 Q}{4\pi^2 V} \quad (1.3)$$

where  $\lambda_c$  is the wavelength of light within the cavity of refractive index  $n$ ,  $Q$  is the quality factor, and  $V$  is the mode volume of the cavity.<sup>9</sup> The Purcell effect has triggered extensive research on

photonic and plasmonic engineering.<sup>10,11</sup>

**Non-radiative Decay** Radiative decay competes with non-radiative decay processes that deplete the excited state population without the emission of photons. This will lower the efficiency (quantum yield) of luminescent material and is often undesired. For lanthanide ions, a prominent mechanism for non-radiative decay is multi-phonon relaxation (MPR). The MPR rate is connected with the electron-phonon interaction strength. The non-radiative decay rate  $k_{nr}$  for MPR depends on the energy gap  $\Delta E$  of two adjacent states, the maximum phonon energy  $\hbar\omega$  and the temperature  $T$ , and is given by

$$k_{nr} = k_0 (n + 1)^p = \left[ \frac{\exp(\hbar\omega/kT)}{\exp(\hbar\omega/kT) - 1} + 1 \right]^{\frac{\Delta E}{\hbar\omega}} \quad (1.4)$$

where  $k_0$  is the multi-phonon relaxation rate at  $T = 0$ ,  $n$  is the phonon occupation number, and  $p$  is the number of phonon that is required to bridge the energy gap to the next lower  $4f^n$  level.<sup>12,13</sup> A simplified expression is

$$k_{nr} = \beta \exp(-\alpha\Delta E) \quad (1.5)$$

where  $\beta$  is a parameter that contains the electronic coupling for the transition between the two  $4f^n$  levels and  $\alpha$  is a constant that is in first approximation for all f-f transitions of different lanthanide ions in a specific host.<sup>14</sup> The non-radiative decay becomes non-negligible if less than five phonons can bridge the energy gap. This is known as the energy gap law.<sup>15</sup> The energy gap law also reflects the exponential decrease in non-radiative decay rate with increasing energy gap.<sup>16</sup> Typically, the spontaneous emission rate is temperature independent, while non-radiative decay is not and is often enhanced at elevated temperatures, giving rise to thermal quenching (**Chs. 5, 6**). However, anomalous phenomena are sometimes observed, for example for upconversion luminescence in nanocrystals where the upconversion efficiency increases upon heating (**Ch. 6**).

**Decay Dynamics** The decay time  $\tau$  is the inverse of the total decay rate  $k_t$  that contains radiative  $k_r$  and non-radiative  $k_{nr}$  parts. The temporal evolution of the excited state population  $N(t)$  with time  $t$  follows

$$dN(t) = -k_t N(t) dt \quad (1.6)$$

The solution is an exponential expression

$$N(t) = N_0 e^{-tk_t} \quad (1.7)$$

where  $N_0$  is the excited state population at  $t = 0$ . The emission intensity  $I(t)$  is proportional to the excited state population  $N(t)$ . As a result, we observe a single-exponential decay of emission intensity

$$I(t) = I_0 e^{-tk_t} \quad (1.8)$$

with  $I_0$  the initial intensity. Time-resolved measurements provide a decay time that includes the contribution of both radiative and non-radiative decay processes. The analysis will be more complicated for an ensemble of emitters that have different decay rates. This is often the case as radiative decay rates and non-radiative decay rates can vary. For example, if different crystallographic sites are available for the luminescent ion, typically the radiative decay rate will be different as the local environment influences the radiative decay rate. The experimentally observed decay curve has then (at least) two components and deviates from a single-exponential. It is important to analyze the decay curves as it can help to understand the physical mechanism responsible for non-radiative decay processes.

**Quantum Yield** Quantum yield (QY) for luminescent materials is an important parameter. For practical applications, it is evident that a higher QY is usually desired. Also for a physical understanding of radiative and non-radiative decay processes, insight in the QY is important. There are two types of QY. One is internal QY, defined as the ratio of the emitted photon flux and the absorbed photon flux (number of photons emitted/number of photons absorbed). Changing the denominator to the incident photon flux gives the external QY that is (much) lower than internal QY. Especially for weakly absorbing materials, the external QY is low. QY for phosphors is generally below 100% due to the non-radiative processes. Absolute QYs can be measured by using an integrating sphere. QY measurements are not trivial and require careful calibration procedures.

Measuring decay dynamics provides an alternative approach to determine QY via the observed decay time  $\tau_{\text{obs}}$  ( $= 1/(k_r + k_{\text{nr}})$ ) divided by the radiative decay time  $\tau_0$  ( $= 1/k_r$ ):

$$\text{QY} = \frac{k_r}{k_r + k_{\text{nr}}} = \frac{\tau_{\text{obs}}}{\tau_0} \quad (1.9)$$

This method is applied in **Chs. 2, 3** assuming the QY in bulk material is 100%.

## 1.2 Multi-Photon Processes

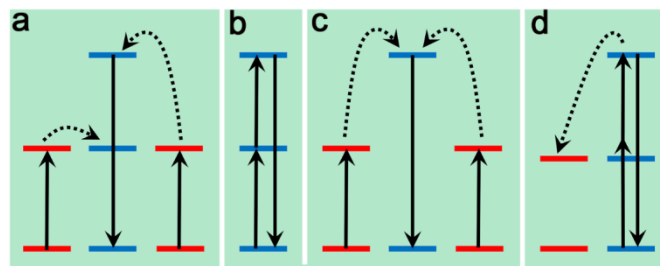
Traditionally optical properties of emitters involve absorption of one high-energy photon and emission of one lower-energy photon. As the energy of the emitted photon is (usually) lower than that of the absorbed photon, the emission maximum is shifted to longer wavelengths and this process

is called downshifting. The shift to lower energies is known as the Stokes shift. However, other more exotic processes have also been observed. We call these multi-photon processes and divide them into upconversion and downconversion. In case of upconversion, two lower-energy photons are absorbed and result in the emission of one higher-energy photon. Downconversion is the opposite process: one high-energy photon is absorbed and results in emission of two lower-energy photons. In this section, both multi-photon processes are discussed as well as basic theory for energy transfer (ET) between emitters as ET plays a key role in both up- and downconversion.

**Upconversion** The term of upconversion describes an anti-Stokes process, first proposed by Bloembergen in 1959, and not much later discovered independently by Auzel in France, and by Ovsyakin and Feoflov in the Soviet Union.<sup>17-19</sup> After this, also higher-order upconversion processes were discovered where 3 or even 4 photons were absorbed to yield one high-energy photon. In general, upconversion is a nonlinear  $n$ -photon process for which the integrated emission intensity  $I$  scales with the  $n$ th power of excitation power density  $P$  ( $I \propto P^n$ ).<sup>20,21</sup> This makes the upconversion quantum efficiency excitation power dependent and it can be determined experimentally that how many photons are involved to give a specific upconversion emission. In practice, the power dependence shows a weaker dependence on  $P$  ( $n$  smaller than the actual number of photons involved) due to the saturation effects.

The mechanism for upconversion can vary. There are four classes of upconversion mechanisms as shown in **Fig. 1.3**: energy transfer upconversion (ETU), excited state absorption (ESA), cooperative sensitization and photon avalanche. ETU (**Fig. 1.3a**) occurs when two donors (D) after ground state absorption (GSA) non-radiatively transfer their energy to a neighboring acceptor (A) with a real intermediate energy level. This mechanism is usually the most efficient because of the high efficiency of resonant energy transfer between nearest neighbors. On a single isolated ion (**Fig. 1.3b**), upconversion can also occur through sequential absorption of two photons via a meta-stable intermediate level GSA, followed by ESA.<sup>22,23</sup> If there is no real intermediate energy level in the acceptor that is resonant with the donor emission, second-order cooperative sensitization (**Fig. 1.3c**) can take place where two donors cooperatively transfer their energy to a nearby acceptor. Since this is a second-order process, it is much less efficient (typically three orders of magnitude) than ETU.<sup>24,25</sup> The fourth mechanism (**Fig. 1.3d**) is the photon avalanche. This process generates strong upconverted emission after non-resonant GSA absorption of a pump source that is resonant with an ESA or ETU transition. This mechanism was first discovered in  $\text{Pr}^{3+}$ -doped  $\text{LaCl}_3$  and  $\text{LaBr}_3$ .<sup>26</sup> Efficient cross-relaxation takes place over a certain level of population of the excited state so that photon avalanche is triggered only if the excitation power is over a certain threshold.

The ladder-like energy level structure of some lanthanide ions with well-defined energies and long-lived excited states provide the possibility for efficient upconversion in Ln-doped materials.



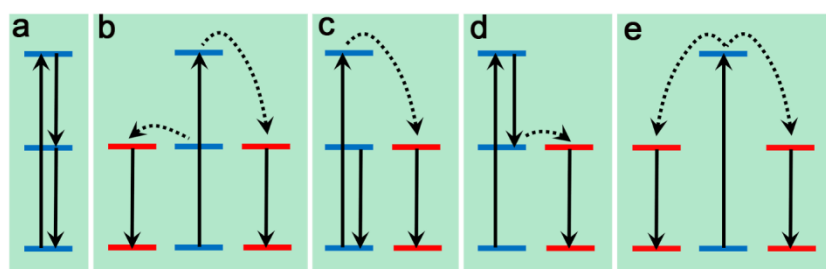
**Figure 1.3.** Schematic diagrams for upconversion processes. (a) Energy Transfer Upconversion. (b) Excited State Absorption. (c) Cooperative Sensitization. (d) Photon Avalanche.

The efficient and by far most studied upconversion couple (also in this thesis) involves the  $\text{Yb}^{3+}$ - $\text{Er}^{3+}$  pair. Absorption of  $\sim 1000$  nm IR radiation by  $\text{Yb}^{3+}$  is followed by energy transfer from two  $\text{Yb}^{3+}$  ions to  $\text{Er}^{3+}$  which emits green or red light. It is important to distinguish between upconversion mechanisms. This is commonly realized by recording excitation spectra, analyzing decay dynamics, and by concentration and power dependent studies. If the ESA mechanism dominates, additional excitation peaks are typically observed since the GSA and ESA steps in the same lanthanide ion are at different energies. In the decay dynamics of the upconversion emission, a clear rise time arises for ETU, whereas for ESA the anti-Stokes emitting level is populated during the excitation pulse and no rise time is expected for the upconversion emission. In addition, from the nature of upconversion (ion couple or single ion, **Fig. 1.3**), it follows that ETU and cooperative sensitization show quadratic concentration dependence while for ESA a linear increase is expected with concentration. Hence, concentration, power and time-resolved measurements are instrumental in identifying the upconversion mechanism.

**Downconversion** As the reverse of upconversion, downconversion, also known as quantum cutting or photon splitting, results in the emission of two or more low-energy photons after absorbing one high-energy photon.<sup>27,28</sup> Downconversion was first predicted in 1957 by Dexter through a mechanism called cooperative energy transfer (the opposite of the cooperative sensitization process in **Fig. 1.3c**).<sup>29</sup> Also four different mechanisms of downconversion can be responsible and are shown in **Fig. 1.4**. The first mechanism is the sequential emission in a single ion: transition from a high excited to a lower excited state results in the emission of a first photon and is followed by emission to the ground state, resulting in a second photon (**Fig. 1.4a**). It is this type of quantum cutting that was first experimentally reported for  $\text{Pr}^{3+}$  ion in fluoride host lattices.<sup>30,31</sup> A second mechanism involves resonant ET between neighboring ions. From a high-excited state of a donor, partial ET (known as cross-relaxation) to a nearby acceptor results in excitation of the first acceptor, leaving the donor in an intermediate excited state. In a consecutive step, the donor transfers its energy from the

intermediate excited state to a second acceptor. Both acceptors in the excited state return to the ground state by emitting a photon. The first experimental evidence for this process was obtained in  $\text{Gd}^{3+}$ - $\text{Eu}^{3+}$  ion couple and the term downconversion was coined here as this photon splitting process is the opposite of the ETU upconversion process.<sup>32,33</sup> Later, other downconversion couples of lanthanide ions were discovered where the emission originates from either only acceptors ( $\text{Pr}^{3+}$ - $\text{Yb}^{3+}$  ion couple in **Ch. 4**) or both donor and acceptor ( $\text{Ho}^{3+}$ - $\text{Yb}^{3+}$  ion couple).<sup>34</sup> The ET steps in downconversion with an intermediate level of the donor are first-order processes and depend on the spectral overlap for donor emission and acceptor absorption. However, without the spectral overlap in the absence of an intermediate level, photon splitting can still occur through a second-order cooperative energy transfer process. This process is depicted in **Fig. 1.4e** and was predicted by Dexter in 1957. Since the probability for second-order processes is orders of magnitude lower than for first-order processes, this photon splitting process is much less efficient and it was not until 2005 that convincing experimental evidence for cooperative energy transfer was reported for the  $\text{Tb}^{3+}$ - $\text{Yb}^{3+}$  ion couple.<sup>35</sup>

In contrast with upconversion that involves adding the energy of two absorbed photons, downconversion may be confused with downshifting. The observation of emission of higher-energy photons upon excitation with lower-energy photons is direct evidence for the occurrence of upconversion. However, the observation of emission of lower-energy photons after excitation with higher-energy photons can result from both downshifting and downconversion. As a result, providing convincing experimental evidence for the occurrence of downconversion is challenging but important. One way is to measure the emission spectra for different excitation energy. For example, in the  $\text{Gd}^{3+}$ - $\text{Eu}^{3+}$  ion couple,<sup>5</sup> only exciting  $\text{Gd}^{3+}$  to  ${}^6\text{G}_J$  state can result in downconversion as the first ET step from the  ${}^6\text{G}_J$  populates the  ${}^5\text{D}_0$  of  $\text{Eu}^{3+}$  by cross-relaxation. This does not occur for excitation to levels lower than the  ${}^6\text{G}_J$  state. Energy transfer from intermediate  $\text{Gd}^{3+}$  levels results in  $\text{Eu}^{3+}$



**Figure 1.4.** Schematic diagrams for downconversion processes. (a) Sequential emission (cascade emission). (b-d) Different options for downconversion by resonant energy transfer between donor and acceptor. (e) Cooperative energy transfer.

emission from different  $^5D_J$  states by ET and MPR. As a result, difference in excitation energy causes different intensity ratios of  $^5D_0/^5D_J$  and the increased relative intensity of the  $^5D_0$  emission upon excitation in the  $^6G_J$  levels serves as evidence for downconversion. This approach does not work if the downconversion emission only originates from the  $Yb^{3+}$  ion. In the case of  $Pr^{3+}$ - $Yb^{3+}$  ion couple, evidence for downconversion could be obtained by comparison of the excitation spectrum of  $Yb^{3+}$  IR emission and the  $Pr^{3+}$  absorption spectrum to examine whether the intensity ratio of  $^3P_J/^1D_2$  lines is two since every photon absorbed into  $^3P_J$  states generates two  $Yb^{3+}$  photons.<sup>36</sup>

**Energy Transfer** Both in upconversion and downconversion, ET between lanthanide ions plays an important role. It is insightful to understand the mechanism and efficiency of ET as it influences the efficiency of up- and downconversion. As the concentration of lanthanide ions increases, ET processes become more important. Different types of ET exist. There is a distinction between radiative and non-radiative ET. In case of radiative ET, a photon is emitted by the donor and reabsorbed by the acceptor. Non-radiative ET proceeds without emission of a photon and is determined by short-range interaction between neighboring ions (multipolar or exchange interaction). Another distinction is between resonant and non-resonant ET. In case of non-resonant ET, there is an energy mismatch between the donor emission and acceptor absorption energies. The mismatch can be overcome by (multi-)phonon emission or absorption but the ET rates will be lower if the energy mismatch is larger. Finally, there are specific terms for ET. One is cross-relaxation, where only part of the energy from the donor excited state is transferred, leaving the donor in an intermediate excited state. In the next case of energy migration, multi-step energy transfer between donor ions at high dopant concentrations leads to diffusion of the excitation energy over the donor sublattice. In **Fig. 1.5**, the different ET processes are depicted.<sup>18</sup>

A powerful method to investigate the mechanism and rates of energy transfer is through luminescence decay measurements, especially of the donor emission. Here we will discuss energy transfer from donor to acceptor. For radiative ET, the decay time of the donor emission is independent of acceptor concentration, leading to a constant decay time that is identical to the radiative decay time. It can occur over a long D-A distance  $R$  with a probability  $P$ .<sup>18</sup>

$$P = \frac{\sigma_A}{4\pi R^2 \tau_D} \int g_D(\nu) g_A(\nu) d\nu \quad (1.10)$$

where  $\tau_D$ ,  $\sigma_A$  and the integral term are the decay time of donor emission, absorption cross-section of acceptor and spectral overlap between the donor emission and acceptor absorption. The distance dependence for radiative ET is  $R^{-2}$  for isotropic emission by the donor. In **Ch. 4**, the decay time of dye emission decreases when the dye is coupled with NCs due to the non-radiative ET. This serves as evidence that the ET mechanism is not radiative ET from dye molecules in the solvent as the decay

time will be constant, independent of the amount of NCs for radiative ET.

When two ions are in close proximity, non-radiative ET can occur via either multipolar interaction (Förster ET) or exchange interaction (Dexter ET). The probability follows

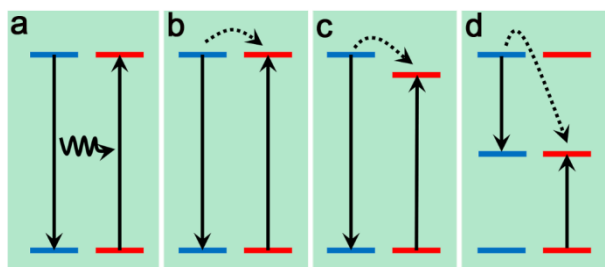
$$P = \frac{2\pi}{\hbar} \left| \int \psi_i H_{DA} \psi_f d\tau \right|^2 \int g_D(v) g_A(v) dv \quad (1.11)$$

with  $H_{DA}$  the interaction Hamiltonian,  $\psi_i$  the initial state (excited donor and grounded acceptor) and  $\psi_f$  the final state (grounded donor and excited acceptor). The squared term contains the distance dependence of transfer probability that varies for different types of interaction. In the case of dipole-dipole Förster ET, the transfer probability scales to the inverse sixth power of  $R$ .<sup>37</sup>

$$P = \frac{1}{\tau_D} \left( \frac{R_0}{R} \right)^6 \quad (1.12)$$

$R_0$  denotes the critical Förster radius in which ET and radiative decay from the excited state of donor have equal probabilities. **Eq. 1.11** can be extended for electric multipolar interactions, giving rise to  $R^{-8}$  and  $R^{-10}$  distance dependence for dipole-quadrupole and quadrupole-quadrupole interactions. The Förster ET is effective over relatively long distances (typically up to ~10 nm for ET between trivalent lanthanides). If donor and acceptor are close enough to have electronic wave function overlap, Dexter ET will become dominant. The distance dependence is exponential and is always in short range (typically < 0.5 nm).<sup>38</sup>

If there is an energy mismatch for the excited states in donor and acceptor, ET can still occur with the assistance of phonon that make up the energy difference.<sup>39</sup> For cross-relaxation between identical ions with different involved states, such as  $\text{Er}^{3+} \ ^4\text{S}_{3/2} + \ ^4\text{I}_{15/2} \rightarrow \ ^4\text{I}_{9/2} + \ ^4\text{I}_{13/2}$  (**Ch. 3**), there is hardly



**Figure 1.5.** Schematic diagrams for energy transfer between donor and acceptor ions. (a) Radiative energy transfer. (b) Resonant non-radiative transfer. (c) Non-resonant non-radiative transfer. (d) Cross-relaxation.

energy mismatch and cross-relaxation effectively quenches the green  $^4S_{3/2}$  emission at elevated  $Er^{3+}$  concentrations. For the red emitting  $^4F_{9/2}$  level, there is no resonant cross-relaxation possible with neighboring  $Er^{3+}$  ions, which explains why the  $^4F_{9/2}$  emission is not strongly quenched for higher  $Er^{3+}$  concentrations. Resonant energy transfer involving identical transitions on neighboring donor ions at high donor concentrations gives rise to energy migration. Thus, it is possible for the excitation energy to diffuse over the donor sublattice in a long range. This can be beneficial and makes it possible that for high concentrations of  $Yb^{3+}$  ions in upconversion systems the energy transfer to  $Er^{3+}$  becomes more efficient. On the other hand, long-distance energy migration can also lead to migration to distant defects or trapping sites where the excitation energy is lost thus reducing the luminescence efficiency.

### 1.3 Nanomaterials

Nanomaterials are an emerging class of materials. They are commonly defined as materials for which at least one dimension is less than 100 nm. The decrease of size to the nanometer scale can give the materials unique chemical and physical properties that are different from bulk materials. One well-known example is the quantum confinement in quantum dots (QDs).<sup>40</sup> QDs are nanocrystals (NCs) of semiconductors, typically 2-20 nm in diameter. The bandgap of semiconductor increases as the NC size decreases below the exciton Bohr radius. As a result, the absorption onset and emission shift to higher energy. Since the discovery of quantum confinement effects in QDs, extensive research has been done to understand the optical properties and this has also resulted in commercial applications as luminescent probes for bioimaging.<sup>41,42</sup> More recently, QDs have been used for generating green and red light in light emitting diode (LED) based TVs.<sup>43</sup>

Research on lanthanide-doped NCs started in the late 1990s. For lanthanide ions doped into insulator NCs, there is no quantum confinement effect. Transitions are localized within the 4f shell of the lanthanides and the exciton Bohr radius in insulators is too small to observe quantum confinement effects. The peak position of f-f transitions is determined by the local surroundings and is therefore the same for lanthanide in nanomaterials and bulk materials. However, interesting and significant differences in optical properties are present as will be discussed below. In this thesis, we studied two types of nanomaterials: fluorides (**Chs. 2-4**) and tungstates (**Chs. 5, 6**). Fluorides have relatively low maximum phonon energies ( $350-400\text{ cm}^{-1}$ ) which reduce the probability of multi-phonon relaxation and make fluorides useful as hosts for certain luminescent materials, for example for upconversion. Tungstates feature a high density, which is an advantage in applications related to detection or conversion of high-energy radiation (e.g. scintillators), and are also self-activated hosts which enable efficient luminescence.

In the past decades, a number of mature protocols has been reported to synthesize nanomaterials

and to fabricate nanostructures. These protocols can be divided into two classes: top-down and bottom-up.<sup>44,45</sup> In the top-down approach, an external tool is used to shape bulk materials into the desired nanomaterials by removing material and leaving nanostructures. Examples are etching and lithography. Another approach that is explored especially by chemists is the bottom-up methodology. In this approach, nanostructures are built from atomic or molecular building blocks in a controlled manner to realize nanostructures with a uniform size and shape. A powerful method is fast nucleation of seed crystallites that are allowed to grow under identical reaction conditions to realize a homogeneous ensemble of NCs. Size and shape control is possible by fine tuning of reaction conditions where the concentration of reactants and type of passivating ligands play important roles. Ligands attach to the surface of NCs and stabilize the NCs, and play a prominent role in the NC growth. In this thesis, bottom-up approaches are used for the synthesis of NCs.

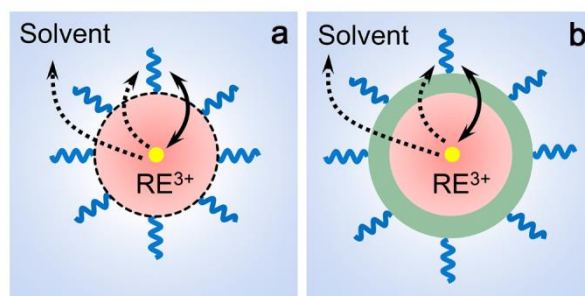
Quantum confinement does not affect lanthanide luminescence. Although the peak position for f-f transitions is unaltered by the size and shape of Ln-doped NCs, there are subtle and also more dramatic changes in the optical properties of lanthanide ions in NCs in comparison to the bulk materials. These can be beneficial or not. It is crucial to understand and explore the cons and pros when lanthanide ions are incorporated in NCs.

**Cons** As the particle size decreases, the surface-to-volume ratio increases, giving rise to the increase of density of surface defects (dashed circle in **Fig. 1.6a**). Energy transfer to defects is often followed by non-radiative process which reduces the quantum efficiency. With optimized synthesis methods, the defect concentration can be limited, but in general, the defect concentration in NCs will be higher than in bulk material. To obtain monodisperse NCs with defined morphology, surface ligands are necessary to control the growth. Oleic acid is one of the most widely used ligands. (**Chs. 2-6**) However, the ligands (oleic acid or other organic molecules) have high-energy vibrations ( $\sim 3000\text{ cm}^{-1}$  for C-H,  $\sim 3500\text{ cm}^{-1}$  for O-H) which coupled to the crystal surface can quench the luminescence by multi-phonon relaxation (mediated by dipole-dipole interaction). The role of high-energy O-H vibration can even lead to the observation of thermal enhancement of upconversion emission in NCs, (**Ch. 6**) in contrast with the expected thermal quenching. Ligand quenching is marked by the dashed single arrow to the ligand in **Fig. 1.6**. For stabilization, NCs are often dispersed in an organic solvent or water. Analogous to the ligands, the high-energy vibrations from solvent also can quench the luminescence (solvent quenching, dashed single arrow to the solvent in **Fig. 1.6**), especially when the vibrational energy is resonant with the energy separation between the emissive energy level and next lower-energy level. Due to these surface-related quenching processes, the luminescence efficiency of lanthanide ions in NCs is lower than in bulk phosphors, often by one or two orders of magnitude. Exceptions are lanthanide ions with emitting states for which the energy gap from the emitting level to the next lower level is large, for example  $\text{Gd}^{3+}$ ,  $\text{Tb}^{3+}$  and  $\text{Ce}^{3+}$ . Here,

phonon relaxation by coupling with the high-energy vibrations of ligand and solvent does not quench the emission and high quantum yields have been realized. There are many approaches to address the issue of surface quenching using surface passivation strategies.<sup>46,47</sup> The coating of an inert (undoped) isocrystalline shell around the core reduces the density of defects and suppresses the non-radiative decay processes (dashed single arrows in **Fig. 1.6b**). The increased distance between the dopants in the core and the surrounding high-energy vibrations of molecules on the outside of the inert shell strongly decreases quenching by (multi-)phonon relaxation. A 5-10 nm shell is sufficient to reduce phonon induced quenching. Experimentally, the elimination of quenching is manifested by an increase in luminescence efficiency and a lengthening of luminescence decay times. This core-shell strategy is applied to the NaYF<sub>4</sub> NCs in this thesis. (**Chs. 2-4**)

**Pros** The reduction in size to nanometer dimension also offers new opportunities and has unique advantages over bulk materials. Since the size of nanomaterials is far below the wavelength of visible light (**Fig. 1.2**), there is no scattering of light and this allows the fabrication of transparent luminescent structures. This is e.g. important for luminescent solar concentrators, lighting and displays. The ligands on the NC surface provide the opportunity to control surface properties.<sup>48</sup> Based on the nature of ligand and solvent, single NC can be used as building blocks to form ordered and complex architectures (superlattices and superparticles) through self-assembly.<sup>49-51</sup> Tuning the polarity of ligand functional group toward the solvent allows the switching of dispersion in apolar (e.g. cyclohexane) and polar (e.g. water) solvents. The nanosize is also advantageous in biological applications as the size of NCs is similar to that of (large) biomolecules. A variety of NCs is explored for applications in bio-imaging, bioanalysis, drug delivery and related therapies, such as photodynamic therapy and photothermal therapy.<sup>52-54</sup>

The large surface of NCs has advantages as it allows interaction between Ln ions inside the NCs and structures or molecules that are coupled to the surface. A successful example is that of dye-sensitized upconversion.<sup>55-57</sup> Dye molecules adsorbed at the surface of an upconversion NC act as antennas that can absorb IR radiation efficiently and transfer the energy to nearby Ln ions inside the NCs. In bulk materials, this type of sensitization is not possible. The possibility of donor-acceptor ET between lanthanide ions inside the NC and luminescent species on the surface can go in both directions, as indicated by the double-headed arrow in **Fig. 1.6**. The possibility of ET from ligands to NCs using an organic molecule with larger absorption cross-section and broad excitation/emission band as antenna to sensitize the emission of lanthanide ion, namely dye-sensitized luminescence, is explored in **Ch. 4** for dye-sensitized downconversion. The opposite process, ET from ions inside luminescent NCs to surface ligands, is the basis for emerging applications of NCs, viz. in photodynamic therapy, to generate cytotoxic reactive oxygen species from a photosensitizer that is sensitized by luminescent NCs,<sup>58</sup> and in biosensors based on the large difference in decay times for emission from lanthanide ions and organic molecules.<sup>59</sup>



**Figure 1.6.** Schematic diagram of NCs. The cons (dash labels: surface-related quenching) and pros (solid labels: energy transfer between ligands and lanthanide-doped NCs) in (a) core and (b) core-shell NCs.

#### 1.4 Scope and Outline of the Thesis

The field of lanthanide-doped NCs offers new opportunities but also faces challenges as discussed above. It is the aim of this thesis to provide new insights that can help to understand and solve questions in the field of Ln-doped NCs. There is a focus on understanding optical properties of NCs which show luminescence based on multi-photon processes (up- and downconversion). The thesis discusses synthesis methods and optical experiments for fluoride and tungstate NCs. Experiments are reported that aim to solve the issues of the low quantum yield of upconversion in NCs, the weak absorption of lanthanide-based downconverters and the role of multi-phonon processes to explain the marked differences in thermal behavior and concentration quenching between lanthanide ions in NCs and bulk materials. The outline of the thesis is as follows:

**Chapter 2** makes use of NaYF<sub>4</sub> NCs doped with Eu<sup>3+</sup> and Gd<sup>3+</sup> as experimental systems to test theoretical prediction on the cubic dependence of magnetic dipole transition probabilities on refractive index. Solvents with higher refractive index give rise to higher transition probabilities. In addition to the measurements on luminescence decay time, the results on ED/MD intensity ratios are consistent with theory to provide strong experimental evidence for an  $n^3$  dependence of magnetic dipole transition probabilities.

In **Chapter 3**, we provide a better understanding of the intrinsic cause for low quantum efficiencies of upconversion in highly doped NCs. We study the concentration quenching in core and core-shell NaYF<sub>4</sub> NCs with varying concentrations of Er<sup>3+</sup> or Yb<sup>3+</sup> ion. Detailed analysis of decay dynamics demonstrates that Er<sup>3+</sup> <sup>4</sup>I<sub>11/2</sub> intermediate level is significantly affected by concentration quenching and high-energy vibrations, giving rise to a large loss of upconversion efficiency. In contrast, there is no concentration quenching for Yb<sup>3+</sup> in core-shell NCs. In addition, the

upconversion emission from  $\text{Er}^{3+}$  is influenced differently: the upconverted green emission is strongly quenched while the upconverted red emission remains efficient at high  $\text{Er}^{3+}$  concentrations.

**Chapter 4** demonstrates a new concept of dye-sensitized downconversion via hybrid Coumarin- $\text{NaYF}_4:\text{Pr}^{3+},\text{Yb}^{3+}$  NCs. The luminescence spectra and decay time measurements give evidence for the occurrence of Förster resonance energy transfer from the Coumarin dye attached to the NC surface to  $\text{Pr}^{3+}$  ions inside the NC core. This is followed by two-step energy transfer to  $\text{Yb}^{3+}$  (downconversion). With an optimal concentration of Coumarin dye molecules, the downconversion emission is enhanced by a factor of  $\sim 30$ .

In **Chapter 5**, a versatile thermolysis protocol is developed to synthesize ultrathin diamond shaped  $\text{NaRE}(\text{WO}_4)_2$  NCs. Oriented attachment for single NC can occur in the [001] direction. Variation of dopant species and doping concentration does not affect the diamond shape and size distribution for the NCs. Being a self-activated phosphor, these tungstate NCs show strong characteristic emission of lanthanide ions upon excitation in the charge transfer band of tungstate group. For example,  $\text{NaRE}(\text{WO}_4)_2:\text{Eu}^{3+}$  NCs show strong red emission with a long  $^5\text{D}_0$  decay time, comparable to that in bulk material.

In **Chapter 6**, we investigate the temperature dependence of upconversion emission intensity in  $\text{NaRE}(\text{WO}_4)_2$  NCs. A strong enhancement of upconversion efficiencies have been observed upon heating until  $\sim 470$  K for different upconversion NCs in ambient atmosphere. The thermal enhancement is reversible. For comparison, bulk materials show thermal quenching as expected. To understand the origin of the thermal enhancement in ambient atmosphere, the upconversion emission is measured upon heating and cooling in dry nitrogen. After an initial thermal enhancement, subsequent cycling experiments show a higher remaining upconversion emission intensity upon cooling and thermal quenching upon heating. These experiments indicate that the cause of thermal enhancement of upconversion is the loss of surface adsorbed water that can be reabsorbed during cooling under ambient conditions. These insights shed the light on the cause of thermal enhancement of upconversion efficiencies in Ln-doped NCs.

**Chapter 7** summarizes the main results through the thesis and gives an outlook for the future study and in relation to potential applications for multi-photon nanomaterials.

### 1.5 References

1. Eliseeva, S. V.; Bünzli, J.-C. G. Rare Earths: Jewels for Functional Materials of the Future. *New J. Chem.* **2011**, *35*, 1165-1176.

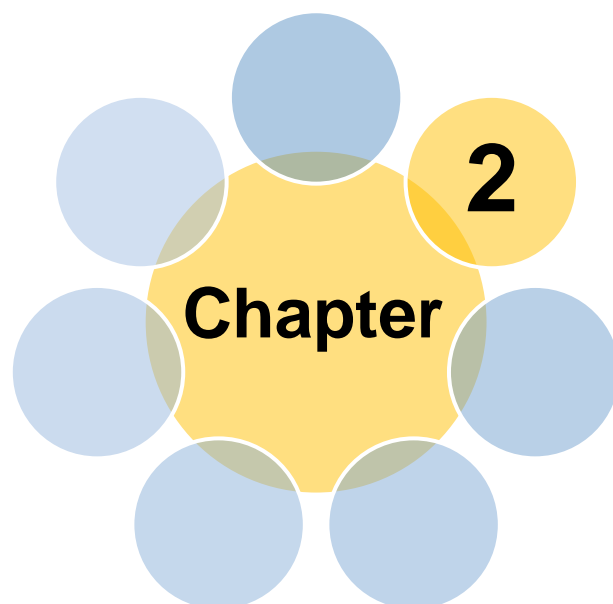
2. Dieke, G. H.; Crosswhite, H. M., Dunn, B. Emission Spectra of the Doubly and Triply Ionized Rare Earths. *J. Opt. Soc. Am.* **1961**, *51*, 820-827.
3. Einstein, A. Zur Quantentheorie der Strahlung. *Physik Z* **1917**, *18*, 121-128.
4. Judd, B. R. Optical Absorption Intensities of Rare-Earth Ion. *Phys. Rev.* **1962**, *127*, 750-761.
5. Ofelt, G. S. Intensities of Crystal Spectra of Rare-Earth Ions. *J. Chem. Phys.* **1962**, *37*, 511-519.
6. Tanner, P. A.; Duan, C. K. Luminescent Lanthanide Complexes: Selection Rules and Design. *Coord. Chem. Rev.* **2010**, *254*, 3026-3029.
7. Tanner, P. A. Some Misconceptions Concerning the Electronic Spectra of Tri-Positive Europium and Cerium. *Chem. Soc. Rev.* **2013**, *42*, 5090-5101.
8. Duan, C. K.; Reid, M. F. Macroscopic Models for the Radiative Relaxation Decay time of Luminescent Centers Embedded in Surrounding Media. *Spectrosc. Lett.* **2007**, *40*, 237-246.
9. Purcell, E. M. Spontaneous Emission Probabilities at Radio Frequencies. *Phys. Rev.* **1946**, *69*, 681.
10. Kuznetsov, A. I.; Miroshnichenko, A. E.; Brongersma, M. L.; Kivshar, Y. S.; Luk'yanchuk, B. Optically Resonant Dielectric Nanostructures. *Science* **2016**, *354*, aag2472.
11. Koenderink, A. F.; Alù, A.; Polman, A. Nanophotonics: Shrinking Light-Based Technology. *Science* **2015**, *348*, 516-521.
12. Riseberg, L. A.; Moos, H. W. Multiphonon Orbit-Lattice Relaxation of Excited States of Rare-Earth Ions in Crystals. *Phys. Rev.* **1968**, *174*, 429-438.
13. Riseberg, L. A.; Moos, H. W. Multiphonon Orbit-Lattice Relaxation in LaBr<sub>3</sub>, LaCl<sub>3</sub>, and LaF<sub>3</sub>. *Phys. Rev. Lett.* **1967**, *25*, 1423-1426.
14. Schuurmans, M. F. H.; Vandijk, J. M. F. On Radiative and Non-Radiative Decay Times in the Weak Coupling Limit. *Physica B + C (Amsterdam)* **1984**, *123*, 131-155.
15. Weber, M. J. Radiative and Multiphonon Relaxation of Rare-Earth Ions in Y<sub>2</sub>O<sub>3</sub>. *Phys. Rev.* **1968**, *171*, 283-291.
16. Ananias, D.; Paz, F. A. A.; Yufit, D. S.; Carlos, L. D.; Rocha, J. Photoluminescent Thermometer Based on a Phase-Transition Lanthanide Silicate with Unusual Structural Disorder. *J. Am. Chem. Soc.* **2015**, *137*, 3051-3058.
17. Bloembergen, N. Solid State Infrared Quantum Counters. *Phys. Rev. Lett.* **1959**, *2*, 84-85.
18. Auzel, F. Upconversion and Anti-Stokes Processes with f and d Ions in Solids. *Chem. Rev.* **2004**, *104*, 139-173.
19. Ovsyakin, V. V.; Feoflov, P. P. Cooperative Sensitization of Luminescence in Crystals Activated with Rare Earth Ions. *JETP Lett. Engl.* **1966**, *4*, 317-318.
20. Pollnau, M.; Gamelin, D. R.; Lüthi, S. R.; Güdel, H. U.; Hehlen, M. P. Power Dependence of Upconversion Luminescence in Lanthanide and Transition-Metal-Ion Systems. *Phys. Rev. B: Condens. Matter Mater. Phys.* **2000**, *61*, 3337-3346.

21. Suyver, J. F.; Aebischer, A.; Garcia-Revilla, S.; Gerner, P.; Güdel, H. U. Anomalous Power Dependence of Sensitized Upconversion Luminescence. *Phys. Rev. B: Condens. Matter Mater. Phys.* **2005**, *71*, 125123.
22. Shalav, A.; Richards, B. S.; Trupke, T.; Krämer, K. W.; Güdel, H. U. Application of NaYF<sub>4</sub>:Er<sup>3+</sup> Up-Converting Phosphors for Enhanced Near-Infrared Silicon Solar Cell Response. *Appl. Phys. Lett.* **2005**, *86*, 013505.
23. Lahoz, F. Ho<sup>3+</sup>-Doped Nanophase Glass Ceramics for Efficiency Enhancement in Silicon Solar Cells. *Opt. Lett.* **2008**, *33*, 2982-2984.
24. Ostermayer, F. M.; Van Uitert, L. G. Cooperative Energy Transfer from Yb<sup>3+</sup> to Tb<sup>3+</sup> in YF<sub>3</sub>. *Phys. Rev. B: Solid State* **1970**, *1*, 4208-4212.
25. Salley, G. M.; Valiente, R.; Güdel, H. U. Cooperative Yb<sup>3+</sup>-Tb<sup>3+</sup> Dimer Excitations and Upconversion in Cs<sub>3</sub>Tb<sub>2</sub>Br<sub>9</sub>:Yb<sup>3+</sup>. *Phys. Rev. B: Condens. Matter Mater. Phys.* **2003**, *67*, 134111.
26. Chivian, J. S.; Case, W. E.; Eden, D. D. The Photon Avalanche: A New Phenomenon in Pr<sup>3+</sup>-Based Infrared Quantum Counters. *Appl. Phys. Lett.* **1979**, *35*, 124-125.
27. Zhang, Q. Y.; Huang, X. Y. Recent Progress in Quantum Cutting Phosphors. *Prog. Mater. Sci.* **2010**, *55*, 353-427.
28. Yu, D. C.; Martín-Rodríguez, R.; Zhang, Q. Y.; Meijerink, A.; Rabouw, F. T. Multi-Photon Quantum Cutting in Gd<sub>2</sub>O<sub>2</sub>S:Tm<sup>3+</sup> to Enhance the Photo-Response of Solar Cells. *Light: Sci. Appl.* **2015**, *4*, e344.
29. Dexter, D. L. Possibility of Luminescent Quantum Yields Greater than Unity. *Phys. Rev.* **1957**, *108*, 630-633.
30. Sommerdijk, J. L.; Bril, A.; de Jager, A. W. Two Photon Luminescence with Ultraviolet Excitation of Trivalent Praseodymium. *J. Lumin.* **1974**, *8*, 341-343.
31. Piper, W. W.; DeLuca, J. A.; Ham, F. S. Cascade Fluorescent Decay in Pr<sup>3+</sup>-Doped Fluorides: Achievement of a Quantum Yield Greater than Unity for Emission of Visible Light. *J. Lumin.* **1974**, *8*, 344-348.
32. Wegh, R. T.; Donker, H.; Oskam, K. D.; Meijerink, A. Visible Quantum Cutting in LiGdF<sub>4</sub>:Eu<sup>3+</sup> through Downconversion. *Science* **1999**, *283*, 663-666.
33. Wegh, R. T.; Donker, H.; van Loef, E. V. D.; Oskam, K. D.; Meijerink, A. Quantum Cutting through Downconversion in Rare-Earth Compounds. *J. Lumin.* **2000**, *87-89*, 1017-1019.
34. Lin, H.; Chen, D. Q.; Yu, Y. L.; Yang, A. P.; Wang, Y. S. Near-Infrared Quantum Cutting in Ho<sup>3+</sup>/Yb<sup>3+</sup> Codoped Nanostructured Glass Ceramic. *Opt. Lett.* **2011**, *36*, 876-878.
35. Vergeer, P.; Vlugt, T. J. H.; Kox, M. H. F.; den Hertog, M. I.; van der Eerden, J. P. J. M.; Meijerink, A. Quantum Cutting by Cooperative Energy Transfer in Yb<sub>x</sub>Y<sub>1-x</sub>PO<sub>4</sub>:Tb<sup>3+</sup>. *Phys. Rev. B: Condens. Matter Mater. Phys.* **2005**, *71*, 014119.
36. van der Ende, B. M.; Aarts, L.; Meijerink, A. Near-Infrared Quantum Cutting for Photovoltaics. *Adv. Mater.* **2009**, *21*, 3073-3077.

37. Förster, T. Zwischenmolekulare Energiewanderung und Fluoreszenz. *Ann. Phys.* **1948**, *437*, 55-75.
38. Dexter, D. L. A Theory of Sensitized Luminescence in Solids. *J. Chem. Phys.* **1953**, *21*, 836-850.
39. Wang, F.; Liu, X. G. Recent Advances in the Chemistry of Lanthanide-Doped Upconversion Nanocrystals. *Chem. Soc. Rev.* **2009**, *38*, 976-989.
40. Rossetti, R.; Nakahara, S.; Brus, L. E. Quantum Size Effects in the Redox Potentials, Resonance Raman Spectra, and Electronic Spectra of CdS Crystallites in Aqueous Solution. *J. Chem. Phys.* **1983**, *79*, 1086-1088.
41. Bruchez, M.; Moronne, M.; Gin, P.; Weiss, S.; Alivisatos, A. P. Semiconductor Nanocrystals as Fluorescent Biological Labels. *Science* **1998**, *281*, 2013-2016.
42. Chan, W. C. W.; Nie, S. M. Quantum Dot Bioconjugates for Ultrasensitive Nonisotopic Detection. *Science* **1998**, *281*, 2016-2018.
43. Talapin, D. V.; Steckel, J. Quantum Dot Light-Emitting Devices. *MRS Bull.* **2013**, *38*, 685-695.
44. Hobbs, R. G.; Petkov, N.; Holmes, J. D. Semiconductor Nanowire Fabrication by Bottom-Up and Top-Down Paradigms. *Chem. Mater.* **2012**, *24*, 1975-1991.
45. Wang, Y. L.; Xia, Y. N. Bottom-Up and Top-Down Approaches to the Synthesis of Monodispersed Spherical Colloids of Low Melting-Point Metals. *Nano Lett.* **2004**, *4*, 2047-2050.
46. Johnson, N. J. J.; Korinek, A.; Dong, C. H.; van Veggel, F. C. J. M. Self-Focusing by Ostwald Ripening: A Strategy for Layer-by-Layer Epitaxial Growth on Upconverting Nanocrystals. *J. Am. Chem. Soc.* **2012**, *134*, 11068-11071.
47. Peng, X. G.; Schlamp, M. C.; Kadavanich, A. V.; Alivisatos, A. P. Epitaxial Growth of Highly Luminescent CdSe/CdS Core/Shell Nanocrystals with Photostability and Electronic Accessibility. *J. Am. Chem. Soc.* **1997**, *119*, 7019-7029.
48. Boles, M. A.; Ling, D. S.; Hyeon, T.; Talapin, D. V. The Surface Science of Nanocrystals. *Nat. Mater.* **2016**, *15*, 141-153.
49. Zhang, Q. B.; Wang, X.; Zhu, Y. M. Multicolor Upconverted Luminescence-Encoded Superparticles via Controlling Self-Assembly Based on Hydrophobic Lanthanide-Doped NaYF<sub>4</sub> Nanocrystals. *J. Mater. Chem.* **2011**, *21*, 12132-12138.
50. Zheng, T.; Sun, L. D.; Zhou, J. C.; Feng, W.; Zhang, C.; Yan, C. H. Construction of NaREF<sub>4</sub>-Based Binary and Bilayer Nanocrystal Assemblies. *Chem. Commun.* **2013**, *49*, 5799-5801.
51. Ye, X. C.; Collins, J. E.; Kang, Y. J.; Chen, J.; Chen, D. T. N.; Yodh, A. G.; Murray C. B. Morphologically Controlled Synthesis of Colloidal Upconversion Nanophosphors and Their Shape-Directed Self-Assembly. *Proc. Natl. Acad. Sci. U. S. A.* **2010**, *107*, 22430-2243.
52. Zhou, J.; Liu, Z.; Li, F. Y. Upconversion Nanophosphors for Small-Animal Imaging. *Chem. Soc. Rev.* **2012**, *41*, 1323-1349.
53. Idris, N. M.; Gnanasammandhan, M. K.; Zhang, J.; Ho, P. C.; Mahendran, R.; Zhang, Y. In Vivo

- Photodynamic Therapy Using Upconversion Nanoparticles as Remote-Controlled Nanotransducers. *Nat. Med.* **2012**, *18*, 1580-1585.
54. Dong, H.; Du, S. R.; Zheng, X. Y.; Lyu, G. M.; Sun, L. D.; Li, L. D.; Zhang, P. Z.; Zhang, C.; Yan, C. H. Lanthanide Nanoparticles: From Design toward Bioimaging and Therapy. *Chem. Rev.* **2015**, *115*, 10725-10815.
55. Xiao, M.; Selvin, P. R. Quantum Yields of Luminescent Lanthanide Chelates and Far-Red Dyes Measured by Resonance Energy Transfer. *J. Am. Chem. Soc.* **2001**, *123*, 7067-7073.
56. Xu, J. T.; Yang, P. P.; Sun, M. D.; Bi, H. T.; Liu, B.; Yang, D.; Gai, S. L.; He, F.; Lin, J. Highly Emissive Dye-Sensitized Upconversion Nanostructure for Dual-Photosensitizer Photodynamic Therapy and Bioimaging. *ACS Nano* **2017**, *11*, 4133-4144.
57. Wang, X. D.; Valiev, R. R.; Ohulchanskyy, T. Y.; Ågren, H.; Yang, C. H.; Chen, G. Y. Dye-Sensitized Lanthanide-Doped Upconversion Nanoparticles. *Chem. Soc. Rev.* **2017**, *46*, 4150-4167.
58. Lucky, S. S.; Soo, K. C.; Zhang, Y. Nanoparticles in Photodynamic Therapy. *Chem. Rev.* **2015**, *115*, 1990-2042.
59. Tu, D. T.; Liu, L. Q.; Ju, Q.; Liu, Y. S.; Zhu, H. M.; Li, R. F.; Chen, X. Y. Time-Resolved FRET Biosensor Based on Amine-Functionalized Lanthanide-Doped NaYF<sub>4</sub> Nanocrystals. *Angew. Chem. Int. Ed.* **2011**, *50*, 6306-6310.





# Photonic effects for magnetic dipole transitions

Based on

Wang, Z. J.; Senden, T.; Meijerink, A. Photonic Effects for Magnetic Dipole Transitions. *J. Phys. Chem. Lett.* **2017**, *8*, 5689-5694.

## 2.1 Abstract

The radiative transition probability is a fundamental property for an optical transition. Extensive research, both theoretical and experimental, has been conducted to establish the relation between the photonic environment of an emitter and electric dipole (ED) transition probabilities. Recent work has demonstrated that the nanocrystal (NC)-cavity model accurately describes the influence of the refractive index  $n$  of a surrounding medium on ED transition rates for emitters in NCs. For magnetic dipole (MD) transition rates, theory predicts a simple  $n^3$  dependence. However, experimental evidence is difficult to obtain. Here, we used  $\text{Eu}^{3+}$  (ED + MD) and  $\text{Gd}^{3+}$  (over 90% MD) doped  $\beta\text{-NaYF}_4$  NCs in solvents with different  $n$ . The influence of  $n$  on ED and MD transition probabilities is probed by luminescence lifetime and ED/MD intensity ratio measurements. The results provide strong experimental proofs for the theoretically predicted  $n^3$  dependence of MD transition probabilities. This insight is important for understanding and controlling the variation in spectral distribution in emission spectra by the photonic environment.

## 2.2 Introduction

The spontaneous emission rate of an emitter is governed by Fermi's golden rule. Both the transition dipole moment and the photon density of states resonant with the transition affect the emission rate. The transition dipole moment depends on the wave functions of the initial and final states involved in the transition. For electric dipole (ED) transitions, the electromagnetic field strength interacting with the transition is influenced by the local environment and a local field correction factor  $\chi$  is required. The transition probability  $k_{\text{ED}}$  is thus given by

$$k_{\text{ED}} = k_{\text{ED}}^0 n \chi^2 \quad (2.1)$$

where  $k_{\text{ED}}$  is the radiative decay rate of ED transition when the emitter is surrounded by a dielectric medium with the refractive index  $n$ , and  $k_{\text{ED}}^0$  is the decay rate in vacuum ( $n = 1$ ). The experimentally observed transition rate  $k$  is proportional to the local density of states (LDOS) as described in the Fermi's golden rule, and can be modified by tuning the dielectric medium in which the emitter is embedded.<sup>1</sup> The distance over which the dielectric properties of the surrounding medium affect the transition rate is of the order of the wavelength of light that is emitted (hundreds of nm). Extensive theoretical work has resulted in a variety of models for the correction factor  $\chi$  of local field. The most prominent models are the virtual cavity model<sup>2-4</sup> and the real cavity model,<sup>5-8</sup> which predict a relation between the refractive index  $n$  of the medium and  $k_{\text{ED}}$  as defined by [Eqs. 2.2, 2.3](#).

$$k_{\text{ED}} = k_{\text{ED}}^0 n \left( \frac{n^2 + 2}{3} \right)^2 \quad (2.2)$$

$$k_{\text{ED}} = k_{\text{ED}}^0 n \left( \frac{3n^2}{2n^2 + 1} \right)^2 \quad (2.3)$$

For emitters doped in a nanocrystal (NC), the refractive index  $n_{\text{NC}}$  of the NC must also be taken into consideration, giving rise to the NC-cavity model:<sup>9</sup>

$$k_{\text{ED}} = k_{\text{ED}}^0 n \left( \frac{3n^2}{2n^2 + n_{\text{NC}}^2} \right)^2 \quad (2.4)$$

The validity of the NC-cavity model has been recently demonstrated by our group.<sup>10,11</sup>

In contrast to the extensive research on photonic effects on ED transition rates, research on the influence of the local surroundings on magnetic dipole (MD) transitions has been very limited. Theoretical work predicts that the situation is simple compared to ED transitions. There are no local field effects since the magnetic susceptibility (in a nonmagnetic medium) is the same as for vacuum and thus a simple cubic dependence of MD transition rate on the refractive index (reflecting the variation of photon density of states with  $n$ ) is predicted:<sup>12</sup>

$$k_{\text{MD}} = k_{\text{MD}}^0 n^3 \quad (2.5)$$

where  $k_{\text{MD}}$  and  $k_{\text{MD}}^0$  are the radiative decay rates of the MD transition for the emitter in a dielectric medium with refractive index  $n$  and in vacuum, respectively.

Experimental results on the variation of MD transition rate with  $n$  are rare. Pure MD transitions are not often to observe, which makes it challenging to test the simple theoretical relationship between  $k_{\text{MD}}$  and  $n$ . In 1995 Rikken<sup>13</sup> and later in 2002 Werts<sup>14</sup> reported on the influence of  $n$  on MD transition probabilities. In **Ref. 13**,  $\text{Eu}^{3+}$  complexes were studied as  $\text{Eu}^{3+}$  has distinct MD ( $^5\text{D}_0\text{-}^7\text{F}_1$ ) and ED ( $^5\text{D}_0\text{-}^7\text{F}_2$  and  $^5\text{D}_0\text{-}^7\text{F}_4$ ) transitions. For the complexes dissolved in solvents with different refractive index, the influence of  $n$  on the MD and ED transition rates was measured and explained using the real cavity model (**Eq. 2.3**) for the ED transitions and the  $n^3$  dependence (**Eq. 2.5**) for the MD transitions. A good agreement was obtained taking into account non-radiative decay (partial quenching) and a  $k_{\text{MD}}^0$  of  $10 \text{ s}^{-1}$  for the  $^5\text{D}_0\text{-}^7\text{F}_1$  transition. This rate is significantly lower than the theoretically calculated value of  $k_{\text{MD}}^0$  of  $14.4 \text{ s}^{-1}$ .<sup>15</sup> Variations in ED transition rates resulting from conformational changes in the complexes in different solvents were not considered. These changes may affect the ED transition rates. The forced ED transitions in lanthanide ions are extremely sensitive to small changes in the local geometry, which can affect the transition dipole moments. In the work by Werts,<sup>14</sup> radiative lifetimes of  $\text{Eu}^{3+}$   $^5\text{D}_0$  emission in different complexes and crystalline materials were compared and related to the intensity ratio of the  $^5\text{D}_0\text{-}^7\text{F}_1$  MD emission

lines to the total (ED + MD) emission intensity. Within the experimental accuracy (largely determined by uncertainties in the quantum yields QYs), a good agreement was obtained assuming an  $n^3$  dependence of the MD transition rates.

In spite of these two insightful studies, a systematic and accurate investigation using model systems to study the relation between  $k_{\text{MD}}$  and  $n$  is still lacking. As shown previously, doped NCs serve as ideal probes for refractive index effects on optical properties.<sup>10,11,16-20</sup> The size of the NCs (~10 nm) is far below the length scale of hundreds of nanometers at which photonic effects influence the transitions for emitters embedded in the NC. The local coordination of the emitters is determined by the nanocrystalline host and is the same as in bulk crystalline material. Because the local coordination is completely unaffected by the solvent in which the NCs are dispersed, an ideal model system is realized in which only the variation in refractive index of the medium surrounding the NCs influences the radiative decay rate of the emitters in the NCs.

In the present work, we measured the dependence of MD transitions on the refractive index in two NC model systems. First, the decay dynamics and ED/MD intensity ratios were measured for  $\text{Eu}^{3+}$ -doped  $\beta\text{-NaYF}_4$  core and core-shell NCs suspended in solvents with different refractive index. The results are consistent with a NC-cavity model for ED transition rates ( $^5\text{D}_0\text{-}^7\text{F}_2$ ,  $^5\text{D}_0\text{-}^7\text{F}_4$ ) and an  $n^3$  dependence for the decay rate of the MD transition ( $^5\text{D}_0\text{-}^7\text{F}_1$ ) on  $\text{Eu}^{3+}$ . Next, the decay rate for the  $^6\text{P}_{7/2}\text{-}^8\text{S}_{7/2}$  transition for  $\text{Gd}^{3+}$  in  $\text{NaYF}_4$  core-shell NCs was measured. This transition has over 90% MD character in fluorides<sup>21,22</sup> and this allows for direct evaluation of the relation between  $k_{\text{MD}}$  and  $n$ . Again, a very good agreement was obtained for an  $n^3$  dependence of the MD transition probabilities. The present results provide strong experimental evidence for the theoretically predicted  $n^3$  dependence for MD transition rates using lanthanide-doped NCs as model systems. The NC model systems may be used to not only test theoretical models but also serve as local probes for photonic effects with high spatial resolution by measuring luminescence decay rates and ED/MD intensity ratios for emission from lanthanide dopants in NCs at well-defined positions in a photonic medium.

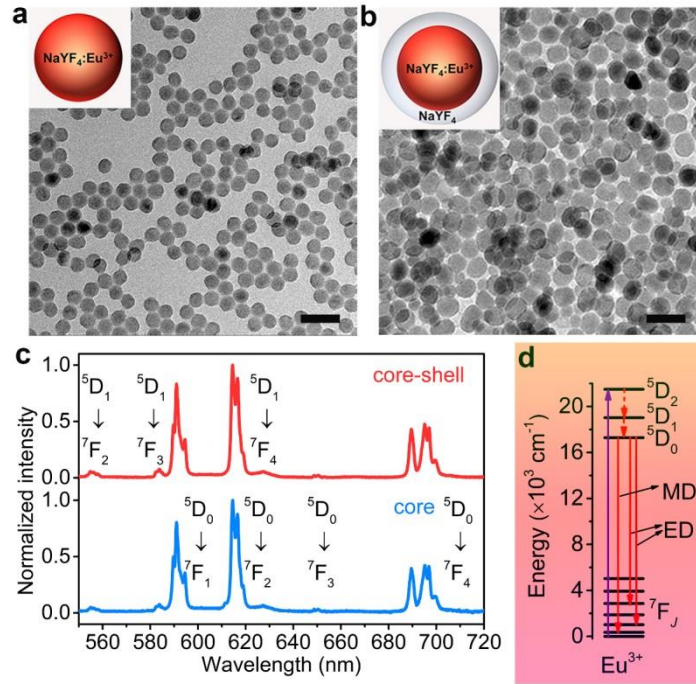
### 2.3 Results and discussion

**$\text{NaYF}_4\text{:Eu}^{3+}$  NCs** Transmission electron microscopy (TEM) images are shown for core (**Fig. 2.1a**) and core-shell (**Fig. 2.1b**) NCs. The  $\text{NaY}_{0.9}\text{Eu}_{0.1}\text{F}_4$  core NCs are monodisperse and nearly spherical with a diameter of ~22 nm. The epitaxial growth of an inert shell gives rise to slightly prolate ~28 × 25 nm  $\text{NaY}_{0.9}\text{Eu}_{0.1}\text{F}_4\text{@NaYF}_4$  core-shell NCs. Unlike the quantum confinement featured in semiconductor NCs, the electronic states of rare earth ions are localized and do not depend on the shape or size of NCs. The oleate ligands on the surface allow the NCs to colloiddally stabilize in apolar solvents as the surrounding dielectric medium. This makes it possible to investigate the influence of the photonic environment (homogeneous dielectric medium) on electronic

transitions.<sup>10,11</sup> Six commonly used solvents with increasing refractive index  $n$  are diethyl ether ( $n = 1.35$ ), hexane ( $n = 1.38$ ), octane ( $n = 1.40$ ), chloroform ( $n = 1.45$ ), toluene ( $n = 1.50$ ) and chlorobenzene ( $n = 1.53$ ). As an example, **Fig. 2.1c** presents the emission spectra (corrected for the instrumental response) for  $\text{Eu}^{3+}$ -doped core and core-shell NCs dispersed in chlorobenzene upon the excitation at 465 nm ( ${}^7\text{F}_0$ - ${}^5\text{D}_2$ ). Both spectra show the same characteristic emission peaks of  $\text{Eu}^{3+}$  (assignments are given in the figure). Variation of solvents does not affect the energy level structure, resulting in identical emission spectra except for a slight change of relative intensities of emission lines due to the photonic effect (*vide infra*). After excitation to the higher excited  ${}^5\text{D}_2$  state, fast non-radiative relaxation occurs to the  ${}^5\text{D}_0$  state. Subsequently, the  ${}^5\text{D}_0$  state decays radiatively through both forced ED transitions ( ${}^5\text{D}_0$ - ${}^7\text{F}_2$  at  $\sim 615$  nm and  ${}^5\text{D}_0$ - ${}^7\text{F}_4$  at  $\sim 695$  nm) and MD transition ( ${}^5\text{D}_0$ - ${}^7\text{F}_1$  at  $\sim 590$  nm) as depicted in the energy level diagram in **Fig. 2.1d**. Emission from the  ${}^5\text{D}_1$  state can be also observed although with low intensity. The low phonon energy of  $\text{NaYF}_4$  ( $\sim 350$   $\text{cm}^{-1}$ ) limits multi-phonon relaxation (MPR) rates and radiative decay from the higher excited  ${}^5\text{D}_1$  state can compete with MPR to the lowest excited  ${}^5\text{D}_0$  state. To reduce the fraction of  ${}^5\text{D}_1$  emission, a relatively high  $\text{Eu}^{3+}$  concentration was used. Efficient cross-relaxation  ${}^5\text{D}_1$ - ${}^5\text{D}_0$  and  ${}^7\text{F}_0$ - ${}^7\text{F}_3$  on neighboring  $\text{Eu}^{3+}$  ions quenches the  ${}^5\text{D}_1$  emission, which can interfere with the analysis of the relative intensities of MD and ED emission from the  ${}^5\text{D}_0$  level due to spectral overlap.

To investigate the refractive index dependence of MD transitions, two methods can be used for  $\text{NaYF}_4:\text{Eu}^{3+}$  NCs. A first method involves luminescence decay time measurements. Emission from the  ${}^5\text{D}_0$  level is dominated by radiative decay and the total decay rate is the sum of decay rates for ED and MD transitions. Measuring the  ${}^5\text{D}_0$  emission decay rate in media with different  $n$  provides information on the refractive index dependence of the ED and MD decay rates. A second method relies on intensity ratio measurements. As discussed above, both ED and MD transitions occur from the  ${}^5\text{D}_0$  level of  $\text{Eu}^{3+}$ . The difference in  $n$  dependence for ED and MD transitions influences the relative intensities of MD and ED transitions. The change in ratio as a function of  $n$  can be used to verify the  $n^3$  dependence of MD transitions. For both methods, we will initially assume that the refractive index dependence of ED transition rates follows the NC-cavity model (**Eq. 2.4**) that was established previously, but also other dependences for the ED transition rates will be considered.

First, we consider the total  ${}^5\text{D}_0$  decay rate for  $\text{NaYF}_4:\text{Eu}^{3+}$  NCs in media with different refractive index. **Fig. 2.2a** shows the decay curves for  ${}^5\text{D}_0$  emission for  $\text{NaY}_{0.9}\text{Eu}_{0.1}\text{F}_4@ \text{NaYF}_4$  core-shell NCs dispersed in different solvents. Ideally, the decay curves are single-exponential, but as a result of coupling with high-energy vibrations of surface ligands, there is a contribution from non-radiative MPR decay, especially for  $\text{Eu}^{3+}$  ions close to the surface. For core-shell NCs, the MPR rate is reduced but still cannot completely be neglected. Therefore, two fitting procedures were used, one based on the average lifetime and one for the lifetime determined from the single-exponential fitting



**Figure 2.1.** Characterization of  $\text{NaY}_{0.9}\text{Eu}_{0.1}\text{F}_4$  core and  $\text{NaY}_{0.9}\text{Eu}_{0.1}\text{F}_4@\text{NaYF}_4$  core-shell NCs. TEM images of (a) core and (b) core-shell NCs (scale bar = 50 nm). (c) Emission spectra of core and core-shell NCs dispersed in chlorobenzene for excitation in the  ${}^7\text{F}_0$ - ${}^5\text{D}_2$  transition at 465 nm with the assignments of emission lines. (d) Energy level diagram of  $\text{Eu}^{3+}$ : absorption of a 465 nm photon excites  $\text{Eu}^{3+}$  to the excited  ${}^5\text{D}_2$  state, followed by a non-radiative decay to the  ${}^5\text{D}_0$  state. Emission in the orange/red spectral region is observed through radiative decay to the ground state multiplet  ${}^7\text{F}_J$ , including forced ED ( ${}^5\text{D}_0$ - ${}^7\text{F}_2$  and  ${}^5\text{D}_0$ - ${}^7\text{F}_4$ ) and MD ( ${}^5\text{D}_0$ - ${}^7\text{F}_1$ ) transitions.

of the decay curve for the  $\text{Eu}^{3+}$  emission in core-shell NCs which is close to single-exponential.

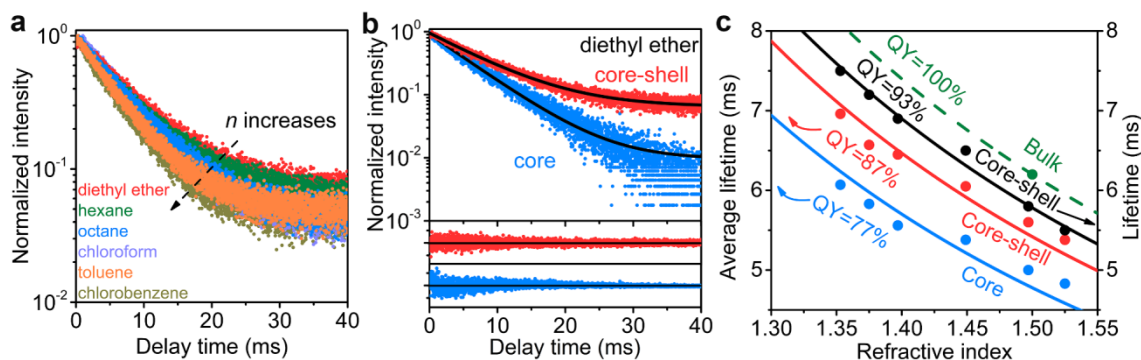
First, we consider the refractive index dependence of the average lifetime  $\tau_{\text{avg}}$ , determined via

$$\tau_{\text{avg}} = \frac{\sum_0^t tI(t)}{\sum_0^t I(t)} \quad (2.6)$$

where  $I(t)$  represents the emission intensity at time  $t$  (after background subtraction). For the  $\text{Eu}^{3+}$ -doped core NCs, the average lifetime of  ${}^5\text{D}_0$  state ranges from 6.1 to 4.8 ms upon increasing the refractive index from 1.35 to 1.53. A similar trend is observed for the core-shell NCs with a longer average lifetime for the  $\text{Eu}^{3+}$  emission in the same photonic environment. This is clearly illustrated in **Fig. 2.2b**, where the  $\text{Eu}^{3+}$  emission decay curves are shown for core and core-shell NCs dispersed in diethyl ether. It can be seen that the average lifetime is longer for the  $\text{Eu}^{3+}$ -doped core-shell NCs (7.0 vs. 6.1 ms for core NCs). The longer lifetime is due to the inert shell that suppresses but not fully

eliminates the quenching by surface defects and MPR involving high-energy vibrations. In the present study, the contributing vibrational modes in highest energy are  $\sim 3000\text{ cm}^{-1}$  C-H stretching vibrations from oleate ligands on the NC surface and solvent molecules.<sup>23,24</sup> The MPR affects only the initial decay and is similar for the different solvents. It is also evident that there is a stronger deviation from single-exponential decay for  $\text{Eu}^{3+}$  in the core-only NCs. The deviation from the single-exponential behavior can be appreciated by comparing the fitting residuals shown under the decay curves. There is a systematic deviation for the core-only decay curves, which show a faster initial decay. The decay curves for  $\text{Eu}^{3+}$  emission in both core and core-shell NCs in different solvents are shown in **Fig. A2.1** with the single-exponential fitting.

The average lifetime  $\tau_{\text{avg}}$  is the inverse of the sum of radiative decay rate  $k_r$  and non-radiative decay rate  $k_{\text{nr}}$ ,  $\tau_{\text{avg}} = 1/(k_r + k_{\text{nr}})$ . The radiative decay rates  $k_r$  for individual  ${}^5\text{D}_0$ - ${}^7\text{F}_J$  transition can be determined from the total radiative decay rate and the relative emission intensities (branching ratio) derived from the emission spectra. The non-radiative decay rate  $k_{\text{nr}}$  also contributes to the total decay rate in NCs and reduces the QY of  $\text{Eu}^{3+}$  emission. If the  ${}^5\text{D}_0$  radiative lifetime for  $\text{Eu}^{3+}$  in



**Figure 2.2.** Luminescence decay time measurements for  $\text{NaY}_{0.9}\text{Eu}_{0.1}\text{F}_4$  core and  $\text{NaY}_{0.9}\text{Eu}_{0.1}\text{F}_4@ \text{NaYF}_4$  core-shell NCs. Luminescence decay curves of the  $\text{Eu}^{3+}$  emission at 615 nm after pulsed 465 nm excitation for (a) core-shell NCs dispersed in solvents with different refractive index ranging from 1.35 for diethyl ether to 1.53 for chlorobenzene, and for (b) core and core-shell NCs dispersed in diethyl ether with a fitting to single-exponential function. The fitting residuals (deviation between the experimentally observed decay curve and single-exponential fitting) are shown in the lower panels for the core (blue) and core-shell (red) NCs. (c) Average lifetimes for core (blue) and core-shell (red) NCs. The black curve gives the lifetimes determined from a single-exponential tail ( $t > 1\text{ ms}$ ) fitting for the core-shell NCs. The green dashed line is based on the  ${}^5\text{D}_0$  emission decay time in  $\text{NaY}_{0.9}\text{Eu}_{0.1}\text{F}_4$  bulk material and gives the expected radiative lifetime as a function of the solvent refractive index. The drawn lines are fittings to **Eq. 2.7** assuming that the QY of  $\text{Eu}^{3+}$ -doped bulk material is 100%.

bulk NaYF<sub>4</sub> is known, the upper limit of the QY of Eu<sup>3+</sup>-doped NCs can be quantitatively determined using [Eq. 2.7](#).

$$\tau_{\text{avg}} = \text{QY} \tau_{\text{bulk}} / \left( \frac{I_{\text{ED}}}{I_{\text{tot}}} \frac{n \chi_{\text{NC}}^2}{n_{\text{NC}}} + \frac{I_{\text{MD}}}{I_{\text{tot}}} \frac{n^3}{n_{\text{NC}}^3} \right) \quad (2.7)$$

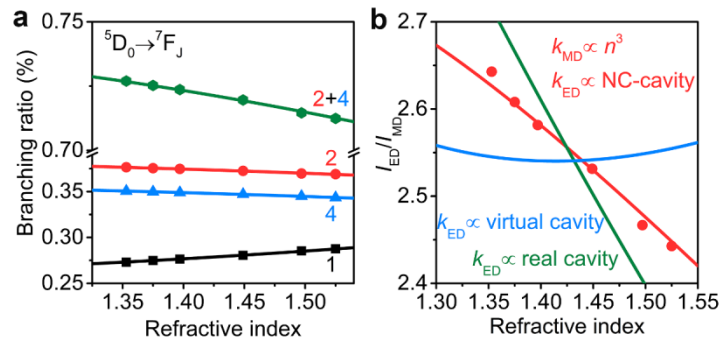
$I_{\text{ED}}/I_{\text{tot}}$  and  $I_{\text{MD}}/I_{\text{tot}}$  denote the fractions of ED and MD emission in the total integrated emission intensity for <sup>5</sup>D<sub>0</sub>-<sup>7</sup>F<sub>*J*</sub> (*J* = 1, 2 and 4) transitions in bulk material. The correction factor  $\chi_{\text{NC}}$  is taken from the NC-cavity model and  $\tau_{\text{bulk}}$  is the <sup>5</sup>D<sub>0</sub> lifetime of Eu<sup>3+</sup> doped in bulk NaYF<sub>4</sub>.  $\tau_{\text{bulk}}$  is determined to be 6.2 ms from lifetime measurements on the microcrystalline NaY<sub>0.9</sub>Eu<sub>0.1</sub>F<sub>4</sub>. This value is consistent with the value of 6.2 ms reported by Tanner<sup>25</sup> and corresponds to the radiative decay time. With this radiative decay time, the observed branching ratios and the refractive index of NaYF<sub>4</sub> (1.5),<sup>26</sup> the values for  $k_{\text{MD}}^0$  and  $k_{\text{ED}}^0$  can be determined. We find for  $k_{\text{MD}}^0$  14.3 s<sup>-1</sup> (very close to the theoretical value of 14.4 s<sup>-1</sup>)<sup>15</sup> and  $k_{\text{ED}}^0$  75.3 s<sup>-1</sup>.

To investigate the measured variation in radiative lifetime with refractive index, [Fig. 2.2c](#) plots the  $\tau_{\text{avg}}$  as a function of the solvent refractive index. Fitting the experimental results with [Eq. 2.7](#) gives a good agreement using a QY of 77 and 87% for the Eu<sup>3+</sup>-doped core and core-shell NCs, respectively. The slightly longer decay times derived from fitting the exponential tail of the Eu<sup>3+</sup> luminescence decay curves for core-shell NCs give an even higher QY of 93%. Note that the actual QYs may be lower as these values reflect the only emissive dopants in the ensemble, thus 87 (core-shell) and 77% (core) are the upper limits of the QY for Eu<sup>3+</sup> emission in the NCs.<sup>11,27</sup> Furthermore, the QY appears to increase for a higher refractive index of the solvent. A similar trend was also observed for Tb<sup>3+</sup>-doped LaPO<sub>4</sub> NCs.<sup>10,11</sup> The explanation is that both  $k_{\text{MD}}$  and  $k_{\text{ED}}$  increase as the refractive index increases, while  $k_{\text{nr}}$  is independent with the solvent refractive index as it involves energy transfer (non-radiative decay through MPR is best described as dipole-dipole energy transfer to high-energy vibrational overtones). Energy transfer rates do not depend on the refractive index of the medium surrounding the donor-acceptor pair. The increased radiative decay rate with constant non-radiative decay rate is responsible for the enhanced QY. In [Fig. A2.2](#), fittings with constant  $k_{\text{nr}}$  are shown to give a better agreement with experiment.

The analysis of the experimentally observed decay times of the Eu<sup>3+</sup> emission for core and core-shell NCs in solvents with different refractive index shows that the combination of the  $n^3$  dependence for  $k_{\text{MD}}$  and the NC-cavity model for  $k_{\text{ED}}$  can quantitatively explain the observed variation of the radiative decay rates. The good agreement between experiment and theory indicates that the MD transition rate indeed follows the theoretically predicted  $n^3$  dependence. However, because of the contribution of non-radiative decay, an additional fitting parameter (QY) was used to obtain the fitting curves in [Fig. 2.2c](#). An alternative method to test the validity of the  $n^3$  model is

based on the refractive index dependence of the intensity ratios of ED and MD emission lines. This method is more accurate as non-radiative decay quenches both types of emission equally. Besides, the variation in the ED/MD intensity ratio is a reliable probe to test refractive index dependence of  $k_{\text{MD}}$  in comparison to  $k_{\text{ED}}$  without the need for QY as an additional fitting parameter.

The difference in refractive index dependence for  $k_{\text{MD}}$  and  $k_{\text{ED}}$  (Eqs. 2.4, 2.5) shows that the intensity ratio of MD and ED transitions is expected to change as a function of  $n$ . The stronger  $n^3$  dependence for MD transitions predicts an increase in relative intensity of  ${}^5\text{D}_0\text{-}{}^7\text{F}_1$  emission with  $n$ . From the emission spectra, the relative intensities of the MD transition  ${}^5\text{D}_0\text{-}{}^7\text{F}_1$  and the ED transitions  ${}^5\text{D}_0\text{-}{}^7\text{F}_2$  and  ${}^5\text{D}_0\text{-}{}^7\text{F}_4$  were determined. There are also much weaker emission lines corresponding to the  ${}^5\text{D}_0\text{-}{}^7\text{F}_{0,3,5,6}$  transitions. Because of their low intensity, these lines are neglected in the present analysis. In Fig. 2.3a, the measured branching ratios for the MD and ED transitions are plotted together with the expected variation of the relative contributions to the total emission spectrum assuming an  $n^3$  dependence for MD transitions (Eq. 2.5) and the NC-cavity model (Eq. 2.4) for ED transitions. The agreement is good and values for  $k_{\text{MD}}^0$  ( $14.4 \text{ s}^{-1}$ ) and  $k_{\text{ED}}^0$  ( $78.2 \text{ s}^{-1}$ ) are determined, which are consistent with theory and the results for the  $\text{Eu}^{3+}$  emission in bulk  $\text{NaYF}_4$ . To further verify the refractive index dependence, Fig. 2.3b shows the experimentally observed ratio  $I_{\text{ED}}/I_{\text{MD}}$



**Figure 2.3.** Variation of emission intensities for ED and MD transitions as a function of the solvent refractive index for  $\text{NaY}_{0.9}\text{Eu}_{0.1}\text{F}_4@ \text{NaYF}_4$  core-shell NCs. (a) Branching ratios of the MD  ${}^5\text{D}_0\text{-}{}^7\text{F}_1$  (black), ED  ${}^5\text{D}_0\text{-}{}^7\text{F}_2$  (red), ED  ${}^5\text{D}_0\text{-}{}^7\text{F}_4$  (blue) and total ED  ${}^5\text{D}_0\text{-}{}^7\text{F}_2 + {}^5\text{D}_0\text{-}{}^7\text{F}_4$  (green) transition intensities. Filled symbols show experimental data and drawn lines are fittings for branching ratios based on an  $n^3$  dependence for  $k_{\text{MD}}$  and a NC-cavity model dependence for  $k_{\text{ED}}$ . (b) Intensity ratios of total ED ( ${}^5\text{D}_0\text{-}{}^7\text{F}_2 + {}^5\text{D}_0\text{-}{}^7\text{F}_4$ ) and MD ( ${}^5\text{D}_0\text{-}{}^7\text{F}_1$ ) emission ( $I_{\text{ED}}/I_{\text{MD}}$ ). The red dots represent the experimental results. The colored lines are the best fittings for an  $n^3$  dependence of  $k_{\text{MD}}$  assuming the NC-cavity model (red line), the virtual cavity model (blue line) or the real cavity model (green line) for the refractive index dependence of  $k_{\text{ED}}$ .

(red dots) and the red line shows the calculated ratio with  $k_{\text{MD}}$  proportional to  $n^3$  with  $k_{\text{MD}}^0 = 14.4 \text{ s}^{-1}$  and  $k_{\text{ED}}$  following the NC-cavity model with  $k_{\text{ED}}^0 = 78.2 \text{ s}^{-1}$ . Clearly, the  $n^3$  dependence for  $k_{\text{MD}}$  is in excellent agreement with the experimentally observed ratios. In Fig. 2.3a, the blue and green lines show the best fittings for ratios with a fixed  $n^3$  dependence for  $k_{\text{MD}}$  and for different refractive index dependencies for the ED transition probabilities, viz. the virtual cavity model (Eq. 2.2, blue line) and the real cavity model (Eq. 2.3, green line). Clearly, only the NC-cavity model can explain the experimentally observed variation in  $I_{\text{ED}}/I_{\text{MD}}$  assuming an  $n^3$  dependence for  $k_{\text{MD}}$ . The variation in  $I_{\text{ED}}/I_{\text{MD}}$  in the narrow refractive index range investigated here is limited (see Fig. 2.3). However, the intensity ratio that changes over an order of magnitude can be realized by making use of high refractive index materials based on metal or semiconductor nanostructures,<sup>28-30</sup> i.e. photonic and plasmonic structures.<sup>31-35</sup> These will allow a complete reversal of ED to MD intensities for emitters showing both types of emission, and give rise to much stronger variations in the luminescence properties.

**NaYF<sub>4</sub>:Gd<sup>3+</sup> NCs** The results on the Eu<sup>3+</sup> emission show a quantitative agreement between the absolute values of MD and ED decay rates as a function of refractive index assuming the  $n^3$  dependence and NC-cavity model. The validity is confirmed by the excellent agreement of the fittings for ED/MD intensity ratios in Fig. 2.3 using these models. To provide further evidence for the  $n^3$  dependence for MD transition rates as described by Eq. 2.5, we also investigated the decay times of MD emission from Gd<sup>3+</sup>. Gd<sup>3+</sup> has the 4f<sup>7</sup> configuration and the first excited state (<sup>6</sup>P<sub>7/2</sub>) for this stable half-filled shell configuration is in the UV. The <sup>6</sup>P<sub>7/2</sub>-<sup>8</sup>S<sub>7/2</sub> emission is around 311 nm and is MD allowed with a large MD transition probability (high value for the MD ( $L + 2S$ ) matrix element of -0.52).<sup>36</sup> In fluoride hosts, opposite parity states (e.g. 4f<sup>n-1</sup>5d or charge transfer states) are at very high energy for lanthanide ions. These states need to be admixed into the 4f<sup>n</sup> states to induce forced ED transition. A large energy difference with opposite parity states reduces mixing and thus gives rise to low values for forced ED transition probabilities. Because of this, in fluorides the <sup>6</sup>P<sub>7/2</sub>-<sup>8</sup>S<sub>7/2</sub> emission has predominant MD character. The emission spectrum of Gd<sup>3+</sup>-doped NaYF<sub>4</sub> NCs is shown in Fig. 2.4a. A narrow emission line around 311 nm is observed and assigned to the <sup>6</sup>P<sub>7/2</sub>-<sup>8</sup>S<sub>7/2</sub> transition. There is also a weak emission line at 305 nm that can be assigned to the MD transition <sup>6</sup>P<sub>5/2</sub>-<sup>8</sup>S<sub>7/2</sub>. The excitation spectrum of the 311 nm emission shows sharp lines around 273 nm that are characteristic of <sup>8</sup>S<sub>7/2</sub>-<sup>6</sup>I<sub>J</sub> transitions. Because of the large energy gap between the excited <sup>6</sup>P<sub>7/2</sub> state and the ground <sup>8</sup>S<sub>7/2</sub> state, the <sup>6</sup>P<sub>7/2</sub> decay should be primarily due to radiative processes (no contribution from MPR).

To obtain insight into the contribution of MD and forced ED character in the <sup>6</sup>P<sub>7/2</sub>-<sup>8</sup>S<sub>7/2</sub> emission for Gd<sup>3+</sup> in NaYF<sub>4</sub>, the emission lifetime in the bulk material was analyzed. The radiative lifetime from <sup>6</sup>P<sub>7/2</sub> state was measured to be 9.3 ms in bulk NaYF<sub>4</sub>. The radiative transition probability for MD transitions can be calculated using<sup>37,38</sup>

$$k_{\text{MD}} = 10^{-42} \nu^3 n^3 \frac{1}{g_{J'}} (L + 2S)^2 \quad (2.8)$$

where  $\nu$  stands for the frequency of transition,  $g_{J'}$  is the statistical weight ( $2J' + 1$ ) of excited states and the term  $(L + 2S)$  is the MD transition operator. Taking  $g_{J'} = 8$ ,  $(L + 2S) = -0.52$  and  $n = 1.5$ , the MD transition rate for the  ${}^6\text{P}_{7/2}$ - ${}^8\text{S}_{7/2}$  transition is  $k_{\text{MD}} = 102 \text{ s}^{-1}$  ( $\tau = 9.8 \text{ ms}$ ). This value is very close to the observed decay rate ( $k = 108 \text{ s}^{-1}$  for  $\tau = 9.3 \text{ ms}$ ). This confirms that the  ${}^6\text{P}_{7/2}$ - ${}^8\text{S}_{7/2}$  transition of  $\text{Gd}^{3+}$  in  $\text{NaYF}_4$  has 95% MD character and makes the  $\text{Gd}^{3+}{}^6\text{P}_{7/2}$ - ${}^8\text{S}_{7/2}$  emission ideal for investigating the influence of refractive index on MD transition probabilities.

For core-only  $\text{Gd}^{3+}$ -doped  $\text{NaYF}_4$  NCs, the emission decay curves are non-exponential and the emission intensity is weaker than that in core-shell  $\text{NaYF}_4$  NCs. This indicates quenching and is probably due to energy transfer to organic impurities in the solvents with energy levels in the UV. Quenching of UV emission in apolar solvents has also been observed in  $\text{Gd}^{3+}$  complexes.<sup>39,40</sup> It can be explained by trace amounts of UV-absorbing organic chromophores in the solvents.

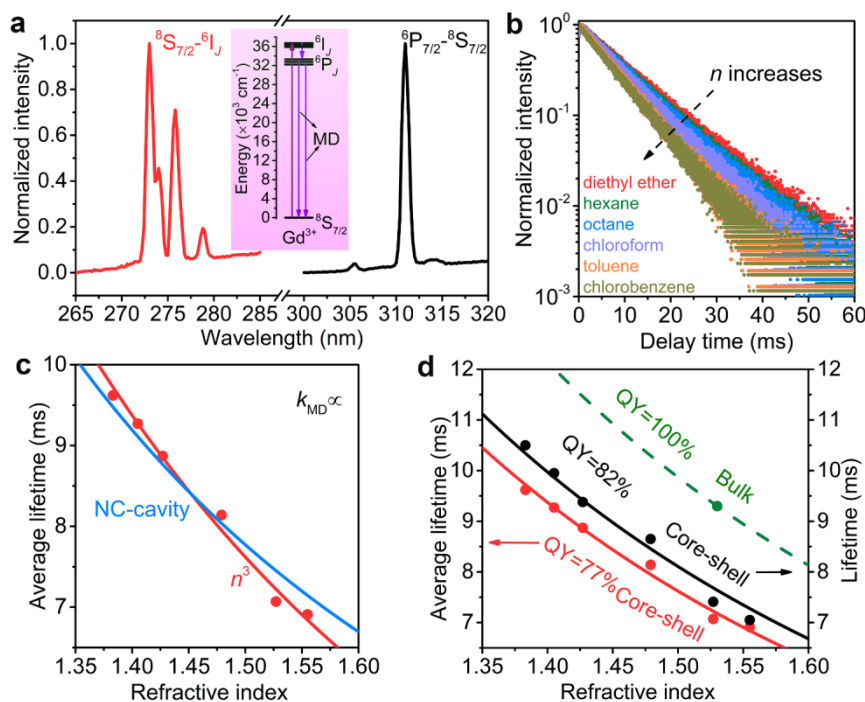
For core-shell NCs dispersed in different solvents, the  $\text{Gd}^{3+}$  emission is more intense. The undoped  $\text{NaYF}_4$  shell forms a protective inert shell that reduces quenching. The  $\text{Gd}^{3+}$  emission decay dynamics is shown in **Fig. 2.4b** for core-shell NCs dispersed in apolar solvents with different  $n$ . A mono-exponential decay behavior is observed in all solvents. In **Fig. A2.3**, the luminescence decay curves can be found with the mono-exponential fitting. Upon increasing the solvent refractive index, the decay becomes faster and the  ${}^6\text{P}_{7/2}$  lifetime decreases from 9.6 to 6.9 ms as the solvent refractive index  $n$  increases from 1.35 to 1.53.

The average lifetime of the  $\text{Gd}^{3+}$  emission in core-shell NCs is plotted as a function of the solvent refractive index in **Fig. 2.4c**. The refractive index dependence is fitted to the  $n^3$  dependence expected for MD transitions (**Eq. 2.5**). An excellent agreement is observed confirming that the MD transition probability increases with  $n^3$  as expected theoretically. Alternatively, this  $n^3$  dependence of  $k_{\text{MD}}$  is confirmed by  $n^3$  fittings in **Fig. A2.4**. Note that this  $n^3$  dependence is stronger than the refractive index dependence for ED transitions, which is also shown for comparison in **Fig. 2.4c**. As a result, the branching ratios in an emission spectrum consisting of mixed MD and ED transitions will change upon increasing  $n$ . The relative intensity of MD transitions will increase with  $n$ . (see also **Fig. 2.3a**)

Similar to our analysis for  $\text{NaYF}_4:\text{Eu}^{3+}$  above and for  $\text{LaPO}_4:\text{Tb}^{3+}$  and  $\text{LaPO}_4:\text{Ce}^{3+}$  NCs reported in **Ref. 11**, we can also estimate the upper limit for the QY of the  $\text{Gd}^{3+}$  emission in  $\text{NaYF}_4:\text{Gd}^{3+}$  core-shell NCs. From the radiative lifetime of the  $\text{Gd}^{3+}$  emission in the bulk material, we can determine the radiative lifetime for the emission in the NCs in different solvents. The calculated radiative lifetimes are longer than the observed lifetimes indicating that there is still some quenching

of the luminescence. The QY of  $\text{Gd}^{3+}$ -doped core-shell NCs is determined by fitting the experimentally observed decay times to

$$\tau_{\text{avg}} = \text{QY}\tau_{\text{bulk}}n_{\text{NC}}^3/n^3 \quad (2.9)$$



**Figure 2.4.** Variation of  $\text{Gd}^{3+}$  emission lifetimes as a function of the solvent refractive index for  $\text{NaY}_{0.95}\text{Gd}_{0.05}\text{F}_4@ \text{NaYF}_4$  core-shell NCs. (a) Excitation ( $\lambda_{\text{em}} = 311$  nm, red) and emission spectra ( $\lambda_{\text{ex}} = 273$  nm, black) of NCs dispersed in chlorobenzene. The inset shows the energy level diagram of  $\text{Gd}^{3+}$ : absorption of a 273 nm photon brings  $\text{Gd}^{3+}$  to the excited  ${}^6I_J$  states, followed by a rapid non-radiative decay to the  ${}^6P_J$  states, from which 311 nm UV emission is observed. (b) Luminescence decay curves of the 311 nm  $\text{Gd}^{3+}$  emission after pulsed 273 nm excitation for NCs dispersed in solvents with different refractive index ranging from 1.35 for diethyl ether to 1.53 for chlorobenzene. (c) Average lifetimes of the  $\text{Gd}^{3+}$   ${}^6P_{7/2}$ - ${}^8S_{7/2}$  emission (red dots) and a fitting for an  $n^3$   $k_{\text{MD}} \propto$  dependence (red line). The blue line is the best fitting assuming the NC-cavity model for the refractive index dependence of  $k_{\text{MD}}$ . (d) Average lifetimes (the same red dots in (c)). The black curve gives the lifetimes determined from a single-exponential tail ( $t > 1$  ms) fitting for the core-shell NCs. The green broken line is based on the  ${}^6P_{7/2}$  emission decay time in  $\text{NaY}_{0.95}\text{Gd}_{0.05}\text{F}_4$  bulk material and gives the expected radiative lifetime as a function of the solvent refractive index. The drawn lines are fitted with Eq. 2.9 assuming that the QY of  $\text{Gd}^{3+}$ -doped bulk material is 100%.

In **Fig. 2.4d**, the results to the fitting are shown. A good agreement between experiment and theory (**Eq. 2.9**) is obtained for a QY of 77% from the average lifetime as well as 82% from the tail fitting results.

## 2.4 Conclusions

In conclusion, the influence of the photonic environment on MD transition probabilities has been systematically investigated using  $\text{Eu}^{3+}$ - and  $\text{Gd}^{3+}$ -doped  $\text{NaYF}_4$  NCs as model systems. Varying the refractive index of the solvent in which the NCs are dispersed reveals a strong increase of the MD transition probability with  $n$ . For  $\text{Eu}^{3+}$ -doped NCs, all experimental results (ED/MD intensity ratios and decay rates) are in excellent agreement with the theoretically predicted  $n^3$  dependence for MD transition probabilities if the variation in ED transition probability is assumed to obey the recently established NC-cavity model.

For  $\text{Gd}^{3+}$ , the variation in MD transition probability can be directly assessed as the  ${}^6\text{P}_{7/2}$ - ${}^8\text{S}_{7/2}$  transition has 95% MD character. The strong refractive index dependence of the  ${}^6\text{P}_{7/2}$ - ${}^8\text{S}_{7/2}$  emission decay time closely follows the theoretical  $n^3$  dependence, providing further experimental evidence for the  $n^3$  dependence of MD transition probabilities observed for  $\text{Eu}^{3+}$ . The present study is the first systematic and accurate investigation providing strong experimental evidence for the theoretically predicted  $n^3$  dependence of MD transition probabilities. Insights into the influence of the local environment on radiative transitions are important for understanding and controlling optical properties through variations in the photonic environment.

## 2.5 Methods

**Chemicals** The synthesis was conducted using commercially available reagents. Ethanol (Analytical Reagent, A.R.), methanol (A.R.), cyclohexane (A.R.), diethyl ether (A.R.), hexane (A.R.), octane (A.R.), chloroform (A.R.), toluene (A.R.), chlorobenzene (A.R.), oleic acid (90%), 1-octadecene (90%), yttrium (III) acetate (99.9%), yttrium (III) fluoride (99.99%), europium (III) acetate (99.9%), europium (III) fluoride (99.99%), gadolinium (III) acetate (99.9%), gadolinium (III) fluoride (99.99%), sodium hydroxide (97%), sodium fluoride (99%), and ammonium fluoride (98%) were purchased from Sigma and Aldrich without further purification.

**Synthesis of core and core-shell  $\text{NaYF}_4$  NCs** The protocol to synthesize  $\text{Eu}^{3+}/\text{Gd}^{3+}$ -doped core and core-shell NCs is based on the method described in **Ref. 41** with some modifications. Stoichiometric amounts of rare earth acetates (totally 1 mmol) were added into a 100 mL three-necked flask, which contained 6 mL oleic acid and 17 mL 1-octadecene. The mixture was stirred vigorously and heated to 390 K for 1.5 h under vacuum and subsequently allowed to cool down to room temperature under a gentle flow of nitrogen gas. This was followed by a rapid injection of a mixture, containing 2.5

mmol NaOH and 4 mmol  $\text{NH}_4\text{F}$  dissolved in 3 and 7 ml methanol, respectively. The reaction was kept at room temperature overnight. Next, the solution was heated to 370 K for 0.5 h under vacuum and to 570 K for 2 h under a protective nitrogen atmosphere. Afterwards, the solution was cooled down and the product was precipitated by adding excess ethanol. The core NCs were washed with ethanol and cyclohexane three times using centrifugation to separate the NCs from the ethanol and cyclohexane. For the synthesis of core-shell NCs, all steps were the same except for the injection of core NCs dissolved in cyclohexane into the flask before adding the mixture of NaOH and  $\text{NH}_4\text{F}$  methanol solutions. Note that an inert shell  $\text{NaYF}_4$  was grown around the core so the reaction mixture for shell growth contained only yttrium acetate as rare earth precursor. The final core and core-shell NCs were analyzed by X-ray diffraction (XRD), which confirmed the hexagonal crystal structure of the NCs obtained (Fig. A2.5). The NCs are capped with oleates on the surface and can be re-dispersed into various apolar solvents. In this study, we used diethyl ether, hexane, octane, chloroform, toluene and chlorobenzene. To visualize the morphology and size of NCs, NCs dropped on amorphous carbon-coated copper grids (200 mesh) were imaged on an FEI Tecnai-12 TEM operating at 120 kV.

**Synthesis of microcrystalline  $\text{NaYF}_4$**  The synthesis of bulk (microcrystalline)  $\text{NaYF}_4$  materials was done through standard solid synthesis techniques described in Ref. 42 with an additional post-treatment. NaF (5% excess) was mixed with stoichiometric amounts of  $\text{YF}_3$  and  $\text{EuF}_3$  or  $\text{GdF}_3$ . The starting materials were thoroughly mixed in an agate mortar, transferred into an alumina crucible, and sintered in an oven together with a second crucible filled with  $\text{NH}_4\text{F}$ . The heating was done in a gas tight alumina tube under a nitrogen flow. The samples were first heated to 570 K for 2 h and then to 820 K for 3 h. After cooling down, the samples were washed with deionized water for three times to remove a trace of NaF and collected after drying at 370 K overnight. XRD measurement determined the hexagonal  $\beta$ -phase of the obtained bulk materials (Fig. A2.5).

**Optical spectroscopy** The photoluminescence spectra were recorded using an Edinburgh Instruments FLS920 spectrometer, with a 450 W xenon lamp as excitation source and a Hamamatsu R928 photomultiplier tube (PMT) for photon detection. To record spectra with high resolution, narrow slits and small step sizes (0.2 nm) were used. Luminescence decay curves for the  $\text{Eu}^{3+}$  emission were measured using the multi-channel scaling (MCS) option integrated in the spectrofluorometer with pulsed excitation by an optical parametric oscillator (OPO) system (Opotek Opolette HE 355 II) pumped by the third harmonic of a YAG: $\text{Nd}^{3+}$  laser (pulse width 10 ns and repetition rate 20 Hz). The lifetimes of the  $\text{Gd}^{3+}$  emission were measured with an Ekspla NT342B-10-SH/DUV OPO system for pulsed excitation in the UV (pulse width 5 ns and repetition rate 10 Hz), a Hamamatsu H7422-02 PMT as photon detector and an EG&G ORTEC Turbo-MCS for recording the time resolved signal. The signal was analyzed in a Stanford Research SR400 gated photon counter and laser pulses were controlled by a Stanford Research DG535 pulse generator.

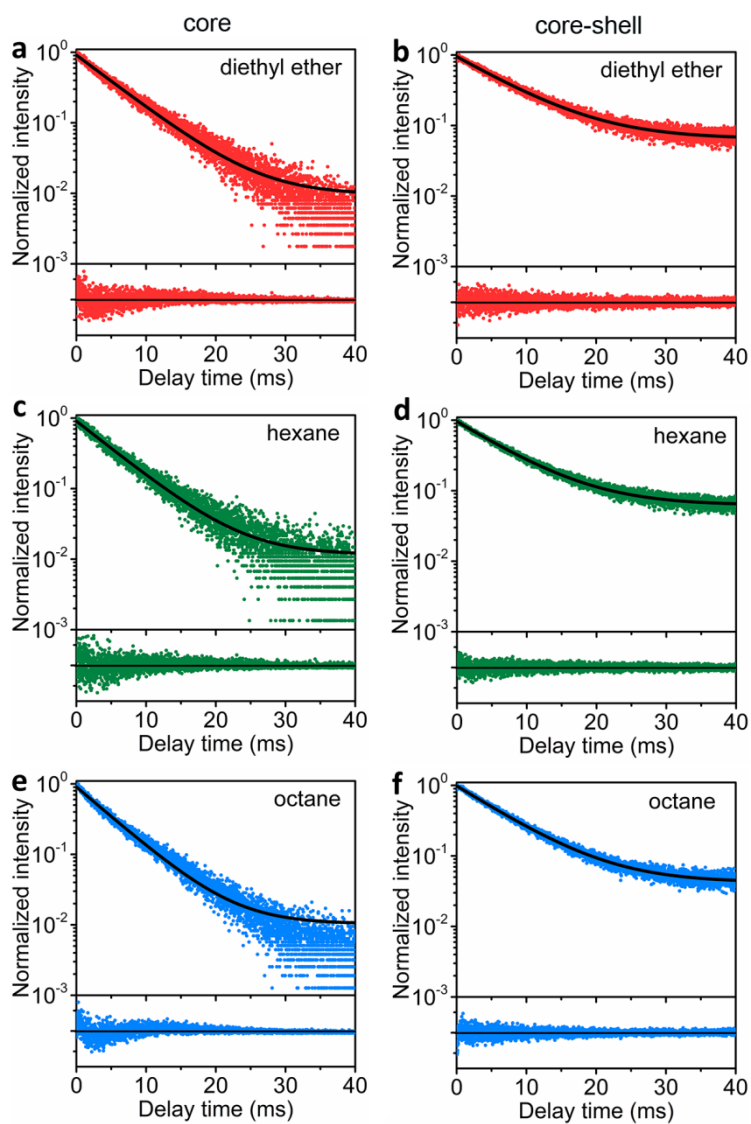
## 2.6 References

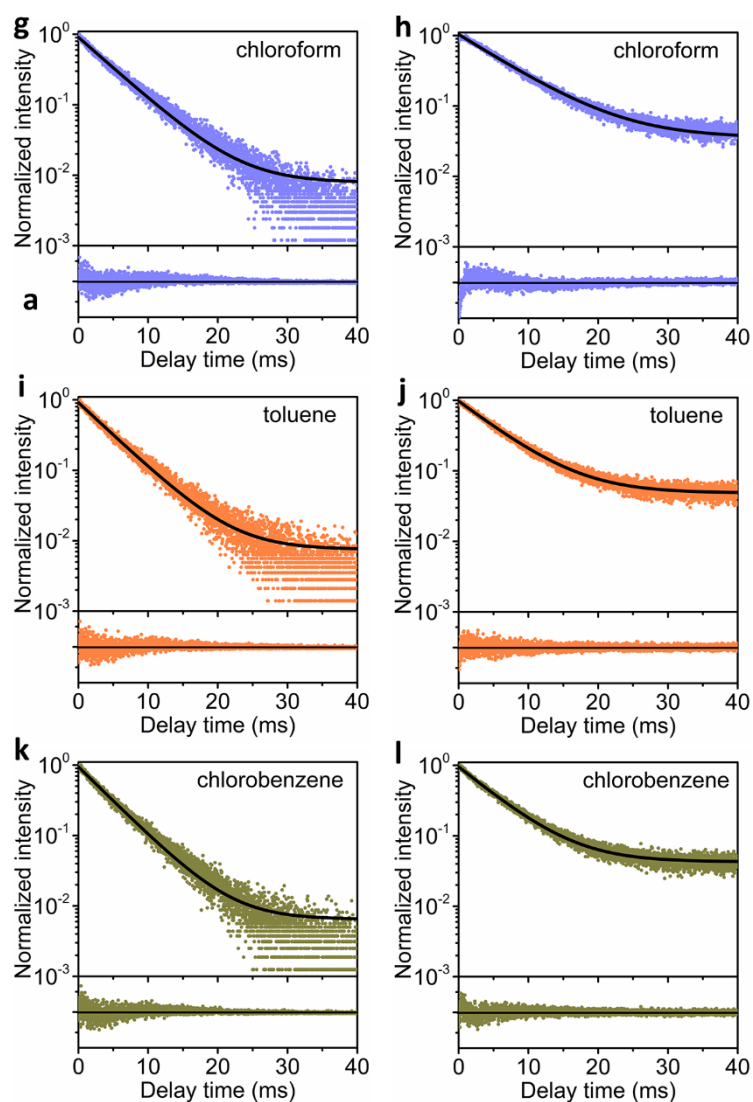
1. Toptygin, D. Effects of the Solvent Refractive Index and Its Dispersion on the Radiative Decay Rate and Extinction Coefficient of a Fluorescent Solute. *J. Fluoresc.* **2003**, *13*, 201-219.
2. de Vries, P.; Lagendijk, A. Resonant Scattering and Spontaneous Emission in Dielectrics: Microscopic Derivation of Local-Field Effects. *Phys. Rev. Lett.* **1998**, *81*, 1381-1384.
3. Duan, C. K.; Reid, M. F. Local Field Effects on the Radiative Lifetimes of Ce<sup>3+</sup> in Different Hosts. *Curr. Appl. Phys.* **2006**, *6*, 348-350.
4. Duan, C. K.; Wen, H. L.; Tanner, P. A. Local-Field Effect on the Spontaneous Radiative Emission Rate. *Phys. Rev. B: Condens. Matter Mater. Phys.* **2011**, *83*, 245123.
5. Glauber, R. J.; Lewenstein, M. Quantum Optics of Dielectric Media. *Phys. Rev. A: At., Mol., Opt. Phys.* **1991**, *43*, 467-491.
6. Kumar, G. M.; Rao, D. N.; Agarwal, G. S. Measurement of Local Field Effects of the Host on the Lifetimes of Embedded Emitters. *Phys. Rev. Lett.* **2003**, *91*, 203903.
7. Schuurmans, F. J. P.; de Lang, D. T. N.; Wegdam, G. H.; Sprik, R.; Lagendijk, A. Local-Field Effects on Spontaneous Emission in a Dense Supercritical Gas. *Phys. Rev. Lett.* **1998**, *80*, 5077-5080.
8. Zhu, Y. S.; Xu, W.; Zhang, H. Z.; Wang, W.; Tong, L.; Xu, S.; Sun, Z. P.; Song, H. W. Highly Modified Spontaneous Emissions in YVO<sub>4</sub>:Eu<sup>3+</sup> Inverse Opal and Refractive Index Sensing Application. *Appl. Phys. Lett.* **2012**, *100*, 081104.
9. Duan, C. K.; Reid, M. F. Macroscopic Models for the Radiative Relaxation Lifetime of Luminescent Centers Embedded in Surrounding Media. *Spectrosc. Lett.* **2007**, *40*, 237-246.
10. Rabouw, F. T.; den Hartog, S. A.; Senden, T.; Meijerink, A. Photonic Effects on the Förster Resonance Energy Transfer Efficiency. *Nat. Commun.* **2014**, *5*, 3610.
11. Senden, T.; Rabouw, F. T.; Meijerink, A. Photonic Effects on the Radiative Decay Rate and Luminescence Quantum Yield of Doped Nanocrystals. *ACS Nano* **2015**, *9*, 1801-1808.
12. Nienhuis, G.; Alkemade, C. Th. J. Atomic Radiative Transition Probabilities in a Continuous Medium. *Physica B+C* **1976**, *81*, 181-188.
13. Rikken, G. L. J. A.; Kessener, Y. A. R. R. Local Field Effects and Electric and Magnetic Dipole Transitions in Dielectrics. *Phys. Rev. Lett.* **1995**, *74*, 880-883.
14. Werts, M. H. V.; Jukes, R. T. F.; Verhoeven, J. W. The Emission Spectrum and the Radiative Lifetime of Eu<sup>3+</sup> in Luminescent Lanthanide Complexes. *Phys. Chem. Chem. Phys.* **2002**, *4*, 1542-1548.
15. Dodson, C. M.; Zia, R. Magnetic Dipole and Electric Quadrupole Transitions in the Trivalent Lanthanide Series: Calculated Emission Rates and Oscillator Strengths. *Phys. Rev. B: Condens. Matter Mater. Phys.* **2012**, *86*, 125102.
16. Meltzer, R. S.; Feofilov, S. P.; Tissue, B.; Yuan, H. B. Dependence of Fluorescence Lifetimes of

- $\text{Y}_2\text{O}_3:\text{Eu}^{3+}$  Nanoparticles on the Surrounding Medium. *Phys. Rev. B: Condens. Matter Mater. Phys.* **1999**, *60*, R14012-R14015.
17. Wuister, S. F.; de Mello Donegá C.; Meijerink, A. Local-Field Effects on the Spontaneous Emission Rate of CdTe and CdSe Quantum Dots in Dielectric Media. *J. Chem. Phys.* **2004**, *121*, 4310-4315.
  18. Aigouy, L.; Cazé A.; Gredin, P.; Mortier, M.; Carminati, R. Mapping and Quantifying Electric and Magnetic Dipole Luminescence at the Nanoscale. *Phys. Rev. Lett.* **2014**, *113*, 076101.
  19. Rabouw, F. T.; Prins, P. T.; Norris, D. J. Europium-Doped  $\text{NaYF}_4$  Nanocrystals as Probes for the Electric and Magnetic Local Density of Optical States throughout the Visible Spectral Range. *Nano Lett.* **2016**, *16*, 7254-7260.
  20. Pillonnet, A.; Fleury, P.; Chizhik, A. I.; Chizhik, A. M.; Amans, D.; Ledoux, G.; Kulzer, F.; Meixner, A. J.; Dujardin, C. Local Refractive Index Probed via the Fluorescence Decay of Semiconductor Quantum Dots. *Opt. Express* **2012**, *20*, 3200-3208.
  21. Sytsma, J.; van Schaik, W.; Blasse, G. Vibronic Transitions in the Emission Spectra of  $\text{Gd}^{3+}$  in Several Rare-Earth Compounds. *J. Phys. Chem. Solids* **1991**, *52*, 419-429.
  22. Binnemans, K.; Görrler-Walrand, C.; Adam, J. L. Spectroscopic Properties of  $\text{Gd}^{3+}$ -Doped Fluorozirconate Glass. *Chem. Phys. Lett.* **1997**, *280*, 333-338.
  23. Wang, F.; Wang, J.; Liu, X. G. Direct Evidence of a Surface Quenching Effect on Size-Dependent Luminescence of Upconversion Nanoparticles. *Angew. Chem. Int. Ed.* **2010**, *49*, 7456-7460.
  24. Wang, Z. J.; Zhang, Y. L.; Zhong, J. P.; Yao, H. H.; Wang, J.; Wu, M. M.; Meijerink, A. One-Step Synthesis and Luminescence Properties of Tetragonal Double Tungstates Nanocrystals. *Nanoscale* **2016**, *8*, 15486-15489.
  25. Jia, G. H.; Tanner, P. A. Energy Transfer between  $\text{UO}_2^{2+}$  and  $\text{Eu}^{3+}$  in  $\beta\text{-NaYF}_4$ . *J. Alloys Compd.* **2009**, *471*, 557-560.
  26. Ivaturi, A.; MacDougall, S. K. W.; Martín-Rodríguez, R.; Quintanilla, M.; Marques-Hueso, J.; Krämer, K. W.; Meijerink, A.; Richards, B. S. Optimizing Infrared to Near Infrared Upconversion Quantum Yield of  $\beta\text{-NaYF}_4:\text{Er}^{3+}$  in Fluoropolymer Matrix for Photovoltaic Devices. *J. Appl. Phys.* **2013**, *114*, 013505.
  27. Würth, C.; Geißler, D.; Behnke, T.; Kaiser, M.; Resch-Genger, U. Critical Review of the Determination of Photoluminescence Quantum Yields of Luminescent Reporters. *Anal. Bioanal. Chem.* **2015**, *407*, 59-78.
  28. Shin, J.; Shen, J.-T.; Fan, S. H. Three-Dimensional Metamaterials with an Ultrahigh Effective Refractive Index over a Broad Bandwidth. *Phys. Rev. Lett.* **2009**, *102*, 093903.
  29. Savelev, R. S.; Makarov, S. V.; Krasnok, A. E.; Belov, P. A. From Optical Magnetic Resonance to Dielectric Nanophotonics. *Opt. Spectrosc.* **2015**, *119*, 551-568.
  30. Kuznetsov, A. I.; Miroshnichenko, A. E.; Brongersma, M. L.; Kivshar, Y. S.; Luk'yanchuk, B. Optically Resonant Dielectric Nanostructures. *Science* **2016**, *354*, aag2472.

31. Karaveli, S.; Zia, R. Spectral Tuning by Selective Enhancement of Electric and Magnetic Dipole Emission. *Phys. Rev. Lett.* **2011**, *106*, 193004.
32. Choi, B.; Iwanaga, M.; Sugimoto, Y.; Sakoda, K.; Miyazaki, H. T. Selective Plasmonic Enhancement of Electric- and Magnetic-Dipole Radiations of Er Ions. *Nano Lett.* **2016**, *16*, 5191-5196.
33. Noda, S.; Fujita, M.; Asano, T. Spontaneous-Emission Control by Photonic Crystals and Nanocavities. *Nat. Photonics* **2007**, *1*, 449-458.
34. Leistikow, M. D.; Mosk, A. P.; Yeganegi, E.; Huisman, S. R.; Lagendijk, A.; Vos, W. L. Inhibited Spontaneous Emission of Quantum Dots Observed in a 3D Photonic Band Gap. *Phys. Rev. Lett.* **2011**, *107*, 193903.
35. Curto, A. G.; Volpe, G.; Taminiau, T. H.; Kreuzer, M. P.; Quidant, R.; van Hulst, N. F. Unidirectional Emission of a Quantum Dot Coupled to a Nanoantenna. *Science* **2010**, *329*, 930-933.
36. Detrio, J. A. Line Strengths for  $Gd^{3+}$  at a  $C_{4v}$  Site in  $SrF_2$ . *Phys. Rev. B: Solid State* **1971**, *4*, 1422-1427.
37. Sytsma, J.; Imbusch, G. F.; Blasse, G. The Spectroscopy of  $Gd^{3+}$  in Yttriumoxychloride: Judd-Ofelt Parameters from Emission Data. *J. Chem. Phys.* **1989**, *91*, 1456-1461.
38. Meijerink, A. Spectroscopy and Vibronic Transitions of Divalent Europium in  $LiBaF_3$ . *J. Lumin.* **1993**, *55*, 125-138.
39. Buono-Core, G. E.; Li, H.; Marciniak, B. Quenching of Excited States by Lanthanide Ions and Chelates in Solution. *Coord. Chem. Rev.* **1990**, *99*, 55-87.
40. de Sá G. F.; Malta, O. L.; de Mello Doneg á C.; Simas, A. M.; Longo, R. L.; Santa-Cruz, P. A.; da Silva, E. F., Jr. Spectroscopic Properties and Design of Highly Luminescent Lanthanide Coordination Complexes. *Coord. Chem. Rev.* **2000**, *196*, 165-195.
41. Wang, F.; Deng, R. R.; Liu, X. G. Preparation of Core-Shell  $NaGdF_4$  Nanoparticles Doped with Luminescent Lanthanide Ions to be Used as Upconversion-Based Probes. *Nat. Protoc.* **2014**, *9*, 1634-1644.
42. Aarts, L.; van der Ende, B. M.; Meijerink, A. Downconversion for Solar Cells in  $NaYF_4:Er, Yb$ . *J. Appl. Phys.* **2009**, *106*, 023522.

## 2.7 Appendices

Decay Curves and Average Lifetimes of  $\text{Eu}^{3+}$  Emission

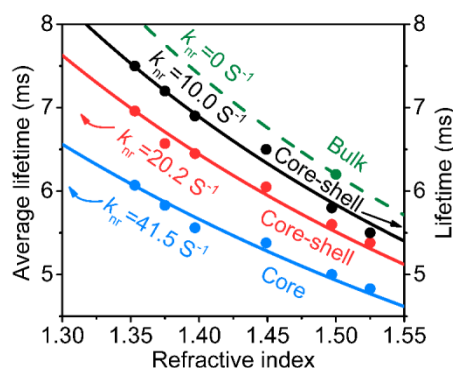


**Figure A2.1.** Luminescence decay curves of  $\text{Eu}^{3+}$  emission at 615 nm after pulsed 465 nm excitation for  $\text{NaY}_{0.9}\text{Eu}_{0.1}\text{F}_4$  core (left side) and  $\text{NaY}_{0.9}\text{Eu}_{0.1}\text{F}_4@ \text{NaYF}_4$  core-shell (right side) NCs in solvents. The curves are fitted to single-exponential function (drawn lines). Fitting residuals are shown in the panels below the decay curves.

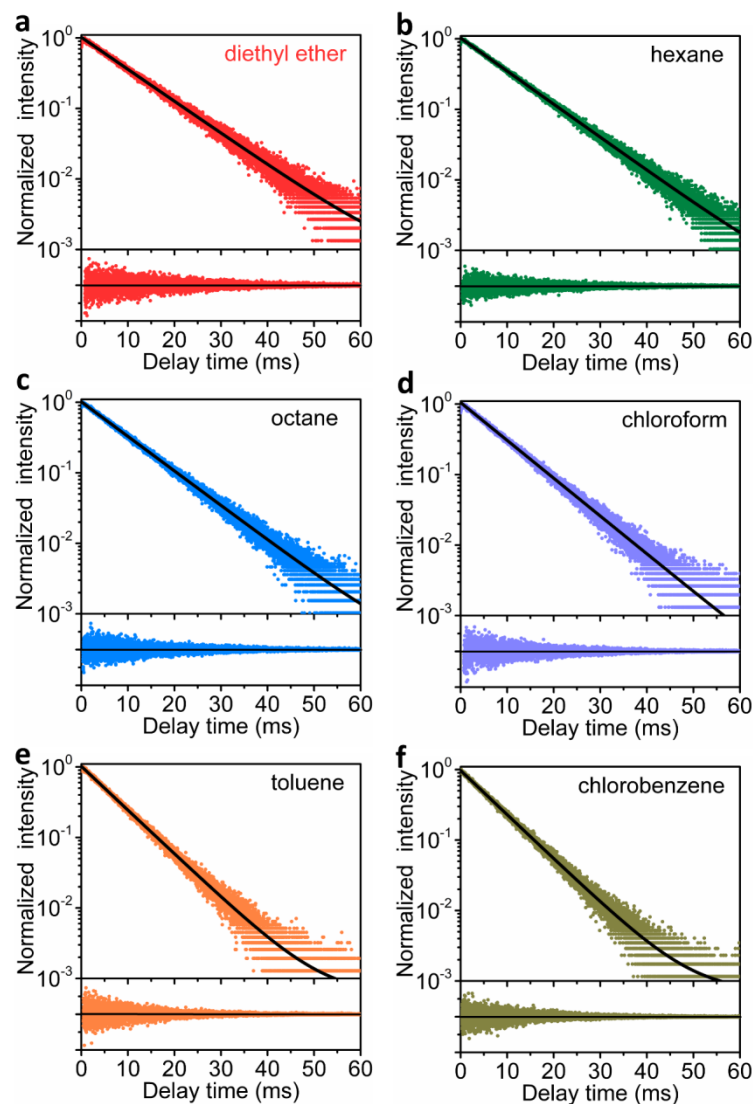
### Fittings of $\text{Eu}^{3+}$ Lifetimes for Constant Non-Radiative Decay Rate

The variation of lifetime with refractive index as plotted in **Fig. 2.2c** of the main text assumes a constant QY. Alternatively, the data can be plotted assuming a constant average non-radiative decay rate. In the figure below, a constant non-radiative decay rate is assumed. The drawn lines in the figure are fittings to **Eq.** below.

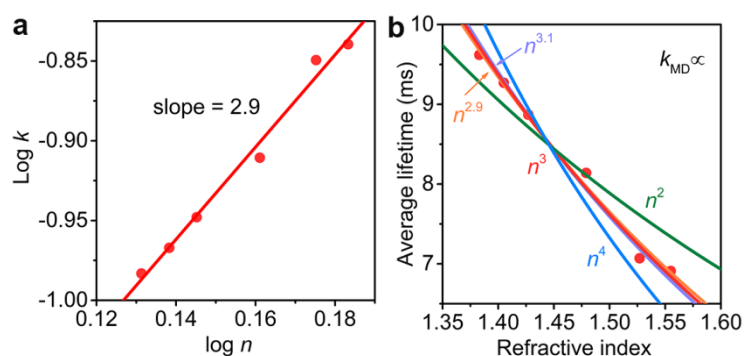
$$\tau_{\text{avg}} = 1 / \left( \frac{I_{\text{ED}}}{I_{\text{tot}}} \frac{n \chi_{\text{NC}}^2}{\tau_{\text{bulk}} n_{\text{NC}}} + \frac{I_{\text{MD}}}{I_{\text{tot}}} \frac{n^3}{\tau_{\text{bulk}} n_{\text{NC}}^3} + k_{\text{nr}} \right)$$



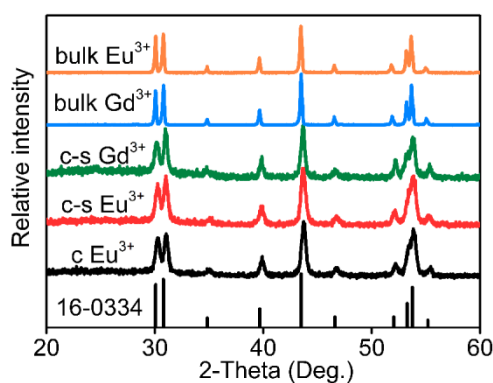
**Figure A2.2.** Average lifetimes for  $\text{NaY}_{0.9}\text{Eu}_{0.1}\text{F}_4$  core (blue) and  $\text{NaY}_{0.9}\text{Eu}_{0.1}\text{F}_4@ \text{NaYF}_4$  core-shell (red) NCs as a function of the solvent refractive index. The black dots give lifetimes determined from a single-exponential tail ( $t > 1$  ms) fitting for core-shell NCs. The green dot marks the radiative lifetime based on bulk material.

Decay Curves and Average Lifetimes of  $Gd^{3+}$  Emission


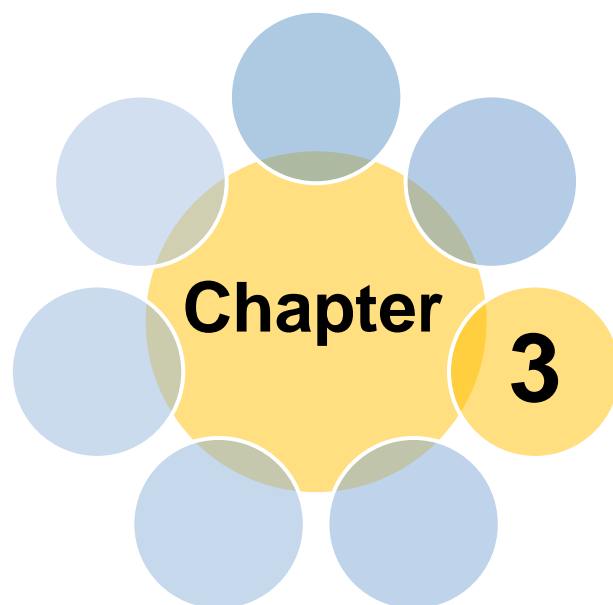
**Figure A2.3.** Luminescence decay curves of  $Gd^{3+}$  emission at 311 nm after pulsed 273 nm excitation for  $NaY_{0.95}Gd_{0.05}F_4@NaYF_4$  core-shell NCs in different solvents. The curves are fitted to single-exponential function (drawn lines) and fitting residuals are shown in the panels below the decay curves.



**Figure A2.4.** (a) Log-log plot and fitting for average decay rate of  $\text{Gd}^{3+}$  emission. (b) Fittings for the average lifetime of  $\text{Gd}^{3+}$  emission for different power dependences of the MD decay rate on  $n$ .



**Figure A2.5.** XRD patterns of NCs for  $\text{NaY}_{0.9}\text{Eu}_{0.1}\text{F}_4$  core (black),  $\text{NaY}_{0.9}\text{Eu}_{0.1}\text{F}_4@ \text{NaYF}_4$  core-shell (red) and  $\text{NaY}_{0.95}\text{Gd}_{0.05}\text{F}_4@ \text{NaYF}_4$  core-shell (green), and bulk materials for  $\text{NaY}_{0.9}\text{Eu}_{0.1}\text{F}_4$  (orange) and  $\text{NaY}_{0.95}\text{Gd}_{0.05}\text{F}_4$  (blue) with the bottom black lines as the reference pattern of hexagonal  $\text{NaYF}_4$  (pdf 16-0334).



# Concentration quenching in upconversion nanocrystals

Based on

Wang, Z. J.; Meijerink, A. Concentration Quenching in Upconversion Nanocrystals. *J. Phys. Chem.*

*C* **2018**, *122*, 26298-26306.

### 3.1 Abstract

Despite considerable effort to improve upconversion (UC) in lanthanide-doped nanocrystals (NCs), the maximum reported efficiencies remain below 10%. Recently, we reported on low  $\text{Er}^{3+}$ - and  $\text{Yb}^{3+}$ -doped  $\text{NaYF}_4$  NCs giving insight into fundamental processes involved in quenching for isolated ions. In practice, high dopant concentrations are required and there is a trend toward bright UC in highly doped NCs. Here, additional quenching processes due to energy transfer and migration add to a reduction in UC efficiency. However, a fundamental understanding on how concentration quenching affects the quantum efficiency is lacking. Here, we report a systematic investigation on concentration-dependent decay dynamics for  $\text{Er}^{3+}$  or  $\text{Yb}^{3+}$  doped at various concentrations (1-100%) in core and core-shell  $\text{NaYF}_4$  NCs. The qualitative and quantitative analyses of luminescence decay curves and emission spectra show strong concentration quenching for the green-emitting  $\text{Er}^{3+}$   $^4\text{S}_{3/2}$  and NIR-emitting  $^4\text{I}_{11/2}$  levels, while concentration quenching for the red-emitting  $^4\text{F}_{9/2}$  level and the IR-emitting  $^4\text{I}_{13/2}$  level is limited. The NIR emission of  $\text{Yb}^{3+}$  remains efficient even at concentration as high as 60%  $\text{Yb}^{3+}$ , especially in core-shell NCs. Finally, the role of solvent quenching was investigated and reveals a much stronger quenching in aqueous media that can be explained by the high-energy O-H vibrations. The present study uncovers a more complete picture of quenching processes in highly doped UC NCs and serves to identify methods to further optimize the efficiency by careful tuning of lanthanide concentrations and core-shell design.

### 3.2 Introduction

Upconversion (UC) luminescence has become an active field of research since the pioneering work by Auzel, Ovsyankin, and Feofilov in 1960s. Especially in the past two decades, the advent of UC nanocrystals (NCs) has triggered renewed interests by emerging applications of UC NCs in bio-imaging, solar cells, sensors, anti-counterfeiting and three-dimensional (3D) displays.<sup>1-5</sup> Upconverting two (or more) low-energy photons to one high-energy photon has been demonstrated for a variety of combinations of lanthanide ions and in different spectral regions, ranging from IR  $\rightarrow$  NIR UC to VIS  $\rightarrow$  UV UC.<sup>1-8</sup> The  $\text{Yb}^{3+}$ - $\text{Er}^{3+}$  ion couple is one of the most efficient UC couples showing efficient conversion of NIR ( $\sim 980$  nm) to green and red light.<sup>7,9</sup> The intensity ratio of green and red emission can be tuned by varying experimental parameters, such as host matrix, dopant concentration, excitation power, dispersion medium and size of NCs.<sup>3</sup> Trivalent  $\text{Er}^{3+}$  ion without sensitizer also shows NIR-to-green UC, although less efficient, by excitation at 980 nm.<sup>10</sup> Also, an efficient IR (1520 nm)-to-NIR (980 nm) conversion has been reported for  $\text{Er}^{3+}$ .<sup>11</sup>

In spite of the great potential of UC materials, applications are often hampered by the low quantum yield (QY), especially in NCs. The UC QY in NCs is typically below a few percent, in spite of approaches aimed at enhancing the efficiency, including surface passivation, shell growth,

broadband sensitization, and photonic and plasmonic engineering.<sup>12</sup> Recently reported strategies of incorporating high dopant concentrations combined with increased excitation densities have shown superior UC brightness. The explanation is the enhanced absorption (related to higher concentrations of absorbing ions) and the quadratic dependence of UC rates on excitation power and dopant concentration. All of these factors cause the UC to rapidly gain importance over other processes, such as quenching and IR emission from intermediate levels that do not have a quadratic power/concentration dependence.<sup>13,14</sup> The extreme brightness of UC in highly doped UC NCs under high power density excitation is promising, but it is crucial for many applications to reduce the excitation power to prevent heating and allow for safe operation conditions. Therefore, it is important to quantify and understand the underlying additional (concentration) quenching mechanisms in highly doped UC NCs to realize high UC brightness under reduced excitation densities. Recently, progress has been made in reducing excitation powers for single NC experiments by optimizing Yb- and Er-concentrations and single UC NC imaging was reported in highly doped NaYF<sub>4</sub> core/shell NCs at excitation powers below 10 W/cm<sup>2</sup>.<sup>15,16</sup>

The efficiency of UC NCs is lower than in bulk materials. One reason is the surface-related quenching by defects, surface ligands and surrounding solvent molecules with high-energy vibrational modes.<sup>17,18</sup> These quenching mechanisms are especially pronounced for dopants on or near the NC surface. Coating of an inert (undoped) shell can effectively isolate the optically active lanthanide ions from the surface and surrounding energy vibrations to reduce surface quenching.<sup>19-22</sup> Recently, our group has established a model that accurately models solvent quenching for isolated lanthanide ions in UC NCs.<sup>23</sup> In this model, low dopant concentrations of Er<sup>3+</sup> or Yb<sup>3+</sup> were used to quantitatively describe and understand the quenching processes involved for individual dopant ions inside the NC. However, since UC relies on multi-step energy transfer (ET), high dopant concentrations are crucial to realize efficient ET between lanthanide neighbors to enhance the UC efficiency. On the other hand, the high density of dopants opens additional channels for quenching and thus efficiency loss by concentration quenching via non-radiative processes, such as energy migration and cross-relaxation.<sup>24-27</sup> The trade-off between efficiency loss by concentration quenching and efficiency gain by ET UC determines the maximum UC QY. In addition, the higher absorption strength for higher dopant concentrations results in higher brightness, even at reduced QYs.

In spite of the various studies on UC in highly doped NCs, the role of concentration quenching in UC NCs is still not well understood and is not easy to model. To gain insight into the role of quenching processes at high dopant concentrations, here we present a systematic investigation on the concentration dependence of UC dynamics of respective Er<sup>3+</sup> and Yb<sup>3+</sup> excited states for core and core-shell NaYF<sub>4</sub> NCs doped with 1-100% Er<sup>3+</sup> or Yb<sup>3+</sup>. Luminescence spectra and lifetime measurements under direct excitation in the emitting level are reported and analyzed to quantify

concentration quenching for individual levels involved in UC processes. The results demonstrate that concentration quenching varies for different emitting levels and reveal how it is suppressed in core-shell NCs, e.g., the  $\text{Er}^{3+} {}^4\text{I}_{11/2}$  NIR level is highly susceptible to concentration quenching even in core-shell NCs, while for  $\text{Yb}^{3+}$  in core-shell NCs, concentration quenching is very limited. Finally, the role of solvent quenching was investigated and reveals the role of UC quenching in NCs due to coupling with high-energy vibrations of the solvent. The present results give insight into the role of ET processes in the quenching of emission for energy levels of  $\text{Er}^{3+}$  and  $\text{Yb}^{3+}$  involved in IR to VIS UC in NCs and provide design rules for highly doped NCs with improved UC quantum efficiencies.

### 3.3 Results and Discussion

#### 3.3.1 Concentration quenching for UC NCs

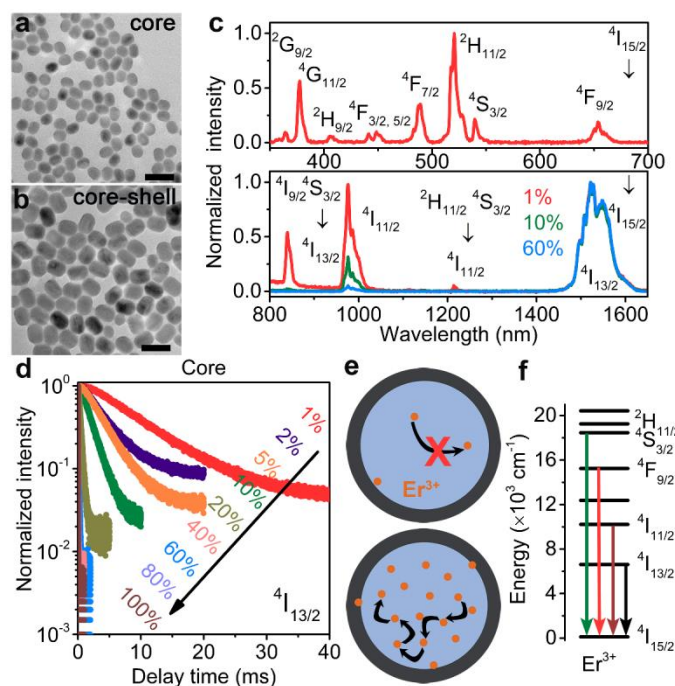
**Characterization of NCs** The  $\text{Yb}^{3+}$ - $\text{Er}^{3+}$  ion couple is widely used to upconvert IR radiation through ground state absorption by two  $\text{Yb}^{3+}$  ions followed by a two-step ET to an  $\text{Er}^{3+}$  neighbor.  $\text{NaYF}_4:\text{Yb,Er}$  is an efficient UC material that serves as a model system both for bulk (microcrystalline) and nanocrystalline materials. In the present study, we analyze  $\text{NaYF}_4$  core NCs that are singly doped with 1-100%  $\text{Er}^{3+}$  or  $\text{Yb}^{3+}$ . In addition, we investigate the influence of an inert 5 nm  $\text{NaYF}_4$  shell coated on a selection of concentrations (1, 10, and 60%) of  $\text{Er}^{3+}$ - or  $\text{Yb}^{3+}$ -doped core NCs. These three concentrations are selected to represent NCs with limited interaction between dopant ions (low concentration, 1%), ET between neighboring ions but with no energy migration (intermediate concentration, 10%), and a concentration above the percolation point allowing for 3D energy migration (high concentration, 60%). This allows to distinguish between two types of energy transfer: energy migration (involving energy transfer among dopants to the same excited state of identical neighboring ions) which in principle does not lead to quenching or shortening of the life time because the excited state population of the level involved does not change. However, it can induce quenching by diffusion (multiple ET steps) of the excited state from ions in the center (no quenching sites nearby) to identical ions at the surface (close to quenching sites) where quenching occurs. This will result in a faster decay time for high doping concentrations, typically above 10% because multi-step energy transfer is needed. The second type of energy transfer is cross-relaxation which depopulates the excited state by partial energy transfer to a neighboring ion. This directly quenches the excited state and shortens the decay time and is already observed at lower doping concentrations.

Details on synthesis are in **Methods**. First, we focus on the  $\text{Er}^{3+}$ -doped NCs. **Figs. 3.1a, b** show the representative transmission electron microscopy (TEM) images for monodisperse  $\text{NaYF}_4:1\%\text{Er}^{3+}$  core (25 × 18 nm) and  $\text{NaYF}_4:1\%\text{Er}^{3+}@\text{NaYF}_4$  core-shell (35 × 28 nm) NCs. At higher  $\text{Er}^{3+}$  doping concentrations, the size and morphology of NCs are maintained (**Fig. A3.1**). The 5 nm thick inert

shell helps to suppress but will not fully eliminate surface quenching.<sup>22,23,28</sup>

First, the optical properties were analyzed by recording luminescence spectra. **Fig. 3.1c** shows the emission and excitation spectra for Er<sup>3+</sup>-doped core-shell NCs. The excitation lines at 377, 489, 520, 540 and 654 nm are assigned to characteristic Er<sup>3+</sup> transitions from the <sup>4</sup>I<sub>15/2</sub> ground state to the <sup>4</sup>G<sub>11/2</sub>, <sup>4</sup>F<sub>7/2</sub>, <sup>2</sup>H<sub>11/2</sub>, <sup>4</sup>S<sub>3/2</sub> and <sup>4</sup>F<sub>9/2</sub> states. The emission spectrum in lower panel of **Fig. 3.1c** recorded for <sup>2</sup>H<sub>11/2</sub> excitation (520 nm) shows that, in addition to emission in the visible (green <sup>4</sup>S<sub>3/2</sub> and red <sup>4</sup>F<sub>9/2</sub> emission, not shown), the NCs emit in the IR at 840 (<sup>4</sup>I<sub>9/2</sub> → <sup>4</sup>I<sub>15/2</sub> and <sup>4</sup>S<sub>3/2</sub> → <sup>4</sup>I<sub>13/2</sub>), 976 (<sup>4</sup>I<sub>11/2</sub> → <sup>4</sup>I<sub>15/2</sub>) and 1522 nm (<sup>4</sup>I<sub>13/2</sub> → <sup>4</sup>I<sub>15/2</sub>). It is clearly observed in the emission spectra that upon increasing the Er<sup>3+</sup> concentration the relative emission intensities from levels higher than <sup>4</sup>I<sub>13/2</sub> decrease by concentration quenching. In core-only NCs, emission from each excited state, including the <sup>4</sup>I<sub>13/2</sub> state, is quenched for higher dopant concentrations because of stronger surface-related quenching. Quenching of emission can be accurately probed by luminescence decay measurements. With a fixed radiative decay rate, the presence of additional non-radiative (quenching) pathways will result in a faster decay. As an example, in **Fig. 3.1d** the luminescence decay curves of the <sup>4</sup>I<sub>13/2</sub> emission are shown for increasing Er<sup>3+</sup> concentrations in core-only NCs. Significant quenching is observed, especially for concentrations higher than 10% when long-range energy migration becomes possible. To reduce quenching, an inert shell<sup>18,21</sup> is grown on the a selection of cores with 1, 10 and 60% Er<sup>3+</sup>. The actual Er<sup>3+</sup> concentrations incorporated in the NCs are verified by inductively coupled plasma (ICP) analysis. The results in **Table A3.1** show that these concentrations in the NCs are close to the nominally added concentrations. In **Fig. 3.1e** the ET processes for the two extreme concentrations are schematically indicated (1%, limited interaction/no ET between Er<sup>3+</sup> ions, and 60%, energy migration over a network of multiple Er<sup>3+</sup> ions).

**Luminescence decay dynamics for Er<sup>3+</sup> IR-emitting levels** Luminescence decay curves provide important information on luminescence quenching processes. In the present study, we focus on the <sup>4</sup>S<sub>3/2</sub>, <sup>4</sup>F<sub>9/2</sub>, <sup>4</sup>I<sub>11/2</sub> and <sup>4</sup>I<sub>13/2</sub> excited states which are all involved in UC processes (**Fig. 3.1f**). Note that cyclohexane is the solvent we used for the decay dynamics measurements if without specific mention. We first consider the concentration dependence of the luminescence decay for the IR-emitting <sup>4</sup>I<sub>13/2</sub> and <sup>4</sup>I<sub>11/2</sub> excited states, which serve as intermediate levels for IR → NIR and NIR → VIS UC.<sup>29-31</sup> **Fig. 3.2** shows the <sup>4</sup>I<sub>13/2</sub> and <sup>4</sup>I<sub>11/2</sub> decay dynamics after direct excitation in the emitting level for core and core-shell NCs with 1, 10 and 60% Er<sup>3+</sup> in the core. There is a deviation from single-exponential decay, especially for Er<sup>3+</sup> emission in core-only NCs. The initial fast decay is explained by faster quenching for near-surface Er<sup>3+</sup> ions. Growth of a 5 nm protective shell reduces the initial fast decay. To obtain a better insight into the quenching of the emission, the luminescence decay is quantified by a lifetime obtained from single-exponential fitting and also by an average lifetime defined by  $\sum_0^t tI(t) / \sum_0^t I(t)$ , where  $I(t)$  is the emission intensity at time  $t$ . The average lifetimes (indicated in

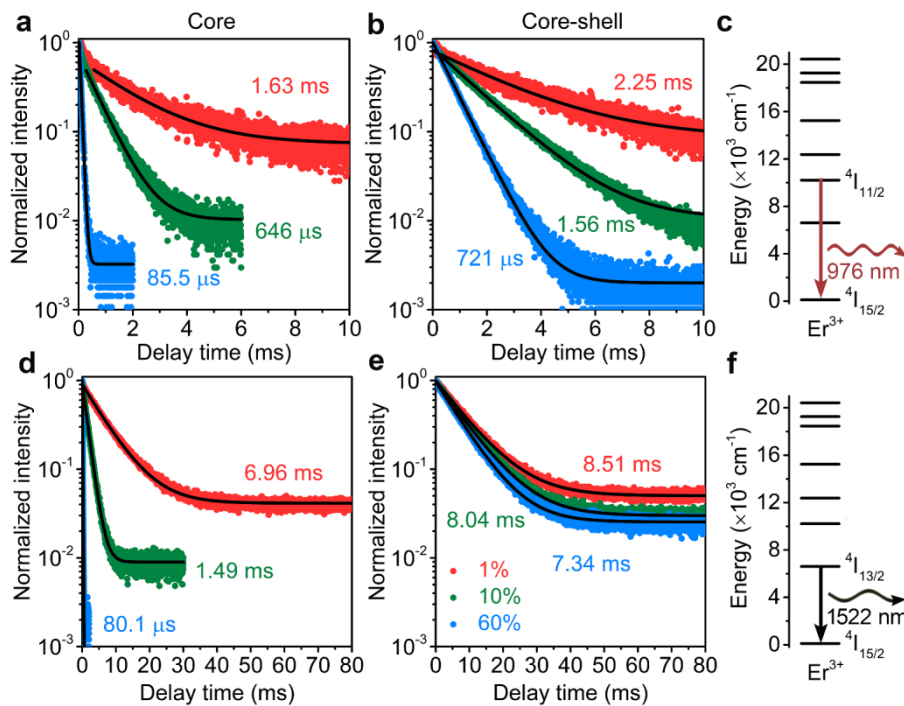


**Figure 3.1.** Characterization of core and core-shell NCs. TEM images of (a) NaYF<sub>4</sub>:1%Er<sup>3+</sup> core and (b) NaYF<sub>4</sub>:1%Er<sup>3+</sup>@NaYF<sub>4</sub> core-shell NCs (scale bar = 50 nm). (c) Excitation spectrum of NaYF<sub>4</sub>:1%Er<sup>3+</sup>@NaYF<sub>4</sub> core-shell NCs for 1522 nm emission and emission spectra of NaYF<sub>4</sub>:X%Er<sup>3+</sup>@NaYF<sub>4</sub> core-shell NCs (X = 1, 10, 60) for 520 nm excitation. (d) Luminescence decay curves of <sup>4</sup>I<sub>13/2</sub> emission excited at 520 nm for NaYF<sub>4</sub>:X%Er<sup>3+</sup> core NCs (X = 1-100). (e) Schematic illustration of interaction between Er<sup>3+</sup> ions for low and high concentrations of Er<sup>3+</sup>. (f) Energy level diagram of Er<sup>3+</sup> showing emission (colored arrows) from levels studied in this work.

the figures) are close to the values obtained from a single-exponential fitting. For core and core-shell NCs, the same trend is observed: the <sup>4</sup>I<sub>13/2</sub> and <sup>4</sup>I<sub>11/2</sub> emission lifetimes decrease as Er<sup>3+</sup> concentration increases due to concentration quenching. However, the reduction in lifetime is much stronger in the core-only NCs, especially for high Er<sup>3+</sup> concentrations. There is also a significant difference between concentration quenching observed for the <sup>4</sup>I<sub>13/2</sub> and <sup>4</sup>I<sub>11/2</sub> levels. Both emissions are strongly quenched in the core-only NCs. Based on the reduction in <sup>4</sup>I<sub>13/2</sub> and <sup>4</sup>I<sub>11/2</sub> lifetimes from over 1 ms (1% Er<sup>3+</sup>) to ~80 μs (60% Er<sup>3+</sup>) in the core-only NCs, it is evident that there is strong concentration quenching giving rise to a quantum yield below 10% in core-only NCs. For the 1522 nm emission from the <sup>4</sup>I<sub>13/2</sub> level, the lifetime increases upon growth of an inert shell and a lifetime of ~8 ms is observed, which is close to the radiative lifetime. The slight reduction from 8.51 (1% Er<sup>3+</sup>) to 7.34 ms (60% Er<sup>3+</sup>) reveals that the (concentration) quenching of the <sup>4</sup>I<sub>13/2</sub> level is almost exclusively surface-related and can be successfully suppressed by shell growth. As a result, the absolute intensity of the <sup>4</sup>I<sub>13/2</sub> emission increases in highly Er-doped core-shell NCs for excitation in higher energy levels (<sup>4</sup>I<sub>11/2</sub>, <sup>4</sup>F<sub>9/2</sub> or <sup>4</sup>S<sub>3/2</sub>) as relaxation to the <sup>4</sup>I<sub>13/2</sub> level is enhanced by cross-relaxation and energy

migration while the  ${}^4I_{13/2}$  emission is not quenched upon increasing the Er-doping concentration.

The situation is different for the  ${}^4I_{11/2}$  level. Shell growth reduces quenching, but still the decay time significantly changes in core-shell NCs upon raising the  $\text{Er}^{3+}$  concentration from 1 (2.25 ms) to 10 (1.56 ms) to 60% (721  $\mu\text{s}$ ). This difference indicates that for the  ${}^4I_{11/2}$  level, in addition to surface quenching, additional quenching pathways contribute. In our recent paper,<sup>23</sup> we suggested a role of the high-energy (3300-3500  $\text{cm}^{-1}$ ) O-H vibrations which are resonant with the  ${}^4I_{11/2}$  to  ${}^4I_{13/2}$  energy gap. It is hard to prevent the incorporation of  $\text{OH}^-$  groups on  $\text{F}^-$  lattice sites in view of their chemical similarity. The present observations are consistent with the presence of  $\text{OH}^-$  quenching centers inside the NC core. At higher  $\text{Er}^{3+}$  concentrations, energy migration to  $\text{OH}^-$  centers inside the core will occur, which reduces the luminescence efficiency and gives rise to faster luminescence decay even when quenching by surface sites is reduced by growth of an inert shell. For the emission from the  ${}^4I_{13/2}$  level (with a larger  $\sim 6500 \text{ cm}^{-1}$  energy gap to the ground state), quenching occurs through multi-phonon relaxation at the surface which can be effectively eliminated by shell growth, making the  ${}^4I_{13/2}$  emission highly efficient (close to 100% QY) even at high (60%)  $\text{Er}^{3+}$  concentrations.



**Figure 3.2.** Decay dynamics for  $\text{Er}^{3+}$  IR-emitting levels. Luminescence decay curves of  ${}^4I_{11/2}$  ((a) core, (b) core-shell and (c) corresponding energy level diagram) and  ${}^4I_{13/2}$  ((d) core, (e) core-shell and (f) corresponding energy level diagram) emissions by direct excitations at 960 and 1500 nm for  $\text{NaYF}_4:\text{X}\%\text{Er}^{3+}$  core and  $\text{NaYF}_4:\text{X}\%\text{Er}^{3+}@\text{NaYF}_4$  core-shell NCs ( $X = 1, 10, \text{ and } 60$  in red, green and blue color).

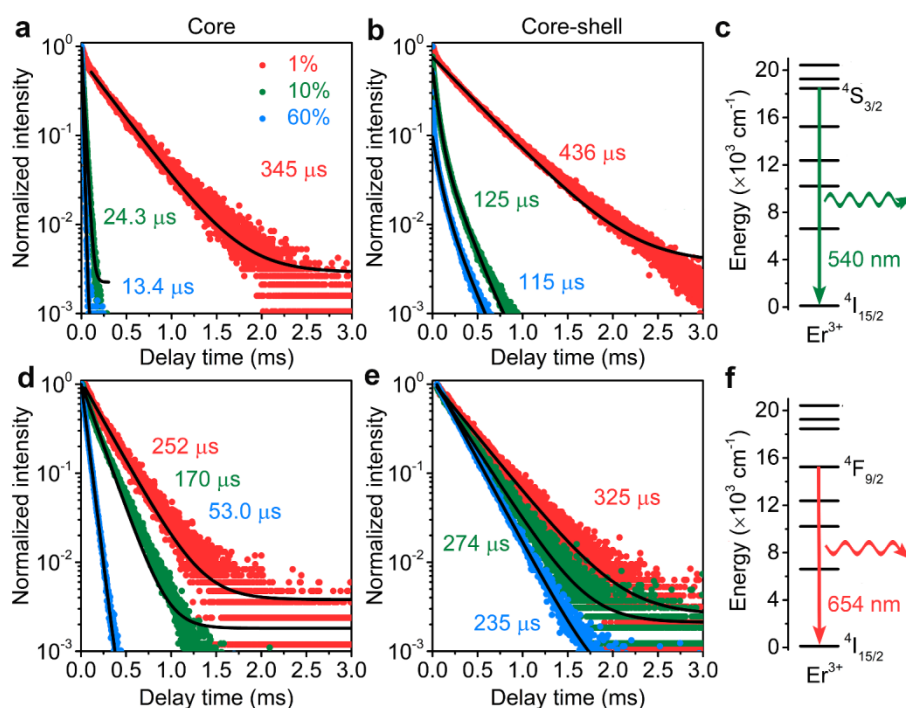
For comparison, we also measured the decay dynamics for  ${}^4\text{I}_{13/2}$  and  ${}^4\text{I}_{11/2}$  emissions after indirect excitation at 520 nm ( ${}^4\text{I}_{15/2} \rightarrow {}^2\text{H}_{11/2}$ , **Fig. A3.2**). Because the  ${}^4\text{S}_{3/2}/{}^2\text{H}_{11/2}$  state acts as an energy reservoir that feeds the IR-emitting states through multi-phonon relaxation, radiative decay, and cross-relaxation processes, a rise time can be observed. The rise time becomes shorter for higher  $\text{Er}^{3+}$  concentrations, resulting from faster ET and cross-relaxation.<sup>32</sup> Qualitatively, the influence of  $\text{Er}^{3+}$  concentration and shell growth on decay times after indirect (**Fig. A3.2**) and direct (**Fig. 3.2**) excitations is the same. However, the absolute values of the lifetimes are different and longer lifetimes are measured after indirect excitation and even can be longer than the radiative lifetime.<sup>33</sup> This makes it difficult to make a meaningful comparison of lifetimes and gain insight into the intrinsic luminescence quenching for the levels of  $\text{Er}^{3+}$  and  $\text{Yb}^{3+}$  involved in the UC. This illustrates that it is cumbersome to retrieve quantitative information on luminescence quenching for specific energy levels following excitation in higher (feeding) energy levels and the importance to analyze luminescence decay curves following direct excitation in the emitting state.

**Luminescence decay dynamics for  $\text{Er}^{3+}$  VIS-emitting levels** After ET UC, the higher-energy  ${}^4\text{S}_{3/2}$  and  ${}^4\text{F}_{9/2}$  states are populated and emit green and red UC emissions. It is also interesting to investigate efficiency losses related to concentration quenching for these emitting levels. **Fig. 3.3** shows the  ${}^4\text{S}_{3/2}$  and  ${}^4\text{F}_{9/2}$  decay dynamics as a function of  $\text{Er}^{3+}$  concentration under direct excitation. As for the IR-emitting levels, concentration quenching shortens the lifetime and the inert shell reduces the effect of concentration quenching. However, there are clear differences between the two levels. Upon increasing the  $\text{Er}^{3+}$  concentration, a much stronger quenching is observed for the green-emitting  ${}^4\text{S}_{3/2}$  level than for the red-emitting  ${}^4\text{F}_{9/2}$  level. This is explained by cross-relaxation<sup>34</sup> of  ${}^4\text{S}_{3/2} + {}^4\text{I}_{15/2} \rightarrow {}^4\text{I}_{9/2} + {}^4\text{I}_{13/2}$  as an additional  ${}^4\text{S}_{3/2}$  decay channel that becomes available at higher  $\text{Er}^{3+}$  concentrations and causes a more than 10-fold decrease in lifetime upon raising the  $\text{Er}^{3+}$  concentration from 1 to 10% (345 to 24  $\mu\text{s}$ ). In the literature, energy migration was suggested to be the mechanism of concentration quenching of the  ${}^4\text{S}_{3/2}$  emission, excluding cross-relaxation.<sup>33</sup> The present results show pronounced quenching of the  ${}^4\text{S}_{3/2}$  emission both in core and core-shell NCs already for 10%  $\text{Er}^{3+}$  where energy migration is limited. Efficient cross-relaxation quenching for  $\text{Er}^{3+}$   ${}^4\text{S}_{3/2}$  emission has been reported, both in bulk and nanocrystalline materials.<sup>35</sup> The strong contribution to cross-relaxation quenching is confirmed by lifetime measurements of the green  $\text{Er}^{3+}$  emission in the core-shell NCs. Shell growth reduces the quenching, but still a strong decrease of the decay time is observed from 436 (1%  $\text{Er}^{3+}$ ) to 125  $\mu\text{s}$  (10%  $\text{Er}^{3+}$ ). This is a clear signature of cross-relaxation quenching and not surface-related quenching.

The luminescence decay curves for the red  ${}^4\text{F}_{9/2}$  emission (**Figs. 3.3d, e**) in core-only NCs show only limited quenching at 10% doping (decrease in lifetime from 252 to 170  $\mu\text{s}$ ). This is consistent with the fact that there is no resonant cross-relaxation path for the  ${}^4\text{F}_{9/2}$  level. At 60%  $\text{Er}^{3+}$ , a stronger decrease in lifetime is observed (53  $\mu\text{s}$ ) that can be explained by energy migration to the surface

where quenching occurs. Upon shell growth, surface quenching is suppressed and the  $^4F_{9/2}$  emission lifetimes lengthen to values close to those in the 1% sample, showing that concentration quenching for the  $^4F_{9/2}$  emission is very limited up to very high (60%)  $Er^{3+}$  concentrations in core-shell NCs.

Based on the results above, important information on the concentration quenching in highly  $Er^{3+}$ -doped  $NaYF_4$  NCs can be obtained. Under low excitation powers, strong concentration quenching is observed for all emitting levels ( $^4S_{3/2}$ ,  $^4F_{9/2}$ ,  $^4I_{11/2}$  and  $^4I_{13/2}$ ) in core-only NCs with 60%  $Er^{3+}$ . The quenching for the  $^4S_{3/2}$  (545 nm) and  $^4I_{11/2}$  (976 nm) emissions is stronger and is caused not only by surface quenching, but also by cross-relaxation ( $^4S_{3/2}$ ) and O-H vibrations ( $^4I_{11/2}$ ) inside the NC core. Growth of an inert shell cannot eliminate these quenching pathways. For the  $^4F_{9/2}$  (654 nm) and  $^4I_{13/2}$  (1522 nm) levels, the dominant mechanism for concentration quenching is energy migration to the surface where multi-phonon relaxation and possibly also surface defect states quench the emission. Growth of an inert shell (5 nm thickness here) can effectively eliminate these quenching processes and efficient red ( $^4F_{9/2}$ ) or IR ( $^4I_{13/2}$ ) emission is observed up to the highest  $Er^{3+}$  concentrations.



**Figure 3.3.** Decay dynamics for  $Er^{3+}$  VIS-emitting levels. Luminescence decay curves of  $Er^{3+}$   $^4S_{3/2}$  ((a) core, (b) core-shell and (c) corresponding energy level diagram) and  $^4F_{9/2}$  ((d) core, (e) core-shell and (f) corresponding energy level diagram) emissions by direct excitations of 520 and 640 nm for  $NaYF_4:X\%Er^{3+}$  core and  $NaYF_4:X\%Er^{3+}@NaYF_4$  core-shell NCs ( $X = 1, 10,$  and  $60$  in red, green and blue color).

To analyze the concentration quenching for UC more quantitatively, we determined lifetime ratios for core and core-shell NCs for the three different  $\text{Er}^{3+}$  concentrations (1, 10 and 60%), as summarized in **Table 3.1**. The lifetime ratios for 1%  $\text{Er}^{3+}$ -doped core-shell and core NCs (1st row) are a measure for how well the 5 nm shell shields the respective levels from quenching by high-energy vibrations of the solvent/ligand. The ratios are similar (around 1.3) for the four different levels. This indicates that vibrational quenching is an active quenching mechanism in the 1% doped NCs and that shell growth is effective in reducing the losses for all emitting levels. This is consistent with previous reports.<sup>36-38</sup> The role of ET and concentration quenching processes is quantified in the 2nd to 4th row where ratios of emission lifetimes for core-shell NCs are tabulated for different doping concentrations. Shell growth limits surface quenching and the ratios reflect the role of quenching processes inside the NC core. The ratio of emission lifetimes in the core-shell NCs with 1 and 10%  $\text{Er}^{3+}$  is the highest for the  $^4\text{S}_{3/2}$  level (3.49 vs. 1.06-1.44 for other levels). This is explained by efficient  $^4\text{S}_{3/2}$  cross-relaxation quenching between  $\text{Er}^{3+}$  neighbors that is effective at moderate  $\text{Er}^{3+}$  concentrations, well below the percolation point for energy migration. The ratio of the lifetimes for the 1/60% core-shell samples provides insight into the role of long-distance energy migration. The relatively large value for the  $^4\text{I}_{11/2}$  emission (3.12 vs.  $\sim 1.3$  for the  $^4\text{F}_{9/2}$  and  $^4\text{I}_{13/2}$  levels) shows that energy migration to quenching sites (possibly  $\text{OH}^-$ ) is important for quenching of the  $^4\text{I}_{11/2}$  emission in 60%  $\text{Er}^{3+}$ -doped NCs. The fourth row gives the ratio of lifetimes in 10 over 60%  $\text{Er}^{3+}$ -doped core-shell NCs and signifies the role of (long-range) energy migration vs. (short-range) cross-relaxation ET quenching. The high number for the  $^4\text{I}_{11/2}$  level reflects that for this level quenching through energy migration is important, while for the  $^4\text{S}_{3/2}$  level, short-range cross-relaxation is the dominant quenching process. For the  $^4\text{F}_{9/2}$  and  $^4\text{I}_{13/2}$  levels, the lifetime ratios in the core-shell NCs are between 1.1 and 1.4 for all  $\text{Er}^{3+}$  concentrations as quenching processes in the NC core are inefficient. Both the  $^4\text{F}_{9/2}$  and  $^4\text{I}_{13/2}$  levels are efficiently luminescing up to high  $\text{Er}^{3+}$  concentrations for core-shell NCs. Finally, in the fifth row, the ratios of the radiative decay time and the decay time in 1% doped core-shell NCs are tabulated. The intrinsic radiative lifetime  $\tau_0$  is determined taking into account the correction for local field effects<sup>39-42</sup> (see **Appendices** for details). The ratio of the radiative and observed lifetimes is the highest for the  $^4\text{I}_{11/2}$  state (3.8), more than twice the ratios obtained for the  $^4\text{S}_{3/2}$ ,  $^4\text{F}_{9/2}$  and  $^4\text{I}_{13/2}$  states. The relative strong quenching of the  $^4\text{I}_{11/2}$  emission in low-doped core-shell NCs has been observed before and was attributed to efficient quenching by O-H vibrations resonant with the  $^4\text{I}_{11/2}$  to  $^4\text{I}_{13/2}$  energy gap.<sup>38,43</sup> Recently, confirmation for hypothesis was reported:  $\text{NaYF}_4:\text{Er},\text{Yb}$  NCs with superior UC QYs, close to the highest QYs obtained in bulk  $\text{NaYF}_4:\text{Er},\text{Yb}$ , were realized by using a synthesis method in which all reactants containing OH groups (such as water and MeOH) were excluded.<sup>44</sup>

The present results on lifetime ratios in  $\text{NaYF}_4$  core-shell NCs with 1, 10 and 60%  $\text{Er}^{3+}$  reveal that emission from the  $^4\text{I}_{11/2}$  and the  $^4\text{S}_{3/2}$  levels is strongly quenched at higher  $\text{Er}^{3+}$  concentrations, in

spite of an inert NaYF<sub>4</sub> shell. The <sup>4</sup>I<sub>11/2</sub> emission is sensitive to quenching sites inside the core that can be effectively reached by energy migration at elevated Er<sup>3+</sup> concentrations. This will give rise to a significant reduction of UC efficiency, especially for the highest dopant concentration (60% Er<sup>3+</sup>) at low excitation densities. Because of the resonance of the Er<sup>3+</sup> <sup>4</sup>I<sub>11/2</sub> and Yb<sup>3+</sup> <sup>2</sup>F<sub>5/2</sub> levels, energy migration to defect sites in co-doped Yb<sup>3+</sup>-Er<sup>3+</sup> NCs with a high total Yb + Er concentration can also lead to strongly reduced UC efficiencies. Emission from the <sup>4</sup>S<sub>3/2</sub> level is quenched by effective cross-relaxation, already at Er<sup>3+</sup> concentration of 10%. Emission from the <sup>4</sup>F<sub>9/2</sub> and <sup>4</sup>I<sub>13/2</sub> levels remains efficient (QY > 50%) up to the highest Er<sup>3+</sup> concentration (60%) in core-shell NCs. This also indicates that IR (1.5 μm) to NIR (1000 nm) UC from the <sup>4</sup>I<sub>13/2</sub> level can be more efficient than the more commonly used NIR (980 nm) to visible (545 nm) UC.<sup>25</sup>

**Luminescence decay dynamics for Yb<sup>3+</sup> IR-emitting level** To further understand and optimize the UC efficiency in highly doped core-shell NCs under low excitation densities, lifetime measurements were also done for Yb<sup>3+</sup>-doped NCs. The Yb<sup>3+</sup> ion has a single (<sup>2</sup>F<sub>5/2</sub>) excited state and is commonly used as a sensitizer to realize brighter UC emission. Energy transfer from Yb<sup>3+</sup> to Er<sup>3+</sup> feeds the UC emission and it has been established that UC QYs correlate with the lifetime of the Yb<sup>3+</sup> excited state.<sup>37</sup> Faster relaxation of the Yb<sup>3+</sup> emission through energy migration to quenching sites reduces the UC efficiency. Modelling of energy migration is complex but rate equation models have been able to reproduce excited state dynamics in concentrated UC NCs.<sup>37</sup> In **Fig. A3.3**, <sup>2</sup>F<sub>5/2</sub> emission decay curves are displayed as a function of Yb<sup>3+</sup> concentration for NaYF<sub>4</sub>:X%Yb<sup>3+</sup> core-only NCs (X = 1-100). The lifetime shortens with increasing Yb<sup>3+</sup> concentration, which can be explained by concentration quenching related to energy migration to surface quenching sites at elevated Yb<sup>3+</sup> concentrations. To investigate the influence of shell growth, **Fig. 3.4** displays the luminescence decay curves for the Yb<sup>3+</sup> emission in core-only and core-shell NaYF<sub>4</sub> NCs with 1, 10 and 60% Yb<sup>3+</sup>. The lifetime ratios are also included in **Table 3.1**. For core-only NCs, a rapid decrease in lifetime is

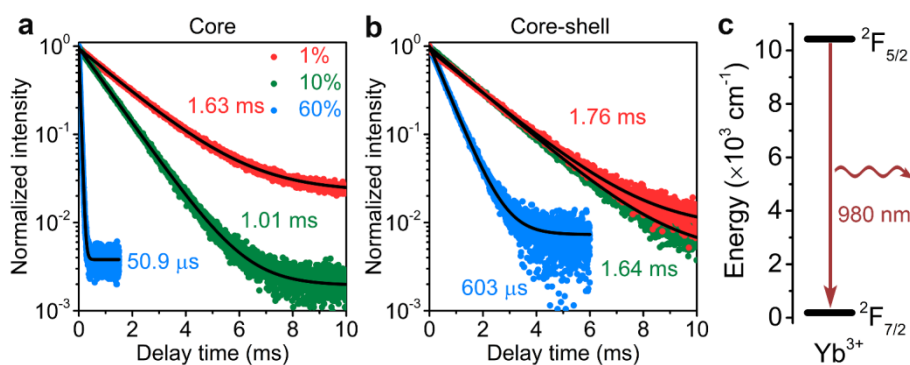
**Table 3.1. Quantitative analysis of concentration quenching.** Ratios of emission lifetimes for various levels of Er<sup>3+</sup> (<sup>4</sup>S<sub>3/2</sub>, <sup>4</sup>F<sub>9/2</sub>, <sup>4</sup>I<sub>11/2</sub> and <sup>4</sup>I<sub>13/2</sub>) and Yb<sup>3+</sup> (<sup>2</sup>F<sub>5/2</sub>) doped in core-only (τ<sub>c</sub>) and core-shell (τ<sub>c-s</sub>) NCs with different concentrations (1, 10 or 60%) of Er<sup>3+</sup> or Yb<sup>3+</sup>.

	<sup>4</sup> S <sub>3/2</sub>	<sup>4</sup> F <sub>9/2</sub>	<sup>4</sup> I <sub>11/2</sub>	<sup>4</sup> I <sub>13/2</sub>	<sup>2</sup> F <sub>5/2</sub>
τ <sub>c-s/1%</sub> /τ <sub>c/1%</sub>	1.26	1.29	1.38	1.22	1.08
τ <sub>c-s/1%</sub> /τ <sub>c-s/10%</sub>		1.19	1.44	1.06	1.07
τ <sub>c-s/1%</sub> /τ <sub>c-s/60%</sub>		1.38	3.12	1.22	2.92
τ <sub>c-s/10%</sub> /τ <sub>c-s/60%</sub>		1.17	2.16	1.16	2.72
τ <sub>0</sub> /τ <sub>c-s/1%</sub>	1.66	1.81	3.80	1.06	1.10

observed, especially in the 60% doped NC. After shell growth,  ${}^2F_{5/2}$  emission decay time is similar for the 1 and 10%  $\text{Yb}^{3+}$ -doped NCs and close to the radiative decay time (1.93 ms, see [Appendix](#) for details). Upon doping with 60%  $\text{Yb}^{3+}$ , the decay time drops to 603  $\mu\text{s}$  corresponding to a QY of  $\sim 30\%$ . The high efficiency and limited quenching of the  $\text{Yb}^{3+} {}^2F_{5/2}$  emission can be understood from the large energy separation ( $\sim 10000 \text{ cm}^{-1}$ ) between  ${}^2F_{5/2}$  excited state and  ${}^2F_{7/2}$  ground state, which limits multi-phonon relaxation. The present results indicate that in spite of this large gap concentration quenching does occur at concentrations above 10%. It can cause a reduction in UC efficiency at low excitation densities in highly  $\text{Yb}^{3+}$ -doped NCs, as reported in the literature.<sup>45,46</sup> Optimizing the Er-concentration to enhance the  $\text{Yb}^{3+}$ - $\text{Er}^{3+}$  energy transfer rate can provide a more efficient competing UC channel and reduce the role of concentration quenching. Indeed, in a recent study, it was found that for low excitation powers in a concentrated Yb NCs ( $\text{NaYb}_{1-x}\text{Er}_x\text{F}_4$ ) the optimum Er concentration is 8% ( $x = 0.08$ ), significantly higher than the typically used  $\text{Er}^{3+}$  concentration of 2%.<sup>15</sup>

### 3.3.2 Solvent quenching for UC NCs

**$\text{Er}^{3+}$  IR-emitting levels** In addition to dopant concentration, the solvents in which the NCs are dispersed also affect the UC efficiency. In a recent paper,<sup>23</sup> we demonstrated how by coupling with high-energy vibrations of surrounding solvent molecules the various energy levels involved in the UC process are quenched. Shell growth strongly reduces the quenching by increasing the distance between the optically active centers and the high-energy vibrations.<sup>22,23</sup> To further understand the role of solvent quenching, the luminescence decay dynamics of  $\text{Er}^{3+}$  and  $\text{Yb}^{3+}$  states was investigated for  $\text{NaYF}_4:1\%\text{Er}^{3+}@/\text{NaYF}_4$  and  $\text{NaYF}_4:1\%\text{Yb}^{3+}@/\text{NaYF}_4$  core-shell NCs in three solvents:



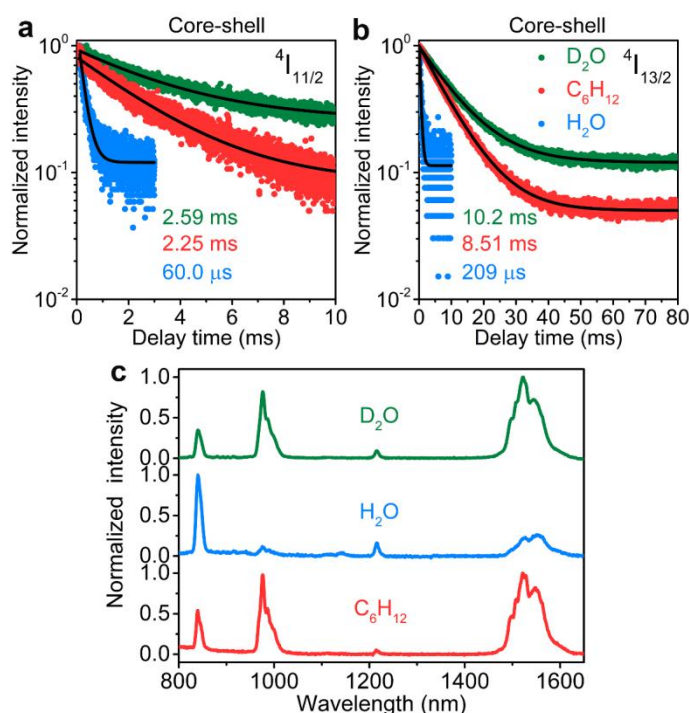
**Figure 3.4.** Decay dynamics for  $\text{Yb}^{3+}$  IR-emitting level. Luminescence decay curves of  $\text{Yb}^{3+} {}^2F_{5/2}$  emission for direct excitation at 960 nm for (a)  $\text{NaYF}_4:\text{X}\%\text{Yb}^{3+}$  core and (b)  $\text{NaYF}_4:\text{X}\%\text{Yb}^{3+}@/\text{NaYF}_4$  core-shell NCs ( $X = 1, 10, 60$  in red, green and blue color) and (c) corresponding energy level diagram.

cyclohexane (with 2900-3000  $\text{cm}^{-1}$  of C-H vibrations from surrounding solvent molecules and surface ligands), water  $\text{H}_2\text{O}$  (3200-3700  $\text{cm}^{-1}$  of O-H vibrations) and heavy water  $\text{D}_2\text{O}$  (chemically the same as water but with much lower vibrational energies 2200-2500  $\text{cm}^{-1}$  for O-D vibrations). Low doping concentrations were used to prevent interference with concentration quenching. Hydrophobic NCs passivated with oleate ligands are dispersed in cyclohexane. Acid treatment (see **Method** for details) removes the oleate ligands and allows NCs to dissolve in deionized water  $\text{H}_2\text{O}$  and heavy water  $\text{D}_2\text{O}$ .<sup>47,48</sup> **Figs. 3.5a, b** show the decay curves of IR  $^4\text{I}_{11/2}$  and  $^4\text{I}_{13/2}$  emission for  $\text{NaYF}_4:1\%\text{Er}^{3+}@\text{NaYF}_4$  core-shell NCs in the three solvents. The decay time decreases in the order of  $\text{D}_2\text{O}$ , cyclohexane and  $\text{H}_2\text{O}$ . When considering the influence of local field effects ( $n$  (cyclohexane) = 1.43 and  $n$  ( $\text{H}_2\text{O}/\text{D}_2\text{O}$ ) = 1.33), the radiative lifetimes are 8.54 and 10.26 ms for  $^4\text{I}_{11/2}$  emission, and 9.06 and 11.01 ms for  $^4\text{I}_{13/2}$  emission in cyclohexane and  $\text{H}_2\text{O}/\text{D}_2\text{O}$ , respectively.

The lifetimes observed for the  $^4\text{I}_{11/2}$  and  $^4\text{I}_{13/2}$  emissions are similar for the NCs in cyclohexane and  $\text{D}_2\text{O}$ , indicating similar QY for IR emission in the two solvents. For the  $^4\text{I}_{13/2}$  level, the lifetimes in the core-shell NCs are close to the radiative lifetimes in  $\text{D}_2\text{O}$  and cyclohexane. The energy gap to the ground state of  $\sim 6500 \text{ cm}^{-1}$  requires more than two vibrations in  $\text{D}_2\text{O}$  and cyclohexane. Clearly, the three-phonon relaxation rate for the  $\text{Er}^{3+}$  ions in core-shell NCs is much lower than the radiative decay rate, and the efficiency of the  $^4\text{I}_{13/2}$  level is close to 100% in cyclohexane and  $\text{D}_2\text{O}$ . For the NCs in water, the two-vibrational overtone of the O-H vibrations is resonant with the  $6500 \text{ cm}^{-1}$  energy gap. Even with the 5 nm protective shell, two-phonon relaxation can compete with radiative decay, giving rise to a faster (209  $\mu\text{s}$ ) decay of the  $^4\text{I}_{13/2}$  emission in  $\text{H}_2\text{O}$ . The  $^4\text{I}_{11/2}$ - $^4\text{I}_{13/2}$  energy gap of  $\sim 3500 \text{ cm}^{-1}$  is small enough to allow the two-phonon relaxation process in  $\text{D}_2\text{O}$  and cyclohexane, and this gives rise to a shortening of the lifetime to 2.2-2.6 ms for the  $^4\text{I}_{11/2}$  emission of  $\text{Er}^{3+}$  in the core-shell NCs (radiative decay time 8.54 ms). As a single O-H vibration can bridge the energy gap to the  $^4\text{I}_{13/2}$  level, the  $^4\text{I}_{11/2}$  emission is very sensitive to the presence of O-H vibrations. In  $\text{H}_2\text{O}$ , the emission decay time is 60  $\mu\text{s}$  and the  $^4\text{I}_{11/2}$  emission is strongly quenched by phonon relaxation, in spite of the 5 nm inert shell. The sensitivity to water is further illustrated in **Fig. A3.4** where the  $^4\text{I}_{11/2}$  decay dynamics is shown for gradual  $\text{H}_2\text{O}$  addition to  $\text{NaYF}_4:1\%\text{Er}^{3+}@\text{NaYF}_4$  core-shell NCs in  $\text{D}_2\text{O}$ . For small amounts of  $\text{H}_2\text{O}$ , strong quenching of the  $^4\text{I}_{11/2}$  emission is observed. The emission spectra upon excitation in the  $^2\text{H}_{11/2}$  level at 520 nm shown in **Fig. 3.5c** provide further evidence for the solvent effect. Taking the  $^4\text{S}_{3/2}$ - $^4\text{I}_{13/2}/^4\text{I}_{9/2}$ - $^4\text{I}_{15/2}$  emission at 840 nm as a reference, the emissions at 976 and 1522 nm ( $^4\text{I}_{11/2}$ ,  $^4\text{I}_{13/2} \rightarrow ^4\text{I}_{15/2}$ ) are strongly quenched in  $\text{H}_2\text{O}$ , but are equally strong for the NCs in  $\text{D}_2\text{O}$  and cyclohexane.

**$\text{Er}^{3+}$  VIS-emitting levels** We also investigated the role of vibration induced quenching in water for the visible UC emission (**Fig. A3.5**). The emission lifetimes are similar for the  $^4\text{S}_{3/2}$  and  $^4\text{F}_{9/2}$  levels in cyclohexane and  $\text{D}_2\text{O}$  (436 and 471  $\mu\text{s}$  for the  $^4\text{S}_{3/2}$  level, and 325 and 379  $\mu\text{s}$  for the  $^4\text{F}_{9/2}$  level). In  $\text{H}_2\text{O}$ , the lifetimes become faster (241 and 262  $\mu\text{s}$  for  $^4\text{S}_{3/2}$  and  $^4\text{F}_{9/2}$  emissions). The decrease in

lifetime by changing the solvent from D<sub>2</sub>O to H<sub>2</sub>O is 49% for the <sup>4</sup>S<sub>3/2</sub> emission and 31% for the <sup>4</sup>F<sub>9/2</sub> emission. The fact that the O-H vibrational energy is closer in resonance to the energy separation between <sup>4</sup>S<sub>3/2</sub> and <sup>4</sup>F<sub>9/2</sub> states (~3200 cm<sup>-1</sup>) than for <sup>4</sup>F<sub>9/2</sub> to <sup>4</sup>I<sub>9/2</sub> energy gap (~2800 cm<sup>-1</sup>), can explain the stronger quenching for <sup>4</sup>S<sub>3/2</sub> state in H<sub>2</sub>O. This result is in agreement with the observation that changing to H<sub>2</sub>O as solvent can enhance red emission at the expense of green emission upon a 980 nm excitation.<sup>47</sup> Previously, an unexpected longer lifetime for red <sup>4</sup>F<sub>9/2</sub> emission was reported for Er<sup>3+</sup>-doped NCs in H<sub>2</sub>O compared to that for D<sub>2</sub>O under 380 nm excitation in the <sup>4</sup>G<sub>11/2</sub> state.<sup>49</sup> This was interpreted as an increased <sup>4</sup>F<sub>9/2</sub> population through multi-phonon relaxation from higher-energy levels. Here, lifetime measurement under direct excitation (Fig. A3.5b) clearly demonstrates more pronounced quenching for the red-emitting <sup>4</sup>F<sub>9/2</sub> level by O-H vibrations (emission lifetime 262 μs) in comparison to O-D vibrations (379 μs), in line with what is expected based on higher vibrational energy of O-H vibrations. Note that all experiments for solvent quenching were conducted on core-shell NCs. Much stronger vibrational quenching is observed for core-only NCs.



**Figure 3.5.** Solvent quenching for Er<sup>3+</sup> IR-emitting levels. Luminescence decay curves of (a) Er<sup>3+</sup> <sup>4</sup>I<sub>11/2</sub> and (b) <sup>4</sup>I<sub>13/2</sub> emission by direct excitations of 960 and 1500 nm, and (c) emission spectra of 520 nm excitation for NaYF<sub>4</sub>:1%Er<sup>3+</sup>@NaYF<sub>4</sub> core-shell NCs in heavy water D<sub>2</sub>O, cyclohexane C<sub>6</sub>H<sub>12</sub> and deionized water H<sub>2</sub>O.

The present analysis of luminescence decay times under direct excitation for various energy levels of  $\text{Er}^{3+}$  in core-shell NCs dispersed in different solvents reveals a clear difference for the role of the high-energy O-H vibrations of water. Both IR levels ( $^4\text{I}_{11/2}$  and  $^4\text{I}_{13/2}$ ) which serve as intermediate levels in UC processes show significant quenching by ET to the high-energy O-H vibrations, even in core-shell NCs. The presently used shell thickness of 5 nm is not sufficient to protect the IR-emitting levels from quenching by ET to the fundamental O-H vibration ( $3500\text{ cm}^{-1}$ ) for the  $^4\text{I}_{11/2}$  level or the two-phonon mode for the  $^4\text{I}_{13/2}$  level. The reason for the strong quenching is a combination of a high oscillator strength for O-H vibrations (favoring ET as the Förster-type ET rate is proportional to the acceptor oscillator strength) and a long radiative lifetime for the IR-emitting levels ( $\sim 8\text{ ms}$ ) which makes it harder for the slow radiative decay to compete with ET. To enhance UC efficiencies in aqueous media, a thicker inert shell will be beneficial. For the visible UC emission in the green and red spectral region, the transition from apolar aliphatic solvents to water induces additional non-radiative decay, but the effect is less than a factor of 2.

**$\text{Yb}^{3+}$  IR-emitting level** In  $\text{Er}^{3+}, \text{Yb}^{3+}$  co-doped UC NCs, quenching of the 980 nm NIR emission from  $\text{Yb}^{3+}$  in different solvents is known to reduce the UC efficiency. To investigate the role of  $\text{Yb}^{3+}$  quenching, we measured the solvent dependence of  $^2\text{F}_{5/2}$  decay for singly doped  $\text{NaYF}_4:1\% \text{Yb}^{3+}@\text{NaYF}_4$  core-shell NCs (Fig. A3.6). The decay times for the  $\text{Yb}^{3+}$  NIR emission are very similar and independent of the solvent, indicating a limited contribution of water vibrations in quenching the  $\sim 980\text{ nm}$  IR emission.<sup>23,38,49</sup> The absence of solvent quenching is not unexpected in view of a large energy gap between  $^2\text{F}_{5/2}$  and  $^2\text{F}_{7/2}$  states of  $10000\text{ cm}^{-1}$  that requires three-phonon relaxation in water (vs. four phonons in organic solvents). For the core-shell NCs, the minimum distance of 5 nm imposed by the inert shell is sufficient to virtually eliminate multi-phonon quenching. The small decrease in the luminescence decay time of the  $^2\text{F}_{5/2}$  emission from 2.10 in  $\text{D}_2\text{O}$  to 1.98 ms in  $\text{H}_2\text{O}$  can be ascribed to some multi-phonon quenching in  $\text{H}_2\text{O}$  and the quenching rate can be estimated to be  $\sim 30\text{ s}^{-1}$ . Note that water quenching is present in core-only NCs,<sup>43</sup>  $\text{Yb}^{3+}$  complexes,<sup>50</sup> and silica-encapsulated NCs,<sup>49</sup> where  $\text{Yb}^{3+}$  ions are directly coupled to water molecules and ligands with high-energy vibrational modes. However, doping in crystalline dielectric media with a 5 nm shell passivation gives rise to efficient  $\text{Yb}^{3+}$  emission and sensitization of ET UC. The quenching of 980 nm NIR emission in  $\text{Er}^{3+}, \text{Yb}^{3+}$  co-doped NCs in water is primarily due to rapid ET between the  $^2\text{F}_{5/2}$  level of  $\text{Yb}^{3+}$  and the resonant  $^4\text{I}_{11/2}$  level of  $\text{Er}^{3+}$ , and quenching of the  $^4\text{I}_{11/2}$  level by O-H vibrations as discussed above.

### 3.4 Conclusions

There is a trend toward higher doping concentrations for both  $\text{Yb}^{3+}$  and  $\text{Er}^{3+}$  to achieve higher brightness of UC NCs. High brightness and superior quantum yields of UC emission have been reported under high power density excitation for these highly doped NCs. Insight into concentration

and solvent quenching processes is however lacking and requires studies at low excitation powers where UC rates are low and decay dynamics is dominated by non-radiative and radiative decay of excited states. Here, we have presented a systematic investigation of decay dynamics for  $\text{Er}^{3+}$  and  $\text{Yb}^{3+}$  in core and core-shell NCs under direct excitation in various emitting levels involved in UC processes for a wide range of concentrations (1-100% doping).

Core-only NCs suffer from strong concentration quenching. Fast migration to surface ions that are strongly quenched by vibrational coupling with nearby high-energy vibrations of solvent and capping molecules can explain the pronounced concentration quenching. For core-shell NCs, surface quenching is suppressed but still concentration quenching is observed. A detailed analysis on decay behavior following direct excitation in the emitting levels demonstrates that both the  $^4\text{S}_{3/2}$  (green) and  $^4\text{I}_{11/2}$  (NIR) levels are strongly quenched upon raising the  $\text{Er}^{3+}$  concentration. For the  $^4\text{S}_{3/2}$  level, cross-relaxation has been identified as the main quenching mechanism, while for the  $^4\text{I}_{11/2}$  level, energy migration to defects/impurities in the core (possibly  $\text{OH}^-$ ) is responsible for the observed concentration quenching. The IR-emitting  $^4\text{I}_{13/2}$  and the red-emitting  $^4\text{F}_{9/2}$  levels do not show strong concentration quenching and their emissions remain efficient up to high (60%) doping concentrations in core-shell NCs. Also for  $\text{Yb}^{3+}$ , limited quenching is observed in highly (60%)  $\text{Yb}^{3+}$ -doped core-shell NCs.

The role of solvent vibrations was investigated by studying decay dynamics for emission from various levels of  $\text{Er}^{3+}$  and for the NIR emission of  $\text{Yb}^{3+}$  in core-shell NCs. The results show a much stronger quenching for the IR-emitting levels  $^4\text{I}_{11/2}$  and  $^4\text{I}_{13/2}$  (intermediate levels in the UC process) than for the  $^4\text{S}_{3/2}$  and  $^4\text{F}_{9/2}$  levels responsible for the green and red UC emission. Our work provides a better understanding and deeper insight on quenching pathways in highly doped UC NCs, and provides important information on design rules for efficient UC under lower power densities that are required in many applications.

### 3.5 Methods

**Chemicals** The synthesis was conducted using commercially available reagents. Ethanol (Analytical Reagent, A.R.), cyclohexane (A.R.), heavy water (99.9%), oleic acid (90%), 1-octadecene (90%), yttrium (III) acetate (99.9%), erbium (III) acetate (99.9%), ytterbium (III) acetate (99.9%), sodium hydroxide (97%), ammonium fluoride (98%), acetone (A.R.), diethyl ether (A.R.) and hydrochloric acid (HCl, 37%, A.R.) were purchased from Sigma-Aldrich without further purification.

**Synthesis of core and core-shell  $\text{NaYF}_4$  NCs** Stoichiometric amounts of rare earth acetates (totally 1 mmol) were added into a 100 mL three-necked flask, which contained 6 mL oleic acid and 17 mL 1-octadecene. The mixture was stirred vigorously and heated to 390 K for 1.5 h under vacuum and subsequently allowed to cool down to room temperature under a gentle flow of nitrogen gas. This

was followed by a rapid injection of a mixture, containing 2.5 mmol NaOH and 4 mmol  $\text{NH}_4\text{F}$  dissolved in 3 and 7 ml methanol. The reaction mixture was kept at room temperature overnight. Next, the solution was heated to 370 K for 0.5 h under vacuum and to 570 K for 2 h under a protective nitrogen atmosphere. Afterwards, the solution was cooled down and the product was precipitated by adding excess ethanol. The NCs were washed with ethanol and cyclohexane three times and dissolved in cyclohexane again. For the synthesis of core-shell NCs, all steps were the same except for the injection of core NCs in cyclohexane into the flask before adding the mixture of NaOH and  $\text{NH}_4\text{F}$  methanol solutions. Note that an inert shell  $\text{NaYF}_4$  was grown around the core so the reaction mixture for shell growth contained only yttrium acetate as rare earth precursor. Core-shell NCs were also dispersed in cyclohexane. The final core and core-shell NCs were analyzed by X-ray diffraction (XRD), which confirmed the hexagonal crystal structure of the NCs. To visualize the morphology and size of NCs, NCs dropped on amorphous carbon-coated copper grids (200 mesh) were imaged on an FEI Tecnai-12 TEM operating at 120 kV.

**Ligand-free NCs** To disperse NCs in deionized water and heavy water, the oleate ligands on the surface of NCs were removed by acid treatment.<sup>51</sup> A 10 mL dispersion of NCs in cyclohexane (10 mg/mL) in a vial was dried in vacuum to obtain a precipitation, to which deionized water (10 mL) was then added. The pH value was adjusted to ~2 using 0.1 M HCl. The mixture was sonicated for about 3 h to remove the oleate ligands from the NC surface as carboxylate group of oleate is protonated to form oleic acid. Subsequently, diethyl ether was added three times and mixed with the aqueous solution to remove oleic acid through extraction. The ligand-free NCs were precipitated with acetone via high-speed centrifugation and finally redispersed in deionized water or heavy water. TEM measurements demonstrated that shape and size are maintained after ligand removal and Fourier transform infrared (FT-IR) measurement confirmed the removal of oleate ligands from NC surface.

**Optical spectroscopy** Photoluminescence spectra were recorded using an Edinburgh Instruments FLS920 spectrometer with a 450 W xenon lamp as excitation source. In the visible range of 400-800 nm, emission was recorded with a Hamamatsu R928 photomultiplier tube (PMT). A liquid-nitrogen cooled Hamamatsu R5507-73 PMT was used for the IR (800-1600 nm) region. Luminescence decay curves were measured using the multi-channel scaling (MCS) option integrated in the spectrofluorometer with pulsed excitation by an optical parametric oscillator (OPO) system (410-2200 nm, Oportek Opolette HE 355 II) pumped by the third harmonic of a YAG:Nd<sup>3+</sup> laser (~1 mJ pulses with a 10 ns pulse duration and repetition rate 20 Hz).

## 3.6 References

1. Zheng, W.; Huang, P.; Tu, D. T.; Ma, E.; Zhu, H. M.; Chen, X. Y. Lanthanide-Doped Upconversion Nano-Bioprobes: Electronic Structures, Optical Properties, and Biodetection. *Chem. Soc. Rev.* **2015**, *44*, 1379-1415.
2. Goldschmidt, J. C.; Fischer, S. Upconversion for Photovoltaics - a Review of Materials, Devices and Concepts for Performance Enhancement. *Adv. Opt. Mater.* **2015**, *3*, 510-535.
3. Wang F.; Liu. X. G. Recent Advances in the Chemistry of Lanthanide-Doped Upconversion Nanocrystals. *Chem. Soc. Rev.* **2009**, *38*, 976-989.
4. Wang, X. D.; Valiev, R. R.; Ohulchansky, T. Y.; Ågren, H.; Yang, C. H.; Chen, G. Y. Dye-Sensitized Lanthanide-Doped Upconversion Nanoparticles. *Chem. Soc. Rev.* **2017**, *46*, 4150-4167.
5. Wang, F.; Han, Y.; Lim, C. S.; Lu, Y. H.; Wang, J.; Xu, J.; Chen, H. Y.; Zhang, C.; Hong, M. H.; Liu, X. G. Simultaneous Phase and Size Control of Upconversion Nanocrystals through Lanthanide Doping. *Nature* **2010**, *463*, 1061-1065.
6. Boyer, J.-C.; Cuccia, L. A.; Capobianco, J. A. Synthesis of Colloidal Upconverting NaYF<sub>4</sub>: Er<sup>3+</sup>/Yb<sup>3+</sup> and Tm<sup>3+</sup>/Yb<sup>3+</sup> Monodisperse Nanocrystals. *Nano Lett.* **2007**, *7*, 847-852.
7. Wang F.; Liu. X. G. Upconversion Multicolor Fine-Tuning: Visible to Near-Infrared Emission from Lanthanide-Doped NaYF<sub>4</sub> Nanoparticles. *J. Am. Chem. Soc.* **2008**, *130*, 5642-5643.
8. Wang, Y. F.; Liu, G. Y.; Sun, L. D.; Xiao, J. W.; Zhou, J. C.; Yan, C. H. Nd<sup>3+</sup>-Sensitized Upconversion Nanophosphors: Efficient in Vivo Bioimaging Probes with Minimized Heating Effect. *ACS Nano* **2013**, *7*, 7200-7206.
9. Liu. X. G., Yan, C. H.; Capobianco, J. A. Photon Upconversion Nanomaterials. *Chem. Soc. Rev.* **2015**, *44*, 1299-1301.
10. Zhou, J.; Liu, Z.; Li. F. Y. Upconversion Nanophosphors for Small-Animal Imaging. *Chem. Soc. Rev.* **2012**, *41*, 1323-1349.
11. Choi, B.; Iwanaga, M.; Sugimoto, Y.; Sakoda, K.; Miyazaki, H. T. Selective Plasmonic Enhancement of Electric- and Magnetic-Dipole Radiations of Er Ions. *Nano Lett.* **2016**, *16*, 5191-5196.
12. Han. S. Y.; Deng, R. R.; Xie, X. J.; Liu, X. G. Enhancing Luminescence in Lanthanide-Doped Upconversion Nanoparticles. *Angew. Chem. Int. Ed.* **2014**, *53*, 11702-11715.
13. Zhao, J. B.; Jin, D. Y.; Schartner, E. P.; Lu, Y. Q.; Liu, Y. J.; Zvyagin, A. V.; Zhang, L. X.; Dawes, J. M.; Xi, P.; Piper, J. A.; Goldys, E. M.; Monroe, T. M. Single-Nanocrystal Sensitivity Achieved by Enhanced Upconversion Luminescence. *Nat. Nanotechnol.* **2013**, *8*, 729-734.
14. Gargas, D. J.; Chan, E. M.; Ostrowski, A. D.; Aloni, S.; Altoe, M. V. P.; Barnard, E. S.; Sani, B.; Urban, J. J.; Milliron, D. J.; Cohen, B. E.; Schuck, P. J. Engineering Bright Sub-10-nm Upconverting Nanocrystals for Single-Molecule Imaging. *Nat. Nanotechnol.* **2014**, *9*, 300-305.

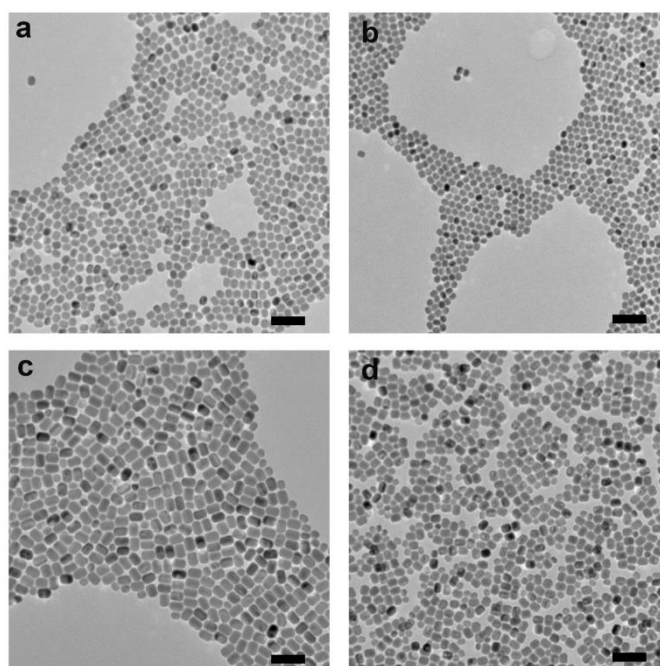
15. Liu, Q.; Zhang, Y. X.; Peng, C. S.; Yang, T.; Joubert, L.-M.; Chu, S. Single Upconversion Nanoparticle Imaging at Sub-10 W cm<sup>-2</sup> Irradiance. *Nat. Photonics* **2018**, *12*, 548-553.
16. Tian, B. N.; Fernandez-Bravo, A.; Najafiaghdam, H.; Torquato, N. A.; Altoe, M. V. P.; Teitelboim, A.; Tajon, C. A.; Tian, Y.; Borys, N. J.; Barnard, E. S.; Anwar, M.; Chan, E. M.; Schuck, P. J.; Cohen, B. E. Low Irradiance Multiphoton Imaging with Alloyed Lanthanide Nanocrystals. *Nat. Commun.* **2018**, *9*, 3082.
17. Haase, M.; Schäfer, H. Upconverting Nanoparticles. *Angew. Chem. Int. Ed.* **2011**, *50*, 5808-5829.
18. Boyer, J.-C.; van Veggel, F. C. J. M. Absolute Quantum Yield Measurements of Colloidal NaYF<sub>4</sub>:Er<sup>3+</sup>, Yb<sup>3+</sup> Upconverting Nanoparticles. *Nanoscale* **2010**, *2*, 1417-1419.
19. Zhang, F.; Che, R. C.; Li, X. M.; Yao, C.; Yang, J. P.; Shen, D. K.; Hu, P.; Li, W.; Zhao, D. Y. Direct Imaging the Upconversion Nanocrystal Core/Shell Structure at the Subnanometer Level: Shell Thickness Dependence in Upconverting Optical Properties. *Nano Lett.* **2012**, *12*, 2852-2858.
20. Li, D. H.; Liu, X. F.; Qiu, J. R. Probing Interaction Distance of Surface Quenchers in Lanthanide-Doped Upconversion Core-Shell Nanoparticles. *J. Phys. Chem. C* **2018**, *122*, 10278-10283.
21. Yi, G.-S.; Chow, G.-M. Water-Soluble NaYF<sub>4</sub>:Yb,Er(Tm)/NaYF<sub>4</sub>/Polymer Core/Shell/Shell Nanoparticles with Significant Enhancement of Upconversion Fluorescence. *Chem. Mater.* **2007**, *19*, 341-343.
22. Fischer, S.; Bronstein, N. D.; Swabeck, J. K.; Chan, E. M.; Alivisatos, A. P. Precise Tuning of Surface Quenching for Luminescence Enhancement in Core-Shell Lanthanide-Doped Nanocrystals. *Nano Lett.* **2016**, *16*, 7241-7247.
23. Rabouw, F. T.; Prins, P. T.; Villanueva-Delgado, P.; Castelijns, M.; Geitenbeek, R. G.; Meijerink, A. Quenching Pathways in NaYF<sub>4</sub>:Er<sup>3+</sup>,Yb<sup>3+</sup> Upconversion Nanocrystals. *ACS Nano* **2018**, *12*, 4812-4823.
24. Vetrone, F.; Boyer, J.-C.; Capobianco, J. A.; Speghini, A.; Bettinelli, M. Concentration-Dependent Near-Infrared to Visible Upconversion in Nanocrystalline and Bulk Y<sub>2</sub>O<sub>3</sub>:Er<sup>3+</sup>. *Chem. Mater.* **2003**, *15*, 2737-2743.
25. Martín-Rodríguez, R.; Rabouw, F. T.; Trevisani, M.; Bettinelli, M.; Meijerink, A. Upconversion Dynamics in Er<sup>3+</sup>-Doped Gd<sub>2</sub>O<sub>2</sub>S: Influence of Excitation Power, Er<sup>3+</sup> Concentration, and Defects. *Adv. Opt. Mater.* **2015**, *3*, 558-567.
26. Vetrone, F.; Boyer, J.-C.; Capobianco, J. A.; Speghini, A.; Bettinelli, M. Significance of Yb<sup>3+</sup> Concentration on the Upconversion Mechanisms in Codoped Y<sub>2</sub>O<sub>3</sub>:Er<sup>3+</sup>, Yb<sup>3+</sup> Nanocrystals. *J. Appl. Phys.* **2004**, *96*, 661-667.

27. Chan, E. M.; Levy, E. S.; Cohen, B. E. Rationally Designed Energy Transfer in Upconverting Nanoparticles. *Adv. Mater.* **2015**, *27*, 5753-5761.
28. Su, Q. Q.; Han, S. Y.; Xie, X. J.; Zhu, H. M.; Chen, H. Y.; Chen, C. K.; Liu, R. S.; Chen, X. Y.; Wang, F.; Liu, X. G. The Effect of Surface Coating on Energy Migration-Mediated Upconversion. *J. Am. Chem. Soc.* **2012**, *134*, 20849-20857.
29. Shalav, A.; Richards, B. S.; Trupke, T.; Krämer, K. W.; Güdel, H. U. Application of NaYF<sub>4</sub>:Er<sup>3+</sup> Up-Converting Phosphors for Enhanced Near-Infrared Silicon Solar Cell Response. *Appl. Phys. Lett.* **2005**, *86*, 013505.
30. Yan, R. X.; Li, Y. D. Down/Up Conversion in Ln<sup>3+</sup>-Doped YF<sub>3</sub> Nanocrystals. *Adv. Funct. Mater.* **2005**, *15*, 763-770.
31. Krämer, K. W. Resonance in Er<sup>3+</sup> Upconversion Excitation. *J. Lumin.* **2017**, *189*, 78-83.
32. Auzel, F. Upconversion and Anti-Stokes Processes with f and d Ions in Solids, *Chem. Rev.* **2004**, *104*, 139-173.
33. Johnson, N. J. J.; He, S.; Diao, S.; Chan, E. M.; Dai, H. J.; Almutairi, A. Direct Evidence for Coupled Surface and Concentration Quenching Dynamics in Lanthanide-Doped Nanocrystals. *J. Am. Chem. Soc.* **2017**, *139*, 3275-3282.
34. Schietinger, S.; Menezes, L. de S.; Lauritzen, B.; Benson, O. Observation of Size Dependence in Multicolor Upconversion in Single Yb<sup>3+</sup>, Er<sup>3+</sup> Codoped NaYF<sub>4</sub> Nanocrystals. *Nano Lett.* **2009**, *9*, 2477-2481.
35. Capobianco, J. A.; Vetrone, F.; D'Alesio, T.; Tessari, G.; Speghini, A.; Bettinelli, M. Optical Spectroscopy of Nanocrystalline Cubic Y<sub>2</sub>O<sub>3</sub>:Er<sup>3+</sup> Obtained by Combustion Synthesis. *Phys. Chem. Chem. Phys.* **2000**, *2*, 3203-3207.
36. Hebbink, G. A.; Stouwdam, J. W.; Reinhoudt, D. N.; van Veggel, F. C. J. M. Lanthanide(III)-Doped Nanoparticles That Emit in the Near-Infrared. *Adv. Mater.* **2002**, *14*, 1147-1150.
37. Hossan, M. Y.; Hor, A.; Luu, Q.; Smith, S. J.; May, P. S.; Berry, M. T. J. Explaining the Nanoscale Effect in the Upconversion Dynamics of β-NaYF<sub>4</sub>:Yb<sup>3+</sup>, Er<sup>3+</sup> Core and Core-Shell Nanocrystals. *J. Phys. Chem. C* **2017**, *121*, 16592-16606.
38. Wang, F.; Wang, J.; Liu, X. G. Direct Evidence of a Surface Quenching Effect on Size-Dependent Luminescence of Upconversion Nanoparticles. *Angew. Chem. Int. Ed.* **2010**, *49*, 7456-7460.
39. Toptygin, D. Effects of the Solvent Refractive Index and Its Dispersion on the Radiative Decay Rate and Extinction Coefficient of a Fluorescent Solute. *J. Fluoresc.* **2003**, *13*, 201-219.
40. Rabouw, F. T.; den Hartog, S. A.; Senden, T.; Meijerink, A. Photonic Effects on the Förster Resonance Energy Transfer Efficiency. *Nat. Commun.* **2014**, *5*, 3610.
41. Senden, T.; Rabouw, F. T.; Meijerink, A. Photonic Effects on the Radiative Decay Rate and Luminescence Quantum Yield of Doped Nanocrystals. *ACS Nano* **2015**, *9*, 1801-1808.

42. Wang, Z. J.; Senden, T.; Meijerink, A. Photonic Effects for Magnetic Dipole Transitions. *J. Phys. Chem. Lett.* **2017**, *8*, 5689-5694.
43. Boyer, J. C.; Manseau, M. P.; Murray, J. I.; Van Veggel, F. C. J. M. Surface Modification of Upconverting NaYF<sub>4</sub> Nanoparticles with PEG-Phosphate Ligands for NIR (800 nm) Biolabeling within the Biological Window. *Langmuir* **2010**, *26*, 1157-1164.
44. Homann, C.; Krukewitt, L.; Frenzel, F.; Grauel, B.; Wurth, C.; Resch-Genger U.; Haase, M. NaYF<sub>4</sub>:Yb,Er/NaYF<sub>4</sub> Core/Shell Nanocrystals with High Upconversion Quantum Yield. *Angew. Chem. Int. Ed.* **2018**, *57*, 8765-8769.
45. Ma, C. S.; Xu, X. X.; Wang, F.; Zhou, Z. G.; Liu, D. M.; Zhao, J. B.; Guan, M.; Lang, C. I.; Jin, D. Y. Optimal Sensitizer Concentration in Single Upconversion Nanocrystals. *Nano Lett.* **2017**, *17*, 2858-2864.
46. Chen, G. Y.; Ohulchanskyy, T. Y.; Kumar, R.; Agren, H.; Prasad, P. N. Ultrasmall Monodisperse NaYF<sub>4</sub>:Yb<sup>3+</sup>/Tm<sup>3+</sup> Nanocrystals with Enhanced Near-Infrared to Near-Infrared Upconversion Photoluminescence. *ACS Nano* **2010**, *4*, 3163-3168.
47. Bogdan, N.; Vetrone, F.; Ozin, G. A.; Capobianco, J. A. Synthesis of Ligand-Free Colloidally Stable Water Dispersible Brightly Luminescent Lanthanide-Doped Upconverting Nanoparticles. *Nano Lett.* **2011**, *11*, 835-840.
48. Lappi, S. E.; Smith, B.; Franzen, S. Infrared Spectra of H<sub>2</sub><sup>16</sup>O, H<sub>2</sub><sup>18</sup>O and D<sub>2</sub>O in the Liquid Phase by Single-Pass Attenuated Total Internal Reflection Spectroscopy. *Spectrochim. Acta, Part A* **2004**, *60*, 2611-2619.
49. Arppe, R.; Hyppänen, I.; Perälä, N.; Peltomaa, R.; Kaiser, M.; Würth, C.; Christ, S.; Resch-Genger, U.; Schäferling, M.; Soukka, T. Quenching of the Upconversion Luminescence of NaYF<sub>4</sub>:Yb<sup>3+</sup>,Er<sup>3+</sup> and NaYF<sub>4</sub>:Yb<sup>3+</sup>,Tm<sup>3+</sup> Nanophosphors by Water: The Role of the Sensitizer Yb<sup>3+</sup> in Non-Radiative Relaxation. *Nanoscale* **2015**, *7*, 11746-11757.
50. Moore, E. G.; Seitz M.; Raymond, K. N. Use of Yb<sup>III</sup>-Centered Near-Infrared (NIR) Luminescence to Determine the Hydration State of a 3, 2-HOPO-Based MRI Contrast Agent. *Inorg. Chem.* **2008**, *47*, 8571-8573.
51. Chen, G. Y.; Ohulchanskyy, T. Y.; Liu, S.; Law, W.-C.; Wu, F.; Swihart, M. T.; Ågren, H.; Prasad, P. N. Core/Shell NaGdF<sub>4</sub>:Nd<sup>3+</sup>/NaGdF<sub>4</sub> Nanocrystals with Efficient Near-Infrared to Near-Infrared Downconversion Photoluminescence for Bioimaging Applications. *ACS Nano* **2012**, *6*, 2969-2977.
52. Weber, M. J. Probabilities for Radiative and Nonradiative Decay of Er<sup>3+</sup> in LaF<sub>3</sub>. *Phys. Rev.* **1967**, *157*, 262-272.
53. Villanueva-Delgado, P.; Biner, D.; Kramer, K. W. Judd-Ofelt Analysis of β-NaGdF<sub>4</sub>:Yb<sup>3+</sup>, Tm<sup>3+</sup> and β-NaGdF<sub>4</sub>:Er<sup>3+</sup> Single Crystals. *J. Lumin.* **2017**, *189*, 84-90.

54. Dodson, C. M.; Zia, R. Magnetic Dipole and Electric Quadrupole Transitions in the Trivalent Lanthanide *Phys. Rev Series: Calculated Emission Rates and Oscillator Strength. Phys. Rev. B: Condens. Matter Mater. Phys.* **2012**, *86*, 125102.

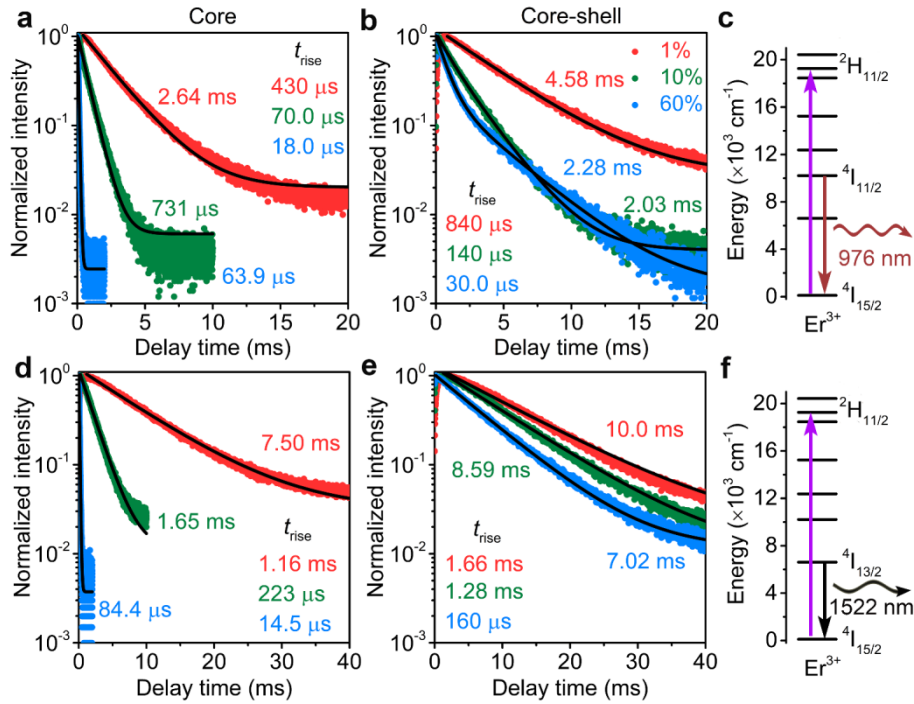
## 3.7 Appendices



**Figure A3.1.** TEM images of core ((a)  $\text{NaYF}_4:10\%\text{Er}^{3+}$ , (b)  $\text{NaYF}_4:60\%\text{Er}^{3+}$ ) and core-shell ((c)  $\text{NaYF}_4:10\%\text{Er}^{3+}@\text{NaYF}_4$ , (d)  $\text{NaYF}_4:60\%\text{Er}^{3+}@\text{NaYF}_4$ ) NCs. (scale bar = 100 nm).

**Table A3.1.** ICP results for  $\text{NaYF}_4:X\%\text{Er}^{3+}$  ( $X = 1, 10, 60$ ) core NCs.

$\text{Er}^{3+}/\%$ (nominal)	$\text{Y}^{3+}/\%$ (measured)	$\text{Er}^{3+}/\%$ (measured)
1	$99.20 \pm 1.09$	$0.80 \pm 0.02$
10	$91.08 \pm 0.55$	$8.92 \pm 0.11$
60	$41.95 \pm 0.50$	$58.05 \pm 0.64$



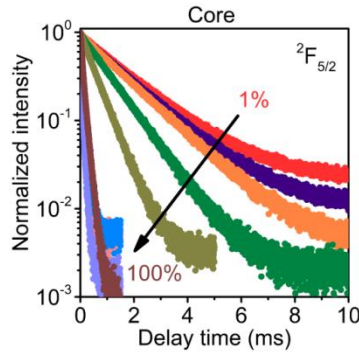
**Figure A3.2.** Luminescence decay curves of  $\text{Er}^{3+} {}^4\text{I}_{11/2}$  ((a) core, (b) core-shell and (c) corresponding energy level diagram) and  ${}^4\text{I}_{13/2}$  ((d) core, (e) core-shell and (f) corresponding energy level diagram) emissions following indirect excitation at 520 nm for  $\text{NaYF}_4:\text{X}\%\text{Er}^{3+}$  core and  $\text{NaYF}_4:\text{X}\%\text{Er}^{3+}@\text{NaYF}_4$  core-shell NCs ( $X = 1, 10, 60$  in red, green and blue color).

### Calculation of intrinsic lifetime for $\text{Er}^{3+}$ states and $\text{Yb}^{3+} {}^2\text{F}_{5/2}$ state

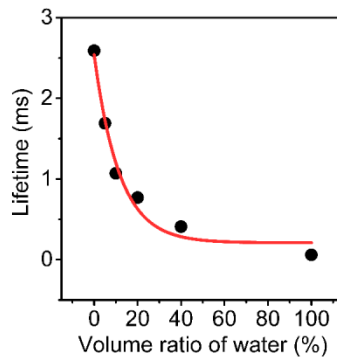
With the intrinsic radiative decay rates for  $\text{Er}^{3+}$  states in bulk material and refractive index  $n$  of medium, we can calculate the intrinsic radiative lifetime for excited states of  $\text{Er}^{3+}$  doped in NCs in any solvent. The experimental lifetime from bulk  $\text{NaYF}_4:0.1\%\text{Er}^{3+}$  is 645  $\mu\text{s}$ , 524  $\mu\text{s}$ , 7.60 ms and 7.99 ms for  ${}^4\text{S}_{3/2}$ ,  ${}^4\text{F}_{9/2}$ ,  ${}^4\text{I}_{11/2}$  and  ${}^4\text{I}_{13/2}$  states.<sup>23</sup> The total decay rate  $k$  is the sum of electric dipole ED transition rates and magnetic dipole MD transition rates ( $k = 1/\tau = k_{\text{ED}} + k_{\text{MD}}$ ,  $k_{\text{ED}} = n k_{\text{ED}(0)}$  and  $k_{\text{MD}} = n^3 k_{\text{MD}(0)}$ , where the subscript of 0 means in vacuum). For NCs, the NC-cavity model  $k_{\text{ED}} = n k_{\text{ED}(0)} (3n^2 / (2n^2 + n_{\text{NC}}^2))^2$  can be used to calculate ED transition probabilities for luminescent ions in NCs dispersed in medium with refractive index  $n$ . In our case,  $n_{\text{NC}} = n(\text{NaYF}_4) = 1.50$  and  $n(\text{cyclohexane}) = 1.43$ . The emissions from  ${}^4\text{S}_{3/2}$ ,  ${}^4\text{F}_{9/2}$  states are pure forced ED transitions, whereas  ${}^4\text{I}_{11/2}$  and  ${}^4\text{I}_{13/2}$  emissions are a combination of forced ED and MD transitions. Taking the decay rate ratio of ED/MD as 9.25 and 1.44 for  ${}^4\text{I}_{11/2}$  and  ${}^4\text{I}_{13/2}$  states in  $\text{LaF}_3$  bulk material<sup>52</sup> and assuming 100% quantum yield of luminescence in  $\text{NaYF}_4:\text{Er}^{3+}$  bulk material, we can determine the intrinsic lifetime  $\tau_0$  for  $\text{Er}^{3+}$  excited states for  $\text{NaYF}_4:\text{Er}^{3+}$  NCs in cyclohexane by the equation below. The results are  $\tau_0({}^4\text{S}_{3/2}) = 723 \mu\text{s}$ ,  $\tau_0({}^4\text{F}_{9/2}) = 587 \mu\text{s}$ ,  $\tau_0({}^4\text{I}_{11/2}) = 8.54 \text{ ms}$  and  $\tau_0({}^4\text{I}_{13/2}) = 9.06 \text{ ms}$ .

For  $\text{Yb}^{3+} \ ^2\text{F}_{5/2}$  state, the measured lifetime is 1.72 ms in bulk  $\text{NaYF}_4:0.01\% \text{Yb}^{3+}$  material<sup>23</sup> with 12% MD and 88% ED contributions.<sup>53,54</sup> The radiative  $^2\text{F}_{5/2}$  lifetime  $\tau_0$  for  $\text{Yb}^{3+}$  doped in  $\text{NaYF}_4$  NCs in cyclohexane is determined to be 1.93 ms.

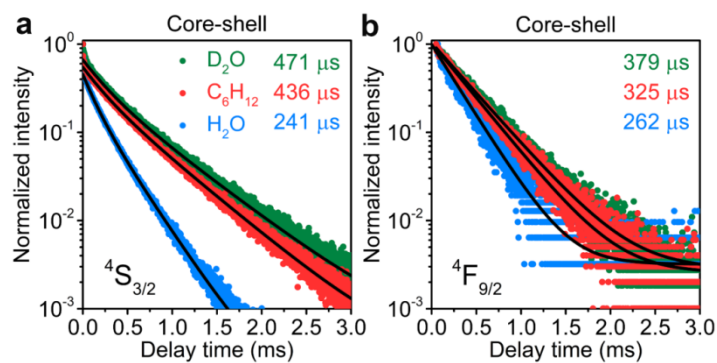
$$\tau_0 = \tau_{\text{bulk}} / \left( \frac{I_{\text{ED}} n \chi_{\text{NC}}^2}{I_{\text{tot}} n_{\text{NC}}} + \frac{I_{\text{MD}} n^3}{I_{\text{tot}} n_{\text{NC}}^3} \right)$$



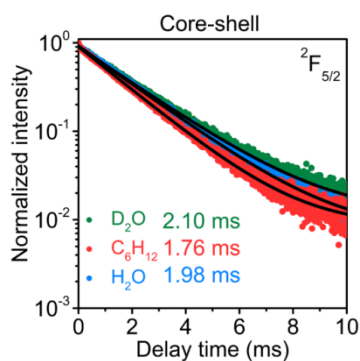
**Figure A3.3.** Luminescence decay curves of  $^2\text{F}_{5/2}$  emission by direct excitation of 960 nm for  $\text{NaYF}_4:\text{X}\% \text{Yb}^{3+}$  core NCs ( $X = 1, 2, 5, 10, 20, 40, 60, 80$  and 100).



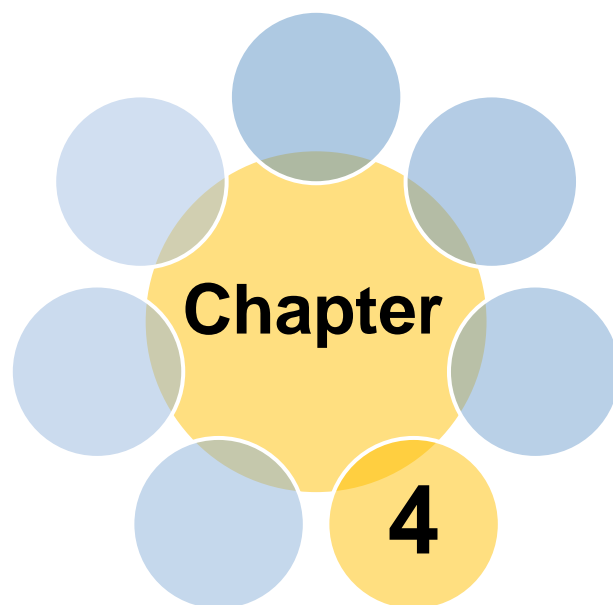
**Figure A3.4.** Lifetime of  $^4\text{I}_{11/2}$  emission by direct excitation of 960 nm for  $\text{NaYF}_4:1\% \text{Er}^{3+} @ \text{NaYF}_4$  core-shell NCs as a function of volume ratio between water and heavy water, keeping the NCs concentration the same.



**Figure A3.5.** Luminescence decay curves of  $\text{Er}^{3+}$  (a)  $^4\text{S}_{3/2}$  and (b)  $^4\text{F}_{9/2}$  emissions by direct excitations of 520 and 640 nm for  $\text{NaYF}_4:1\%\text{Er}^{3+}@\text{NaYF}_4$  core-shell NCs in heavy water, cyclohexane and deionized water.



**Figure A3.6.** Luminescence decay curves of  $\text{Yb}^{3+}$   $^2\text{F}_{5/2}$  emission by direct excitation of 960 nm for  $\text{NaYF}_4:1\%\text{Yb}^{3+}@\text{NaYF}_4$  core-shell NCs in heavy water, cyclohexane and deionized water.



# Dye-sensitized downconversion

Based on

Wang, Z. J.; Meijerink, A. Dye-Sensitized Downconversion. *J. Phys. Chem. Lett.* **2018**, *9*, 1522-1526.

## 4.1 Abstract

Splitting one high-energy photon into two lower-energy photons through downconversion has been demonstrated for a variety of combinations of rare earth (RE) ions. However, the low absorption cross section of  $\text{RE}^{3+}$  4f-4f transitions hampers practical application. Therefore, enhancing the absorption by sensitization is crucial. We demonstrate efficient dye-sensitized downconversion using a strong blue/UV absorbing Coumarin dye to sensitize downconversion of the  $\text{Pr}^{3+}$ - $\text{Yb}^{3+}$  couple in  $\text{NaYF}_4$  nanocrystals (NCs). Photoluminescence spectra and lifetime measurements reveal Förster resonance energy transfer (FRET) from Coumarin on NC surface to  $\text{Pr}^{3+}$  in  $\text{NaYF}_4:\text{Pr}^{3+}\text{Yb}^{3+}$  NCs, followed by downconversion, resulting in  $\text{Yb}^{3+}$  IR emission with ~30 times enhancement. The present study demonstrates the feasibility of dye-sensitized downconversion as a promising strategy to engineer strongly absorbing downconversion NCs to enhance the efficiency of photovoltaic cells.

## 4.2 Introduction

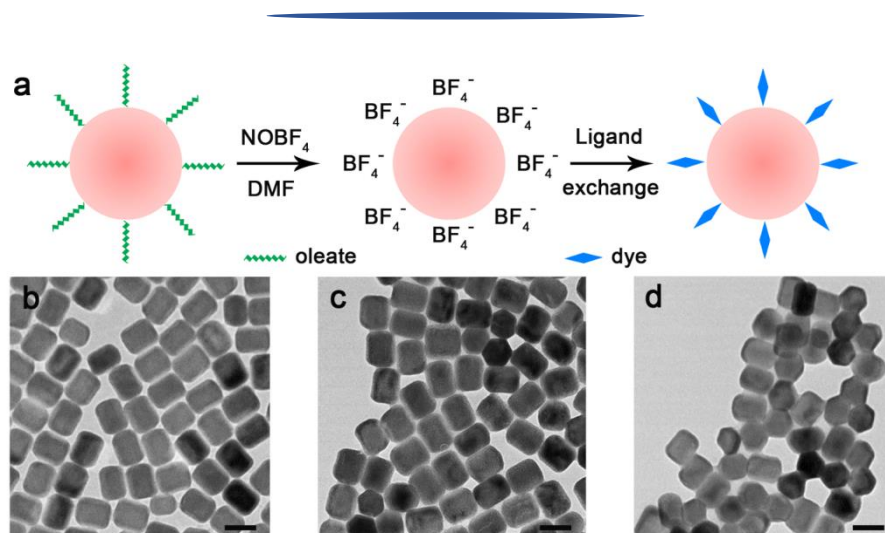
Downconversion, also known as quantum cutting, is a process in which one high-energy photon is split into two low-energy photons (theoretical quantum efficiency of 200%). This luminescence phenomenon has been reported for quantum dots (multiple exciton generation),<sup>1,2</sup> dye molecules (singlet fission),<sup>3</sup> and couples of rare earth (RE) ions (downconversion).<sup>4</sup> Recently, many examples of downconversion through energy transfer (ET) have been reported for a variety of combinations of  $\text{RE}^{3+}$  ions.<sup>4,5</sup> The search for downconversion materials was initially driven by the need for more efficient phosphors in lighting and displays, and more recently, by the potential application in photovoltaics.<sup>6-8</sup> Converting one high-energy (UV and blue) photon into two IR photons above the crystalline-Si band gap gives rise to current (and thus efficiency) doubling for the high-energy part of the solar spectrum.<sup>9</sup> Even though downconversion has been explored and demonstrated for a variety of materials, downconversion materials are still far from practical application. The most efficient downconversion is realized in  $\text{RE}^{3+}$ -doped materials. Unfortunately, absorption of the solar spectrum is inefficient due to the intrinsic low absorption cross section (in the order of  $10^{-21}$   $\text{cm}^2$ ) of  $\text{RE}^{3+}$  ions (intraconfigurational parity forbidden 4f-4f transitions) and the discrete sharp absorption lines covering only a small part of the solar spectrum. As a result, only a fraction of the solar spectrum can be harvested by conventional downconversion materials.

To improve the absorption and the response to the solar spectrum, there is a worldwide search for broadband sensitizers with high absorption cross sections. So far, especially  $\text{Ce}^{3+}$  and  $\text{Eu}^{2+}$  have been explored as sensitizers but with limited success.<sup>10,11</sup> For the efficient  $\text{Pr}^{3+}$ - $\text{Yb}^{3+}$  downconversion couple, incorporation of  $\text{Ce}^{3+}$  and  $\text{Eu}^{2+}$  as sensitizers unfortunately leads to quenching of the excited  $4f^{n-1}5d$  state of the sensitizers via metal-to-metal charge transfer states involving nearby  $\text{Yb}^{3+}$  or  $\text{Pr}^{3+}$

ions.<sup>12,13</sup> An alternative option is to use organic dye that was first demonstrated to sensitize IR emission in RE-doped NCs.<sup>14</sup> The use of NCs is crucial. Efficient ET from dyes (donor, D) to RE ions (acceptor, A) requires a small D-A distance  $R$  as the probability for Förster resonance energy transfer (FRET) scales with  $R^{-6}$ . A close proximity can be realized by adsorbing dye molecules at the surface of RE-doped NCs where a significant fraction of RE ions is close to the surface. Later, the same principle was successfully applied in using dye-sensitization to enhance the efficiency for upconversion luminescence in NCs.<sup>15</sup> This pioneering work triggered research to further increase the upconversion efficiency.<sup>16-20</sup> Surprisingly, the concept of dye-sensitized downconversion has so far not been reported. In the present study, we investigate dye-sensitized downconversion for a combination of a blue/UV absorbing Coumarin dye and  $\text{Pr}^{3+}, \text{Yb}^{3+}$ -co-doped  $\text{NaYF}_4$  NCs. Adsorption of the Coumarin dye on  $\text{NaYF}_4:\text{Pr}, \text{Yb}$  NCs results in a significant (30-fold) enhancement of  $\text{Yb}^{3+}$  IR emission. This strategy of dye-sensitization can be exploited to enhance the downconversion efficiency for a wide range of lanthanide-doped materials and improve the efficiency of solar cells.

### 4.3 Results and Discussion

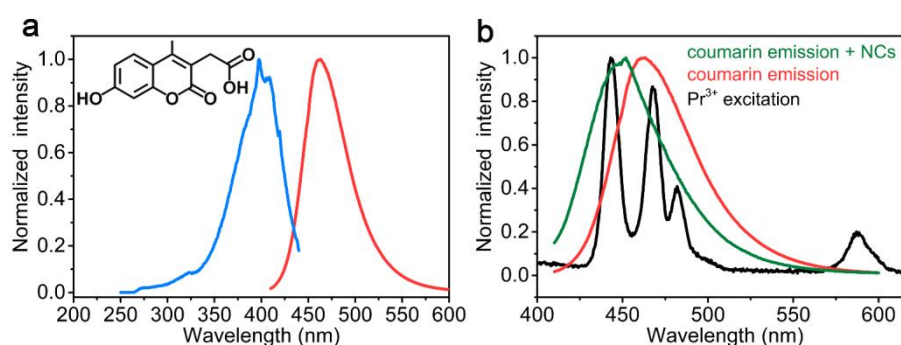
The  $\beta\text{-NaYF}_4:1\%\text{Pr}^{3+}20\%\text{Yb}^{3+}$  NCs were synthesized using well-established colloidal synthesis techniques.<sup>21</sup> (see **Methods**) Originally, the ligand on NC surface is oleate (hydrophobic surface). A two-step ligand exchange is employed to realize the dye-sensitization, as illustrated in **Fig. 4.1a**. First, the oleate ligands are exchanged with ionic nitronium tetrafluoroborate ( $\text{NOBF}_4$ ),<sup>22</sup> stabilizing the NCs (hydrophilic surface) in polar solvents, such as  $N,N$ -dimethylformamide (DMF) used in the present study. Next, the Coumarin dye dissolved in DMF is added, allowing the dye-sensitization.



**Figure 4.1.** Two-step ligand exchange to realize dye-sensitized NCs. (a) Schematic diagram of ligand exchange for the dye-sensitized NCs. TEM images of  $\text{NaYF}_4:1\%\text{Pr}^{3+}20\%\text{Yb}^{3+}$  NCs (b),  $\text{NOBF}_4$  modified NCs (c), and dye-sensitized NCs (d). Scale bar = 50 nm.

Transmission electron microscopy (TEM) images in **Figs. 4.1b-d** show the monodisperse NCs of  $\sim 22 \times 55$  nm, in both top and side views. The size is important to calculate the number of dye molecule per NC (*vide infra*).

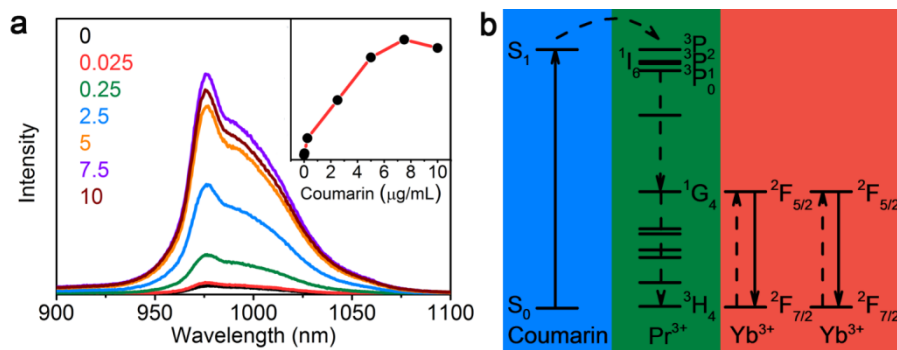
The commercially available 7-hydroxy-4-methyl-3-coumarinylacetic acid is chosen as dye molecule. Coumarin molecules can bind to the NC surface via electrostatic attraction of carboxylic groups and surface  $\text{RE}^{3+}$  ions (see molecular structure as inset in **Fig. 4.2a**). **Fig. 4.2a** shows the emission (red) and excitation (blue) spectra for Coumarin in DMF. The emission band has a maximum at 462 nm. A blue shift is observed for the Coumarin emission after the addition of NCs (compare the green and red lines in **Fig. 4.2b**), implying the binding of Coumarin on NC surface. A similar blue shift of dye emission after dye binding to  $\text{NaYF}_4$  NCs was also reported in **Ref. 15**. The excitation spectrum of Coumarin spans a broad spectral region (320-450 nm) with a maximum around 400 nm. **Fig. 4.2b** shows the excitation spectrum of  $\text{Yb}^{3+}$  emission for  $\text{NaYF}_4:1\% \text{Pr}^{3+}20\% \text{Yb}^{3+}$  NCs (black). Excitation lines are observed at around 443, 467, 482, and 587 nm, attributed to transitions of  $\text{Pr}^{3+}$  from the  $^3\text{H}_4$  ground state to the  $^3\text{P}_2$ ,  $^3\text{P}_1$ ,  $^1\text{I}_6$ ,  $^3\text{P}_0$ , and  $^1\text{D}_2$  excited states.<sup>8</sup> There is a good spectral overlap between the Coumarin emission and the  $^1\text{I}_6$  and  $^3\text{P}_J$  absorption lines of  $\text{Pr}^{3+}$ , which indicates that efficient ET from Coumarin to  $\text{Pr}^{3+}$  is possible.<sup>23</sup> The hybrid NCs consisting of organic Coumarin molecules adsorbed at the inorganic nanomaterial surface can efficiently absorb and downconvert the blue and UV spectral region in the solar spectrum.<sup>24</sup> The strong spectral overlap of Coumarin emission and  $\text{Pr}^{3+}$  absorption and the large absorption spectral width with high molar extinction coefficient ( $19000 \text{ M}^{-1} \text{ cm}^{-1}$  in the absorption maximum)<sup>25</sup> make Coumarin a highly promising dye to sensitize downconversion.



**Figure 4.2.** Coumarin spectra and spectral overlap for FRET. (a) Excitation (blue,  $\lambda_{\text{em}} = 462$  nm) and emission (red,  $\lambda_{\text{ex}} = 397$  nm) spectra of Coumarin (5  $\mu\text{g}/\text{mL}$ ) in DMF. The inset shows the molecular structure of Coumarin. (b) Excitation (black,  $\lambda_{\text{em}} = 980$  nm) spectrum of  $\text{NaYF}_4:1\% \text{Pr}^{3+}20\% \text{Yb}^{3+}$  NCs and emission ( $\lambda_{\text{ex}} = 397$  nm) spectra of Coumarin (red: the same red line as in panel (a)); green: 0.5 mg/mL  $\text{NaYF}_4:1\% \text{Pr}^{3+}20\% \text{Yb}^{3+}$  NCs with 0.025  $\mu\text{g}/\text{mL}$  Coumarin in DMF).

To investigate the occurrence and efficiency of dye-sensitized downconversion in the Coumarin@NaYF<sub>4</sub>:Pr,Yb NC system, Yb<sup>3+</sup> emission spectra were measured for dispersions of NaYF<sub>4</sub>:1%Pr<sup>3+</sup>20%Yb<sup>3+</sup> NCs with different concentrations of Coumarin. In **Fig. 4.3a**, emission spectra are shown in the IR spectral region between 900 and 1100 nm for excitation at 397 nm, in the maximum of Coumarin absorption band. For comparison, the emission spectrum for NCs without Coumarin is shown (under excitation in the strongest 4f-4f excitation line at 443 nm). All spectra were measured under identical conditions such that absolute emission intensities can be compared. The IR emission intensity strongly increases with increasing Coumarin concentration until the optimal concentration of 7.5 μg/mL. This enhancement of IR emission is due to the increased absorption of 397 nm excitation light as Coumarin concentration increases. A further increase in the concentration induces self-quenching of Coumarin, leading to an overall drop of the emission intensity. The inset in **Fig. 4.3a** depicts the trend of integrated emission intensity versus Coumarin concentration. Quantitative analysis reveals a 30-fold enhancement for Yb<sup>3+</sup> emission in comparison with 4f-4f excitation in the <sup>3</sup>P<sub>2</sub> level of Pr<sup>3+</sup>. The results provide clear evidence that the strategy of the dye-sensitized downconversion works. It is interesting to estimate the number of dye molecule and intermolecular distance. For the optimum 7.5 μg/mL Coumarin concentration (see the **Methods**), the molecule number is estimated to be 1080 per NC with an intermolecular distance of ~3.0 nm. This distance is similar to those found for the optimum dye concentrations of dye-sensitized upconversion in the literature (~3.4 nm in **Ref. 15** and ~3 nm in **Ref. 19**).

The dye-sensitized downconversion involves two ET steps, as shown in **Fig. 4.3b**. After absorbing UV radiation, the excited Coumarin molecules non-radiatively transfer the energy to the <sup>3</sup>P<sub>J</sub> and <sup>1</sup>I<sub>6</sub>



**Figure 4.3.** The enhancement of downconversion emission by Coumarin sensitization. (a) Emission spectra of 0.5 mg/mL NaYF<sub>4</sub>:1%Pr<sup>3+</sup>20%Yb<sup>3+</sup> NCs without Coumarin ( $\lambda_{\text{ex}} = 443$  nm) and with different Coumarin concentrations (0.025 to 10 μg/mL,  $\lambda_{\text{ex}} = 397$  nm). The inset shows the integrated intensity of Yb<sup>3+</sup> emission as a function of Coumarin concentration. (b) Energy level diagram of Coumarin-sensitized downconversion in Pr<sup>3+</sup>,Yb<sup>3+</sup>-co-doped NCs.

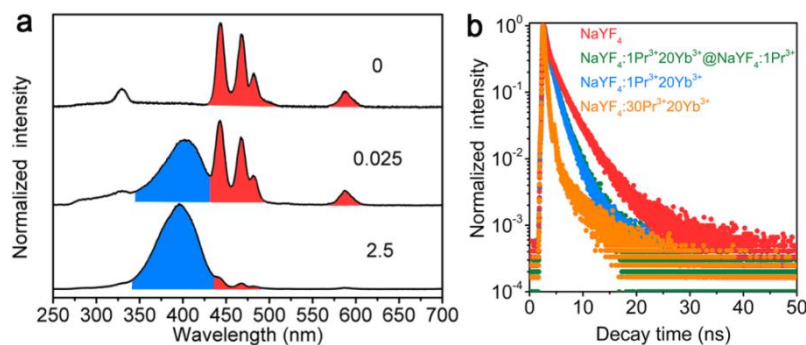
states of nearby  $\text{Pr}^{3+}$  ions. Because the separation between Coumarin at the surface and  $\text{Pr}^{3+}$  ions in the NC surface layer is relatively large, the dipole-dipole FRET dominates the dye-sensitization.<sup>15,26,27</sup> Dexter ET via exchange interaction is not expected over the NC interface because this type of ET relies on wave function overlap and only occurs over distances up to  $0.5 \text{ \AA}$ .<sup>28</sup> After Coumarin to  $\text{Pr}^{3+}$  ET, fast relaxation to the  $^3\text{P}_0$  state of  $\text{Pr}^{3+}$  is followed by the second ET process that involves a resonant two-step ET to two neighbouring  $\text{Yb}^{3+}$  ions through  $\text{Pr}^{3+}$  ( $^3\text{P}_0$ - $^1\text{G}_4$ )  $\rightarrow$   $\text{Yb}^{3+}$  ( $^2\text{F}_{7/2}$ - $^2\text{F}_{5/2}$ ) and  $\text{Pr}^{3+}$  ( $^1\text{G}_4$ - $^3\text{H}_4$ )  $\rightarrow$   $\text{Yb}^{3+}$  ( $^2\text{F}_{7/2}$ - $^2\text{F}_{5/2}$ ).<sup>6,8,29,30</sup> The excited  $\text{Yb}^{3+}$  ions emit IR radiation with a theoretical quantum efficiency of 200%. On the basis of previous work, the efficiency of this downconversion process is high, as determined from a comparison of absorption and excitation spectra.<sup>8</sup> More recently, direct evidence of downconversion has been obtained through correlated photon counting experiments.<sup>31</sup>

To provide further evidence of dye-sensitized downconversion, we measured the excitation spectra (**Fig. 4.4a**) of the 980 nm  $\text{Yb}^{3+}$  emission for  $\text{NaYF}_4:\text{Pr},\text{Yb}$  NC dispersions with different concentrations of Coumarin. In the absence of Coumarin, the excitation spectrum only shows excitation lines from  $\text{Pr}^{3+}$  f-f  $^3\text{H}_4 \rightarrow ^3\text{P}_{0,1,2}, ^1\text{I}_6, ^1\text{D}_2$  transitions (red area in **Fig. 4.4a**). After the addition of Coumarin, the dye-sensitization occurs and the broad Coumarin excitation band between 320 and 450 nm (blue area) appears. Already for the lowest Coumarin concentration ( $0.025 \mu\text{g/mL}$ ), the relative intensities for Coumarin excitation band and  $\text{Pr}^{3+}$  excitation lines are similar. The relative intensity of Coumarin excitation band rapidly increases with Coumarin concentration and dominates the excitation spectrum for a concentration of  $2.5 \mu\text{g/mL}$ , confirming the high efficiency gain for dye-sensitized downconversion. The stability of the NC-dye complex was evaluated by measuring IR emission spectra under continuous UV-A excitation. In the first hour, a  $\sim 40\%$  intensity decrease is observed, possibly because of photoinduced desorption of dye molecules (**Fig. A4.2**). For longer times, the signal stabilizes.

Insight into the mechanism and efficiency of the Coumarin-to- $\text{Pr}^{3+}$  ET can be gained from luminescence decay curves of Coumarin emission. These were measured for Coumarin coupled to four different types of  $\text{NaYF}_4$  NCs (**Fig. 4.4b**, all for the Coumarin concentration of  $7.5 \mu\text{g/mL}$ ). The decay is non-exponential and is characterized by average lifetime  $\tau_{\text{avg}} = \sum_0^t tI(t) / \sum_0^t I(t)$ , where  $I(t)$  is the emission intensity at time  $t$ .<sup>32</sup> As a reference, the luminescence decay for Coumarin bound to undoped  $\text{NaYF}_4$  NCs was measured (red) with a  $\tau_{\text{avg}}$  of 4.73 ns. The Coumarin emission in the presence of  $\text{NaYF}_4:1\%\text{Pr}^{3+}20\%\text{Yb}^{3+}$  NCs (blue) shows a faster decay with a  $\tau_{\text{avg}}$  of 3.78 ns, indicating that FRET from Coumarin to  $\text{Pr}^{3+}$  occurs and reduces the lifetime by introducing an extra decay channel through FRET. Note that in the case of radiative ET, no shortening of luminescence lifetime is expected and the observation of a shorter Coumarin emission lifetime for  $\text{Pr}^{3+}$ -doped NCs is a direct evidence of non-radiative ET. In addition, luminescence decay curves were investigated for  $\text{NaYF}_4:1\%\text{Pr}^{3+}20\%\text{Yb}^{3+}@\text{NaYF}_4:1\%\text{Pr}^{3+}$  core-shell NCs (green) to study the influence of an

Yb-free shell on the  $\text{Yb}^{3+}$  emission efficiency. Coumarin decay curve was also measured to confirm that the faster decay in the Pr,Yb co-doped NCs is caused by ET to  $\text{Pr}^{3+}$  and not  $\text{Yb}^{3+}$ . The Yb-free shell around the core NCs results in a longer  $\tau_{\text{avg}}$  for  $\text{Yb}^{3+}$  emission (44.2  $\mu\text{s}$  for core-shell vs. 21.7  $\mu\text{s}$  for core, **Fig. A4.1**) and stronger  $\text{Yb}^{3+}$  emission. The beneficial influence of Yb-free shell can be explained by a reduction in surface quenching of the  $\text{Yb}^{3+}$  emission by surface-related defects and multiphonon relaxation by high-energy vibrations of surface-bound ligand and solvent. The Coumarin emission decay time does not change for core-shell NCs ( $\tau_{\text{avg}} = 3.83$  ns, very similar to 3.78 ns measured for Coumarin-sensitized core NCs with the same 1%  $\text{Pr}^{3+}$  doping concentration in the shell). This confirms that the shortening of decay time is caused by Coumarin to  $\text{Pr}^{3+}$  FRET. The surface passivation can be a strategy to obtain enhanced downconversion emission. For the low (1%)  $\text{Pr}^{3+}$  concentration in the shell or core, the FRET probability is relatively low. More efficient FRET is expected for higher  $\text{Pr}^{3+}$  concentrations. In **Fig. 4.4b**, the decay curve of Coumarin emission in the presence of  $\text{NaYF}_4:30\%\text{Pr}^{3+}20\%\text{Yb}^{3+}$  NCs (orange) is shown. As a consequence of a higher  $\text{Pr}^{3+}$  concentration, a faster decay of 3.18 ns is observed, reflecting a higher FRET efficiency. Despite the higher FRET probability, the intensity of the downconversion luminescence does not increase because cross-relaxation quenching of  $^3\text{P}_0$  state of  $\text{Pr}^{3+}$  is very efficient at elevated  $\text{Pr}^{3+}$  concentrations.<sup>33,34</sup>

The present experiments have demonstrated the feasibility of dye-sensitized downconversion. Further research will be aimed at enhancing the FRET and downconversion efficiency by optimization of  $\text{RE}^{3+}$  concentrations and synthesis conditions, and through more complex core-shell architectures. Optimization of the downconversion efficiency can be realized by varying the  $\text{Pr}^{3+}$  and  $\text{Yb}^{3+}$  concentrations, and by reducing multiphonon quenching of the  $\text{Yb}^{3+}$  emission by nearby high-energy C-H and O-H vibrations (e.g. by using C-H and O-H free solvents). The results can be verified by IR quantum yield measurements. For practical applications, the photostability of the dye is also important. Inorganic NCs have a high photostability, but dye molecules suffer from photodegradation. Coumarin dyes are known for their relatively high stability. The stability depends on the solvent and can be enhanced by structural modifications of the Coumarin.<sup>35</sup> Efficiency enhancement in more complex architectures may involve an intermediate sensitizer as  $\text{Tb}^{3+}$ , which can be introduced in high concentration in a  $\text{NaYF}_4:\text{Tb}^{3+}$  shell surrounding the  $\text{NaYF}_4:\text{Pr}^{3+}\text{Yb}^{3+}$  core. The  $^5\text{D}_4$  level of  $\text{Tb}^{3+}$  is situated just above the  $^3\text{P}_0$  level of  $\text{Pr}^{3+}$ . As the  $^5\text{D}_4$  emission from  $\text{Tb}^{3+}$  does not suffer from cross-relaxation quenching, a high  $\text{Tb}^{3+}$  concentration can be incorporated in the outer shell, allowing efficient dye- $\text{Tb}^{3+}$  FRET, followed by  $\text{Tb}^{3+}$ - $\text{Pr}^{3+}$  ET and  $\text{Pr}^{3+}$ - $\text{Yb}^{3+}$  downconversion. In addition, alternative dyes may be used besides Coumarin and show more efficient absorption, higher stability, or enhanced ET to  $\text{RE}^{3+}$  acceptors in the downconversion NCs.



**Figure 4.4.** Evidences of dye-sensitization from Coumarin to  $\text{Pr}^{3+}$  ion. (a) Excitation spectra monitoring 980 nm  $\text{Yb}^{3+}$  emission for 0.5 mg/mL  $\text{NaYF}_4:1\%\text{Pr}^{3+}20\%\text{Yb}^{3+}$  NCs with 0, 0.025, and 2.5  $\mu\text{g}/\text{mL}$  Coumarin in DMF. (b) Luminescence decay curves of Coumarin emission (excited by a 405 nm ps pulsed diode laser) for a 7.5  $\mu\text{g}/\text{mL}$  Coumarin solution in the presence of  $\text{NaYF}_4$  NCs (red),  $\text{NaYF}_4:1\%\text{Pr}^{3+}20\%\text{Yb}^{3+}@NaYF_4:1\%\text{Pr}^{3+}$  core-shell NCs (green),  $\text{NaYF}_4:1\%\text{Pr}^{3+}20\%\text{Yb}^{3+}$  NCs (blue), and  $\text{NaYF}_4:30\%\text{Pr}^{3+}20\%\text{Yb}^{3+}$  NCs (orange).

#### 4.4 Conclusions

In summary, dye-sensitized downconversion has been realized by a combination of organic Coumarin dye molecules and inorganic  $\text{NaYF}_4:\text{Pr}^{3+}\text{Yb}^{3+}$  NCs. The favorable spectral overlap between Coumarin emission and  $\text{Pr}^{3+}$  absorption gives rise to efficient Coumarin- $\text{Pr}^{3+}$  FRET, which sensitizes the  $\text{Pr}^{3+}$ - $\text{Yb}^{3+}$  downconversion couple. Because of the high absorption cross-section of Coumarin, the dye-sensitization enhances the downconversion emission intensity by more than an order of magnitude and extends the spectral range that can be utilized for spectral conversion from several sharp lines between 450 and 500 nm to a wide spectral range spanning the blue and near-UV region. Further optimization of synthesis conditions and dopant concentrations and using core-shell architectures with directional ET can further improve the FRET and downconversion efficiency. The presently reported dye-sensitized downconversion can be applied to other lanthanide-doped downconversion nanomaterials and serves as a stepping-stone for application of downconversion materials in photovoltaic devices.

#### 4.5 Methods

**Chemicals** The synthesis was conducted using commercially available reagents. Ethanol (Analytical Reagent, A.R.), methanol (A.R.), cyclohexane (A.R.), hexane (A.R.), toluene (A.R.), DMF (99.8%), dichloromethane (99.8%), oleic acid (90%), 1-octadecene (90%),  $\text{NOBF}_4$  (95%), yttrium (III) acetate (99.9%), praseodymium (III) acetate (99.9%), ytterbium (III) acetate (99.9%), sodium hydroxide

(97%), ammonium fluoride (98%) and 7-hydroxy-4-methyl-3-coumarinylacetic acid (98%) were purchased from Sigma and Aldrich and used without further purification.

**Synthesis of core and core-shell NaYF<sub>4</sub> NCs** Stoichiometric amounts of rare earth acetates (totally 1 mmol) were added into a 100 mL three-necked flask, which contained 6 mL oleic acid and 17 mL 1-octadecene. The mixture was stirred vigorously and heated to 390 K for 1.5 h under vacuum and subsequently allowed to cool down to room temperature under a gentle flow of nitrogen gas. This was followed by a rapid injection of a mixture, containing 2.5 mmol NaOH and 4 mmol NH<sub>4</sub>F dissolved in 3 and 7 ml methanol. The reaction was kept at room temperature overnight. Next, the solution was heated to 370 K for 0.5 h under vacuum and to 570 K for 2 h under a protective nitrogen atmosphere. Afterwards, the solution was cooled down and the product was precipitated by adding excess ethanol. The core NCs were washed with ethanol and cyclohexane three times using centrifugation to separate the NCs from the ethanol and cyclohexane. Finally, core NCs were dissolved in cyclohexane. For the synthesis of core-shell NCs, all steps were the same except for the injection of core NCs in cyclohexane into the flask before adding the mixture of NaOH and NH<sub>4</sub>F methanol solutions. Core-shell NCs were also dissolved in cyclohexane.

**NOBF<sub>4</sub> modification of core and core-shell NCs** To realize Coumarin-sensitized NCs, the surface ligand of core and core-shell NCs was first exchanged with inorganic molecule NOBF<sub>4</sub>. NCs in 5 mL cyclohexane (10 mL/mL) were mixed with 5 mL 0.01 M dichloromethane solution of NOBF<sub>4</sub> at room temperature. The mixture became turbid once with gentle shaking. The precipitation was separated by centrifugation and washed by adding hexane and toluene (*v/v* = 1). Subsequently, NOBF<sub>4</sub> modified NCs were weighted and dissolved in DMF for further Coumarin-sensitized experiments.

**Coumarin-sensitized core and core-shell NCs** The same portion of NOBF<sub>4</sub> modified NCs (2 mg) was mixed with a variable volume of Coumarin solution in DMF (0.1 mg/mL). The mixtures were stirred at room temperature for 2 h. The Coumarin-sensitized NCs were washed with hexane and toluene (*v/v* = 1) and dissolved in 4 mL DMF.

**Characterization** The photoluminescence spectra were recorded using an Edinburgh Instruments FLS920 spectrometer with a 450 W xenon lamp as excitation source. In the visible region, a Hamamatsu R928 photomultiplier tube (PMT) was used for photon detection. For the IR region, the detector was an R5509-72 PMT cooled by liquid nitrogen. Luminescence decay curves were measured using the multi-channel scaling (MCS) option integrated in the spectrofluorometer. The pulsed excitation was realized by an optical parametric oscillator (OPO) system (Opotek Opolette HE 355 II) pumped by the third harmonic of a YAG:Nd<sup>3+</sup> laser (pulse width 10 ns and repetition rate 20 Hz) for the Yb<sup>3+</sup> emission. For the lifetime of Coumarin dye in the ns regime, the detector was a

fast Hamamatsu H7422-02 PMT with the pulsed excitation from EPL-405 diode laser emitting at 405 nm (pulse width 59 ps) in a time-correlated single photon counting mode. To visualize the NCs and determine the morphology and size, NCs dropped on amorphous carbon-coated copper grids (200 mesh) were imaged on an FEI Tecnai-10 TEM operating at 100 kV.

**Estimation of the number and the intermolecular distance of dye molecule** The Coumarin density on a single NC is estimated as follows. The mean edge length ( $a$ ) of hexagonal prism shaped NaYF<sub>4</sub>: 1%Pr<sup>3+</sup>20%Yb<sup>3+</sup> NCs is ~22 nm and the mean height ( $h$ ) of hexahedron is ~55 nm. The volume  $V$  of the NCs is determined to be  $6.9 \times 10^4 \text{ nm}^3$  according to  $V = 3\sqrt{3}a^2h/2$ . Based on the density of hexagonal-phase NaYF<sub>4</sub> ( $\rho = 4.2 \text{ g/cm}^3$ ),<sup>36</sup> the average weight  $m_{\text{NC}}$  of a single NC is  $2.9 \times 10^{-16} \text{ g}$  by  $m_{\text{NC}} = \rho V$ . Subsequently, with the Avogadro's constant  $N_A$ ,  $M_{\text{NC}} = m_{\text{NC}} N_A$  is used to calculate the molecular weight  $M_{\text{NC}}$  ( $1.7 \times 10^8 \text{ g/mol}$ ) of a single NC. For every measurement for Coumarin-sensitized downconversion, 2.0 mg NCs were added assuming that the washing process induces no loss of NCs. The number  $N_{\text{NC}}$  of NCs is  $2.0 \times 10^6 \text{ ng}/(1.7 \times 10^8 \text{ g/mol}) = 0.012 \text{ nmol}$ . The lowest mass of Coumarin used in the experiment is 0.10  $\mu\text{g}$ . With the molecular weight of Coumarin of 234 g/mol, the number of Coumarin in total is 0.43 nmol. Finally, the number of Coumarin molecules per NC is estimated to be  $0.43/0.012 = 36$ . For the optimal concentration of 30  $\mu\text{g}$  and higher concentration of 40  $\mu\text{g}$  for Coumarin, the number is 1080 and 1440, respectively. With the surface area ( $A$ ) of a single NC of  $9775 \text{ nm}^2$  ( $A = 3\sqrt{3}a^2 + 6ah$ ), the NC surface coverage is 9.1 and 6.8  $\text{nm}^2$  for each Coumarin molecule in the two cases. Correspondingly, the distance for two neighbouring Coumarin molecules is 3.0 and 2.6 nm.

#### 4.6 References

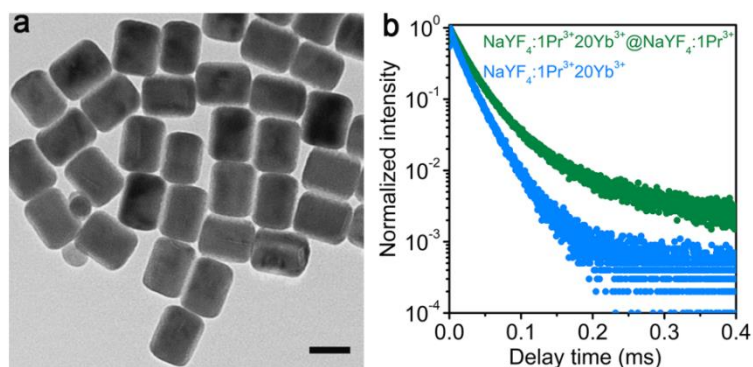
1. Kagan, C. R.; Lifshitz, E.; Sargent, E. H.; Talapin, D. V. Building Devices from Colloidal Quantum Dots. *Science* **2016**, *353*, aac5523.
2. McGuire, J. A.; Sykora, M.; Joo, J.; Pietryga, J. M.; Klimov, V. I. Apparent Versus True Carrier Multiplication Yields in Semiconductor Nanocrystals. *Nano Lett.* **2010**, *10*, 2049-2057.
3. Smith, M. B.; Michl, J. Singlet Fission. *Chem. Rev.* **2010**, *110*, 6891-6936.
4. Huang, X. Y.; Han, S. Y.; Huang, W.; Liu, X. G. Enhancing Solar Cell Efficiency: the Search for Luminescent Materials as Spectral Converters. *Chem. Soc. Rev.* **2013**, *42*, 173-201.
5. Wegh, R. T.; Donker, H.; Oskam, K. D.; Meijerink, A. Visible Quantum Cutting in LiGdF<sub>4</sub>:Eu<sup>3+</sup> through Downconversion. *Science* **1999**, *283*, 663-666.
6. Zhang, Q. Y.; Huang, X. Y. Recent Progress in Quantum Cutting Phosphors. *Prog. Mater. Sci.* **2010**, *55*, 353-427.
7. Timmerman, D.; Izeddin, I.; Stallinga, P.; Yassievich, I. N.; Gregorkiewicz, T. Space-Separated Quantum Cutting with Silicon Nanocrystals for Photovoltaic Applications. *Nat. Photonics* **2008**, *2*, 105-109.

8. van der Ende, B. M.; Aarts, L.; Meijerink, A. Near-Infrared Quantum Cutting for Photovoltaics. *Adv. Mater.* **2009**, *21*, 3073-3077.
9. de la Mora, M. B.; Amelines-Sarria, O.; Monroy, B. M.; Hernández-Pérez, C. D.; Lugo, J. E. Materials for Downconversion in Solar Cells: Perspectives and Challenges. *Sol. Energy Mater. Sol. Cells* **2017**, *165*, 59-71.
10. Sun, T. Y.; Chen, X.; Jin, L. M.; Li, H.-W.; Chen, B.; Fan, B.; Moine, B.; Qiao, X.; Fan, X. P.; Tsang, S.-W.; Yu, S. F.; Wang, F. Broadband Ce(III)-Sensitized Quantum Cutting in Core-Shell Nanoparticles: Mechanistic Investigation and Photovoltaic Application. *J. Phys. Chem. Lett.* **2017**, *8*, 5099-5104.
11. Zhou, J. J.; Zhuang, Y. X.; Ye, S.; Teng, Y.; Lin, G.; Zhu, B.; Xie, J. H.; Qiu, J. R. Broadband Downconversion Based Infrared Quantum Cutting by Cooperative Energy Transfer from  $\text{Eu}^{2+}$  to  $\text{Yb}^{3+}$  in Glasses. *Appl. Phys. Lett.* **2009**, *95*, 141101.
12. Yu, D. C.; Rabouw, F. T.; Boon, W. Q.; Kieboom, T.; Ye, S.; Zhang, Q. Y.; Meijerink, A. Insights Into the Energy Transfer Mechanism in  $\text{Ce}^{3+}$ - $\text{Yb}^{3+}$  Codoped YAG Phosphors. *Phys. Rev. B: Condens. Matter Mater. Phys.* **2014**, *90*, 165126.
13. Ueda, J.; Tanabe, S. Visible to Near Infrared Conversion in  $\text{Ce}^{3+}$ - $\text{Yb}^{3+}$  Co-Doped YAG Ceramics. *J. Appl. Phys.* **2009**, *106*, 043101.
14. Zhang, J.; Shade, C. M.; Chengelis, D. A.; Petoud, S. A Strategy to Protect and Sensitize Near-Infrared Luminescent  $\text{Nd}^{3+}$  and  $\text{Yb}^{3+}$ : Organic Tropolonate Ligands for the Sensitization of  $\text{Ln}^{3+}$ -Doped  $\text{NaYF}_4$  Nanocrystals. *J. Am. Chem. Soc.* **2007**, *129*, 14834-14835.
15. Zou, W. Q.; Visser, C.; Maduro, J. A.; Pshenichnikov, M. S.; Hummelen, J. C. Broadband Dye-Sensitized Upconversion of Near-Infrared Light. *Nat. Photonics* **2012**, *6*, 560-564.
16. Wang, X. D.; Valiev, R. R.; Ohulchansky, T. Y.; Ågren, H.; Yang, C. H.; Chen, G. Y. Dye-Sensitized Lanthanide-Doped Upconversion Nanoparticles. *Chem. Soc. Rev.* **2017**, *46*, 4150-4167.
17. Wei, W.; Chen, G. Y.; Baev, A.; He, G. S.; Shao, W.; Damasco, J.; Prasad, P. N. Alleviating Luminescence Concentration Quenching in Upconversion Nanoparticles through Organic Dye Sensitization. *J. Am. Chem. Soc.* **2016**, *138*, 15130-15133.
18. Lee, J.; Yoo, B.; Lee, H.; Cha, G. D.; Lee, H.-S.; Cho, Y.; Kim, S. Y.; Seo, H.; Lee, W.; Son, D.; Kang, M.; Kim, H. M.; Park, Y. Il; Hyeon, T.; Kim, D.-H. Ultra-Wideband Multi-Dye-Sensitized Upconverting Nanoparticles for Information Security Application. *Adv. Mater.* **2017**, *29*, 1603169.
19. Chen, G. Y.; Damasco, J.; Qiu, H. L.; Shao, W.; Ohulchansky, T. Y.; Valiev, R. R.; Wu, X.; Han, G.; Wang, Y.; Yang, C. H.; Ågren, H.; Prasad, P. N. Energy-Cascaded Upconversion in an Organic Dye-Sensitized Core/Shell Fluoride Nanocrystal. *Nano Lett.* **2015**, *15*, 7400-7407.
20. Wu, X.; Zhang, Y. W.; Takle, K.; Bilsel, O.; Li, Z. J.; Lee, H.; Zhang, Z. J.; Li, D. S.; Fan, W.; Duan, C. Y.; Chan, E. M.; Lois, C.; Xiang, Y.; Han, G. Dye-Sensitized Core/Active Shell

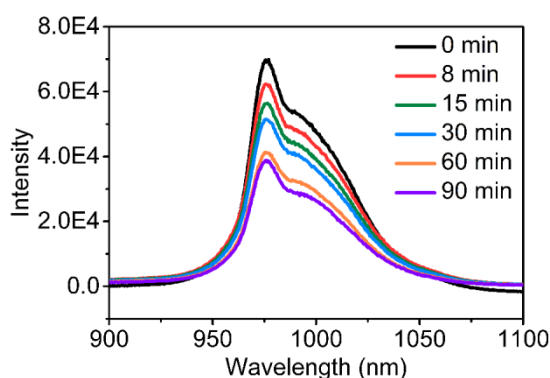
- Upconversion Nanoparticles for Optogenetics and Bioimaging Applications. *ACS Nano*, **2016**, *10*, 1060-1066.
21. Wang, F.; Deng, R. R.; Liu, X. G. Preparation of Core-Shell NaGdF<sub>4</sub> Nanoparticles Doped with Luminescent Lanthanide Ions to be Used as Upconversion-Based Probes. *Nat. Protoc.* **2014**, *9*, 1634-1644.
  22. Dong, A. G.; Ye, X. C.; Chen, J.; Kang, Y. J.; Gordon, T.; Kikkawa, J. M.; Murray, C. B. A Generalized Ligand-Exchange Strategy Enabling Sequential Surface Functionalization of Colloidal Nanocrystals. *J. Am. Chem. Soc.* **2011**, *133*, 998-1006.
  23. Förster, T. Zwischenmolekulare Energiewanderung und Fluoreszenz. *Ann. Phys.* **1948**, *437*, 55-75.
  24. Richards, B. S. Luminescent Layers for Enhanced Silicon Solar Cell Performance: Down-Conversion. *Sol. Energy Mater. Sol. Cells* **2006**, *90*, 1189-1207.
  25. Sabnis, R. W. *Handbook of Fluorescent Dyes and Probes*; John Wiley & Sons: Hoboken, NJ, 2015.
  26. Agbo, P.; Abergel, R. J. Ligand-Sensitized Lanthanide Nanocrystals: Merging Solid-State Photophysics and Molecular Solution Chemistry. *Inorg. Chem.* **2016**, *55*, 9973-9980.
  27. Chen, G. Y.; Shao, W.; Valiev, R. R.; Ohulchanskyy, T. Y.; He, G. S.; Ågren, H.; Prasad, P. N. Efficient Broadband Upconversion of Near-Infrared Light in Dye-Sensitized Core/Shell Nanocrystals. *Adv. Opt. Mater.* **2016**, *4*, 1760-1766.
  28. Dexter, D. L. A Theory of Sensitized Luminescence in Solids. *J. Chem. Phys.* **1953**, *21*, 836-850.
  29. Katayama, Y.; Tanabe, S. Near Infrared Downconversion in Pr<sup>3+</sup>-Yb<sup>3+</sup> Codoped Oxyfluoride Glass Ceramics. *Opt. Mater.* **2010**, *33*, 176-179.
  30. Zhu, W. J.; Chen, D. Q.; Lei, L.; Xu, J.; Wang, Y. S. An Active-Core/Active-Shell Structure with Enhanced Quantum-Cutting Luminescence in Pr-Yb Co-Doped Monodisperse Nanoparticles. *Nanoscale* **2014**, *6*, 10500-10504.
  31. de Jong, M.; Meijerink, A.; Rabouw, F. T. Non-Poissonian Photon Statistics from Macroscopic Photon Cutting Materials. *Nat. Commun.* **2017**, *8*, 15537.
  32. Wang, Z. J.; Senden, T.; Meijerink, A. Photonic Effects for Magnetic Dipole Transitions. *J. Phys. Chem. Lett.* **2017**, *8*, 5689-5694.
  33. Naccache, R.; Vetrone, F.; Speghini, A.; Bettinelli, M.; Capobianco, J. A. Cross-Relaxation and Upconversion Processes in Pr<sup>3+</sup> Singly Doped and Pr<sup>3+</sup>/Yb<sup>3+</sup> Codoped Nanocrystalline Gd<sub>3</sub>Ga<sub>5</sub>O<sub>12</sub>: the Sensitizer/Activator Relationship. *J. Phys. Chem. C* **2008**, *112*, 7750-7756.
  34. de Mello Donegá C.; Meijerink, A.; Blasse, G. Non-Radiative Relaxation Processes of the Pr<sup>3+</sup> Ion in Solids. *J. Phys. Chem. Solids* **1995**, *56*, 673-685.
  35. Jivaramonaikul, W.; Rashatasakhon, P.; Wanichwecharungruang, S. UVA Absorption and Photostability of Coumarins. *Photochem. Photobiol. Sci.* **2010**, *9*, 1120-1125.

36. Carling, C.-J.; Nourmohammadian, F.; Boyer, J.-C.; Brand, N. R. Remote-Control Photorelease of Caged Compounds Using Near-Infrared Light and Upconverting Nanoparticles. *Angew. Chem. Int. Ed.* **2010**, *49*, 3782-3785.

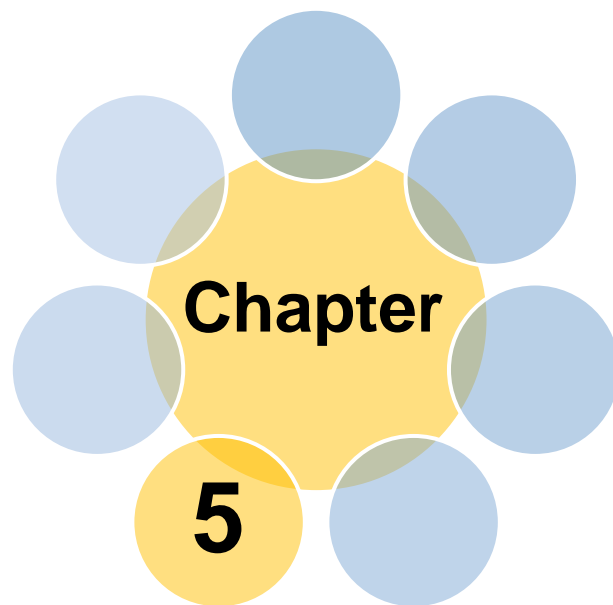
## 4.7 Appendices



**Figure A4.1.** (a) TEM image of  $\text{NaYF}_4:1\text{Pr}^{3+}20\text{Yb}^{3+}@NaYF_4:1\text{Pr}^{3+}$  core-shell NCs. Scale bar = 50 nm. (b) Luminescence decay curves for  $\text{Yb}^{3+}$  emission (excited at 443 nm) for  $\text{NaYF}_4:1\text{Pr}^{3+}20\text{Yb}^{3+}@NaYF_4:1\text{Pr}^{3+}$  core-shell NCs (green) and  $\text{NaYF}_4:1\text{Pr}^{3+}20\text{Yb}^{3+}$  NCs (blue) before dye-sensitization.



**Figure A4.2.** IR emission spectra ( $\lambda_{\text{ex}} = 397$  nm) during continuous UV excitation (365 nm, 6W handheld UV-lamp) of dye-coupled  $\text{NaYF}_4:1\text{Pr}^{3+}20\text{Yb}^{3+}$  NCs (30  $\mu\text{g/mL}$  Coumarin). After an initial drop in intensity, the signal stabilizes after  $\sim 1\text{h}$ .



# **One-step synthesis and luminescence properties of tetragonal double tungstates nanocrystals**

Based on

Wang, Z. J.; Zhang, Y. L.; Zhong, J. P.; Yao, H. H.; Wang, J.; Wu, M. M.; Meijerink, A. One-Step Synthesis and Luminescence Properties of Tetragonal Double Tungstates Nanocrystals. *Nanoscale* **2016**, *8*, 15486-15489.

## 5.1 Abstract

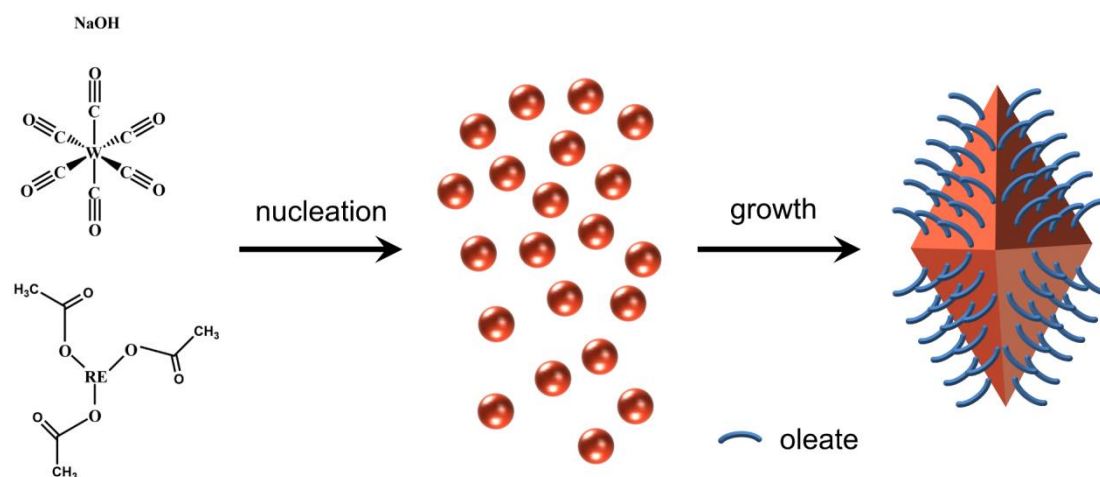
A versatile one-step thermolysis protocol is demonstrated to produce a uniform dispersion of tetragonal double tungstates  $\text{NaRE}(\text{WO}_4)_2$  (RE = rare earth) nanocrystals (NCs). Oriented attachment can occur in the [001] direction. Doping with luminescent  $\text{RE}^{3+}$  ions results in highly luminescent NCs showing characteristic line emissions of the dopant as well as a blue emission assigned to surface adsorbed organic species.

## 5.2 Introduction

Nanocrystals (NCs) doped with rare-earth (RE) ions can have high luminescence efficiency, characteristic sharp line emission, low toxicity, high physical and chemical stabilities, and therefore have attracted much attention for applications in bio-detection, bio-imaging, drug delivery, tumor diagnosis and therapeutics.<sup>1-3</sup> In the past decades, extensive synthetic work concerning RE-doped NCs has been carried out for binary and ternary compounds.<sup>4,5</sup> However, there are only a few reports on NCs in more complicated quaternary system. The double tungstates with the formula  $\text{MRE}(\text{WO}_4)_2$  (M = alkali metals) are excellent hosts for luminescent materials for applications in lighting, displays, lasers and scintillators.<sup>6</sup> These double salts possess compact packing of the crystal lattice, giving rise to outstanding chemical and physical stabilities, which is an important requirement of functional materials. A variety of synthesis protocols has been reported including solid state reaction,<sup>7</sup> liquid phase methods,<sup>8,9</sup> and single crystal growth.<sup>10</sup> The different synthesis methods have resulted in highly luminescent macro- and microcrystalline materials of varying sizes and shapes with luminescent dopants ions, such as  $\text{Eu}^{3+}$ ,  $\text{Tb}^{3+}$  and  $\text{Er}^{3+}$ . However, monodisperse  $\text{MRE}(\text{WO}_4)_2$  nanomaterials with crystal sizes below 50 nm have never been reported and especially for applications in bio-imaging these small sizes are essential. To our knowledge, this study presents the first successful attempt to prepare uniform tetragonal double tungstates  $\text{NaRE}(\text{WO}_4)_2$  NCs with sizes smaller than 50 nm by a one-step thermolysis method. Oriented attachment was observed to occur for these small diamond-shaped NCs. The photoluminescence properties of the as-synthesized NCs were investigated and compared with those of bulk  $\text{NaLa}(\text{WO}_4)_2:\text{Eu}^{3+}$  (microcrystals, MCs).

## 5.3 Results and Discussion

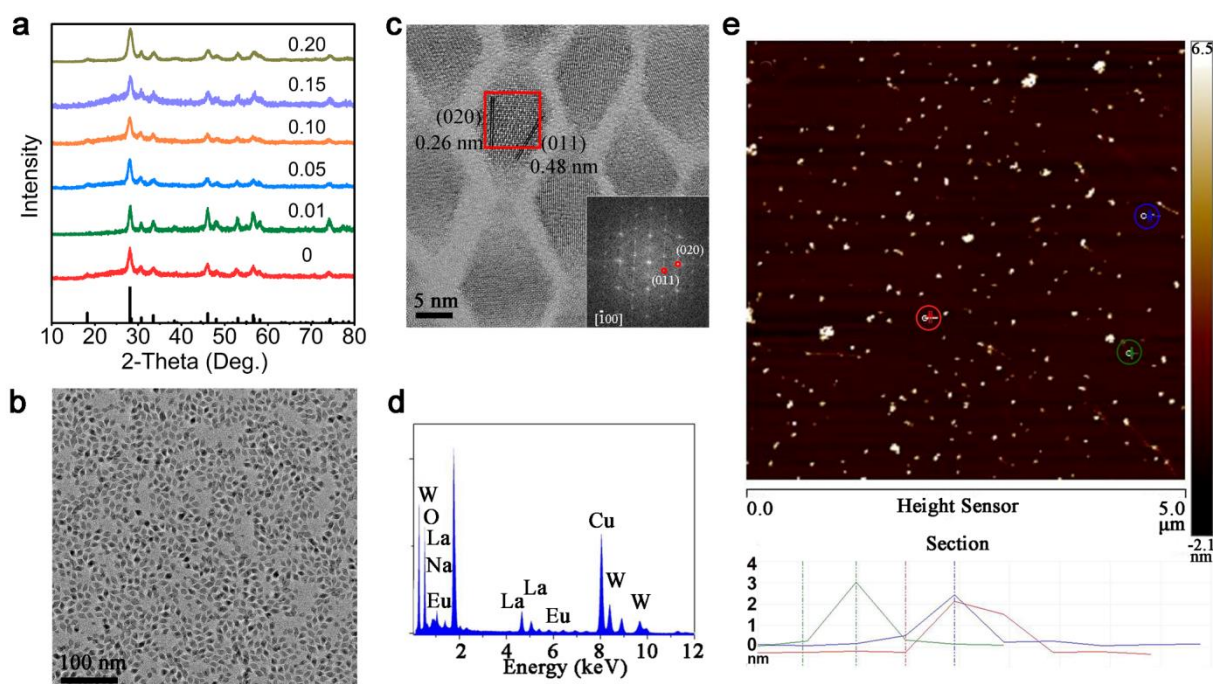
The  $\text{NaRE}(\text{WO}_4)_2$  NCs were produced by a one-step thermolysis method with a special precursor of hexacarbonyl tungsten (see the **Methods** for details). The process for  $\text{NaRE}(\text{WO}_4)_2$  NC growth is displayed in **Scheme 5.1**. This synthesis methodology was used to prepare  $\text{NaLa}(\text{WO}_4)_2$  NCs with different  $\text{Eu}^{3+}$ -doping concentrations. The X-ray diffraction (XRD) patterns shown in **Fig. 5.1a** reveal that all the diffraction peaks of samples are characteristic of the tetragonal structure (JCPDS 79-1118:  $\text{NaLa}(\text{WO}_4)_2$ ,  $a = b = 5.349 \text{ \AA}$ ,  $c = 11.628 \text{ \AA}$ , space group  $I4_1/a$ ). Recent research has shown that the correct space group is  $I\bar{4}$  with two different crystal sites shared by Na and RE instead



**Scheme 5.1.** Schematic display of the synthesis strategy for NaRE(WO<sub>4</sub>)<sub>2</sub> NCs.

of  $I4_1/a$  with only a single shared site for Na and RE.<sup>10-12</sup> Note that although the space group in the JCPDS file is not correct, the position of the diffraction peaks is not affected. The peak broadening is ascribed to the nano-size of particles. In addition, a series of NaRE(WO<sub>4</sub>)<sub>2</sub> (RE = Y, La-Lu) were produced. The XRD diffractograms in **Fig. A5.1** demonstrate the applicability of this preparation method to all RE elements for the synthesis of nanocrystalline NaRE(WO<sub>4</sub>)<sub>2</sub> compounds. The decrease of unit cell parameters in NaRE(WO<sub>4</sub>)<sub>2</sub> along RE series induces the shift of diffraction peaks toward higher angles, in agreement with the decreasing ionic radii of the RE ions along the lanthanide series.

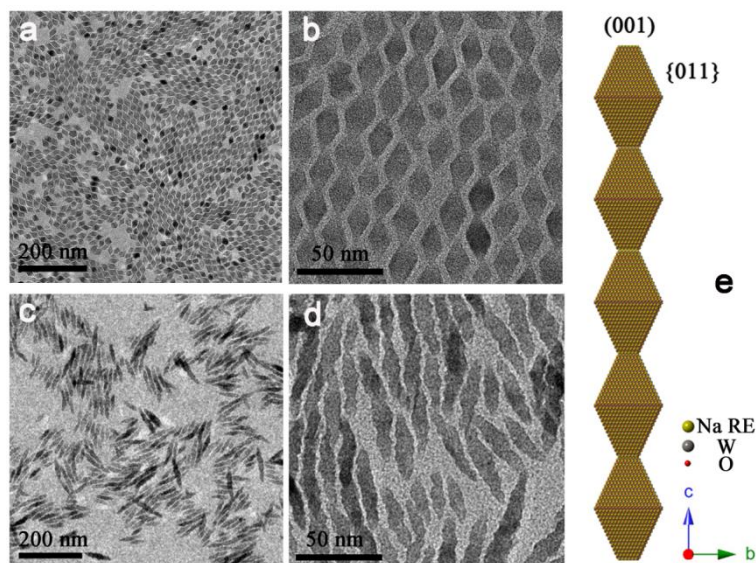
Transmission electron microscopy (TEM) images of NaLa<sub>0.9</sub>Eu<sub>0.1</sub>(WO<sub>4</sub>)<sub>2</sub> NCs and other double tungstates are displayed in **Figs. 5.1b, c** and **Fig. A5.2**, respectively. Analysis of the TEM images reveals that monodisperse diamond shaped NaRE(WO<sub>4</sub>)<sub>2</sub> NCs of  $12 \pm 1 \text{ nm} \times 29 \pm 1 \text{ nm}$  with a small size distribution can be produced through the used synthesis method. Crystals of similar morphology with sizes over 100 nm have been obtained by hydrothermal method.<sup>8,13</sup> The hydrothermal synthesis route allows for size variation but has not been able to produce monodisperse sub-50 nm nanoparticles. In the high resolution TEM image of a single NC shown in **Fig. 5.1c**, lattice planes can be observed with lattice spacings of 0.26 and 0.48 nm which can be indexed as (020) and (011) planes. Based on the orientation of these lattice planes, it can be derived that the crystal is bound to {110} facets with [001] orientation along two vertices. This orientation is further verified by the fast Fourier transform (FFT) analysis shown in the inset of **Fig. 5.1c** viewing from [100] direction. Since the surface energy of (001) facets is higher than that of {110} ones,<sup>14</sup> the (001) facets are prone to diminish, even vanish, leaving behind the {110} facets to define the morphology of crystal. The elemental composition of the product was confirmed by the energy-dispersive X-ray spectroscopy



**Figure 5.1.** Characterization of double tungstates NCs. (a) XRD patterns of  $\text{NaLa}_{1-x}\text{Eu}_x(\text{WO}_4)_2$  ( $x = 0, 0.01, 0.05, 0.10, 0.15, 0.20$ ) with reference pattern of tetragonal  $\text{NaLa}(\text{WO}_4)_2$  (pdf 79-1118). (b, c) TEM images of  $\text{NaLa}_{0.9}\text{Eu}_{0.1}(\text{WO}_4)_2$  NCs in different magnifications showing the lattice fringe with FFT analysis. (d) EDS spectrum. (e) AFM image and height profiles of  $\text{NaLa}_{0.9}\text{Eu}_{0.1}(\text{WO}_4)_2$  NCs after post-sintering at 570 K for 2 h.

(EDS, **Fig. 5.1d**), where the Cu signal is from the carbon-copper grid. The thickness of NCs was determined to be 2-3 nm via atomic force microscope (AFM) presented in **Fig. 5.1e**.

The phenomenon of oriented attachment of the NCs was observed for samples deposited from the concentrated NCs dispersed in toluene. **Fig. 5.2a** exhibits a large area with a monolayer of ordered NCs. The magnified image (**Fig. 5.2b**) demonstrates a parallel alignment of elongated chains and each chain consists of numbers of ultrathin NCs with chain in length up to hundreds of nanometer. Adjacent NCs align along [100] direction by means of attachment to each other via the (001) facets, driven by the reduction of surface energy and inherently anisotropic growth of tetragonal phase. In contrast, the NCs synthesized using the RE (III) acetylacetonate precursors also show oriented attachment (**Figs. 5.2c, d**), but these aggregates have irregular surfaces as well as shorter lengths of alignment. The corresponding NCs form small clusters via oriented attachment and are no longer visible as individual NC. Therefore, we speculate that a single NC in the case of RE-acetylacetonate precursor contains a higher proportion of exposed (001) facets in comparison with the situation for

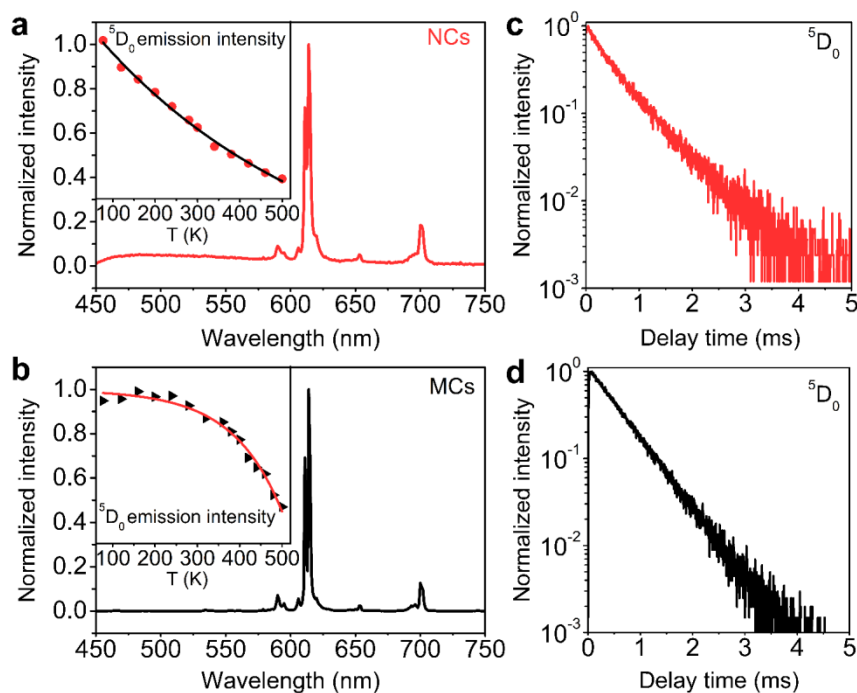


**Figure 5.2.** Oriented attachment of  $\text{NaLa}_{0.9}\text{Eu}_{0.1}(\text{WO}_4)_2$  NCs. (a-d) TEM images in different resolutions, prepared using RE-acetate (a, b) and RE-acetylacetonate (c, d) precursors, respectively. (e) Atomic reconstruction of five NCs showing oriented attachment.

RE-acetate precursor. The difference in decomposition rate and reaction activity of the two  $\text{RE}^{3+}$  precursors may account for the different extents of exposed (001) facets as well as nucleation and growth of NCs. The schematic is illustrated in **Fig. 5.2e** for the proposed oriented attachment of  $\text{NaLa}(\text{WO}_4)_2$  NCs via the (001) facets.

The as-synthesized NCs were used to investigate their unique luminescence behavior. **Fig. A5.3** depicts the excitation spectra at various temperatures while monitoring the  $\text{Eu}^{3+}$  f-f emission at 614 nm. The excitation spectrum shows sharp lines between 350 and 550 nm. In addition, a strong broad excitation band was observed between 250 and 300 nm as well as a broad shoulder extending from 300 to 400 nm. The narrow peaks are assigned to the f-f transitions of  $\text{Eu}^{3+}$  and are located at the characteristic wavelength for  $\text{Eu}^{3+}$  (see assignments in **Fig. A5.3**). The broad band at around 270 nm was also observed in bulk  $\text{NaLa}(\text{WO}_4)_2:\text{Eu}^{3+}$  and is assigned to the charge transfer band (CTB) of the host  $\text{O}^{2-}-\text{W}^{6+}$ , possibly overlapping with an  $\text{O}^{2-}-\text{Eu}^{3+}$  CTB that is also expected in this spectral region. The broad band at around 350 nm was not observed in bulk  $\text{NaLa}(\text{WO}_4)_2:\text{Eu}^{3+}$ . In the past, near UV absorption band (and blue emission) has been reported for NCs prepared in the presence of organic molecules like oleic acid.<sup>15</sup> The origin of the emitting species is not clear but is well known. During synthesis procedures at elevated temperatures in the presence of organic capping molecules, luminescent molecules can be formed with an extended conjugated  $\pi$ -system, giving rise to visible emission upon UV excitation.<sup>16</sup> In our system, the presence of surface capping oleate ligand is

confirmed by the Fourier transform infrared (FT-IR) spectrum in **Fig. A5.4**. The observation of the near UV band in the excitation spectrum of the  $\text{Eu}^{3+}$  emission suggests that there is an energy transfer from the organic luminescent species to the 4f states of  $\text{Eu}^{3+}$ , providing additional evidence that this species is adsorbed at the NC surface in a close proximity to  $\text{Eu}^{3+}$  ions. The intensities of the two broad bands and excitation peaks continuously decrease as temperature rises, in agreement with the discussion on thermal quenching of the corresponding emission (*vide infra*). Note that the emission intensity of hot band from the  ${}^7\text{F}_1$ - ${}^5\text{D}_1$  transition rises until 280 K as a result of thermal population of  ${}^7\text{F}_1$  state. The emission spectrum of  $\text{NaLa}_{0.9}\text{Eu}_{0.1}(\text{WO}_4)_2$  NCs is shown in **Fig. 5.3a** together with an emission spectrum for the microcrystalline analogue (**Fig. 5.3b**) for comparison. The microcrystalline material was produced by the solid state method described in previous work.<sup>7</sup> Both the emission spectra show the characteristic  $\text{Eu}^{3+}$  emission peaks at around 590 ( ${}^5\text{D}_0$ - ${}^7\text{F}_1$ ), 610 ( ${}^5\text{D}_0$ - ${}^7\text{F}_2$ ) and 700 nm ( ${}^5\text{D}_0$ - ${}^7\text{F}_4$ ). The spectra are very similar, as expected since the local environment determined by the crystal structure is the same for  $\text{Eu}^{3+}$  in the NCs and MCs. While, the spectra for  $\text{Eu}^{3+}$  in the MCs show slightly sharper emission lines. Analysis of high-resolution emission spectra (**Fig. A5.5**) recorded at low temperature of 4 K shows that the full width at half maximum (FWHM)



**Figure 5.3.** Comparison of luminescence for  $\text{NaLa}_{0.9}\text{Eu}_{0.1}(\text{WO}_4)_2$  NCs and MCs. Emission spectra ( $\lambda_{\text{ex}} = 394$  nm) of (a) NCs and (b) MCs counterparts, and (c, d) corresponding decay curves ( $\lambda_{\text{ex}} = 394$  nm and  $\lambda_{\text{em}} = 614$  nm) at 300 K. The insets in (a, b) show the integrated emission intensity from  ${}^5\text{D}_0$  state versus temperature.

of the two dominant  ${}^5D_0$ - ${}^7F_2$  emission peaks at ~610 and 613 nm is 0.6 and 1.0 nm for the MCs, and 0.9 and 2.2 nm for the NCs. This is explained by a larger inhomogeneous broadening for the  $\text{Eu}^{3+}$  emission in the NCs where variations in the local environment of  $\text{Eu}^{3+}$  due to (surface) disorder will give rise to more inhomogeneous broadening in the nanocrystalline material. Note that also for the  $\text{Eu}^{3+}$  emission in the MCs, the linewidth is relatively broad due to the cation disorder in the crystal structure.<sup>11</sup> In the emission spectrum for the nanocrystalline material, a broad emission band was also observed in the blue spectral region, which is consistent with the observation of broad band in the excitation spectrum between 300 and 400 nm. The temperature-dependent emission spectra were measured in the range of 77-500 K. When excited at 394 nm ( ${}^7F_0$ - ${}^5L_6$ ), the emission of  $\text{Eu}^{3+}$  in both the NCs and MCs materials shows thermal quenching. The insets in **Figs. 5.3a, b** show the temperature dependence of the integrated emission intensity. For  $\text{Eu}^{3+}$  in the NCs, there is a continuous decrease in emission intensity from 77 to 500 K. There is an additional thermally activated non-radiative decay process that maybe related to thermally activated energy transfer to (surface) defects or the surface adsorbed organic species. For  $\text{Eu}^{3+}$  emission in the MCs, the onset of the quenching is at around 350 K, where the quenching behavior reflects the intrinsic quenching for  $\text{Eu}^{3+}$  in this host material.

The luminescence decay curves of  ${}^5D_0$ - ${}^7F_2$  emission at room temperature are shown in **Figs. 5.3c, d** under the excitation of 394 nm. In the MCs, a single-exponential decay was observed with a decay time of 0.54 ms, which reflects the radiative decay rate for the  ${}^5D_0$  state of  $\text{Eu}^{3+}$  in  $\text{NaLa}(\text{WO}_4)_2$ . For the  $\text{Eu}^{3+}$  emission in the NCs, a deviation of mono-exponential decay was observed. A bi-exponential fitting reveals a fast initial decay with a decay time of 0.2 ms and a slower component with a 0.64 ms decay. The average lifetime is 0.58 ms. Due to the presence of high-energy vibrations (e.g.  $3000\text{ cm}^{-1}$  C-H vibration of surface capping molecules), multi-phonon relaxation (MPR) can quench the luminescence. The MPR rate depends on the proximity of C-H vibrations and dopant ions, and will vary for  $\text{Eu}^{3+}$  ions closer to the surface and those more in the center of the NCs, giving rise to a non-exponential decay with a faster initial decay. Possibly, an overgrowth with an undoped  $\text{NaLa}(\text{WO}_4)_2$  layer can reduce the MPR quenching as has been observed for other RE-doped NCs.<sup>17</sup> The decay component for the  $\text{Eu}^{3+}$  emission in the NCs of 0.64 ms is longer than the radiative decay time for  $\text{Eu}^{3+}$  in the MCs (0.54 ms) as a result of the lower effective refractive index which results in a lower local density of states (LDOS).<sup>18,19</sup> To vary the emission color and demonstrate the possibility to make a variety of luminescent nanolabels for bio-imaging based on RE-doped  $\text{NaLa}(\text{WO}_4)_2$  NCs, we also incorporated  $\text{Tb}^{3+}$  and the  $\text{Yb}^{3+}$ - $\text{Er}^{3+}$  upconversion ion couple in the  $\text{NaLa}(\text{WO}_4)_2$  NCs. In **Fig. A5.6**, the emission spectrum of  $\text{Tb}^{3+}$ -doped NCs is shown with characteristic  $\text{Tb}^{3+}$  emission lines. **Fig. A5.7** presents the upconversion emission spectrum of  $\text{Er}^{3+}$ ,  $\text{Yb}^{3+}$  co-doped sample, which emits upconverted strong green and weak red emission lines under the 980 nm excitation.

## 5.4 Conclusions

In conclusion, a one-step thermolysis approach is presented to synthesize complex quaternary  $\text{NaRE}(\text{WO}_4)_2$  NCs. The small ( $12 \times 29$  nm) diamond shaped and ultrathin ( $\sim 2$  nm) NCs are highly monodisperse in apolar solvents. The NCs can also show oriented attachment along [001] direction via adhesion in (001) facets of neighboring NCs. The  $\text{Eu}^{3+}$ -doped NCs show the characteristic  $\text{Eu}^{3+}$  line emission as well as a blue emission that can be assigned to luminescent organic species adsorbed at the NC surface. The presently synthesized luminescent RE-doped  $\text{NaRE}(\text{WO}_4)_2$  NCs may find applications in transparent luminescent media and bio-imaging while the newly reported synthesis route may serve to aid the development of synthesis routes for other quaternary NCs.

## 5.5 Methods

**Chemicals** The synthesis was conducted with commercially available reagents. Absolute ethanol (Analytical Reagent, A.R.), toluene (A.R.), oleic acid (90%), oleylamine (80-90%), 1-octadecene (90%), RE (Y, La-Lu) (III) acetate (99.9%)/acetylacetonate (99.9%), hexacarbonyl tungsten (97%), sodium oleate (A.R.) and sodium hydroxide (A.R.) were used without further purification.

**Synthesis** In a three-necked flask, oleic acid (10 mL), oleylamine (10 mL) and 1-octadecene (20 mL) were added while stirring and heating to 390 K for 0.5 h. After cooling down to  $\sim 320$  K, the RE (III) acetate (1 mmol), hexacarbonyl tungsten (2 mmol) and sodium hydroxide (1.5 mmol) were added to the solution. The mixture was heated to 570 K and kept for 2 h while refluxing under a protective nitrogen atmosphere. When the solution was cooled down, the product was washed with ethanol and toluene for three times via centrifugation, then dried at 370 K overnight. The final NCs can be re-dispersed in apolar solvents. For the RE (III) acetylacetonate involved synthesis method, the ingredients are RE (III) acetylacetonate (1 mmol), hexacarbonyl tungsten (2 mmol) and sodium oleate (1 mmol), keeping other reaction parameters the same.

**Characterizations** XRD patterns were collected using a D8 ADVANCE (Bruker Co., Germany) X-ray diffractometer (Cu  $K\alpha$  radiation,  $\lambda = 1.5406$  Å). Solution samples dropped on amorphous carbon-coated copper grids were imaged on a JEM-2010HR TEM (200 kV) with an energy-dispersive X-ray spectrometer. The thickness of the NCs was measured on a Dimension Fast Scan AFM (Bruker Co., Germany) in tapping mode on the substrate of mica. FT-IR spectra were measured in a Vertex 70 (Bruker Co., Germany) infrared spectrometer with the KBr pellet technique. Photoluminescence spectra were measured on an Edinburgh Instruments FLS 920 spectrometer with a 450 W xenon lamp and a Hamamatsu R928 photomultiplier tube (PMT). Luminescence decay curves were measured using the multi-channel scaling (MCS) option integrated in the spectrofluorometer and excitation source was a 60 W  $\mu\text{F920H}$  microsecond flash lamp with a pulse width of 1.5-3.0  $\mu\text{s}$  and a pulse repetition rate of 50 Hz. Liquid nitrogen was used for the

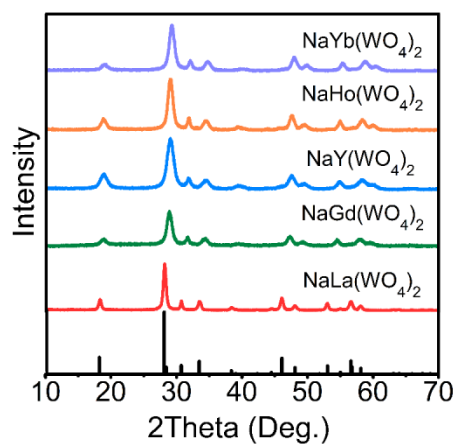
temperature-dependent measurements of emission spectra, regulated by a temperature controller (Oxford, OptistatDN2). Low temperature at 4 K was realized by liquid helium, where the high-resolution spectra were measured under an identical setting of parameters for MCs and NCs. For the upconversion emission spectrum of the Yb<sup>3+</sup>, Er<sup>3+</sup>-co-doped sample, a diode laser was used for excitation.

## 5.6 References

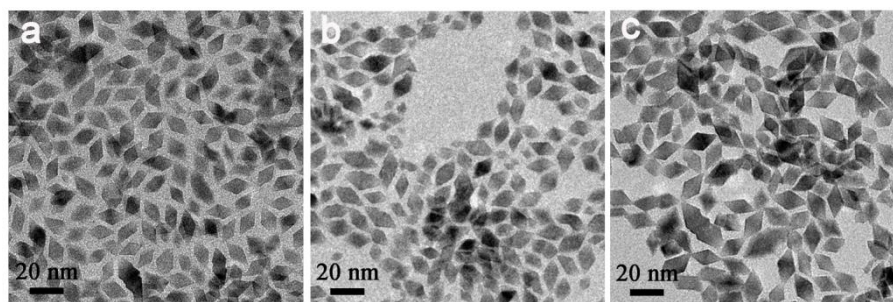
1. Wang, F.; Han, Y.; Lim, C. S.; Lu, Y. H.; Wang, J.; Xu, J.; Chen, H. Y.; Zhang, C.; Hong, M. H.; Liu, X. G. Simultaneous Phase and Size Control of Upconversion Nanocrystals through Lanthanide Doping. *Nature* **2010**, *463*, 1061-1065.
2. Zhou, J.; Liu Z.; Li, F. Y. Upconversion Nanophosphors for Small-Animal Imaging. *Chem. Soc. Rev.* **2012**, *41*, 1323-1349.
3. Sun, L. D.; Wang, Y. F.; Yan, C. H. Paradigms and Challenges for Bioapplication of Rare Earth Upconversion Luminescent Nanoparticles: Small Size and Tunable Emission/Excitation Spectra. *Acc. Chem. Res.* **2014**, *47*, 1001-1009.
4. Wang, G. F.; Peng, Q.; Li, Y. D. Upconversion Luminescence of Monodisperse CaF<sub>2</sub>:Yb<sup>3+</sup>/Er<sup>3+</sup> Nanocrystals. *J. Am. Chem. Soc.* **2009**, *131*, 14200-14201.
5. Wang, J.; Deng, R. R.; MacDonald, M. A.; Chen, B. L.; Yuan, J. K.; Wang, F.; Chi, D. Z.; Hor, T. S. A.; Zhang, P.; Liu, G. K.; Han, Y.; Liu, X. G. Enhancing Multiphoton Upconversion through Energy Clustering at Sublattice Level. *Nat. Mater.* **2014**, *13*, 157-162.
6. Kaczmarek, A. M.; Van Deun, R. Rare Earth Tungstate and Molybdate Compounds - from 0D to 3D Architectures. *Chem. Soc. Rev.* **2013**, *42*, 8835-8848.
7. Wang, Z. J.; Zhong, J. P.; Liang, H. B.; Wang, J. Luminescence Properties of Lutetium Based Red-Emitting Phosphor NaLu(WO<sub>4</sub>)<sub>2</sub>:Eu<sup>3+</sup>. *Opt. Mater. Express* **2013**, *3*, 418-425.
8. Wang, Z. J.; Zhong, J. P.; Jiang, H. X.; Wang, J.; Liang, H. B. Controllable Synthesis of NaLu(WO<sub>4</sub>)<sub>2</sub>:Eu<sup>3+</sup> Microcrystal and Luminescence Properties for LEDs. *Cryst. Growth&Des.* **2014**, *14*, 3767-3773.
9. Wang, Y. F.; Xu, W.; Zhu, Y. S.; Xu, S.; Cui, H. N.; Song, H. W. Phonon-Modulated Upconversion Luminescence Properties in Some Er<sup>3+</sup> and Yb<sup>3+</sup> Co-Activated Oxides. *J. Mater. Chem. C* **2014**, *2*, 4642-4650.
10. Han, X. M.; Garc á-Cort és, A.; Serrano, M. D.; Zaldo, C.; Cascales, C. Structural and Thermal Properties of Tetragonal Double Tungstate Crystals Intended for Ytterbium Laser Composites. *Chem. Mater.* **2007**, *19*, 3002-3010.
11. Cascales, C.; Blas, A. M.; Rico, M.; Volkov, V.; Zaldo, C. The Optical Spectroscopy of Lanthanides R<sup>3+</sup> in ABi(XO<sub>4</sub>)<sub>2</sub> (A = Li, Na; X = Mo, W) And LiYb(MoO<sub>4</sub>)<sub>2</sub> Multifunctional Single Crystals: Relationship with the Structural Local Disorder. *Opt. Mater.* **2005**, *27*, 1672-1680.

12. Cascales, C.; Serrano, M. D.; Esteban-Betegón, F.; Zaldo, C.; Peters, R.; Petermann, K.; Huber, G.; Ackermann, L.; Rytz, D.; Dupré, C.; Rico, M.; Liu, J.; Griebner, U.; Petrov, V. Structural, Spectroscopic, and Tunable Laser Properties of Yb<sup>3+</sup>-doped NaGd(WO<sub>4</sub>)<sub>2</sub>. *Phys. Rev. B: Condens. Matter Mater. Phys.* **2006**, *74*, 174114.
13. Bu, W. B.; Chen, Z. X.; Chen, F.; Shi, J. L. Oleic Acid/Oleylamine Cooperative-Controlled Crystallization Mechanism for Monodisperse Tetragonal Bipyramid NaLa(MoO<sub>4</sub>)<sub>2</sub> Nanocrystals. *J. Phys. Chem. C* **2009**, *113*, 12176-12185.
14. Donnay, J. D. H.; Harker, D. A New Law of Crystal Morphology Extending the Law of Bravais. *Amer. Mineral.* **1937**, *22*, 446-467.
15. Fu, Y. S.; Du, X. W.; Kulinich, S. A.; Qiu, J. S.; Qin, W. J.; Li, R.; Sun, J.; Liu, J. Stable Aqueous Dispersion of ZnO Quantum Dots with Strong Blue Emission via Simple Solution Route. *J. Am. Chem. Soc.* **2007**, *129*, 16029-16033.
16. de Mello Donegá, C.; Hickey, S. G.; Wuister, S. F.; Vanmaekelbergh, D.; Meijerink, A. Single-Step Synthesis to Control the Photoluminescence Quantum Yield and Size Dispersion of CdSe Nanocrystals. *J. Phys. Chem. B* **2003**, *107*, 489-496.
17. Wang, F.; Wang, J.; Liu, X. G. Direct Evidence of a Surface Quenching Effect on Size-Dependent Luminescence of Upconversion Nanoparticles. *Angew. Chem. Int. Ed.* **2010**, *49*, 7456-7460.
18. Senden, T.; Rabouw, F. T.; Meijerink, A. Photonic Effects on the Radiative Decay Rate and Luminescence Quantum Yield of Doped Nanocrystals. *ACS Nano* **2015**, *9*, 1801-1808.
19. Meltzer, R. S.; Feofilov, S. P.; Tissue, B.; Yuan, H. B. Dependence of Fluorescence Lifetimes of Y<sub>2</sub>O<sub>3</sub>:Eu<sup>3+</sup> Nanoparticles on the Surrounding Medium. *Phys. Rev. B: Condens. Matter Mater. Phys.* **1999**, *60*, R14012-R14015.

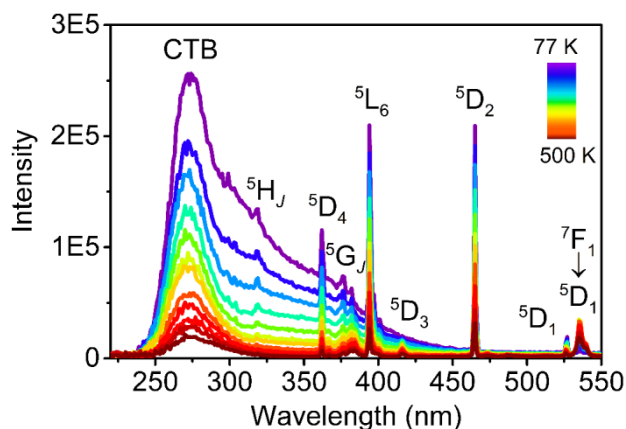
## 5.7 Appendices



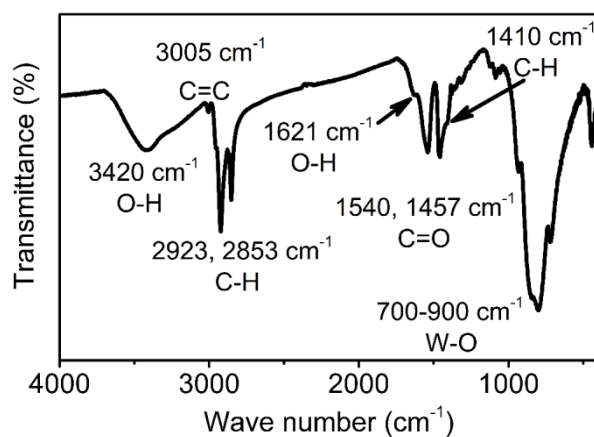
**Figure A5.1.** XRD patterns of NaRE(WO<sub>4</sub>)<sub>2</sub> NCs with reference pattern of tetragonal NaLa(WO<sub>4</sub>)<sub>2</sub> (pdf 79-1118).



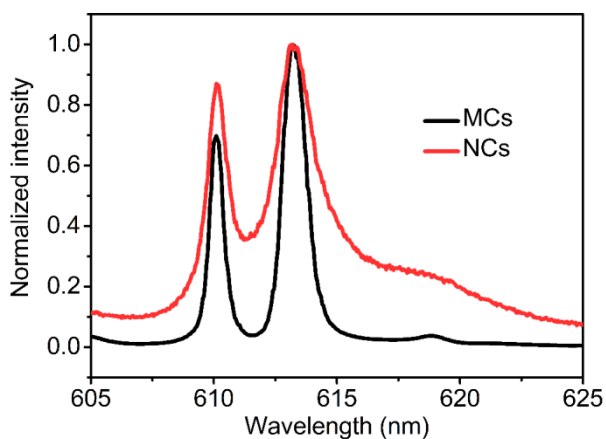
**Figure A5.2.** TEM images of NaRE(WO<sub>4</sub>)<sub>2</sub> NCs. (a) RE = Gd, (b) RE = Y and (c) RE = Yb.



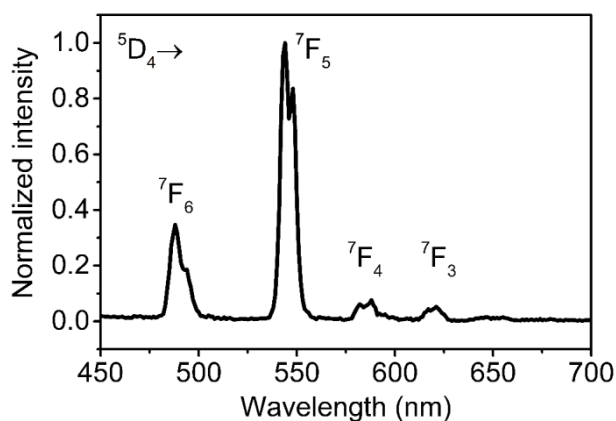
**Figure A5.3.** Temperature-dependent excitation spectra of  $\text{NaLa}_{0.9}\text{Eu}_{0.1}(\text{WO}_4)_2$  NCs with monitoring the emission at 614 nm. Excitation lines are labelled by the final state for excitation from the  ${}^7\text{F}_0$  ground state, except for the lines around 535 nm corresponding to the transition from the thermally populated  ${}^7\text{F}_1$  state.



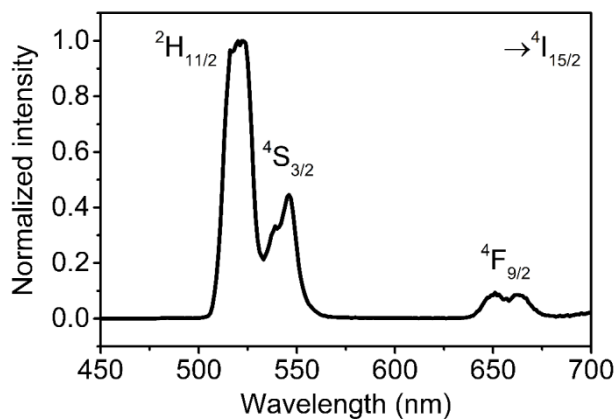
**Figure A5.4.** Fourier transform infrared (FT-IR) spectrum of  $\text{NaLa}_{0.9}\text{Eu}_{0.1}(\text{WO}_4)_2$  NCs.



**Figure A5.5.** High-resolution emission spectra ( $\lambda_{\text{ex}} = 394 \text{ nm}$ ) of  $\text{NaLa}_{0.9}\text{Eu}_{0.1}(\text{WO}_4)_2$  NCs and MCs recorded at low temperature of 4 K.

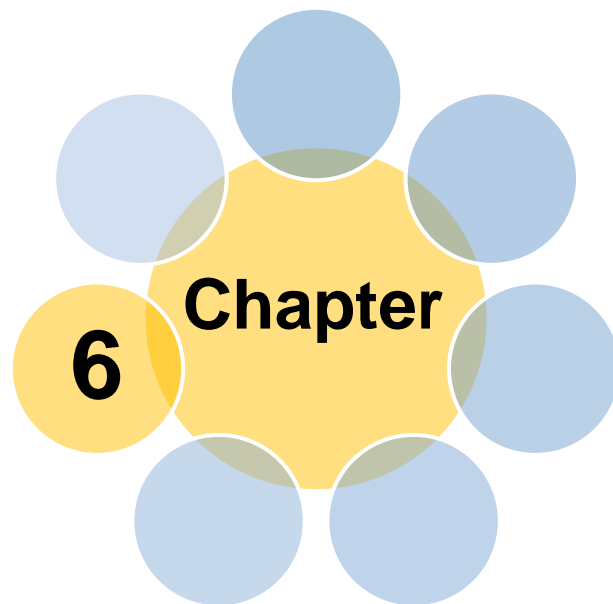


**Figure A5.6.** Emission spectrum ( $\lambda_{\text{ex}} = 266 \text{ nm}$ ) of  $\text{NaLa}_{0.9}\text{Tb}_{0.1}(\text{WO}_4)_2$  NCs.



**Figure A5.7.** Emission spectrum ( $\lambda_{\text{ex}} = 980 \text{ nm}$  laser) of  $\text{NaLa}_{0.8}\text{Er}_{0.02}\text{Yb}_{0.18}(\text{WO}_4)_2$  NCs.





# **Thermal enhancement and quenching of upconversion emission in nanocrystals**

Based on

Wang, Z. J.; Christiansen, J.; Wezendonk, D.; Xie, X. B.; van Huis, M. A.; van Blaaderen, A.; Meijerink, A. Thermal Enhancement and Quenching of Upconversion Emission in Nanocrystals. *In preparation.*

## 6.1 Abstract

Photoluminescence is a powerful tool in temperature sensing. Recently, the application of upconversion (UC) nanocrystal (NC) has shown great potential for nanothermometry due to the combination of high spatial resolution, superior accuracy and its non-invasive nature. In addition to spectral changes upon heating, anomalous thermal enhancement of UC emission has also been reported for UC NCs, but the underlying mechanism remains unclear. Here, we report on NaY(WO<sub>4</sub>)<sub>2</sub> doped with the Er<sup>3+</sup>-Yb<sup>3+</sup> UC couple in NCs and in bulk material, and investigate the temperature-dependent luminescence both in ambient atmosphere and in dry nitrogen. In ambient atmosphere, strong thermal enhancement of UC emission is observed with good reversibility and accompanied by a lengthening of decay time for the Er<sup>3+</sup> UC emission and Yb<sup>3+</sup> IR emission. In contrast, the measurements carried out in dry nitrogen demonstrate thermal enhancement in the first cycle, but thermal quenching in subsequent cycles. For bulk materials, the UC emission shows similar thermal quenching in both ambient atmosphere and nitrogen. Thermogravimetric analysis (TGA) and Fourier transform infrared (FT-IR) measurements reveal the presence of water adsorbed on the NC surface that is removed upon heating up to ~470 K but re-adsorbed upon cooling below ~370 K in ambient atmosphere. Based on these observations, we explain the anomalous thermal enhancement in UC NCs in ambient atmosphere by quenching of the Yb<sup>3+</sup> and Er<sup>3+</sup> excited states via surface adsorbed water molecules. The present study highlights the careful characterization of surface adsorbed molecules that are important for understanding luminescence properties of NCs, and enables the exploration of UC NCs with higher quantum efficiencies.

## 6.2 Introduction

Temperature is an important parameter in physical and chemical processes. Measuring temperature is therefore important. However, conventional thermometry is not always capable to detect and map temperatures in high spatial resolution to measure local temperatures e.g. in biological systems, catalysis, microelectronics and microfluidics.<sup>1</sup> In this regard, nanothermometry based on luminescent (upconversion, UC) nanocrystals (NCs) has emerged in recent years because of important advantages, such as its non-invasive nature, high spatial resolution, and a fast response in a wide range of temperatures.<sup>2-4</sup> The field of applications initially involved bio-medicine/therapy/imaging (with a typical temperature range 270-330 K), and recently, has expanded to include sensing of higher temperatures (even beyond 900 K), which is required for chemical reactors, microfluidics and electronics.<sup>2-4</sup> The basis for temperature sensing is the variation of luminescence intensity or intensity ratios, decay time, polarization dependence, width and position of emission line/band with temperature. The self-referenced technique of ratiometric thermometry<sup>5-10</sup> is especially promising and the use of lanthanide-doped UC NCs for nanothermometry has been investigated extensively. The use of the efficient NIR-to-visible UC makes it possible to record almost background free

emission spectra and the sharp emission lines of lanthanides allow for an accurate determination of intensity ratios for emission from different energy levels. The changes in intensity ratios with temperature can be determined with high accuracy. Two beautiful examples of the superior performance of UC NCs for high-resolution temperature sensing are physiological sensing<sup>5</sup> and measurement of Brownian motion.<sup>6</sup>

For practical use of nanothermometry, a critical parameter is the reversibility of luminescence. It is challenging for NCs due to the high surface-to-volume ratio and complex surface chemistry (e.g. ligands and defects)<sup>11</sup> and variations in optical properties originating from differences in the synthesis procedure, even for seemingly identical reaction conditions (e.g. presence of water and variations in heating rate and reaction temperature). The advantage of ratiometric methods is the independence of absolute emission intensities, but generally, one ignores measurement of reversibility of luminescence intensities and only checks the reversibility of the temperature dependence of the intensity ratio.<sup>7,9</sup> The emission intensity ratio can be described by Boltzmann statistics if the two excited states are thermally coupled, and the same temperature dependence is observed with a continuous decrease (or increase) of absolute luminescence intensity during cycles of heating and cooling. The examination of reversibility of absolute luminescence intensity is however important as it affects the signal-to-noise ratio which is important in determining the speed, accuracy and spatial resolution with which temperature can be measured. Some studies<sup>12-14</sup> have been reported for the temperature range just above room temperature. With the advent of lanthanide based nanothermometry, it is useful to extend studies on UC emission to higher temperatures.

Luminescence intensity, typically, shows thermal quenching<sup>15-20</sup> resulting from the enhanced non-radiative processes at higher temperatures. However, thermally enhanced luminescence has been observed for UC emission in UC NCs. As examples, size-dependent UC thermal enhancement (stronger thermal enhancement in smaller NCs) was demonstrated in NaYF<sub>4</sub>:Er,Yb NCs and attributed to phonon-assisted energy transfer and a role for phonon confinement effects.<sup>21</sup> Recently, strong (~2000-fold) UC emission enhancement was reported in NaYF<sub>4</sub>:Yb,Tm NCs and was explained by phonon-assisted energy transfer enabled by higher-energy vibrations from Yb-O bonds with surface ligands compared to lower-energy Yb-F vibrations for bonds inside the fluoride crystallites.<sup>22</sup> The strong increase of UC emission intensity upon a small change in phonon energy (500 vs. 350 cm<sup>-1</sup>) is however unexpected and further research is needed to provide insight on the mechanism behind the thermal enhancement of UC emission in NCs.

Here, we investigate the temperature dependence of UC emission in NaY(WO<sub>4</sub>)<sub>2</sub> NCs doped with the Er-Yb ion couple. The thermal stability of tungstates is high which allows studies in a wide range of temperature. Photoluminescence spectra, luminescence decay dynamics and thermal cycling experiments were measured in two types of atmospheres: ambient atmosphere and dry nitrogen. In

ambient conditions, a strong thermal enhancement of the UC emission intensity is observed upon heating up to  $\sim 470$  K and shows a good reversibility. If the NCs are in dry nitrogen, a strong increase of the UC emission intensity is present only during the first heating stage. However, upon subsequent cooling, the UC emission intensity increases further and conventional thermal quenching occurs with high reversibility in following cycles of heating. For comparison, the UC emission intensity was also measured for  $\text{NaY}(\text{WO}_4)_2:\text{Er},\text{Yb}$  bulk material. The thermal behavior is similar to that of the NCs in dry nitrogen after the first heating cycle and shows reversible thermal quenching upon heating. The results reveal a role of surface adsorbed water molecules. This is further confirmed by thermogravimetric analysis (TGA) and Fourier transform infrared spectroscopy (FT-IR). As the temperature increases, the water molecules adsorbed to the NC surface are removed. The high-energy O-H vibration is known to strongly quench the UC emission and removal of surface adsorbed water can explain the observed UC thermal enhancement. Cooling in ambient atmosphere results in readsorption of water, but this is prevented in dry nitrogen. We suggest that this is a general phenomenon that can also explain the thermal enhancement of UC emission in other NCs. Our study sheds the light on the mechanism of UC thermal enhancement in NCs, and serves for understanding and controlling absolute intensity variations that are important in the accuracy and sensitivity of nanothermometry based on lanthanide-doped UC NCs.

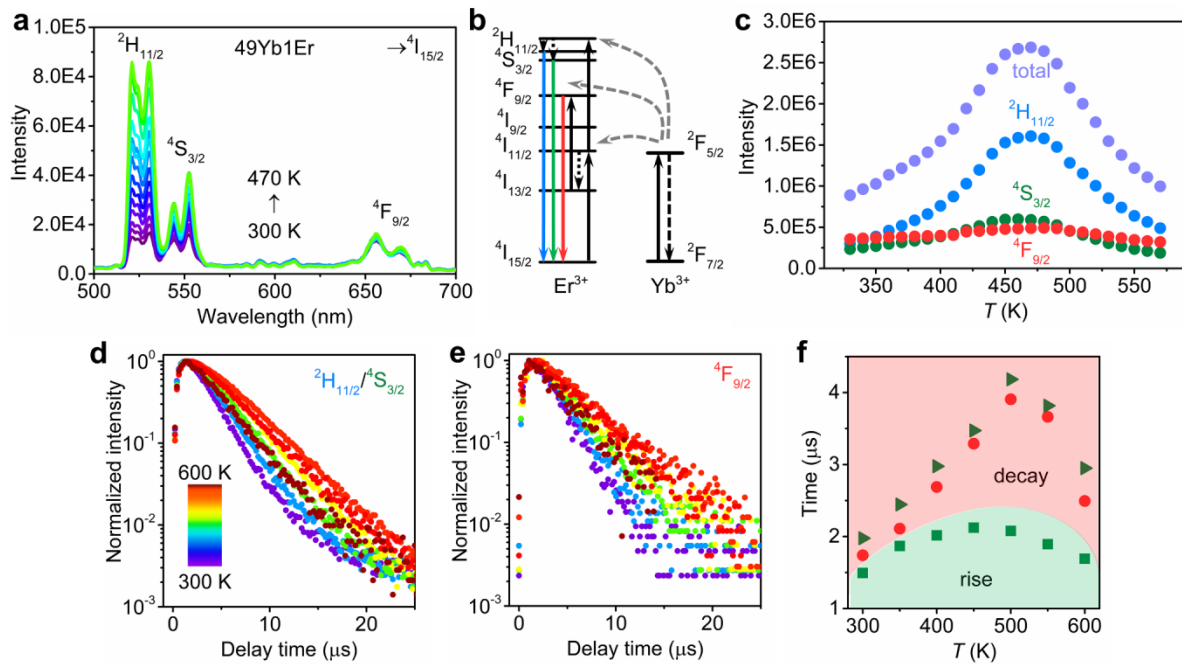
### 6.3 Results and Discussion

**Thermal enhancement of UC for NCs in ambient atmosphere**  $\text{NaY}(\text{WO}_4)_2$  UC NCs were synthesized by a one-step thermolysis protocol<sup>23</sup> as established in **Ch. 5** and were dried at 370 K overnight to reduce adsorbed water on NC surface. A variety of NCs was synthesized: Er/Yb co-doped UC NCs with varying  $\text{Yb}^{3+}$  concentrations (10, 25 and 49%) and a fixed  $\text{Er}^{3+}$  concentration (1%). All percentages are mole% relative to  $\text{Y}^{3+}$ . Other UC couples were also incorporated in  $\text{NaY}(\text{WO}_4)_2$  NCs (1Tm/49Yb and 1Ho/49Yb) to investigate the thermal enhancement in these UC systems for comparison. For UC luminescence measurements, a fixed configuration was used to allow for comparison of absolute emission intensities. The power density of the NIR (980 nm) laser was constant at  $1 \text{ W/cm}^2$  which is important given the quadratic power dependence of the UC emission intensity. Details on the synthesis and experimental set-ups are described in the **Methods**.

Photoluminescence spectra were measured for  $\text{NaY}(\text{WO}_4)_2:49\text{Yb}1\text{Er}$  NCs in ambient atmosphere under 980 nm laser excitation in the temperature range of 300-600 K. **Fig. 6.1a** shows the emission spectra at different temperatures. The typical green emission from the thermally coupled  $^2\text{H}_{11/2}$  and  $^4\text{S}_{3/2}$  levels is observed at around 540 nm, as well as the red emission from the  $^4\text{F}_{9/2}$  level at around 660 nm. The energy transfer scheme responsible for the NIR-to-visible UC is shown in **Fig. 6.1b**.<sup>24,25</sup> Two excited  $\text{Yb}^{3+}$  ions after NIR absorption transfer their energy to one neighbouring  $\text{Er}^{3+}$  ion that emits green or red photons. The position of the intraconfigurational f-f transitions does not change

but all the emission lines are enhanced with increased temperature until 470 K, followed by thermal quenching. For a quantitative analysis, the integrated emission intensities are plotted as a function of temperature for each transition as well as the total (Fig. 6.1c). The total integrated intensity ( ${}^2\text{H}_{11/2}$ ,  ${}^4\text{S}_{3/2}$ ,  ${}^4\text{F}_{9/2} \rightarrow {}^4\text{I}_{15/2}$ ) is enhanced by a factor of 3.0 from 330 to 470 K. In addition to the total intensity increase, the individual  ${}^2\text{H}_{11/2} \rightarrow {}^4\text{I}_{15/2}$  and  ${}^4\text{S}_{3/2} \rightarrow {}^4\text{I}_{15/2}$  emission lines show their typical temperature-dependent change in intensity with increasing intensity of emission from the upper thermally coupled state ( ${}^2\text{H}_{11/2}$ ) relative to the lower state ( ${}^4\text{S}_{3/2}$ ). Similar temperature-dependent behavior is observed for other  $\text{Yb}^{3+}$  (10 and 25%, Fig. A6.1).

To test whether the thermal enhancement is specific for the Yb/Er couple, temperature-dependent UC emission spectra were also recorded for  $\text{NaY}(\text{WO}_4)_2$  UC NCs with  $\text{Ho}^{3+}$ - $\text{Yb}^{3+}$  and  $\text{Tm}^{3+}$ - $\text{Yb}^{3+}$  ion couples under 980 nm excitation (Fig. A6.2). For  $\text{NaY}(\text{WO}_4)_2$ :49Yb1Ho NCs, the UC emission is at 541 and 646 nm ( ${}^5\text{F}_4/{}^5\text{S}_2$ ,  ${}^5\text{F}_5 \rightarrow {}^5\text{I}_8$  transitions) and for  $\text{NaY}(\text{WO}_4)_2$ :49Yb1Tm at 796 nm ( ${}^3\text{H}_4 \rightarrow {}^3\text{H}_6$



**Figure 6.1.** Temperature-dependent UC emission of  $\text{NaY}(\text{WO}_4)_2$ :49Yb1Er NCs in ambient atmosphere. (a) Emission spectra under 980 nm excitation. (b) Energy levels of  $\text{Er}^{3+}$ - $\text{Yb}^{3+}$  ion couple showing the UC processes. (c) Integrated intensity of  $\text{Er}^{3+}$  emission lines ( ${}^2\text{H}_{11/2}$ ,  ${}^4\text{S}_{3/2}$ ,  ${}^4\text{F}_{9/2} \rightarrow {}^4\text{I}_{15/2}$  transitions and their sum) determined from the emission spectra. (d, e) Luminescence decay curves of (d) green  ${}^2\text{H}_{11/2}/{}^4\text{S}_{3/2}$  and (e) red  ${}^4\text{F}_{9/2}$  emitting levels under pulsed (5 ns) 980 nm excitation. (f) Decay times (green triangles for  ${}^2\text{H}_{11/2}/{}^4\text{S}_{3/2}$  emission and red circles for  ${}^4\text{F}_{9/2}$  emission) and rise time (green squares for  ${}^2\text{H}_{11/2}/{}^4\text{S}_{3/2}$  emission) determined from the decay curves in (d, e).

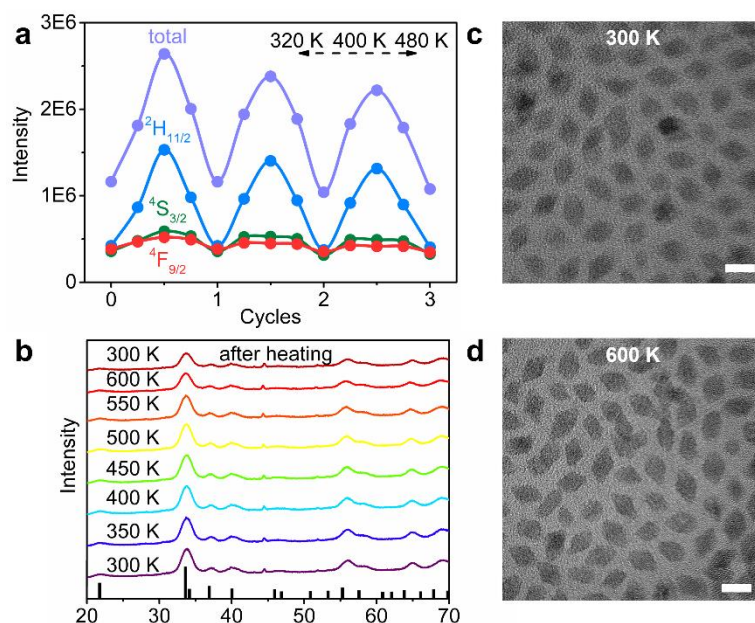
transition). The  $\text{Tm}^{3+}$  UC emission line at  $\sim 475$  nm ( $^1\text{G}_4 \rightarrow ^3\text{H}_6$  transition) was too weak to observe. All the observed UC emissions involve a two-photon energy transfer process from  $\text{Yb}^{3+}$  ions. Again, the thermal enhancement of UC emission is evident until  $\sim 500$  K for  $^5\text{F}_4/^5\text{S}_2 \rightarrow ^5\text{I}_8$  green emission and  $^5\text{F}_5 \rightarrow ^5\text{I}_8$  red emission of  $\text{NaY}(\text{WO}_4)_2:49\text{Yb}1\text{Ho}$  NCs (enhancement factor of 5.0 for the total emission intensity) and for  $^3\text{H}_4 \rightarrow ^3\text{H}_6$  IR emission of  $\text{NaY}(\text{WO}_4)_2:49\text{Yb}1\text{Tm}$  NCs (enhancement factor of 7.7). The results demonstrate that thermal enhancement of UC emission is a general phenomenon for different UC couples in NCs.

To further confirm the occurrence of thermal enhancement and to obtain insight into the origin, temperature-dependent decay dynamics was measured for the  $\text{Er}^{3+}$  emission. **Figs. 6.1d, e** show the luminescence decay curves of the green  $^2\text{H}_{11/2}/^4\text{S}_{3/2}$  and red  $^4\text{F}_{9/2}$  emissions under pulsed 980 nm excitation. Since the  $^2\text{H}_{11/2}$  and  $^4\text{S}_{3/2}$  states are thermally coupled, the decay for  $^2\text{H}_{11/2}$  and  $^4\text{S}_{3/2}$  emissions is indistinguishable. The decay time  $\tau$  and the rise time  $\tau_r$  are determined by fitting the decay curves with  $I = a \exp(-t/\tau) (1 - b \exp(-t/\tau_r))$ , where  $I$  is the luminescence intensity at time  $t$ , and  $a$  and  $b$  are constants. The luminescence decay curves for both emissions show a lengthening of the decay and rise time with increasing temperature. The results from the fitting of decay curves at different temperatures are plotted in **Fig. 6.1f**. The decay time for the green and red emitting levels lengthens to 4.2 and 3.9  $\mu\text{s}$  at 500 K (vs. 2.0 and 1.7  $\mu\text{s}$  at 300 K). Likewise, the rise time increases from 1.5  $\mu\text{s}$  at 300 K to 2.1  $\mu\text{s}$  at 500 K. The lengthening of the decay and rise time upon heating are consistent with the observed total enhancement of the  $\text{Er}^{3+}$  UC emission intensity until 470 K (**Figs. 6.1a, b**). Longer rise and decay times result from longer lived intermediate ( $\text{Yb}^{3+}$ ) and emitting ( $\text{Er}^{3+}$ ) excited states. Temperature-dependent decay dynamics was also measured for  $\text{NaY}(\text{WO}_4)_2:10\text{Yb}1\text{Er}$  and  $\text{NaY}(\text{WO}_4)_2:25\text{Yb}1\text{Er}$  NCs (**Fig. A6.3**). From the comparison of the rise and decay times for the three samples doped with 10, 25 and 49%  $\text{Yb}^{3+}$  ions, it is clear that the decay of the  $\text{Er}^{3+}$   $^2\text{H}_{11/2}/^4\text{S}_{3/2}$  and  $^4\text{F}_{9/2}$  emissions is faster for higher  $\text{Yb}^{3+}$  concentrations. The faster decay at higher  $\text{Yb}^{3+}$  concentrations is generally observed and explained by a shorter lifetime of the feeding  $^2\text{F}_{5/2}$  state of  $\text{Yb}^{3+}$  due to concentration quenching and higher back transfer rates to  $\text{Yb}^{3+}$ .

Luminescence decay curves were also measured following direct pulsed excitation at 480 nm (into the  $^4\text{F}_{7/2}$  excited level, just above the emitting  $^2\text{H}_{11/2}/^4\text{S}_{3/2}$  levels) for the temperature dependence of the decay dynamics of the green emitting  $^2\text{H}_{11/2}/^4\text{S}_{3/2}$  levels. For  $\text{NaY}(\text{WO}_4)_2:49\text{Yb}1\text{Er}$  NCs, **Figs. A6.4a, b** show the temperature-dependent luminescence decay curves and decay times determined from the experimental decay curves. There is no  $\mu\text{s}$  rise time since the emitting level is populated by fast relaxation from the  $^4\text{F}_{7/2}$  to  $^2\text{H}_{11/2}/^4\text{S}_{3/2}$ . As the decay curves deviate from single exponential decay, the luminescence decay curves are characterized by an average lifetime that is determined using  $\tau_{\text{av}} = \sum_0^t tI / \sum_0^t I$ . There is a good agreement with the decay times found after pulsed 980 nm excitation (**Fig. 6.1f**). Again, higher temperatures lead to lengthening of the decay time from 2.6  $\mu\text{s}$  at

300 K to 3.8  $\mu\text{s}$  at 500 K and a small decrease above 500 K, in agreement with the trend of thermal enhancement of the UC intensity. Further, **Figs. A6.4c, d** show the temperature-dependent luminescence decay for singly 1%  $\text{Er}^{3+}$ -doped NCs. The decay times increase from 3.9 to 7.9  $\mu\text{s}$  between 300 and 600 K. The trend of lengthened decay time at higher temperature is the same as for the  $\text{Er}^{3+}$  emission in co-doped Yb, Er sample. However, the decay times are about two times longer, attributed to back energy transfer from  $\text{Er}^{3+}$  to  $\text{Yb}^{3+}$  in co-doped NCs. The lengthening of decay times at elevated temperatures for  $\text{Er}^{3+} \ ^2\text{H}_{11/2}/^4\text{S}_{3/2}$  emission following direct excitation indicates that non-radiative decay from the  $^2\text{H}_{11/2}/^4\text{S}_{3/2}$  levels is suppressed upon heating giving rise to higher quantum yields for these emitting levels. Therefore, in ambient atmosphere, the thermal enhancement of UC emission is universal for  $\text{NaY}(\text{WO}_4)_2$  UC NCs singly  $\text{Er}^{3+}$ -doped, and co-doped with  $\text{Yb}^{3+}$  and  $\text{Er}^{3+}$ ,  $\text{Tm}^{3+}$  or  $\text{Ho}^{3+}$  in the temperature range of 300-500 K, as demonstrated by measurements of temperature-dependent emission spectra and decay dynamics.

**Reversibility and thermal stability of UC NCs in ambient atmosphere** Now that the phenomenon of thermal enhancement of the UC emission has been established, we focus on exploring the reasons behind. First, we examine the reversibility of temperature-dependent luminescence and the thermal stability of  $\text{NaY}(\text{WO}_4)_2$  NCs. As an example, a cycling experiment (repeated heating and cooling between 320 and 480 K) is shown in **Fig. 6.2a**. The temperature dependence of the emission intensity of the  $^2\text{H}_{11/2}$ ,  $^4\text{S}_{3/2}$ ,  $^4\text{F}_{9/2} \rightarrow ^4\text{I}_{15/2}$  transitions and the sum for the  $\text{NaY}(\text{WO}_4)_2:49\text{Yb1Er}$  NCs indicates that the observed thermal UC enhancement is reversible. To further investigate the thermal stability and exclude the presence of a phase transition at elevated temperatures, temperature-dependent X-ray diffraction (XRD) patterns were recorded. In **Fig. 6.2b**, the XRD patterns recorded between 300 and 600 K are shown and no peak shift is observed in the diffraction pattern. This indicates that there is no phase transition when heating up to 600 K and cooling back to 300 K. The diffraction peaks shift  $\sim 0.1$  degree to smaller angles because of slight thermal expansion of lattice. The thermal stability of NCs is further demonstrated by in-situ transmission electron microscopy (TEM) measurements in **Figs. 6.2c, d** and **Figs. A6.5a-d**. The  $\text{NaY}(\text{WO}_4)_2$  NCs have a diamond shape with a size of  $\sim 10$  nm. The in-situ TEM images at 300 and 600 K show that size and shape do not change upon heating to 600 K. The observation that morphology and monodispersity of the NCs are maintained indicates superior thermal stability of core-only  $\text{NaY}(\text{WO}_4)_2$  NCs in comparison with core-only  $\text{NaYF}_4$  NCs (showing aggregation above 575 K)<sup>9</sup>. The in-situ heating was carried out in vacuum for TEM measurement. To test if there is a difference with ambient atmosphere, the NCs were heated ex-situ in air at 600 K and the corresponding TEM image (**Fig. A6.5e**) shows that the NCs have retained their morphology and crystal structure. Therefore, the thermal stability of  $\text{NaY}(\text{WO}_4)_2$  NCs is high and the observed thermal UC enhancement with good reversibility cannot be related to a phase transition.



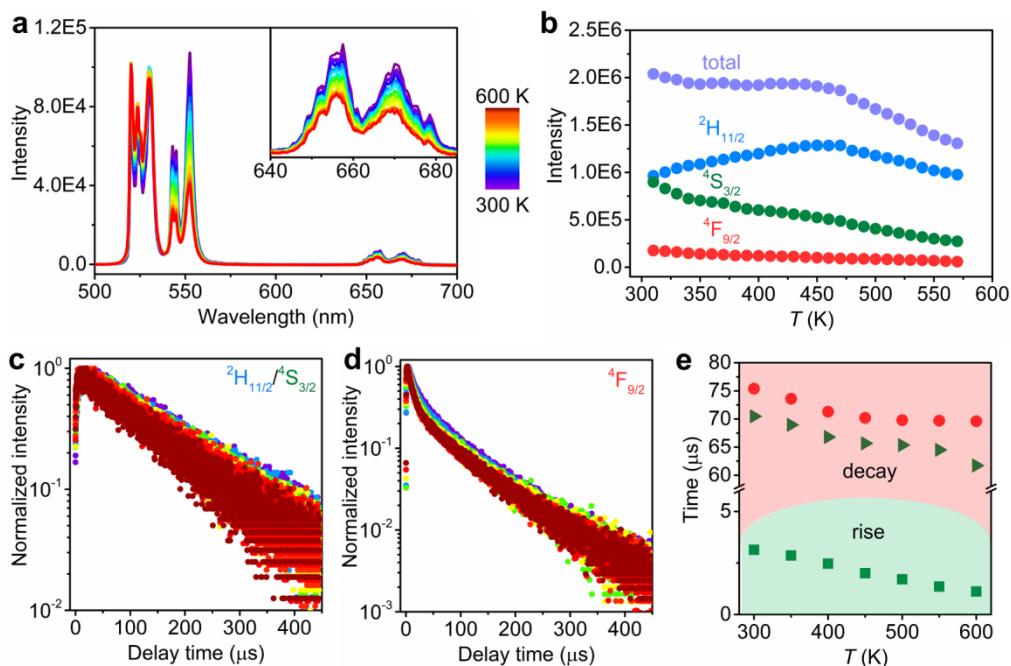
**Figure 6.2.** Thermal stability of  $\text{NaY}(\text{WO}_4)_2:49\text{Yb}1\text{Er}$  NCs. (a) Integrated intensity of emission lines ( ${}^2\text{H}_{11/2}$ ,  ${}^4\text{S}_{3/2}$ ,  ${}^4\text{F}_{9/2} \rightarrow {}^4\text{I}_{15/2}$  transitions and the sum) for three cycles of heating and cooling in air. In each cycle, the integrated emission intensities were measured at 320, 400 and 480 K (heating) and again at 400 and 320 K (cooling). (b) XRD patterns recorded at 300 K and at elevated temperature until 600 K and after cooling back to 300 K. At the bottom, the reference XRD pattern of tetragonal  $\text{NaLu}(\text{WO}_4)_2$  (pdf 27-0729) is shown. (c, d) In-situ TEM images recorded at (c) 300 and (d) 600 K. (scale bar = 10 nm)

**Thermal quenching of UC for microcrystalline materials in ambient atmosphere** It is insightful to compare the temperature dependence of the UC emission of UC NCs with that of the corresponding microcrystalline (bulk) material. If there is a thermally activated (energy transfer) process inherent to the host material, the same thermal enhancement is also expected in the bulk material. If, however, the thermal enhancement is related to surface related effects, a different thermal behavior for bulk material and NCs is expected. In addition, comparison of the luminescence decay times for bulk material and NCs makes it possible to estimate the role of surface quenching that leads to (much) shorter decay times of emission in NCs. Microcrystalline  $\text{NaY}(\text{WO}_4)_2:49\text{Yb}1\text{Er}$  was synthesized by solid state methods<sup>26</sup> and studied by temperature-dependent luminescence and decay measurements. **Fig. 6.3a** shows the emission spectra for  $\text{NaY}(\text{WO}_4)_2:49\text{Yb}1\text{Er}$  bulk material. Emission peaks are observed in the same spectral regions, green  ${}^4\text{S}_{3/2}/{}^2\text{H}_{11/2}$  emission and red  ${}^4\text{F}_{9/2}$  emission. The emission spectra show more structure (sharper lines) which can be explained by more inhomogeneous line broadening in the NCs. The relative intensity of the  ${}^4\text{F}_{9/2}$  emission is much weaker in the microcrystalline material. The higher relative intensity in NCs results from faster  ${}^4\text{S}_{3/2}$

→  ${}^4F_{9/2}$  relaxation in NCs induced by resonant ( $\sim 3000\text{ cm}^{-1}$ ) C-H vibrations of the organic ligands on the NC surface.

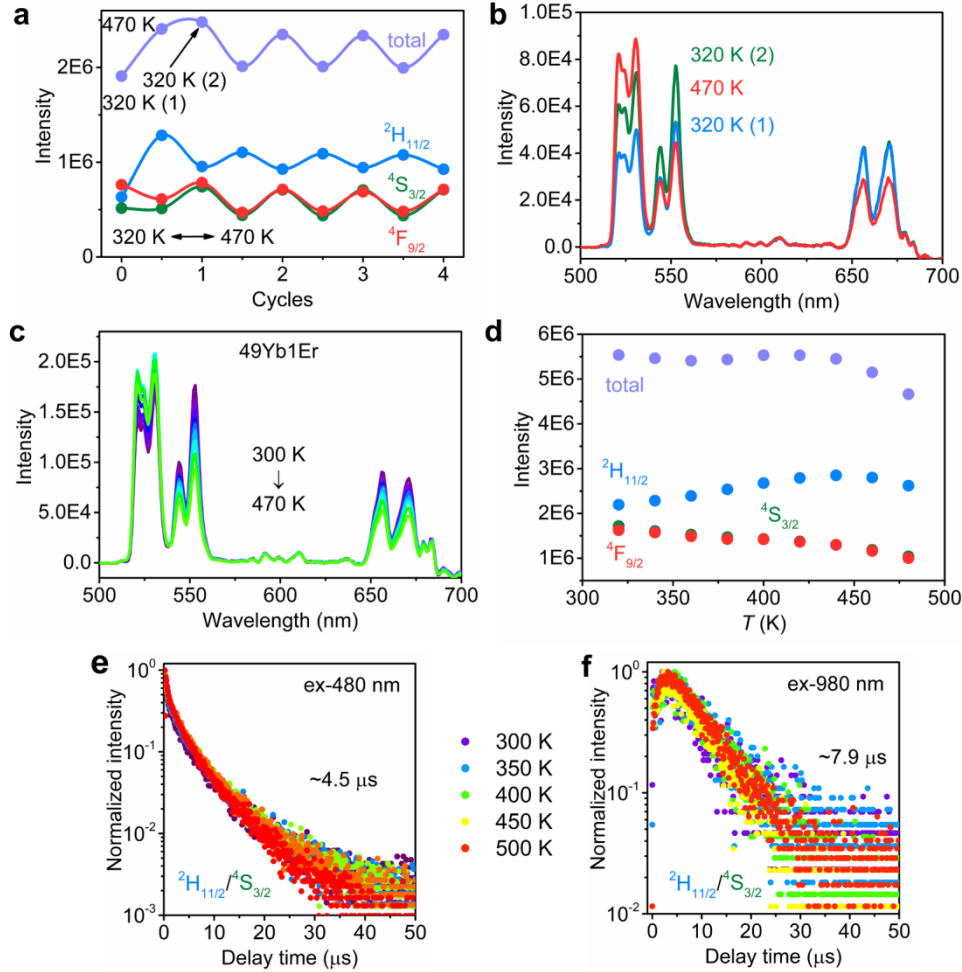
In **Fig. 6.3b**, the temperature dependence of the emission intensities of the three groups of  $\text{Er}^{3+}$  emission lines is shown for microcrystalline  $\text{NaY}(\text{WO}_4)_2:49\text{Yb1Er}$ . The behaviour is different from that in NCs and shows an almost stable total intensity up to 475 K followed by thermal quenching between 475 and 600 K. This thermal quenching is consistent with the typically observed thermal quenching of luminescence by thermally activated quenching pathways. In addition to the  $\text{NaY}(\text{WO}_4)_2:49\text{Yb1Er}$  bulk material, thermal quenching was also measured for microcrystalline  $\text{NaY}(\text{WO}_4)_2:49\text{Yb1Ho}$  and  $\text{NaY}(\text{WO}_4)_2:49\text{Yb1Tm}$  (**Fig. A6.6**). Also, here no thermal enhancement was observed and both bulk materials show weak thermal quenching of the UC emission. **Figs. 6.3c, d** show the temperature-dependent luminescence decay curves of  ${}^2\text{H}_{11/2}/{}^4\text{S}_{3/2}$  and  ${}^4F_{9/2}$  emissions under pulsed 980 nm excitation for  $\text{NaY}(\text{WO}_4)_2:49\text{Yb1Er}$  bulk material. The fitted decay times of the  ${}^2\text{H}_{11/2}/{}^4\text{S}_{3/2}$  and  ${}^4F_{9/2}$  emissions and rise times of  ${}^2\text{H}_{11/2}/{}^4\text{S}_{3/2}$  emission are plotted vs. temperature in **Fig. 6.3e**. The decay times are more than an order of magnitude longer than for  $\text{Er}^{3+}$  in NCs with the same composition. The temperature dependence is also different: the decay becomes somewhat faster with increasing temperature, consistent with the decrease in UC emission intensity with temperature. Based on the measured temperature dependence of the emission intensities and decay times of the UC emission in microcrystalline  $\text{NaY}(\text{WO}_4)_2:49\text{Yb1Er}$ , it can be concluded that thermal enhancement observed in the NCs must be related to the nanocrystalline nature of the material. In bulk material, non-radiative decay processes become somewhat faster at elevated temperatures, leading to a decrease in UC emission intensities. The thermal quenching is limited to less than 50% at 600 K.

Comparison of the decay dynamics of the UC emission for microcrystalline and nanocrystalline  $\text{NaY}(\text{WO}_4)_2:49\text{Yb1Er}$  shows that the decay times are  $\sim 60\text{-}70\ \mu\text{s}$  in microcrystalline vs.  $2\text{-}4\ \mu\text{s}$  in nanocrystalline material. The much faster decay in NCs demonstrates that there is a significant contribution of non-radiative decay that is related to surface quenching and therefore the UC efficiency is much lower in NCs. The luminescence decay curves of  ${}^2\text{H}_{11/2}/{}^4\text{S}_{3/2}$  emission were also measured under 480 nm direct excitation (**Fig. A6.7**). The decay becomes faster at elevated temperatures and the decay time decreases from  $11.4$  to  $7.1\ \mu\text{s}$  (300 to 600 K). Note that the decay times of the green  ${}^2\text{H}_{11/2}/{}^4\text{S}_{3/2}$  emission under direct excitation are shorter than that of the same emission after 980 nm excitation. This indicates that the decay of the UC emission is primarily determined by the decay of the feeding  ${}^2F_{5/2}$  level of  $\text{Yb}^{3+}$ .



**Figure 6.3.** Temperature-dependent luminescence of microcrystalline  $\text{NaY}(\text{WO}_4)_2:49\text{Yb}1\text{Er}$  in ambient atmosphere. (a) UC emission spectra under 980 nm excitation at 300-600 K. (b) Integrated intensity of emission lines ( ${}^2\text{H}_{11/2}$ ,  ${}^4\text{S}_{3/2}$ ,  ${}^4\text{F}_{9/2} \rightarrow {}^4\text{I}_{15/2}$  transitions and their sum) for the emission spectra in (a). (c, d) Luminescence decay curves of (c) green  ${}^2\text{H}_{11/2}/{}^4\text{S}_{3/2}$  emission and (d) red  ${}^4\text{F}_{9/2}$  emission under pulsed 980 nm excitation. (e) Decay times (green triangles for  ${}^2\text{H}_{11/2}/{}^4\text{S}_{3/2}$  emission and red circles for  ${}^4\text{F}_{9/2}$  emission) and rise time (green squares for  ${}^2\text{H}_{11/2}/{}^4\text{S}_{3/2}$  emission) determined from the decay curves in (c, d).

**Thermal behavior of UC in dry nitrogen** To investigate the role of surface adsorption of molecules (especially water) present in ambient atmosphere, the thermal cycling experiments were repeated in a dry nitrogen atmosphere. For the  $\text{NaY}(\text{WO}_4)_2:\text{Yb},\text{Er}$  NCs, there is a transition from thermal enhancement to thermal quenching above  $\sim 500$  K in air. As we want to understand the origin of the thermal enhancement, the thermal cycling experiments in dry nitrogen were done between 300 and 500 K. For the cycling experiments, UC emission spectra under 980 nm excitation were repeatedly recorded for  $\text{NaY}(\text{WO}_4)_2:49\text{Yb}1\text{Er}$  NCs in nitrogen at two extreme temperatures, 320 and 470 K. The integrated intensities of the respective emission lines and their sum are plotted per cycle in **Fig. 6.4a**. The first cycle of heating shows the thermal enhancement of UC emission, similar to that in ambient atmosphere. The emission spectra measured in the first cycle are shown in **Fig. 6.4b**. Upon increasing temperature from 320 to 470 K, the total emission intensity is enhanced, although the enhancement factor is smaller in nitrogen (1.3 vs. 3.0 in air) because some water is already removed during the flushing with dry nitrogen prior to the 320 K measurement. Upon cooling back to 320 K,



**Figure 6.4.** Temperature-dependent luminescence of NaY(WO<sub>4</sub>)<sub>2</sub>:49Yb1Er NCs in dry nitrogen. (a) Thermal cycling experiment showing the integrated UC intensity of Er<sup>3+</sup> emission lines (<sup>2</sup>H<sub>11/2</sub>, <sup>4</sup>S<sub>3/2</sub>, <sup>4</sup>F<sub>9/2</sub> → <sup>4</sup>I<sub>15/2</sub> transitions and their sum). (b) Emission spectra of 980 nm excitation for the first three temperature points in thermal cycling experiment. (c) Temperature-dependent emission spectra under 980 nm excitation for NCs after the first heating cycle. (d) Integrated intensity of Er<sup>3+</sup> emission lines (<sup>2</sup>H<sub>11/2</sub>, <sup>4</sup>S<sub>3/2</sub>, <sup>4</sup>F<sub>9/2</sub> → <sup>4</sup>I<sub>15/2</sub> transitions and their sum) for the emission spectra in (c). (e, f) Luminescence decay curves of green <sup>2</sup>H<sub>11/2</sub>/<sup>4</sup>S<sub>3/2</sub> emission under pulsed (e) 480 and (f) 980 nm excitations as a function of temperature after the first heating cycle.

the total UC emission intensity increases further, different from the observations in ambient atmosphere where a decrease is observed after cooling back to 320 K. The increase is similar to the increase observed in microcrystalline NaY(WO<sub>4</sub>)<sub>2</sub>:49Yb1Er for cooling from ~500 to 300 K. In subsequent cycles (320-470-320 K), the total emission intensity reproducibly decreases upon heating and increases again after cooling to 320 K. The temperature-dependent UC emission spectra during these later cycles are shown in **Fig. 6.4c** and the integrated emission intensities are plotted as a

function of temperature in **Fig. 6.4d**. The thermal coupling of  $^4S_{3/2}$  and  $^2H_{11/2}$  states is confirmed by a good fitting to integrated emission intensity ratio of  $^2H_{11/2}/^4S_{3/2}$  vs. temperature (**Fig. A6.8**). The total emission from the  $^4S_{3/2}/^2H_{11/2}$  and  $^4F_{9/2}$  levels shows some quenching above 450 K, very similar to that observed in microcrystalline material. The absence of thermal enhancement after the first heating cycle is confirmed by decay dynamics measurements. **Figs. 6.4e, f** display the luminescence decay curves of green  $^2H_{11/2}/^4S_{3/2}$  emission under direct 480 nm and indirect 980 nm excitations. The respective decay times are constant at around 4.5 (480 nm excitation) and 7.9  $\mu$ s (980 nm excitation). This is in contrast to the lengthening of decay times measured upon heating in ambient atmosphere followed by shortening upon cooling. The decay time of the green emission for  $\text{NaY}(\text{WO}_4)_2:49\text{Yb1Er}$  NCs in nitrogen is also 2-3 times longer than in air, indicating that the ambient atmosphere is responsible for a quenching process that is suppressed/removed by heating. Besides the  $\text{Er}^{3+}$  UC emission, we also measured the luminescence decay dynamics of  $\text{Yb}^{3+}$  980 nm emission in single  $\text{Yb}^{3+}$ -doped  $\text{NaY}(\text{WO}_4)_2:49\text{Yb}$  NCs in ambient atmosphere and dry nitrogen (**Fig. A6.9**). The ambient atmosphere leads to lengthening of  $\text{Yb}^{3+}$  decay time from 9.1 to 22.4  $\mu$ s when temperature increases from 300 to 500 K. In contrast, in dry nitrogen, the decay time of  $\text{Yb}^{3+}$  emission decreases from 31.5 to 24.3  $\mu$ s. The results are in agreement with the temperature dependence of  $\text{Er}^{3+}$  decay time in the two atmospheres. However, in ambient atmosphere, upon increasing the temperature from 300 to 500 K, the decay time of  $\text{Yb}^{3+}$  980 nm emission is lengthened by 2.5-fold (vs.  $\sim 1.5$ -fold for decay time of  $\text{Er}^{3+}$  green emission in **Fig. A6.4**). It indicates that water quenching has a bigger influence for  $\text{Yb}^{3+}$  emission due to the high concentration of  $\text{Yb}^{3+}$ .

To investigate if the thermal enhancement of the UC emission observed in air for the Yb,Ho and Yb,Tm co-doped  $\text{NaY}(\text{WO}_4)_2$  NCs shows the same change when transferred from air to dry nitrogen, the cycling experiments were repeated for these NCs in nitrogen. The temperature dependence of the total UC emission intensity for  $\text{NaY}(\text{WO}_4)_2:49\text{Yb1Ho}$  NCs is shown in **Fig. A6.10** and **Fig. A6.11** for  $\text{NaY}(\text{WO}_4)_2:49\text{Yb1Tm}$  NCs. The same effect is observed as for the Er,Yb co-doped NCs: during the first heating stage, the UC emission intensity increases. Different from the results in air, upon cooling, a further increase of the UC emission intensity is observed. In subsequent cycles, the UC emission shows some reversible thermal quenching upon heating from 320 to 470 K. For completeness, also the thermal quenching was studied for microcrystalline  $\text{NaY}(\text{WO}_4)_2:49\text{Yb1Er}$  (**Fig. A6.12**). The temperature-dependent total UC emission intensity in nitrogen is similar as in air (**Fig. 6.3b**) with a nearly constant total intensity between 300 and 475 K.

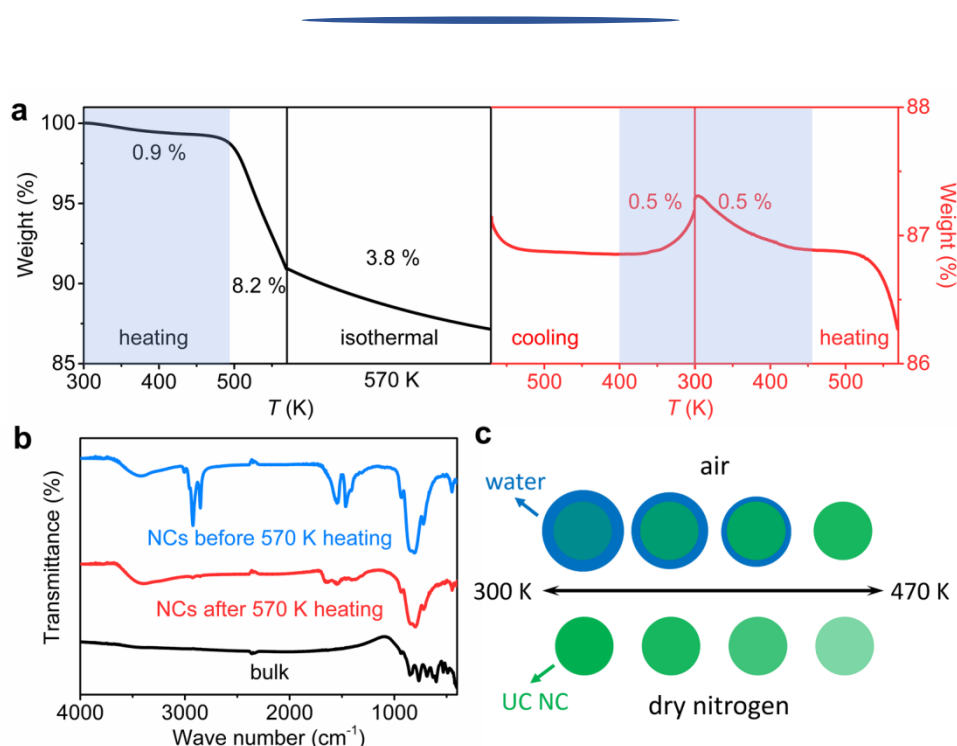
**Mechanism of thermal enhancement in ambient atmosphere for UC NCs** The thermal cycling experiments for the UC emission intensity of  $\text{NaY}(\text{WO}_4)_2:\text{Yb,Er}$  NCs and microcrystalline material in ambient atmosphere and in dry nitrogen show that strong thermal enhancement is only observed in ambient atmosphere. The same is true for other UC couples (Yb/Ho, Yb/Tm). This suggests that the

role of the atmosphere is general. The ambient atmosphere and nitrogen are different in several ingredients: ambient atmosphere contains oxygen, water and carbon dioxide in addition to nitrogen. O<sub>2</sub> and CO<sub>2</sub> are not expected to affect the luminescence of the oxide NCs. However, water is known to effectively quench UC emission through multi-phonon relaxation. Especially, the intermediate level <sup>4</sup>I<sub>11/2</sub> of Er<sup>3+</sup> is susceptible to quenching as the <sup>4</sup>I<sub>11/2</sub>-<sup>4</sup>I<sub>13/2</sub> energy spacing is resonant with the high-energy (3200-3500 cm<sup>-1</sup>) O-H stretching vibrations.<sup>27-30</sup> The large surface area of NCs allows for surface adsorption of water molecules which will be in close proximity to Er<sup>3+</sup>/Yb<sup>3+</sup> ions in the surface layer. In the highly Yb-doped NCs, energy migration over the <sup>2</sup>F<sub>5/2</sub> level of Yb<sup>3+</sup> and the resonant <sup>4</sup>I<sub>11/2</sub> level of Er<sup>3+</sup> allows for rapid feeding of surface Er<sup>3+</sup>/Yb<sup>3+</sup> ions that will be quenched by high-energy O-H vibrations (in addition to other surface quenching processes). Thus, surface adsorbed water molecules can be expected to effectively quench the UC emission in ambient atmosphere. Removal of surface adsorbed water by heating will reduce surface quenching by O-H vibrations and give rise to strongly thermally enhanced UC. At ~470 K, all water will be removed and further heating results in some thermal quenching, similar to what is observed for bulk material. Upon cooling in air, water will be readsorbed and the UC emission intensity will decrease again. In a dry nitrogen flow, no readsorption of water is possible and the O-H surface quenching will not play a role anymore. After the removal of surface water in the first heating cycle, a similar thermal behaviour of the UC emission is expected in NCs as observed in microcrystalline material.

To provide more evidence for the role of surface water in the mechanism proposed for the observed thermal UC enhancement, TGA and FT-IR measurements were carried out. **Fig. 6.5a** shows two cycles of TGA measurement. The first cycle of heating reveals two stages of mass decrease. The first stage in the temperature range of 300-480 K manifests a mass loss of 0.9%. This is attributed to the loss of adsorbed water. Above 500 K, there is a prominent mass loss of 8.2% due to the removal of oleate ligands. Subsequently, during isothermal heating at 570 K, a further loss of mass is observed for 3.8% that is explained by a further loss of oleate ligands. Importantly, during the cooling stage, a mass gain of 0.5% is observed below ~370 K, suggesting water readsorption. This amount of water is lost again in the second cycle of heating from 300 to 500 K. The TGA results are consistent with the presence of desorption and adsorption of water during heating and cooling.

To obtain further evidence for the presence of surface adsorbed water and the removal of the oleate ligands upon heating to 570 K, FT-IR analysis was done for NaY(WO<sub>4</sub>)<sub>2</sub> bulk materials and NaY(WO<sub>4</sub>)<sub>2</sub> UC NCs before and after heating to 570 K, and is shown in **Fig. 6.5b**. For the NCs before heating, the oleate ligands are coupled to NC surface and evidence for their presence can be obtained from IR absorption peaks at around 2900 and 1700 cm<sup>-1</sup> attributed to C-H and C=O vibrations. In addition to these characteristic peaks of the oleate ligands, there is also a broad band at around 3400 cm<sup>-1</sup>, characteristic of the O-H stretching vibration of water molecule.<sup>31</sup> After heating to

570 K, the FT-IR peaks corresponding to the oleate ligands disappear, consistent with the TGA analysis. However, for the NCs, the broad band between 3200 and 3700  $\text{cm}^{-1}$ , characteristic of surface adsorbed water, can still be observed, which indicates that water molecules are again adsorbed at the NC surface. This further supports our model for thermal enhancement of the UC emission in NCs. The FT-IR spectrum for bulk material shows no IR-absorption in the 1200-4000  $\text{cm}^{-1}$  region. The IR absorption lines between 500 and 1000  $\text{cm}^{-1}$  are assigned to host vibrations (related to the tungstate group) and are observed for both microcrystalline and nanocrystalline  $\text{NaY}(\text{WO}_4)_2$ . The small surface-to-volume ratio in bulk material limits surface adsorption of water and thus no significant quenching. This explains why the thermal enhancement is not observed for bulk materials,<sup>32,33</sup> but is observed exclusively in air and not in dry nitrogen for NCs.



**Figure 6.5.** Exploring the mechanism of thermal UC enhancement for  $\text{NaY}(\text{WO}_4)_2$  UC NCs. (a) Thermogravimetric analysis of NCs in four stages: heating from 300 to 570 K at the rate of 5 K/min of a fresh NC sample; isothermal measurement at 570 K for 10 min; cooling from 570 to 300 K at the rate of 20 K/min, and heating up again. The blue areas represent the adsorption or desorption of water on the NC surface. (b) FT-IR measurements for bulk material (black line) and NCs before (blue line) and after (red line) heating to 570 K. (c) Illustration of UC NC and water on surface: in air, the NC surface desorbs water upon heating, giving rise to thermal enhancement of UC emission through reduced water quenching. Upon cooling, water is reabsorbed. Without the presence of surface water (in dry nitrogen, lower picture), the NCs show thermal quenching of UC emission similar to microcrystalline material.

Based on the experiments and analysis presented above, the role of surface adsorbed water is schematically illustrated in **Fig. 6.5c**. The UC emission intensity is enhanced as water molecules are desorbed from the NC surface. For the water-free NCs, the same thermal quenching is expected as for microcrystalline material. Both the thermal enhancement and thermal quenching are reversible. Note that the variation in absolute UC intensity has no influence on the intensity ratio of the  ${}^2\text{H}_{11/2}$  and  ${}^4\text{S}_{3/2}$  emissions with temperature. In both air and nitrogen, the  ${}^2\text{H}_{11/2}/{}^4\text{S}_{3/2}$  emission intensity ratio increases from 1.2 to 2.5 from 320 to 470 K (**Fig. A6.13**) since water quenches both  ${}^2\text{H}_{11/2}$  and  ${}^4\text{S}_{3/2}$  emissions, as expected for thermally coupled energy levels. Therefore, the thermometry based on ratiometric technique remains reliable and the  $\text{NaY}(\text{WO}_4)_2\text{:YbEr}$  NCs can serve as nanothermometry in high temperature range. Also, tungstates based nanothermometry has been demonstrated for a high thermal sensitivity.<sup>8,34,35</sup>

We propose that our model is universal and can explain previous observations in literature. Earlier explanations of thermal enhancement of UC emission in NCs involved phonon confinement and higher-energy Yb-O vibrations. Phonon confinement<sup>21,36,37</sup> cannot explain the thermal enhancement as phonon confinement in NCs only occurs for long wavelength and low-energy ( $< 20 \text{ cm}^{-1}$ ) acoustic phonons. These phonons do not play a role in (multi-)phonon quenching processes of luminescence of lanthanide ions where the highest energy phonons are involved. In **Ref. 22**, the Yb-O bond was proposed to enable thermal UC enhancement.<sup>22</sup> It was not clear how the slightly higher Yb-O vs. Yb-F vibrational energy could explain the strong thermal enhancement. The Yb-O bond is embedded in the present crystalline host of  $\text{NaY}(\text{WO}_4)_2$ . The observation that thermal enhancement is not observed in bulk material or NCs in dry nitrogen shows that, at least for  $\text{NaY}(\text{WO}_4)_2$ , the thermal enhancement is not related to Yb-O bonds. Based on the same reasoning, we can rule out a role of thermally enhanced NIR absorption by  $\text{Yb}^{3+}$ ,  $\text{WO}_4^{2-}$  group induced charge transfer band or new level<sup>38</sup>, and phonon assisted energy transfer.<sup>8,21,34</sup> All these mechanisms would be active in both bulk materials and NCs, and they should present identical thermal enhancement. In fact, the thermal enhancement is only observable for NCs in air, but is absent for NCs in the absence of water and for bulk materials. One may argue that during heat treatment the (surface) defect concentrations can be reduced, resulting in the enhanced emission.<sup>13,39,40</sup> However, since the healing of defect is irreversible, this model is inconsistent with the good reversibility of the thermal enhancement observed for thermal cycling experiment in ambient atmosphere.

Here, we have provided strong evidence for the role of surface adsorbed water to explain the observation of thermal enhancement of UC emission in NCs. Note that until now thermal enhancement in NC system is merely observed for UC emission. For comparison,  $\text{Eu}^{3+}$  emission was examined by measuring temperature-dependent emission spectra of the characteristic orange/red  $\text{Eu}^{3+}$  emission upon 395 nm excitation for  $\text{NaY}(\text{WO}_4)_2\text{:10Eu}$  NCs of the same size of  $\sim 10 \text{ nm}$  (**Fig.**

**A6.14).** The emission lines are due to the transitions from excited state  $^5D_0$  to multiple states  $^7F_{1,2,4}$  at 590, 615 and 695 nm. The thermal quenching for each emission line is obvious in both air and nitrogen, consistent with our previous results.<sup>23</sup> Water quenching has limited influence on the emission of  $Eu^{3+}$  ion. The large energy gap ( $\sim 12000\text{ cm}^{-1}$ ) between  $^5D_0$  and next lower-energy level  $^7F_6$  requires four O-H vibrational modes. This will not be effective through coupling with surface adsorbed water and hence the removal of water from the NC surface will not induce the enhancement of this ‘normal’ (downshifted) emission.

## 6.4 Conclusions

In present study, the mechanism behind the surprising thermal enhancement of UC emission in  $NaY(WO_4)_2$  UC NCs is reported. Temperature-dependent measurements of (UC) emission spectra and emission intensities as well as luminescence decay dynamics were carried out in two types of atmosphere: air and dry nitrogen. Thermal enhancement of UC emission between 300 and 475 K is observed with good reversibility in ambient atmosphere. In dry nitrogen, only in the first heating cycle, strong thermal enhancement of the UC emission is observed. Upon cooling, the UC emission intensity does not drop, but increases even further, and subsequent cycles show some thermal quenching similar to that in bulk material. As temperature increases, the decay times of  $Er^{3+}$  UC emission and  $Yb^{3+}$  IR emission become longer in air, but do not in nitrogen. Based on these observations, the thermal enhancement of UC emission is explained by reversible desorption (upon heating) and adsorption (after cooling) of water at the NC surface. Surface adsorbed water molecules effectively quench UC emission through the high-energy O-H vibrations. TGA and FT-IR measurements provide evidence for water adsorption in support of our model. The present study highlights the significance of surface adsorbed (water) molecules on the quenching of UC emission in NCs and can also explain earlier observations of strong thermal enhancement of UC emission in NC system. Insight into the role of surface adsorbed molecules will benefit the design of UC NCs with higher quantum efficiencies. Our strategy of using cycling experiments on the absolute luminescence intensity is universal to examine the intrinsic thermal behaviour of luminescence that is fundamental in luminescent materials and determines the performance of nanothermometry.

## 6.5 Methods

**Chemicals** The synthesis was conducted with commercially available reagents. Absolute ethanol (Analytical Reagent, A.R.), cyclohexane (A.R.), oleic acid (90%), oleylamine (80-90%), 1-octadecene (90%), RE (III) acetate (RE = Y, Eu, Ho, Er, Tm and Yb, 99.9%), hexacarbonyl tungsten (97%), sodium hydroxide (A.R.), tungsten oxide (A.R.), sodium bicarbonate (A.R.) and RE oxide (RE = Y, Ho, Er, Tm and Yb, 99.99%) were purchased from Sigma and Aldrich without further purification.

**Synthesis of tungstate NCs** In a three-necked flask, oleic acid (10 mL), oleylamine (10 mL) and 1-octadecene (20 mL) were mixed with RE (III) acetate (1 mmol), hexacarbonyl tungsten (2 mmol) and sodium hydroxide (1.5 mmol) with stirring and heating at 390 K for 0.5 h. The reaction was heated to 570 K for 2 h while refluxing under a protective nitrogen atmosphere. Once cooled to room temperature, the product was precipitated and washed with ethanol and cyclohexane for three times via centrifugation, then dried at 370 K overnight for the measurements.

**Synthesis of tungstate bulk materials** Microcrystalline samples with composition  $\text{NaY}(\text{WO}_4)_2:49\text{Yb1RE}$  (RE = Ho, Er and Tm) were prepared by solid state reaction.<sup>26</sup> The stoichiometric raw materials of  $\text{WO}_3$ ,  $\text{NaHCO}_3$  and  $\text{RE}_2\text{O}_3$  were ground in agate mortar and then transferred to alumina crucible. Subsequently, the mixture was first sintered at 773 K for 4 h and then at 1273 K for 4 h in oven with ambient atmosphere.

**Characterizations** The photoluminescence spectra were recorded by an Edinburgh Instruments FLS920 spectrometer. For UC emission spectra, the excitation source and the detector were a 980 nm continuous wave laser ( $\sim 1 \text{ W/cm}^2$ ) and a Hamamatsu R928 photomultiplier tube (PMT). The  $\text{Eu}^{3+}$  emission spectra were excited by the equipped 450 W xenon lamp. The luminescence decay dynamics of  $\text{Er}^{3+}$  UC emission was measured with an Ekspla NT342B-10-SH/DUV OPO system for pulsed excitation (pulse width 5 ns and repetition rate 10 Hz) and a Hamamatsu H7422-02 PMT as photon detector with a Triax 550 monochromator coupled to a PicoQuant TimeHarp 260 photo-counting module at a discriminator level of -100 mV. The decay dynamics of  $\text{Yb}^{3+}$  IR emission was measured by using a liquid-nitrogen cooled Hamamatsu R5507-73 PMT and multi-channel scaling (MCS) option integrated in the spectrofluorometer. The pulsed excitation source was an optical parametric oscillator (OPO) system (410-2200 nm, Oportek Opolette HE 355 II) pumped by the third harmonic of a YAG:Nd<sup>3+</sup> laser ( $\sim 1 \text{ mJ}$  pulses with a 10 ns pulse duration and repetition rate 20 Hz). To control the temperature, a Linkam THMS600 Microscope Stage was used for the temperature range of 300-600 K. The spectrum was collected at an interval of at least 10 minutes to guarantee the temperature stability for sample. The thermocouple allows for monitoring and compensation of IR laser heating effects.

For the TEM measurements, NCs dropcasted on amorphous carbon-coated copper grids were imaged using an FEI Talos F200X TEM microscope operating at 200 kV. For the in-situ heating measurements, NCs were dropcasted on heating chips with SiN membranes, which were mounted on a DENSsolutions MEMS-based heating holder. For the ex-situ measurements, NCs were dropcasted on SiO-coated TEM grids and the prepared grids were sintered in oven at 600 K for 10 min. In-situ XRD measurements were performed on a Bruker5 AXS D8 X-ray diffractometer in combination with an Anton Paar XRK 900 reactor chamber for Co  $K\alpha$  radiation with a wavelength of 1.79 Å and a VANTEC 1D position sensitive detector. FT-IR spectra were measured in a Vertex 70 (Bruker)

spectrometer equipped with KBr/DLaTGS D301 detector using KBr pellet technique. The thermogravimetric analysis was performed on a Perkin Elmer TGA8000 with a temperature ramp from 300 to 570 K at 5 K/min in an atmosphere of 20% oxygen in argon.

## 6.6 References

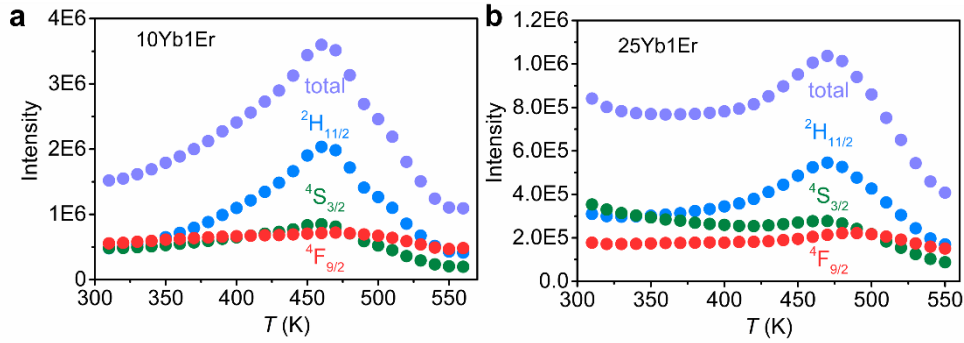
1. Wang, X. D.; Wolfbeis, O. S.; Meier, R. J. Luminescent Probes and Sensors for Temperature. *Chem. Soc. Rev.* **2013**, *42*, 7834-7869.
2. Jaque, D.; Vetrone, F. Luminescence Nanothermometry. *Nanoscale* **2012**, *4*, 4301-4326.
3. Brites, C. D. S.; Lima, P. P.; Silva, N. J. O.; Millan, A.; Amaral, V. S.; Palacio, F.; Carlos, L. D. Thermometry at the Nanoscale. *Nanoscale* **2012**, *4*, 4799-4829.
4. McLaurin, E. J.; Bradshaw, L. R.; Gamelin, D. R. Dual-Emitting Nanoscale Temperature Sensors. *Chem. Mater.* **2013**, *25*, 1283-1292.
5. Vetrone, F.; Naccache, R.; Zamarron, A.; de la Fuente, A. J.; Sanz-Rodriguez, F.; Maestro, L. M.; Rodriguez, E. M.; Jaque, D.; Sole, J. G.; Capobianco, J. A. Temperature Sensing Using Fluorescent Nanothermometers. *ACS Nano* **2010**, *4*, 3254-3258.
6. Brites, C. D. S.; Xie, X. J.; Debasu, M. L.; Qin, X.; Chen, R. F.; Huang, W.; Rocha, J.; Liu, X. G.; Carlos, L. D. Instantaneous Ballistic Velocity of Suspended Brownian Nanocrystals Measured by Upconversion Nanothermometry. *Nat. Nanotech.* **2016**, *11*, 851-856.
7. Brites, C. D. S.; Fuertes, M. C.; Angelome, P. C.; Martinez, E. D.; Lima, P. P.; Soler-Illia, G. J. A. A.; Carlos, L. D. Tethering Luminescent Thermometry and Plasmonics: Light Manipulation to Assess Real-Time Thermal Flow in Nanoarchitectures. *Nano Lett.* **2017**, *17*, 4746-4752.
8. Cascales, C.; Paino, C. L.; Bazan, E.; Zaldo, C. Ultrasmall, Water Dispersible, TWEEN80 Modified Yb:Er:NaGd(WO<sub>4</sub>)<sub>2</sub> Nanoparticles with Record Upconversion Ratiometric Thermal Sensitivity and Their Internalization by Mesenchymal Stem Cells. *Nanotechnology* **2017**, *28*, 185101.
9. Geitenbeek, R. G.; Prins, P. T.; Albrecht, W.; van Blaaderen, A.; Weckhuysen, B. M.; Meijerink, A. NaYF<sub>4</sub>:Er<sup>3+</sup>, Yb<sup>3+</sup>/SiO<sub>2</sub> Core/Shell Upconverting Nanocrystals for Luminescence Thermometry up to 900 K. *J. Phys. Chem. C* **2017**, *121*, 3503-3510.
10. Vlaskin, V. A.; Janssen, N.; van Rijssel, J.; Beaulac, R.; Gamelin, D. R. Tunable Dual Emission in Doped Semiconductor Nanocrystals. *Nano Lett.* **2010**, *10*, 3670-3674.
11. Wang, S. P.; Westcott, S.; Chen, W. Nanoparticle Luminescence Thermometry. *J. Phys. Chem. B* **2002**, *106*, 11203-11209.
12. Lee, J.; Govorov, A. O.; Kotov, N. A. Nanoparticle Assemblies with Molecular Springs: A Nanoscale Thermometer. *Angew. Chem. Int. Ed.* **2005**, *44*, 7439-7442.

13. Wu, W. T.; Shen, J.; Banerjee, P.; Zhou, S. Q. Core-Shell Hybrid Nanogels for Integration of Optical Temperature-Sensing, Targeted Tumor Cell Imaging, and Combined Chemo-Photothermal Treatment. *Biomaterials* **2010**, *31*, 7555-7566.
14. Liang, R. Z.; Tian, R.; Shi, W. Y.; Liu, Z. H.; Yan, D. P.; Wei, M.; Evans, D. G.; Duan, X. A Temperature Sensor Based on CdTe Quantum Dots-Layered Double Hydroxide Ultrathin Films Via Layer-by-Layer Assembly. *Chem. Commun.* **2013**, *49*, 969-971.
15. Pust, P.; Weiler, V.; Hecht, C.; Tucks, A.; Wochnik, A. S.; Henss, A. K.; Wiechert, D.; Scheu, C.; Schmidt, P. J.; Schnick, W. Narrow-Band Red-Emitting Sr[LiAl<sub>3</sub>N<sub>4</sub>]:Eu<sup>2+</sup> as a Next-Generation Led-Phosphor Material. *Nat. Mater.* **2014**, *13*, 891-896.
16. Lin, C. C.; Meijerink, A.; Liu, R. S. Critical Red Components for Next-Generation White LEDs. *J. Phys. Chem. Lett.* **2016**, *7*, 495-503.
17. Ogieglo, J. M.; Katelnikovas, A.; Zych, A.; Justel, T.; Meijerink, A.; Ronda, C. R. Luminescence and Luminescence Quenching in Gd<sub>3</sub>(Ga,Al)<sub>5</sub>O<sub>12</sub> Scintillators Doped with Ce<sup>3+</sup>. *J. Phys. Chem. A* **2013**, *117*, 2479-2484.
18. Chambers, M. D.; Rousseve, P. A.; Clarke, D. R. Decay Pathway and High-Temperature Luminescence of Eu<sup>3+</sup> in Ca<sub>2</sub>Gd<sub>8</sub>Si<sub>6</sub>O<sub>26</sub>. *J. Lumin.* **2009**, *129*, 263-269.
19. Chang, Y. C.; Liang, C. H.; Yan, S. A.; Chang, Y. S. Synthesis and Photoluminescence Characteristics of High Color Purity and Brightness Li<sub>3</sub>Ba<sub>2</sub>Gd<sub>3</sub>(MoO<sub>4</sub>)<sub>8</sub>:Eu<sup>3+</sup> Red Phosphors. *J. Phys. Chem. C* **2010**, *114*, 3645-3652.
20. Tian, Y.; Chen, B. J.; Hua, R. N.; Yu, N. S.; Liu, B. Q.; Sun, J. S.; Cheng, L. H.; Zhong, H. Y.; Li, X. P.; Zhang, J. S.; Tian, B. N.; Zhong, H. Self-Assembled 3D Flower-Shaped NaY(WO<sub>4</sub>)<sub>2</sub>:Eu<sup>3+</sup> Microarchitectures: Microwave-Assisted Hydrothermal Synthesis, Growth Mechanism and Luminescent Properties. *CrystEngComm* **2012**, *14*, 1760-1769.
21. Li, D. D.; Shao, Q. Y.; Dong, Y.; Jiang, J. Q. Anomalous Temperature-Dependent Upconversion Luminescence of Small-Sized NaYF<sub>4</sub>:Yb<sup>3+</sup>,Er<sup>3+</sup> Nanoparticles. *J. Phys. Chem. C* **2014**, *118*, 22807-22813.
22. Zhou, J. J.; Wen, S. H.; Liao, J. Y.; Clarke, C.; Tawfik, S. A.; Ren, W.; Mi, C.; Wang, F.; Jin, D. Y. Activation of the Surface Dark-Layer to Enhance Upconversion in a Thermal Field. *Nat. Photonics* **2018**, *12*, 154-158.
23. Wang, Z. J.; Zhang, Y. L.; Zhong, J. P.; Yao, H. H.; Wang, J.; Wu, M. M.; Meijerink, A. One-Step Synthesis and Luminescence Properties of Tetragonal Double Tungstates Nanocrystals. *Nanoscale* **2016**, *8*, 15486-15489.
24. Wang, Y. F.; Xu, W.; Zhu, Y. S.; Xu, S.; Cui, H. N.; Song, H. W. Phonon-Modulated Upconversion Luminescence Properties in Some Er<sup>3+</sup> and Yb<sup>3+</sup> Co-Activated Oxides. *J. Mater. Chem. C* **2014**, *2*, 4642-4650.
25. Yu, W. G.; Tian, Y.; Xing, M. M.; Fu, Y.; Zhang, H.; Luo, X. X. Up-Conversion Luminescence of NaY(WO<sub>4</sub>)<sub>2</sub>: Yb,Er under 1550 and 980 nm Excitation. *Mater. Res. Bull.* **2016**, *80*, 223-229.

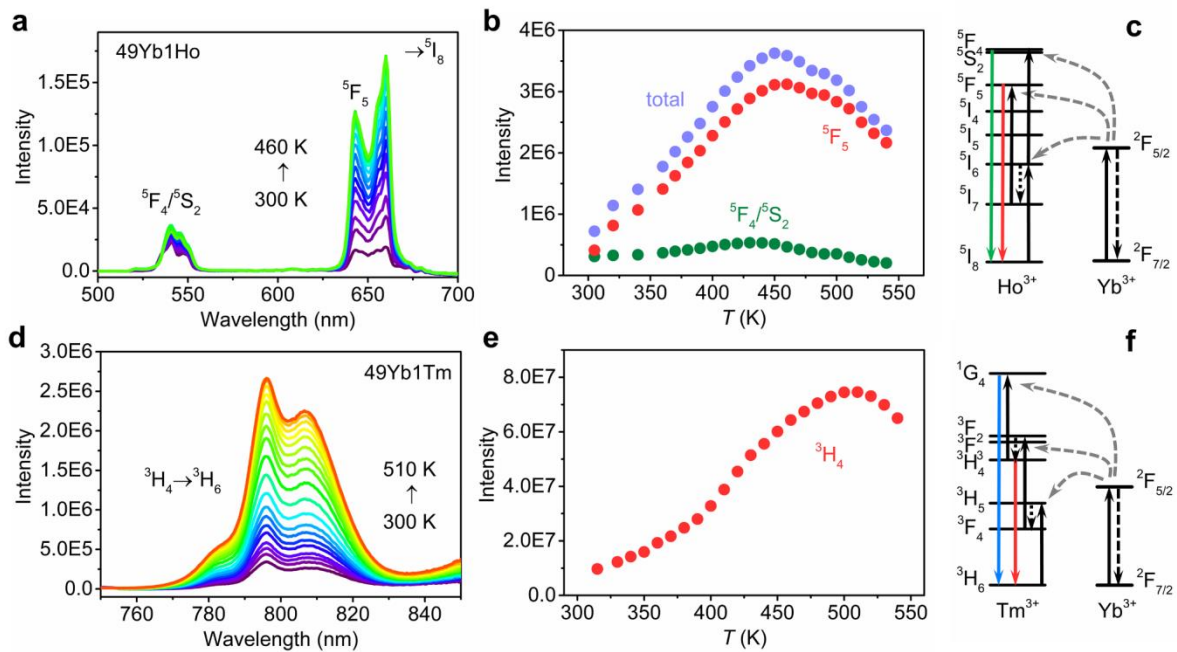
26. Wang, Z. J.; Zhong, J. P.; Liang, H. B.; Wang, J. Luminescence Properties of Lutetium Based Red-Emitting Phosphor  $\text{NaLu}(\text{WO}_4)_2:\text{Eu}^{3+}$ . *Opt. Mater. Express* **2013**, *3*, 418-425.
27. Rabouw, F. T.; Prins, P. T.; Villanueva-Delgado, P.; Castelijns, M.; Geitenbeek, R. G.; Meijerink, A. Quenching Pathways in  $\text{NaYF}_4:\text{Er}^{3+}, \text{Yb}^{3+}$  Upconversion Nanocrystals. *ACS Nano* **2018**, *12*, 4812-4823.
28. Wang, F.; Wang, J. A.; Liu, X. G. Direct Evidence of a Surface Quenching Effect on Size-Dependent Luminescence of Upconversion Nanoparticles. *Angew. Chem. Int. Ed.* **2010**, *49*, 7456-7460.
29. Boyer, J. C.; Manseau, M. P.; Murray, J. I.; van Veggel, F. C. J. M. Surface Modification of Upconverting  $\text{NaYF}_4$  Nanoparticles with PEG-Phosphate Ligands for NIR (800 nm) Biolabeling within the Biological Window. *Langmuir* **2010**, *26*, 1157-1164.
30. Arppe, R.; Hyppanen, I.; Perala, N.; Peltomaa, R.; Kaiser, M.; Wurth, C.; Christ, S.; Resch-Genger, U.; Schaferling, M.; Soukka, T. Quenching of the Upconversion Luminescence of  $\text{NaYF}_4:\text{Yb}^{3+}, \text{Er}^{3+}$  and  $\text{NaYF}_4:\text{Yb}^{3+}, \text{Tm}^{3+}$  Nanophosphors by Water: The Role of the Sensitizer  $\text{Yb}^{3+}$  in Non-Radiative Relaxation. *Nanoscale* **2015**, *7*, 11746-11757.
31. Scatena, L. F.; Brown, M. G.; Richmond, G. L. Water at Hydrophobic Surfaces: Weak Hydrogen Bonding and Strong Orientation Effects. *Science* **2001**, *292*, 908-912.
32. Qiao, J. W.; Ning, L. X.; Molokeyev, M. S.; Chuang, Y. C.; Liu, Q. L.; Xia, Z. G.  $\text{Eu}^{2+}$  Site Preferences in the Mixed Cation  $\text{K}_2\text{BaCa}(\text{PO}_4)_2$  and Thermally Stable Luminescence. *J. Am. Chem. Soc.* **2018**, *140*, 9730-9736.
33. Kim, Y. H.; Arunkumar, P.; Kim, B. Y.; Unithrattil, S.; Kim, E.; Moon, S. H.; Hyun, J. Y.; Kim, K. H.; Lee, D.; Lee, J. S.; Im, W. B. A Zero-Thermal-Quenching Phosphor. *Nat. Mater.* **2017**, *16*, 543-550.
34. Xu, W.; Song, Q. T.; Zheng, L. J.; Zhang, Z. G.; Cao, W. W. Optical Temperature Sensing Based on the Near-Infrared Emissions from  $\text{Nd}^{3+}/\text{Yb}^{3+}$  Codoped  $\text{CaWO}_4$ . *Opt. Lett.* **2014**, *39*, 4635-4638.
35. Gao, Y.; Huang, F.; Lin, H.; Zhou, J. C.; Xu, J.; Wang, Y. S. A Novel Optical Thermometry Strategy Based on Diverse Thermal Response from Two Intervalence Charge Transfer States. *Adv. Funct. Mater.* **2016**, *26*, 3139-3145.
36. Liu, G. K.; Zhuang, H. Z.; Chen, X. Y. Restricted Phonon Relaxation and Anomalous Thermalization of Rare Earth Ions in Nanocrystals. *Nano Lett.* **2002**, *2*, 535-539.
37. Shan, J. N.; Uddi, M.; Yao, N.; Ju, Y. G. Anomalous Raman Scattering of Colloidal  $\text{Yb}^{3+}, \text{Er}^{3+}$  Codoped  $\text{NaYF}_4$  Nanophosphors and Dynamic Probing of the Upconversion Luminescence. *Adv. Funct. Mater.* **2010**, *20*, 3530-3537.
38. Dong, B.; Cao, B. S.; He, Y. Y.; Liu, Z.; Li, Z. P.; Feng, Z. Q. Temperature Sensing and in Vivo Imaging by Molybdenum Sensitized Visible Upconversion Luminescence of Rare-Earth Oxides. *Adv. Mater.* **2012**, *24*, 1987-1993.

39. Dhanaraj, J.; Jagannathan, R.; Kutty, T. R. N.; Lu, C. H. Photoluminescence Characteristics of  $\text{Y}_2\text{O}_3:\text{Eu}^{3+}$  Nanophosphors Prepared Using Sol-Gel Thermolysis. *J. Phys. Chem. B* **2001**, *105*, 11098-11105.
40. Zhang, K.; Ma, C. G.; Zhang, J. Y.; Liu, B. M.; Zhou, Y.; Guo, S. Q.; Xu, J. Y.; Hou, J. S.; Fang, Y. Z.; Zheng, L. R.; Sun, H. T. Giant Enhancement of Luminescence from Phosphors through Oxygen-Vacancy-Mediated Chemical Pressure Relaxation. *Adv. Opt. Mater.* **2017**, *5* 1700448.

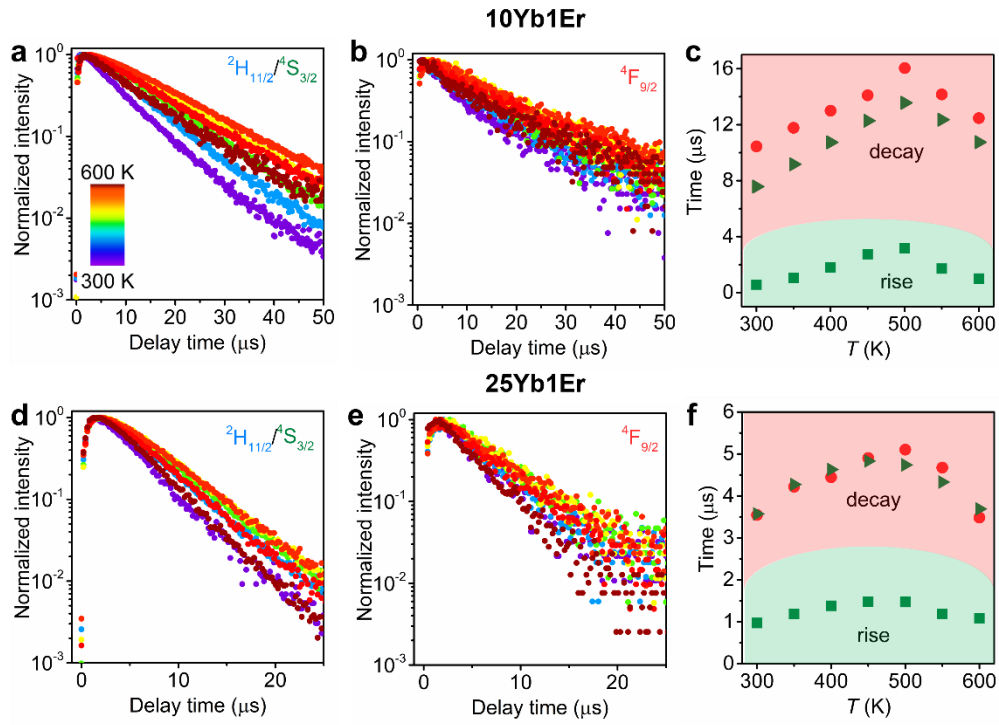
## 6.7 Appendices



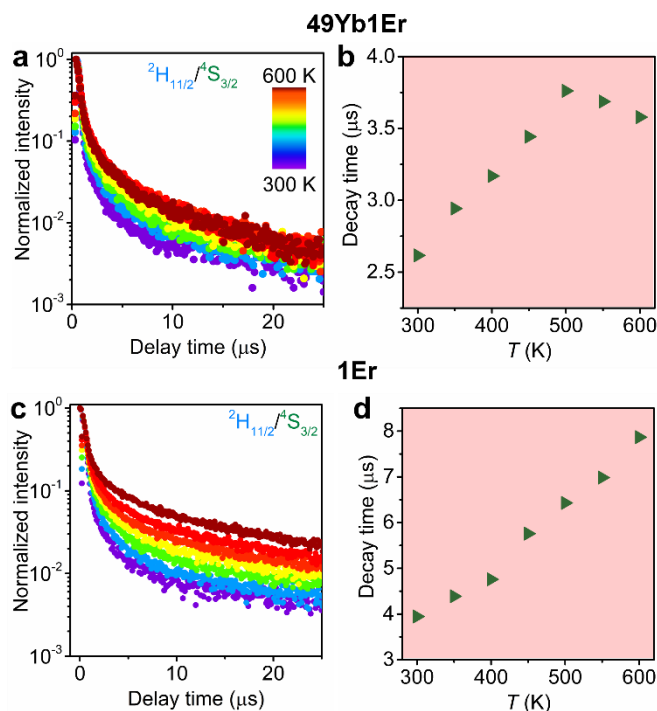
**Figure A6.1.** Temperature-dependent integrated intensity of  $\text{Er}^{3+}$  emission lines ( ${}^2\text{H}_{11/2}$ ,  ${}^4\text{S}_{3/2}$ ,  ${}^4\text{F}_{9/2} \rightarrow {}^4\text{I}_{15/2}$  transitions and the sum) derived from emission spectra of 980 nm excitation for (a)  $\text{NaY}(\text{WO}_4)_2:10\text{Yb1Er}$  and (b)  $\text{NaY}(\text{WO}_4)_2:25\text{Yb1Er}$  NCs in air.



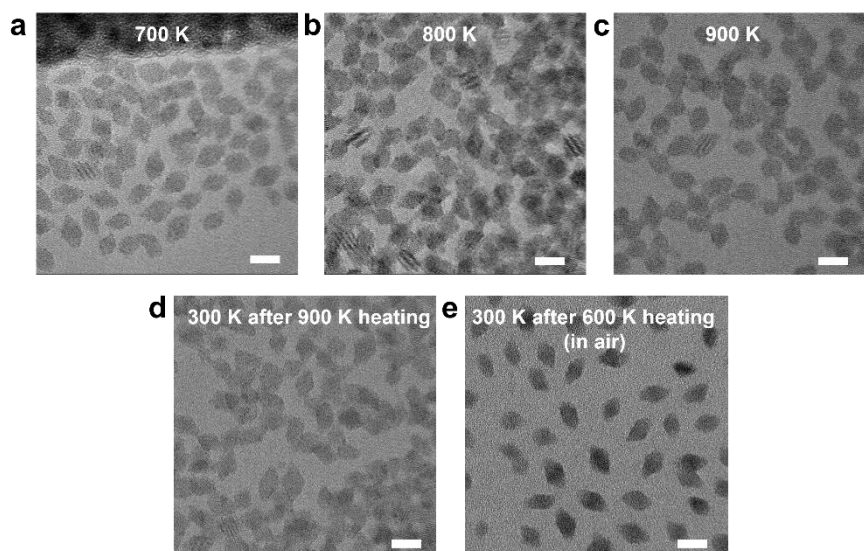
**Figure A6.2.** Temperature-dependent measurements for (a-c)  $\text{NaY}(\text{WO}_4)_2:49\text{Yb1Ho}$  and (d-f)  $\text{NaY}(\text{WO}_4)_2:49\text{Yb1Tm}$  NCs in air. (a, d) Emission spectra under pulsed 980 nm excitation. (b, e) Integrated intensity of  $\text{Ho}^{3+}$  emission lines ( ${}^5\text{F}_4/{}^5\text{S}_2$ ,  ${}^5\text{F}_5 \rightarrow {}^5\text{I}_8$  transitions and the sum) and  $\text{Tm}^{3+}$  emission line ( ${}^3\text{H}_4 \rightarrow {}^3\text{H}_6$  transition) for the emission spectra in (a, d). (c, f) Energy levels of  $\text{Ho}^{3+}\text{-Yb}^{3+}$  and  $\text{Tm}^{3+}\text{-Yb}^{3+}$  ion couples showing the UC processes.



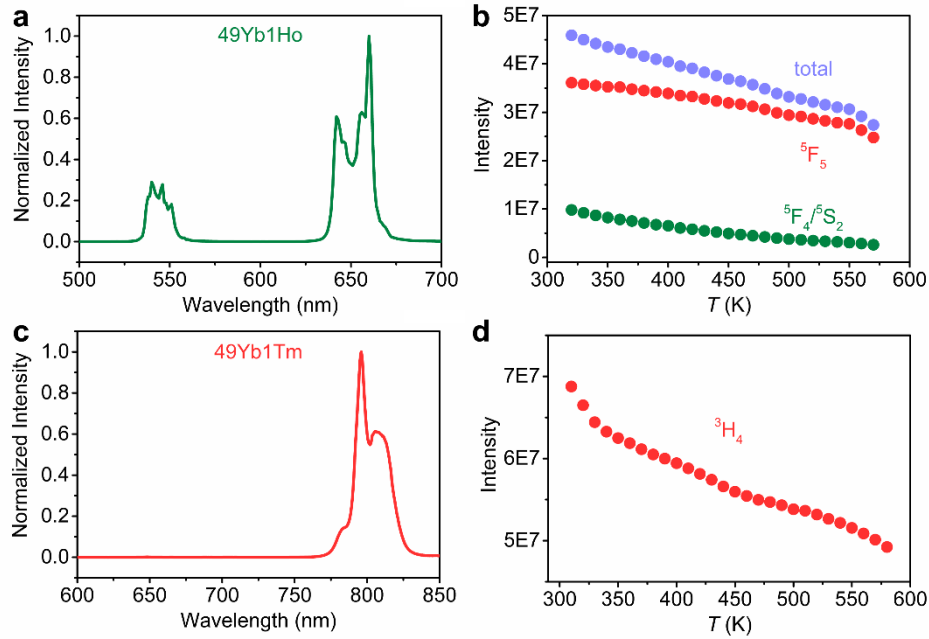
**Figure A6.3.** Temperature-dependent luminescence decay for (a-c) NaY(WO<sub>4</sub>)<sub>2</sub>:10Yb1Er and (d-f) NaY(WO<sub>4</sub>)<sub>2</sub>:25Yb1Er NCs in air under pulsed 980 nm excitation. Luminescence decay curves for (a, d) <sup>2</sup>H<sub>11/2</sub>/<sup>4</sup>S<sub>3/2</sub> states and (b, e) <sup>4</sup>F<sub>9/2</sub> state. (c, f) Decay times (green triangles for <sup>2</sup>H<sub>11/2</sub>/<sup>4</sup>S<sub>3/2</sub> states and red circles for <sup>4</sup>F<sub>9/2</sub> state) and rise time (green squares for <sup>2</sup>H<sub>11/2</sub>/<sup>4</sup>S<sub>3/2</sub> states) determined from the decay curves in (a, b) and (d, e).



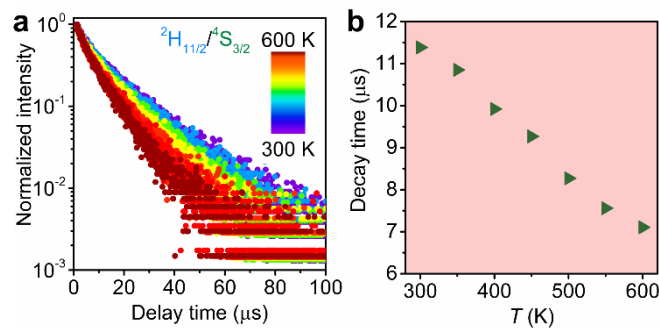
**Figure A6.4.** Temperature-dependent luminescence decay of  ${}^2\text{H}_{11/2}/{}^4\text{S}_{3/2}$  states under pulsed 480 nm excitation for (a, b)  $\text{NaY}(\text{WO}_4)_2:49\text{Yb1Er}$  and (c, d)  $\text{NaY}(\text{WO}_4)_2:1\text{Er}$  NCs in air. (a, c) Luminescence decay curves. (b, d) Decay time.



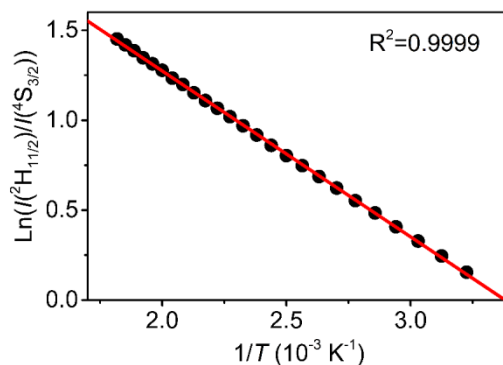
**Figure A6.5.** TEM images of  $\text{NaY}(\text{WO}_4)_2:49\text{Yb1Er}$  NCs recorded at various temperatures during in-situ heating at (a) 700, (b) 800, and (c) 900 K, and (d) after subsequent cooling to 300 K. (e) TEM images recorded at 300 K after ex-situ heating in an oven in air at 600 K for 10 min. (scale bar = 10 nm)



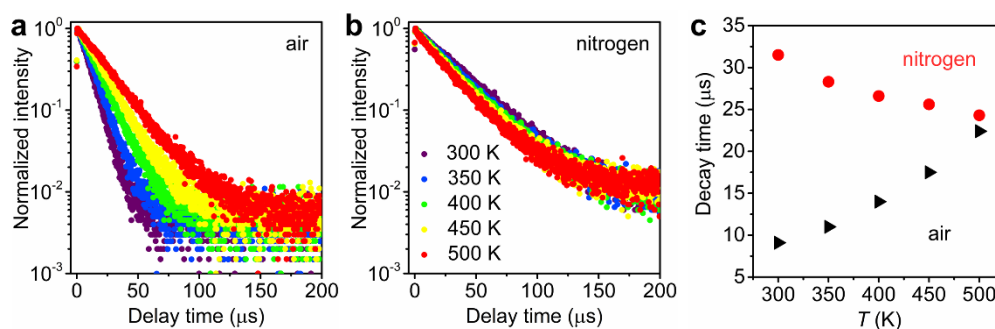
**Figure A6.6.** Temperature-dependent luminescence of NaY(WO<sub>4</sub>)<sub>2</sub>:49Yb1Ho and NaY(WO<sub>4</sub>)<sub>2</sub>:49Yb1Tm bulk materials in air under 980 nm excitation. (a) Emission spectrum at 300 K for Ho<sup>3+</sup>-doped sample. (b) Integrated intensity of Ho<sup>3+</sup> emission lines (5F<sub>4</sub>/5S<sub>2</sub>, 5F<sub>5</sub> → 5I<sub>8</sub> transitions and the sum) for emission spectra. (c) Emission spectrum at 300 K for Tm<sup>3+</sup>-doped sample. (d) Integrated intensity of Tm<sup>3+</sup> emission line (3H<sub>4</sub> → 3H<sub>6</sub> transition) for emission spectra.



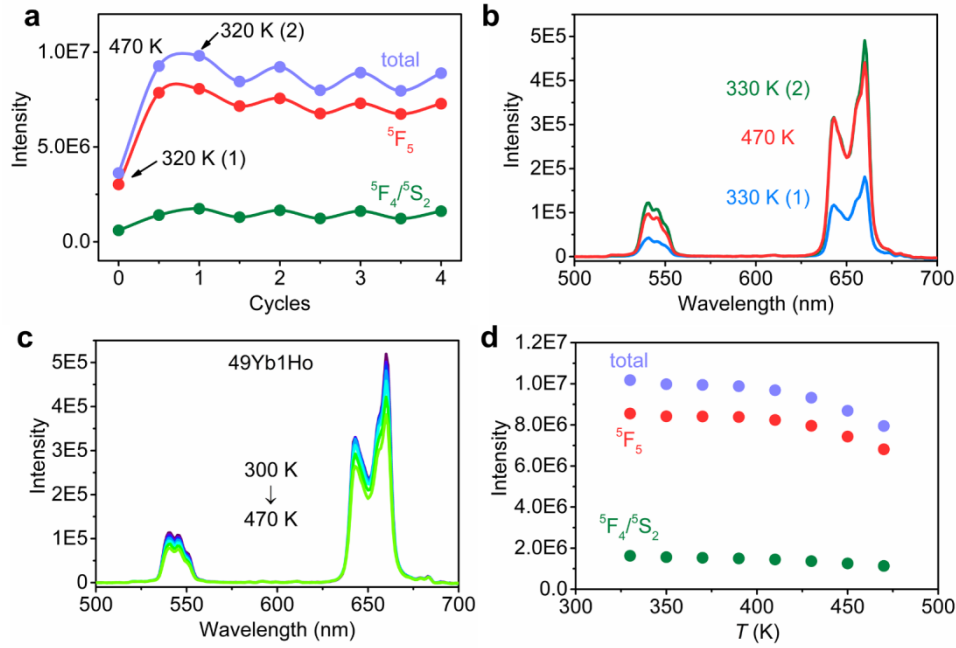
**Figure A6.7.** Temperature-dependent luminescence (a) decay curves and (b) decay time of <sup>2</sup>H<sub>11/2</sub>/<sup>4</sup>S<sub>3/2</sub> states for NaY(WO<sub>4</sub>)<sub>2</sub>:49Yb1Er bulk materials in air under pulsed 480 nm excitation.



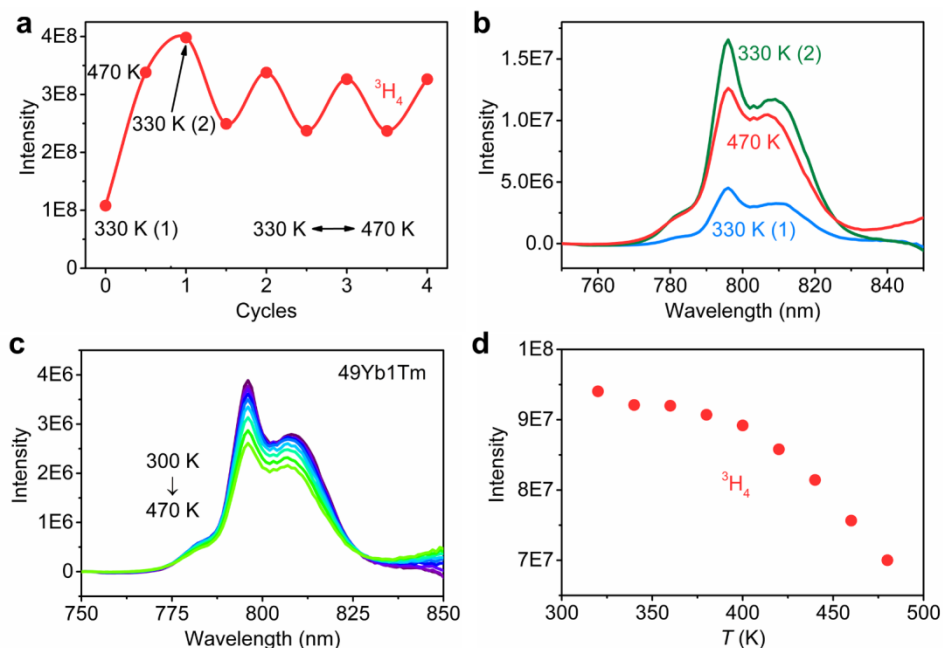
**Figure A6.8.** The linear relation between the natural logarithm of the integrated intensity ratio of the  ${}^2\text{H}_{11/2}$  and  ${}^4\text{S}_{3/2}$  emission lines ( $I({}^2\text{H}_{11/2})/I({}^4\text{S}_{3/2})$ ) and the inverse of temperature  $T$  for  $\text{NaY}(\text{WO}_4)_2:49\text{Yb1Er}$  bulk materials in air. The data are fitted by  $I({}^2\text{H}_{11/2})/I({}^4\text{S}_{3/2}) = A \exp(-\Delta E/(KT))$ , where  $A$  is a constant,  $\Delta E$  is energy separation of  ${}^2\text{H}_{11/2}$  and  ${}^4\text{S}_{3/2}$  levels, and  $K$  is Boltzmann constant.



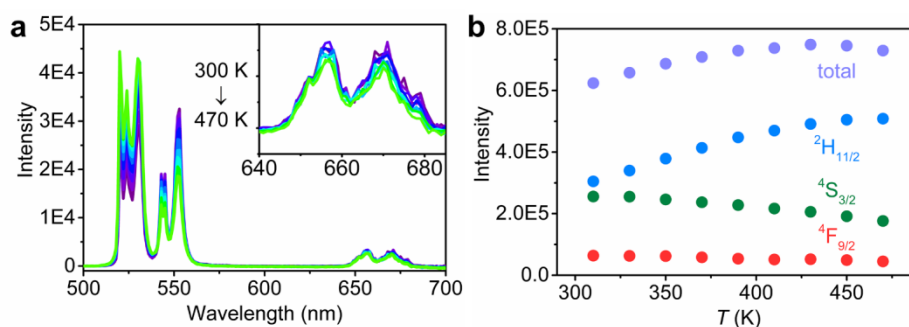
**Figure A6.9.** Temperature-dependent luminescence (a, b) decay curves and (c) decay time of  $\text{Yb}^{3+}$  980 nm emission for  $\text{NaY}(\text{WO}_4)_2:49\text{Yb}$  NCs in (a) air and (b) dry nitrogen under pulsed 960 nm excitation.



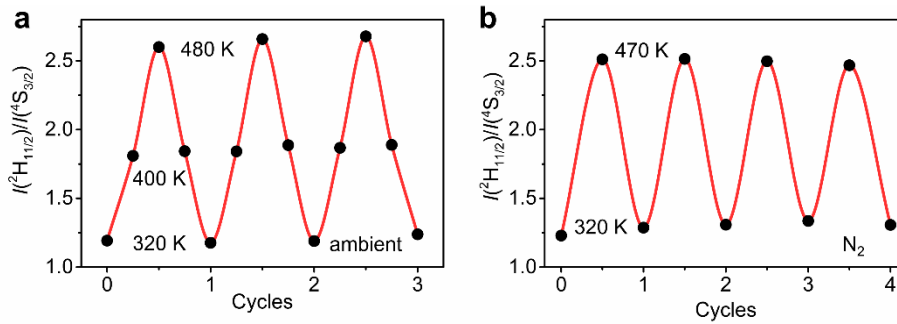
**Figure A6.10.** Temperature-dependent luminescence of NaY(WO<sub>4</sub>)<sub>2</sub>:49Yb1Ho NCs in nitrogen under 980 nm excitation. (a) Cycling experiment for integrated intensity of Ho<sup>3+</sup> emission lines (5F<sub>4</sub>/5S<sub>2</sub>, 5F<sub>5</sub> → 5I<sub>8</sub> transitions and the sum). (b) Emission spectra for the first three temperature points in cycling experiment. (c) Temperature-dependent emission spectra for NCs after first cycle of heating and cooling. (d) Integrated intensity of Ho<sup>3+</sup> emission lines (5F<sub>4</sub>/5S<sub>2</sub>, 5F<sub>5</sub> → 5I<sub>8</sub> transitions and the sum) for the emission spectra in (c).



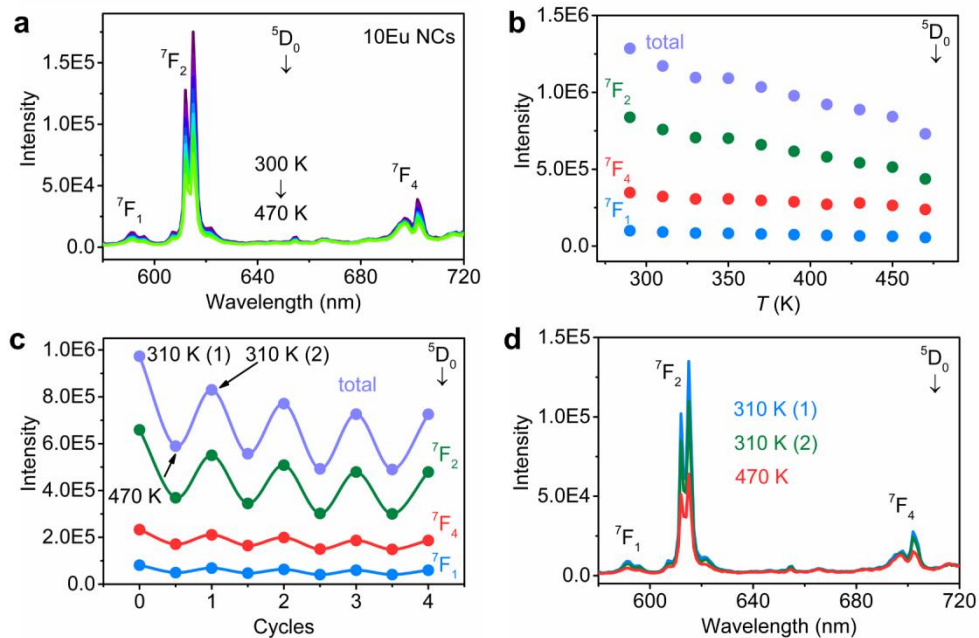
**Figure A6.11.** Temperature-dependent luminescence of NaY(WO<sub>4</sub>)<sub>2</sub>:49Yb1Tm NCs in nitrogen under 980 nm excitation. (a) Cycling experiment for integrated intensity of Tm<sup>3+</sup> emission line (<sup>3</sup>H<sub>4</sub> → <sup>3</sup>H<sub>6</sub> transition). (b) Emission spectra for the first three temperature points in cycling experiment. (c) Temperature-dependent emission spectra for NCs after first cycle of heating and cooling. (d) Integrated intensity of Tm<sup>3+</sup> emission line (<sup>3</sup>H<sub>4</sub> → <sup>3</sup>H<sub>6</sub> transition) for the emission spectra in (c).



**Figure A6.12.** Temperature-dependent luminescence of NaY(WO<sub>4</sub>)<sub>2</sub>:49Yb1Er bulk material in nitrogen under 980 nm excitation. (a) Temperature-dependent emission spectra for sample after first cycle of heating and cooling. (b) Integrated intensity of Er<sup>3+</sup> emission lines (<sup>2</sup>H<sub>11/2</sub>, <sup>4</sup>S<sub>3/2</sub>, <sup>4</sup>F<sub>9/2</sub> → <sup>4</sup>I<sub>15/2</sub> transitions and the sum) for the emission spectra in (a).

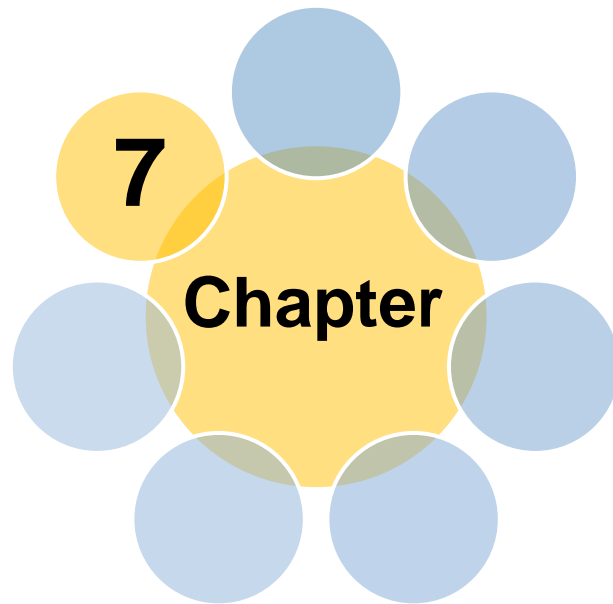


**Figure A6.13.** Cycling experiment for  $\text{Er}^{3+}$  emission intensity ratio of  ${}^2\text{H}_{11/2}/{}^4\text{S}_{3/2}$  derived from emission spectra of 980 nm excitation for  $\text{NaY}(\text{WO}_4)_2:49\text{Yb1Er}$  NCs in (a) air and (b) dry nitrogen.



**Figure A6.14.** Temperature-dependent luminescence of  $\text{NaY}(\text{WO}_4)_2:10\text{Eu}$  NCs under 395 nm excitation. (a) Emission spectra in air. (b) Integrated intensity of  $\text{Eu}^{3+}$  emission lines ( ${}^5\text{D}_0 \rightarrow {}^7\text{F}_{1,2,4}$  transitions and the sum) for the emission spectra in (a). (c) Cycling experiment in nitrogen for integrated intensity of  $\text{Eu}^{3+}$  emission lines ( ${}^5\text{D}_0 \rightarrow {}^7\text{F}_{1,2,4}$  transitions and the sum). (d) Emission spectra for the first three temperature points in cycling experiment.





# Summary & outlook

## 7.1 Summary

Lanthanides (Ln) form the group of elements in the periodic table for which the inner 4f shell is filled with electrons. Lanthanide ions are typically trivalent and have the electron configuration  $[\text{Xe}]4f^n5s^25p^6$  with  $n = 0-14$ . Interaction between the electrons in the partly filled 4f-shell gives rise to a large number of energy levels for different distributions of the  $n$  electrons over the 14 available 4f orbitals. Due to this rich energy level structure, lanthanide ions are widely used for spectral conversion in a wide wavelength range, spanning the ultraviolet to infrared. Traditional luminescent materials (phosphors) for spectral conversion show downshifted emission and convert one high-energy absorbed photon to one low-energy photon. Examples of these phosphors are found in displays, fluorescent tubes, white light LEDs and Euro banknotes. Lanthanide ions, especially  $\text{Ce}^{3+}$ ,  $\text{Eu}^{2+}$ ,  $\text{Eu}^{3+}$  and  $\text{Tb}^{3+}$ , are the most widely used class of ions for spectral conversion.

More recently, multi-photon conversion processes have been discovered where two photons are added up to one higher-energy photon (called upconversion) or one photon is split into two lower-energy photons (called downconversion). Up- and downconversion materials traditionally are microcrystalline materials. For specific applications, it is beneficial to make upconversion or downconversion nanocrystals (NCs). For example, in solar cells, downconversion can be used to split high-energy UV and blue photons into double infrared photons above the bandgap of crystalline silicon. This can result in current doubling for the UV/blue part of the solar spectrum but does require a non-scattering layer on top of the solar cell. This can possibly be realized with downconversion NCs. Upconversion NCs already find application in local temperature sensing and imaging in biological systems and in Chinese Yuan banknotes. However, the poor upconversion quantum efficiency and low absorption strength for the parity forbidden 4f-4f transitions are important drawbacks. This thesis focuses on the multi-photon (upconversion/downconversion) processes in lanthanide-doped NCs. The aim is to explore the underlying reasons for the low quantum efficiency of upconversion in NCs and to try to solve the weak absorption problem. The research involves the synthesis of well-known and new lanthanide-doped NCs, characterization of the materials and a wide range of optical spectroscopy experiments. The results obtained from this work give fundamental insight into quenching mechanisms and sensitization schemes that will contribute to improve the quantum efficiency and brightness of multi-photon NCs.

To quantify the efficiency of luminescent materials, the measurement of luminescence decay curves is a powerful tool. When the radiative decay rate is known, the contribution of non-radiative decay processes can be determined from luminescence decay curves and this allows for an estimate of the quantum efficiency. The radiative decay rate for luminescent ions in NCs is different from that in bulk (microcrystalline) material due to local field effects for electric dipole (ED) transitions. This is now well understood and the radiative decay for ED transitions can be calculated using the

so-called NC-cavity model taking into account the influence of the refractive index  $n$  of a surrounding medium on ED transition rates for emitters in NCs. In **Ch. 2**, the role of the local surroundings on radiative decay rates for magnetic dipole (MD) transitions is investigated. Theory predicts an  $n^3$  dependence and here we provide convincing experimental evidence for the  $n^3$  dependence of MD transition rates. The photonic environment surrounding the emitters is tuned through variation of solvent in which core and core-shell NCs are dispersed. The photonic effect on MD transitions is investigated for  $\text{Eu}^{3+}$  emission (consisting of ED and MD) by measurements of  $^5\text{D}_0$  decay dynamics and ED/MD emission intensity ratios. In addition, an ideal direct probe is investigated, viz.  $\text{Gd}^{3+}$  where the  $^6\text{P}_{7/2}$ - $^8\text{S}_{7/2}$  emission has over 90% MD character. The photonic effects on radiative decay times are important to understand the variation of luminescence behavior in different photonic environments and to make a reliable comparison of quantum efficiencies for NCs in different media and bulk materials possible, as demonstrated in **Chs. 3, 5**.

**Ch. 3** focusses on the upconversion processes in highly doped NCs. High dopant concentrations of lanthanides help to enhance the absorption strength but at the same time lead to concentration quenching. **Ch. 3** provides the insight into concentration quenching for upconversion emission in NCs at low power densities. Concentration dependent decay dynamics is systematically investigated for  $\text{Er}^{3+}$ - or  $\text{Yb}^{3+}$ -doped (1-100%) core and core-shell  $\text{NaYF}_4$  NCs. The lifetimes of green and red upconversion emissions and IR emissions of  $\text{Er}^{3+}$  as well as the NIR emission of  $\text{Yb}^{3+}$  are determined and compared quantitatively for different dopant concentrations. The green-emitting  $\text{Er}^{3+}$   $^4\text{S}_{3/2}$  and NIR-emitting  $^4\text{I}_{11/2}$  levels show strong concentration quenching due to cross-relaxation and energy migration to quenching sites, whereas concentration quenching for the  $\text{Er}^{3+}$  red-emitting  $^4\text{F}_{9/2}$  level and the IR-emitting  $^4\text{I}_{13/2}$  level is limited, as well as for  $\text{Yb}^{3+}$  NIR-emitting  $^2\text{F}_{5/2}$  level. Especially in core-shell NCs, concentration quenching for these levels is weak as a protective (undoped) shell prevents quenching in the surface layer from defects and strong coupling with nearby high-energy vibrational modes of capping and solvent molecules. In addition, in **Ch. 3** the role of solvent quenching is investigated by adding water ( $\text{H}_2\text{O}$ ) and also heavy water ( $\text{D}_2\text{O}$ ) and reveals a much stronger quenching, especially for the  $^4\text{I}_{11/2}$  and  $^4\text{I}_{13/2}$  levels of  $\text{Er}^{3+}$ , in aqueous media due to high-energy O-H vibrations ( $\sim 3400\text{ cm}^{-1}$ ). In  $\text{D}_2\text{O}$ , the much lower-energy D-O vibrations ( $\sim 2500\text{ cm}^{-1}$ ) strongly reduce multi-phonon relaxation processes resulting in reduced quenching of these levels.

For completeness, concentration quenching for  $\text{Ho}^{3+}$  and  $\text{Tm}^{3+}$  upconversion emissions needs an investigation as  $\text{Yb-Ho}$  and  $\text{Yb-Tm}$  upconversion NCs are also widely explored. To make a fully quantitative analysis of the concentration quenching, a microscopic model for energy migration is necessary, but is at present unfortunately too challenging. The conclusions on concentration quenching reported here hold for relatively low excitation power densities. Increased upconversion

efficiencies have been demonstrated for (extremely) high power densities where upconversion processes become more efficient and high population densities in excited states change the energy transfer and energy migration dynamics. For practical applications, however, low power densities are desired and the results in **Ch. 3** give important insights into processes that limit the upconversion quantum efficiency for practical applications.

In addition to upconversion, the other multi-photon process, downconversion, is investigated in **Ch. 4**. The theoretical maximum quantum yield of downconversion is 200% but actually, the external quantum yield is much lower, especially because of the low absorption cross-section of narrow intra-configurational f-f absorption lines. The weak narrow line absorption results in a small fraction of absorbed photons out of the broad solar spectrum. This lowers the external quantum yield which is defined as the number of emitted photons divided by the number of incident photons. To enhance the external quantum yield, a sensitizer can be used which has a strong broadband absorption and can transfer the excitation energy to the downconversion couple. In the past, dye-sensitized upconversion has been demonstrated. Here, we show how the same concept can be used to enhance downconversion emission. A dye with 3-4 orders of magnitude higher absorption cross-section than the 4f-4f transitions, and broad absorption and emission is used to sensitize the downconversion emission of Pr-Yb ion couple through coupling dye molecules to the NC surface.

To realize dye-sensitized downconversion, a Coumarin dye was coupled to the surface of NaYF<sub>4</sub>:Pr,Yb NCs. The measurement of photoluminescence spectra and decay dynamics provides evidence for Förster resonance energy transfer from surface dye molecules to Pr<sup>3+</sup> in the NCs. Downconversion in the Pr-Yb couple results in Yb<sup>3+</sup> IR emission that is enhanced by a factor of ~30 compared to the same NCs without dye molecules coupled to the surface. This study provides a new strategy to enhance the downconversion emission of NCs. However, the downconversion efficiency is still lower than desired because of the low concentration of Pr<sup>3+</sup> ions that are very sensitive to concentration quenching. The low Pr<sup>3+</sup> concentration reduces the probability of energy transfer from dye to Pr<sup>3+</sup>, which scales approximately linearly with the Pr-concentration. One way to enhance the transfer rate is to involve a luminescent ion with intermediate level which is resonant with <sup>6</sup>P<sub>J</sub>/<sup>1</sup>I<sub>6</sub> Pr<sup>3+</sup> states and does not suffer from cross-relaxation quenching allowing for high doping concentrations. Doping this ion in a highly concentrated shell may allow for energy transfer of a larger fraction of the dye-absorbed photons.

The formation of NCs becomes more challenging as the number of constituting elements increases. There are many synthesis protocols for binary (e.g. CdSe) and ternary (e.g. NaYF<sub>4</sub>) NCs but not for quaternary NCs. In **Ch. 5** a one-step thermolysis approach is presented to synthesize complex quaternary NaRE(WO<sub>4</sub>)<sub>2</sub> NCs. The synthesis protocol results in small (12 × 29 nm) diamond shaped and ultrathin (~2 nm) NCs that are highly monodisperse in apolar solvents. The NCs show oriented

attachment along [001] direction via adhesion in (001) facets of neighboring NCs. Tungstates are self-activated hosts which show emission from the tungstate group. In addition, excitation of the tungstate group can be followed by energy transfer to dopants incorporated in the tungstate host and lead to strong characteristic emissions of doped lanthanide ions with high efficiencies. The  $\text{Eu}^{3+}$ -doped NCs show the characteristic  $\text{Eu}^{3+}$  line emission as well as a blue emission that can be assigned to luminescent organic species adsorbed at the NC surface. The synthesized luminescent RE-doped  $\text{NaRE}(\text{WO}_4)_2$  NCs may find applications in transparent luminescent media and bio-imaging while this new synthesis route may also help in the development of synthesis routes for other quaternary NCs.

In **Ch. 6** the  $\text{NaRE}(\text{WO}_4)_2$  NCs (discussed in **Ch. 5**) are doped with lanthanide upconversion couples to investigate the thermal behavior of upconversion emission (thermal enhancement vs. thermal quenching). In recent publications, thermal enhancement of UC emission was reported in NCs. This is unexpected as usually luminescence is quenched at elevated temperatures. In **Ch. 6** the temperature-dependent upconversion emission in NCs doped with Yb-Er, Yb-Ho and Yb-Tm ion couples is investigated by measuring photoluminescence spectra, emission intensities, and decay dynamics in two different atmospheres: air and dry nitrogen. Fully reversible thermal enhancement of upconversion emission is observed for NCs in air. In contrast, in dry  $\text{N}_2$ , the thermally enhanced upconversion is only observed in the first cycle of heating and in subsequent cycles upconversion emission shows reversible thermal quenching that is identical to the thermal (quenching) behavior in microcrystalline bulk materials. The remarkable thermal enhancement of the upconversion emission is explained by the role of water adsorbed on NC surface. The high-energy O-H vibrations quench upconversion emission, as discussed in **Ch. 3**. Heating of the NCs results in desorption of water molecules from the surface and a removal of water quenching explains the observed thermal enhancement of upconversion emission in NCs. The water adsorption/desorption is further confirmed by thermogravimetric analysis and Fourier transform infrared measurements. The results demonstrate that water desorbs from the NC surface upon heating and adsorbs again upon cooling in ambient atmosphere. The findings in **Chs. 3, 6** give important insights into the mechanisms responsible for the low quantum efficiency of upconversion in NCs and serve to design upconversion NCs with higher quantum efficiencies. Especially, we point out the importance of careful characterization of surface molecules (ligands and water) to better understand and optimize the luminescence properties in NCs.

### 7.2 Outlook

The multi-photon processes upconversion and downconversion that are the topic of this thesis depend on the multi-step of energy transfer between lanthanide ions. The ultimate efficiency of the materials is determined by competition between radiative decay, non-radiative decay (quenching)

and the energy transfer processes. The brightness of the upconversion or downconversion emission also strongly depends on the absorption strength of the exciting light. For many applications, such as (bio-)imaging or thermometry using luminescent nanoparticles, it is not the quantum efficiency but the brightness that is crucial. In this thesis, several issues related to the low quantum yield and weak absorption for lanthanide doped up- and downconversion NCs have been discussed, providing new insights that can help to enhance the efficiency and brightness of lanthanide-doped NCs. Challenges however remain both in understanding luminescence quenching and in improving the efficiency and absorption strength in lanthanide-doped NCs. Specific topics that are expected to contribute to a better understanding include:

- The distribution of Ln-ions in NCs
- Identifying the nature of defects and quenching sites
- Determining the theoretical limit of the upconversion quantum yield
- New sensitization schemes of up- and downconversion for Ln-doped NCs

Up- and downconversion processes involve energy transfer between lanthanide ions in excited states. Energy transfer typically is mediated by dipole-dipole interaction that has a strong  $R^{-6}$  (donor-acceptor distance) dependence. The actual ion distribution determines the distance to neighboring lanthanide ions or surface adsorbed molecules or quenching sites in NCs. The distribution of distances from the donor to various nearby acceptors determines the transfer efficiencies. Generally, a homogeneous distribution is assumed for lanthanide dopant ions in NCs and microcrystalline materials based on the similar chemical properties of all Ln-ions that have the same valence electrons ( $5s^2, 5p^6$ ). This assumption may not be correct. Considering the differences in Ln-ions (e.g. ionic radius and electronegativity), Ln-ions may be distributed inhomogeneously and this will affect the energy transfer processes. In the research of (luminescent) NCs, it is therefore important to resolve the three-dimensional (3D) distribution of dopant ions in a single NC. This is challenging as it requires of high (atomic) resolution in microscopy. Recent developments in electron microscopy (EM) allow for 3D tomography with atomic resolution and it is foreseen that in the future elemental mapping with atomic resolution will become possible for Ln-doped NCs. At present, the stability of NCs under longstanding exposure to high-energy electron beam is a problem and initial experiments on our fluoride and tungstate NCs revealed that they were not stable enough for 3D electron tomography. With the further development of EM techniques, this is expected to change. The same EM techniques may allow for identifying defects and quenching sites in NCs.

Potential applications for both upconversion and downconversion materials involve spectral conversion for photovoltaics. The combination of an upconversion layer below and a downconversion layer on top of the solar cell can significantly reduce spectral mismatch losses. Relaxation losses for high-energy (UV and blue) and transmission losses for low-energy (IR) solar

light are reduced if high-energy photons are split into double lower-energy photons above the bandgap of the semiconductor material in solar cells and if two sub-bandgap IR photons are converted to supra-bandgap photons by upconversion. However, presently the performance of both upconversion and downconversion materials is still far away from what is required for solar cells and other applications because of the weak absorption strength and low efficiency. The highest quantum yields reported for upconversion are below 15%. The theoretical limit for the upconversion quantum yield is not clear. Although in single photon conversion processes quantum yields of close to 100% are possible and have been realized, the situation is different for upconversion. In a simple approach, the combination of two low-energy photons to one high-energy photon has a 50% quantum yield limit. However, in real upconversion systems, there is always competition between radiative decay and energy transfer from intermediate states involved in the upconversion process. Even in an ideal case without any quenching losses, this will limit the upconversion efficiency. Future research to enhance the upconversion efficiency and understand the possible highest efficiency is an important challenge in the field of upconversion.

The issue of the poor absorption strength of parity forbidden 4f-4f transitions has been successfully solved in single photon conversion materials by using a co-dopant as sensitizer, e.g. in phosphors applied in fluorescent tubes. For up- and downconversion materials, the weak and narrow 4f-4f absorption lines of lanthanides remain as an issue. For upconversion, dye-sensitization has been shown to enhance the brightness of upconversion NCs and we recently showed how dye-sensitization can also be used for downconversion (see **Ch. 4**). The limited stability of organic dyes is, however, a problem (especially in long term applications as solar cells), and the sensitization efficiency is still well below 100%. For future research, alternative strategies can be explored by making use of core-shell structures that bring luminescent ions in close proximity without actual mixing in the same host lattice.

The field of multi-photon materials has seen an impressive growth in the past two decades, also triggered by the flexibility in design of new multi-photon conversion schemes, and potential applications, which are offered by NCs. In the future, new designs of up- and downconversion NCs for spectral conversion in the UV-VIS-NIR range are expected and, especially if the efficiency and absorption issues are solved, the range of commercial applications is expected to grow.

# Samenvatting en vooruitblik

## Samenvatting

Lanthaniden (Ln) vormen een groep van elementen in het periodiek systeem waarbij de 4f binnenschil wordt opgevuld met elektronen. Lanthanide ionen zijn meestal driewaardig en hebben de elektronenconfiguratie  $[\text{Xe}]4f^n5s^25p^6$  met  $n = 0-14$ . Interactie tussen de elektronen in de gedeeltelijk gevulde 4f-schil zorgt voor een groot aantal energieniveaus voor de diverse verdelingen van de  $n$  elektronen over de 14 beschikbare f-orbitalen. Als gevolg van deze rijke energieniveaustruktuur worden lanthanide ionen op grote schaal gebruikt voor spectrale conversie in een breed golflengtegebied, van het ultraviolet tot het infrarood. Traditionele luminescerende materialen (fosforen) voor spectrale conversie vertonen roodverschoven emissie en zetten één hoogenergetisch foton om in één lagerenergetisch foton. Voorbeelden van dit type fosforen zijn te vinden in TL-buizen, witte LED-lampen en Euro bankbiljetten. Lanthanide ionen, en dan met name  $\text{Ce}^{3+}$ ,  $\text{Eu}^{2+}$ ,  $\text{Eu}^{3+}$  en  $\text{Tb}^{3+}$ , zijn de meest gebruikte ionen voor spectrale conversie.

Meer recent zijn multi-foton processen ontdekt waarbij twee fotonen bij elkaar opgeteld worden tot één hoogenergetisch foton (upconversie genoemd) of één foton wordt geknipt in twee laagenergetische fotonen (downconversie genoemd). Up- en downconversie materialen zijn van oudsher microkristallijne materialen of grote éénkristallen. Voor specifieke toepassingen is het echter nuttig om upconversie en downconversie nanokristallen te maken. Bijvoorbeeld in zonnecellen kan downconversie gebruikt worden om hoogenergetische blauwe en ultraviolette fotonen te knippen in twee infrarood fotonen boven de bandkloof van kristallijn silicium. Dit kan zorgen voor stroomverdubbeling voor het UV/blauwe deel van het zonnenspectrum maar vereist wel een transparante laag voor downconversie bovenop de zonnecel. Dit kan mogelijk gerealiseerd worden met downconversie nanokristallen. Upconversie nanokristallen worden al toegepast, bijv. voor het lokaal meten van temperatuur, beeldvorming in biologische systemen en in de Chinese Yuan bankbiljetten. Echter, de lage kwantumefficiëntie en lage absorptiesterkte voor de pariteitsverboden 4f-4f overgangen vormen belangrijke nadelen. Dit proefschrift bestudeert multi-foton (upconversie en downconversie) processen in lanthanide-gedoteerde nanokristallen. Het doel is een beter inzicht te krijgen in de oorzaken voor de lage kwantumefficiëntie en het probleem van de lage absorptiesterkte op te lossen. Het onderzoek omvat de synthese van bekende en nieuwe lanthanide gedoteerde nanokristallen, karakterisatie van de materialen en een breed scala aan optische spectroscopie experimenten. De resultaten die verkregen zijn in dit onderzoek verschaffen fundamenteel inzicht in de doingsmechanismen en sensibilisatiemogelijkheden en dit kan bijdragen aan een verbetering van de kwantumefficiëntie en helderheid van multi-foton nanokristallen.

Om de efficiëntie van luminescerende materialen te kwantificeren is het meten van luminescentievervalcurven een krachtige techniek. Als de stralende vervalkans bekend is, kan de bijdrage van niet-stralende vervalprocessen bepaald worden uit luminescentievervalcurven en op basis hiervan kan een schatting gemaakt worden van de kwantumefficiëntie. De stralende vervalkans voor luminescerende ionen in nanokristallen verschilt van die in bulk (microkristallijn) materiaal als gevolg van lokale veldeffecten voor elektrische dipoolovergangen (ED-overgangen). Dit wordt nu goed begrepen en de stralende vervalkans voor ED-overgangen kan bepaald worden met behulp van het zogenaamde nanokristal-caviteit model voor de invloed van de brekingsindex van het omringende medium op ED-overgangen van emitterende ionen in nanokristallen. In **Hoofdstuk 2** wordt de invloed van de lokale omgeving op magnetische dipoolovergangen (MD-overgangen) onderzocht. De theorie voorspelt een  $n^3$  afhankelijkheid en hier tonen we overtuigend experimenteel bewijs voor deze  $n^3$  afhankelijkheid voor MD-overgangswaarschijnlijkheden. De fotonische omgeving van de emitterende ionen is hier gevarieerd door het oplosmiddel te veranderen waarin luminescerende kern en kern-schil nanokristallen zijn gedispergeerd. De invloed van de fotonische omgeving op MD-overgangen is onderzocht voor  $\text{Eu}^{3+}$  emissie (bestaande uit ED- en MD-emissie) door de  ${}^5\text{D}_0$  emissie vervalcurven te meten alsook de ED/MD emissie intensiteitsverhoudingen. Daarnaast is een ideale directe probe onderzocht, te weten  $\text{Gd}^{3+}$ , waarvoor de  ${}^6\text{P}_{7/2}$ - ${}^8\text{S}_{7/2}$  emissie meer dan 90% MD karakter heeft. Inzicht in de fotonische effecten op stralende vervaltijden zijn belangrijk om variatie in luminescentiegedrag te begrijpen in verschillende fotonische omgevingen en om een betrouwbare vergelijking mogelijk te maken tussen kwantumefficiënties voor nanokristallen in verschillende media en bulk materialen en dit wordt toegepast in **Hoofdstukken 3 en 5**.

**Hoofdstuk 3** concentreert zich op upconversieprocessen in hooggedoteerde nanokristallen. Hoge doteringsconcentraties helpen om de absorptiesterkte te verhogen maar leiden tegelijkertijd tot concentratiedoving. **Hoofdstuk 3** geeft inzicht in concentratiedoving van de upconversie emissie in nanokristallen voor lage excitatiedichtheden. Concentratieafhankelijke luminescentievervalcurven worden systematisch bestudeerd voor  $\text{Er}^{3+}$ - of  $\text{Yb}^{3+}$ -gedoteerde (1-100%) kern en kern-schil  $\text{NaYF}_4$  nanokristallen. De levensduur van de groene en rode upconversie emissies en de infrarood emissies van  $\text{Er}^{3+}$  alsook nabije infrarood emissie van  $\text{Yb}^{3+}$  worden bepaald en kwantitatief vergeleken voor verschillende doteringsconcentraties. Het groen-emitterende  $\text{Er}^{3+}$   ${}^4\text{S}_{3/2}$  niveau en het nabij infrarood emitterende  ${}^4\text{I}_{11/2}$  niveau vertonen sterke concentratiedoving als gevolg van cross-relaxatie en energiemigratie naar dovingscentra, terwijl de concentratiedoving voor het  $\text{Er}^{3+}$  rood emitterende  ${}^4\text{F}_{9/2}$  niveau en het infrarood emitterende  ${}^4\text{I}_{13/2}$  niveau beperkt is, evenals voor het  $\text{Yb}^{3+}$  nabij-infrarood emitterende  ${}^2\text{F}_{5/2}$  niveau. Vooral in kern-schil nanokristallen is de doving voor deze niveaus beperkt omdat een beschermende (ongedoteerde) schil doving door defecten in de oppervlaktelaag voorkomt en doving door koppeling met hoogenergetische vibraties van oppervlakte- en

oplosmiddelmoleculen vermindert. Daarnaast wordt in **Hoofdstuk 3** de rol van doving door het oplosmiddel bestudeerd door water ( $\text{H}_2\text{O}$ ) en ook zwaar water ( $\text{D}_2\text{O}$ ) toe te voegen en dit laat in water een veel sterkere doving zien, vooral voor de  $^4\text{I}_{11/2}$  en  $^4\text{I}_{13/2}$  niveaus van  $\text{Er}^{3+}$  als gevolg van de hoogenenergetische O-H vibraties ( $\sim 3400\text{ cm}^{-1}$ ). In  $\text{D}_2\text{O}$  zorgen de veel lager energetische O-D vibraties ( $\sim 2500\text{ cm}^{-1}$ ) voor een sterk verminderde multi-fonon relaxatie wat ervoor zorgt dat de doving beperkt wordt.

Voor het verkrijgen van een volledig beeld is het nuttig om ook de concentratiedoving voor  $\text{Ho}^{3+}$  en  $\text{Tm}^{3+}$  upconversie emissie te meten omdat Yb-Ho en Yb-Tm gedoteerde nanokristallen uitgebreid onderzocht worden. Voor een volledig kwantitatieve analyse van de concentratiedoving is een microscopisch model voor energiemigratie nodig maar op dit moment is dat helaas niet mogelijk. De conclusies met betrekking tot concentratiedoving die hier gerapporteerd worden, zijn van toepassing op relatief lage excitatiedichtheden. Hogere upconversie-efficiënties zijn waargenomen voor (extreem) hoge excitatiedichtheden waarbij upconversie processen efficiënter worden en de hoge populatiedichtheid voor aangeslagen toestanden de dynamiek van energiemigratie en energieoverdracht veranderen. Echter, voor praktische toepassing zijn lage excitatiedichtheden vereist en de resultaten in **Hoofdstuk 3** geven belangrijke nieuwe inzichten in processen die de upconversie kwantumefficiëntie begrenzen voor mogelijke praktische toepassingen.

Naast upconversie zijn er andere multi-foton processen, downconversie, en deze worden bestudeerd in **Hoofdstuk 4**. De theoretisch maximale kwantumefficiëntie voor downconversie is 200% maar de werkelijke externe kwantumefficiëntie is veel lager, vooral vanwege de lage absorptie cross-sectie van de smalle intraconfiguratie f-f absorptielijnen. De zwakke en smalbandige lijnabsorptie zorgt ervoor dat maar een klein deel van de fotonen uit het brede zonnenspectrum wordt geabsorbeerd. Dit verlaagt de externe kwantumefficiëntie die is gedefinieerd als het aantal uitgezonden fotonen gedeeld door het aantal opvallende fotonen. Om de externe kwantumefficiëntie te verhogen kan een sensibilisator gebruikt worden met een sterke breedbandige absorptie en die de excitatie-energie kan overdragen naar een downconversie koppel. In het verleden is sensibilisatie met kleurstofmoleculen aangetoond voor upconversie. Hier laten we zien dat dit principe ook gebruikt kan worden voor het versterken van downconversie emissie. Een kleurstof met een 3-4 ordes van grootte hogere absorptie cross-sectie dan de 4f-4f overgangen en met absorptie en emissie over een breed spectraal gebied, wordt gebruikt om downconversie emissie van het Pr-Yb koppel te sensibiliseren door kleurstof moleculen aan het oppervlak van het nanokristal te koppelen.

Om kleurstof gesensibiliseerde downconversie aan te tonen werd een Coumarine kleurstof gekoppeld aan het oppervlak van  $\text{NaYF}_4:\text{Pr},\text{Yb}$  nanokristallen. Het meten van fotoluminescentiespectra en luminescentie vervalcurven geeft bewijs voor Förster resonante energie-overdracht van kleurstofmoleculen aan het oppervlak, naar  $\text{Pr}^{3+}$  in de nanokristallen.

Downconversie in het Pr-Yb koppel resulteert vervolgens in  $\text{Yb}^{3+}$  infrarood emissie die een factor 30 versterkt is vergeleken met dezelfde nanokristallen zonder kleurstofmoleculen aan het oppervlak. Deze studie levert een nieuwe strategie voor het versterken van de downconversie emissie van nanokristallen. Helaas is de downconversie-efficiëntie nog steeds lager dan gewenst door de vrij lage concentratie van  $\text{Pr}^{3+}$  die gebruikt kan worden vanwege de hoge gevoeligheid van  $\text{Pr}^{3+}$  voor concentratiedoving. Een mogelijkheid om de overdrachtsefficiëntie te verhogen is gebruik maken van een ion met een tussenliggend niveau dat resonant is met de  $^3\text{P}_j/^1\text{I}_6$  niveaus van  $\text{Pr}^{3+}$  en geen last heeft van cross-relaxatiedoving waardoor er een hogere doteringsconcentratie gebruikt kan worden. Door dit ion in hoge concentraties in te bouwen in de schil kan er efficiënte energieoverdracht gerealiseerd worden voor een groter deel van de fotonen die door de kleurstofmoleculen geabsorbeerd zijn.

Het vormen van nanokristallen wordt lastiger naarmate het aantal soorten van atomen waaruit het gevormd wordt toeneemt. Er zijn veel synthesevoorschriften voor binaire nanokristallen (bijv. CdSe) en ternaire nanokristallen (bijv.  $\text{NaYF}_4$ ) maar niet voor quaternaire nanokristallen. In **Hoofdstuk 5** wordt een éénstapssynthese beschreven om quaternaire  $\text{NaRE}(\text{WO}_4)_2$  nanokristallen te maken. Het synthesevoorschrift leidt tot kleine ( $12 \times 29$  nm) ruitvormige en ultradunne ( $\sim 2$  nm) nanokristallen die zeer monodispers zijn, gedispergeerd in apolaire oplosmiddelen. De nanokristallen groeien aan elkaar langs de [001] richting door het aan elkaar groeien van (001) facetten van naburige nanokristallen. Wolframaten zijn grondroosters die vanuit zichzelf luminesceren door emissie van de wolframaatgroep. Daarnaast kan excitatie van de wolframaatgroep gevolgd worden door energieoverdracht naar doteringen zoals lanthaniden die zijn ingebouwd in het wolframaat gastrooster en aanleiding geven tot sterke karakteristieke en efficiënte emissie van lanthanide ionen. De  $\text{Eu}^{3+}$ -gedoteerde nanokristallen vertonen de karakteristieke  $\text{Eu}^{3+}$  lijnemissie en ook een blauwe emissie die wordt toegeschreven aan organische moleculen aan het oppervlak van de nanokristallen. De lanthanide-gedoteerde luminescerende  $\text{NaRE}(\text{WO}_4)_2$  nanokristallen kunnen wellicht toegepast worden in transparante luminescerende media en beeldvorming terwijl de nieuwe synthesemethode kan helpen bij de ontwikkeling van synthesemethodes voor andere quaternaire nanokristallen.

In **Hoofdstuk 6** worden de  $\text{NaRE}(\text{WO}_4)_2$  nanokristallen uit **Hoofdstuk 5** gedoteerd met lanthanide upconversiekoppels om het temperatuurgedrag te bestuderen van de upconversie emissie (temperatuurversterking vs. temperaturoving). In recente publicaties is temperatuur geïnduceerde versterking van upconversie-emissie gerapporteerd in nanokristallen. Dit is onverwacht omdat normaalgesproken luminescentie dooft bij hogere temperaturen. In **Hoofdstuk 6** wordt de temperatuurafhankelijke emissie van de Yb-Er, Yb-Ho en Yb-Tm koppels onderzocht door fotoluminescentiespectra, emissie intensiteiten en luminescentievervalcurven te meten in twee verschillende omgevingen: lucht en droge stikstof. Volledig reversibele thermische versterking van

de upconversie emissie wordt waargenomen voor nanokristallen in lucht. In contrast daarmee wordt voor nanokristallen in droge stikstof de temperatuur geïnduceerde versterkte emissie alleen waargenomen tijdens de eerste verwarmingscyclus. In de daaropvolgende cycli vertoont de upconversie emissie reversibele temperatuurdoving die identiek is aan de temperatuurdoving in microkristallijn bulk materiaal. Op basis van deze waarnemingen wordt de opmerkelijke temperatuurversterking van upconversie emissie verklaard door de rol van water dat geadsorbeerd is aan het oppervlak van de nanokristallen. De hoogenergetisch O-H vibraties doven de upconversie emissie, zoals besproken in **Hoofdstuk 3**. Verwarmen van de nanokristallen leidt tot desorptie van watermoleculen van het oppervlak en het verwijderen van het water verklaart de waargenomen toename van intensiteit van de upconversie emissie bij hogere temperaturen. De adsorptie/desorptie van water wordt bevestigd door thermogravimetrische analyse en Fourier transform infrarood metingen. De resultaten laten zien dat water desorbeert van het nanokristal oppervlak bij verhitting en vervolgens weer adsorbeert bij afkoeling in de lucht. De resultaten van **Hoofdstukken 3 en 6** geven belangrijk inzicht in de mechanismen die verantwoordelijk zijn voor de lage kwantumefficiëntie van upconversie nanokristallen en helpen bij het ontwerpen van upconversie nanokristallen met hogere efficiënties. In het bijzonder laten we zien hoe belangrijk de rol is van het zorgvuldig karakteriseren van moleculen (liganden en water) aan het oppervlak om een beter inzicht te krijgen in het optimaliseren van de luminescentie eigenschappen van nanokristallen.

## Vooruitblik

De multi-foton processen upconversie en downconversie die behandeld worden in dit proefschrift zijn gebaseerd op multi-staps energieoverdracht tussen lanthanide ionen. De uiteindelijke efficiëntie van de materialen wordt bepaald door competitie tussen stralend verval, niet-stralend verval (doving) en energieoverdrachtsprocessen. De helderheid van de upconversie of downconversie emissie hangt ook sterk af van de absorptiesterkte voor het exciterende licht. Voor veel toepassingen, zoals beeldvorming of thermometrie met luminescerende nanodeeltjes, is niet de kwantumefficiëntie maar de helderheid bepalend. In dit proefschrift worden diverse aspecten beschreven die verband houden met de lage kwantumefficiëntie en de zwakke absorptie voor lanthanide-gedoteerde up- en downconversie nanokristallen en dit geeft nieuwe inzichten die kunnen bijdragen aan het verhogen van de efficiëntie en helderheid van lanthanide-gedoteerde nanokristallen. Er blijven echter uitdagingen zowel voor het begrijpen van doving van de luminescentie als voor het verbeteren van de efficiëntie en absorptiesterkte voor lanthanide-gedoteerde nanokristallen. Specifieke onderwerpen waarvan verwacht wordt dat ze kunnen bijdragen aan een beter begrip zijn:

- De ruimtelijke distributie van Ln-ionen in NCs
- Identificeren van defecten en doofcentra
- Bepalen van de theoretische limiet voor de upconversie kwantumefficiëntie

- Nieuwe routes voor sensibilisatie van up- en downconversie

Up- en downconversie worden bepaald door energieoverdrachtsprocessen tussen lanthanide ionen in aangeslagen toestanden. Energieoverdracht gebeurt meestal via dipool-dipoolwisselwerking die een sterke  $R^{-6}$  (donor-acceptor afstand) afstands- afhankelijkheid kent. De werkelijke verdeling van ionen over het kristalrooster bepaalt de afstanden tussen naburige lanthanide ionen en de afstand tot moleculen of doofcentra aan het oppervlak van nanokristallen. De verdeling van afstanden van de donor tot verschillende naburige acceptoren bepaalt de overdrachtefficiënties. Veelal wordt een homogene statistische verdeling aangenomen voor lanthanide doteringen in nano- en microkristallijne materialen vanwege de vergelijkbare chemische eigenschappen van lanthanide ionen die allemaal dezelfde valentie-elektronen hebben ( $5s^2, 5p^6$ ). Deze aanname is wellicht niet correct. Gezien de verschillen tussen lanthanide ionen (bijv. ionstraal en elektronegativiteit), zouden lanthanide-ionen niet homogeen verdeeld kunnen zijn en dit zal van invloed zijn op energieoverdrachtsprocessen. In het onderzoek aan (luminescerende) nanokristallen is het daarom belangrijk om de driedimensionale (3D) verdeling van doteringen op te helderen in een enkel nanokristal. Dit is een geweldige uitdaging omdat het hoge (atomaire) resolutie vereist. Recente ontwikkelingen in elektronenmicroscopie (EM) maken 3D tomografie mogelijk met atomaire resolutie en het zal in de toekomst waarschijnlijk mogelijk worden om elementen in een Ln-gedoteerd nanokristal zichtbaar te maken met atomaire resolutie. Op dit moment is de stabiliteit van nanokristallen onder langdurige blootstelling aan een hoogenergetische elektronenbundel nog een probleem en verkennende experimenten aan onze fluoride en wolframaat nanokristallen lieten zien dat ze niet stabiel genoeg waren voor 3D elektrontomografie. Met de voortschrijdende ontwikkeling van EM technieken zal dit waarschijnlijk veranderen. Dezelfde EM technieken kunnen wellicht ook gebruikt worden het identificeren van defecten en doofcentra in nanokristallen.

Potentiële toepassingen voor zowel upconversie als downconversie materialen betreffen spectrale conversie voor zonnecellen. De combinatie van een laag met upconversie materialen onder de zonnecel en een downconversie toplaag kan de spectrale mismatchverliezen aanzienlijk reduceren. Relaxatieverliezen voor hoogenergetische (blauw en UV) fotonen en transmissieverliezen voor laag-energetische (infrarood) fotonen in het zonlicht worden verminderd als hoogenergetische fotonen door downconversie geknipt worden in twee lager-energetische fotonen boven de bandafstand van de halfgeleider in de zonnecel en als twee infrarood fotonen met een energie kleiner dan de bandafstand door upconversie worden opgeteld tot één foton met een energie boven de bandafstand. Op dit moment blijven de prestaties van upconversie en downconversie materialen ver achter bij wat vereist is voor zonnecellen en andere toepassingen vanwege de lage absorptiesterkte en lage efficiëntie. De hoogst gerapporteerde kwantumefficiënties voor upconversie liggen beneden 15%. Het is niet duidelijk wat de theoretisch maximale efficiëntie is. Voor één-foton conversie materialen zijn

kwantumefficiënties van bijna 100% mogelijk en gerealiseerd voor een groot aantal fosforen maar de situatie is anders voor upconversie. In een simpele benadering kan het optellen van twee laagenergetische fotonen tot één hoogenergetisch foton een 50% kwantumefficiëntie geven. Echter, in echte upconversiematerialen is er altijd concurrentie tussen stralend verval en energieoverdracht vanuit tussenliggende energieniveaus die betrokken zijn bij het upconversieproces. Zelfs in een perfect materiaal zonder doofcentra zal dit de maximale kwantumefficiëntie beperken. Verder onderzoek om de upconversie efficiëntie te verhogen en om inzicht te krijgen in wat de maximale upconversie efficiëntie is, vormt een belangrijke uitdaging in het upconversieveld.

Het probleem van de lage absorptie sterkte van de pariteitsverboden 4f-4f overgangen is opgelost in één-foton conversie materialen door een co-dotering toe te voegen als sensibilisator, bijv. in fosforen in TL-buizen. Voor up- en downconversie materialen blijven de zwakke en scherpe 4f-4f absorptielijnen een probleem. Voor upconversie is aangetoond dat sensibilisatie met kleurstofmoleculen de helderheid van upconversie nanokristallen kan verhogen en recent hebben wij laten zien hoe deze sensibilisatie ook gebruikt kan worden voor downconversie (**Hoofdstuk 4**). De beperkt stabiliteit van kleurstofmoleculen is echter een punt van zorg (vooral in lange termijn toepassingen zoals zonnecellen), en de efficiëntie van de sensibilisatie is veel lager dan 100%. Toekomstig onderzoek kan zich richten op alternatieve sensibilisatiemogelijkheden door gebruik te maken van mogelijkheden die kern-schil nanostructuren bieden om luminescerende ionen dicht bij elkaar te brengen zonder ze te mengen in eenzelfde gastrooster.

Het vakgebied van multi-foton materialen heeft een indrukwekkende groei doorgemaakt in de afgelopen twintig jaar, mede door de hoge flexibiliteit die nanokristallen bieden voor het ontwerpen van innovatieve multi-foton conversiepaden. In de toekomst worden nieuwe ontwerpen van up- en downconversie nanokristallen verwacht voor spectrale conversie en, zeker als problemen met de efficiëntie en absorptiesterkte zijn opgelost, is de verwachting dat reikwijdte van commerciële toepassingen sterk zal toenemen.

## List of publications

**Wang, Z. J.**; Christiansen, J.; Wezendonk, D.; Xie, X. B.; van Huis, M. A.; van Blaaderen, A.; Meijerink, A. Thermal Enhancement and Quenching of Upconversion Emission in Nanocrystals. (*In preparation*)

**Wang, Z. J.**; Meijerink, A. Concentration Quenching in Upconversion Nanocrystals. *J. Phys. Chem. C* **2018**, *122*, 26298-26306.

**Wang, Z. J.**; Meijerink, A. Dye-Sensitized Downconversion. *J. Phys. Chem. Lett.* **2018**, *9*, 1522-1526.

**Wang, Z. J.**; Senden, T.; Meijerink, A. Photonic Effects for Magnetic Dipole Transitions. *J. Phys. Chem. Lett.* **2017**, *8*, 5689-5694.

**Wang, Z. J.**; Zhang, Y. L.; Zhong, J. P.; Yao, H. H.; Wang, J.; Wu, M. M.; Meijerink, A. One-Step Synthesis and Luminescence Properties of Tetragonal Double Tungstates Nanocrystals. *Nanoscale* **2016**, *8*, 15486-15489.

### Other publications:

**Wang, Z. J.**; Zhong, J. P.; Jiang, H. X.; Wang, J.; Liang, H. B. Controllable Synthesis of NaLu(WO<sub>4</sub>)<sub>2</sub>:Eu<sup>3+</sup> Microcrystal and Luminescence Properties for LEDs. *Cryst. Growth&Des.* **2014**, *14*, 3767-3773.

**Wang, Z. J.**; Wang, P.; Zhong, J. P.; Liang, H. B.; Wang, J. Phase Transformation and Spectroscopic Adjustment of Gd<sub>2</sub>O<sub>3</sub>:Eu<sup>3+</sup> Synthesized by Hydrothermal Method. *J. Lumin.* **2014**, *152*, 172-175.

**Wang, Z. J.**; Zhong, J. P.; Liang, H. B.; Wang, J. Luminescence Properties of Lutetium Based Red-Emitting Phosphor NaLu(WO<sub>4</sub>)<sub>2</sub>:Eu<sup>3+</sup>. *Opt. Mater. Express* **2013**, *3*, 418-425.

Lin, M.; Xie, L. J.; **Wang, Z. J.**; Richards, B. S.; Gao, G. J.; Zhong, J. P. Facile Synthesis of Mono-Disperse Sub-20 nm NaY(WO<sub>4</sub>)<sub>2</sub>:Er<sup>3+</sup>, Yb<sup>3+</sup> Upconversion Nanoparticles: A New Choice for Nanothermometry. (*Submitted*)

Zhang, X. J.; Si, S. C.; Yu, J. B.; **Wang, Z. J.**; Zhang, R. H.; Lei, B. F.; Liu, Y. L.; Zhuang, J. L.; Hu, C. F.; Cho, Y. J.; Xie, R. J.; Zhang, H. W.; Tian, Z. F.; Wang, J. Improving the Luminous Efficacy and the Resistance to Blue Laser Irradiation of Phosphor-In-Glass Based Solid State Laser Lighting through Employing Dual-Functional Sapphire Plate. *J. Mater. Chem. C* (*Accepted*)

---

Liu, Y. W.; **Wang, Z. J.**; Zhong, J. P.; Pan, F. J.; Liang, H. B.; Xiao, Z. G. Synthesis and Photoluminescence Properties of Red-Emitting Phosphors  $\text{Ba}_2\text{Gd}_8(\text{SiO}_4)_6\text{O}_2:\text{Eu}^{3+}$ . *Mater. Lett.* **2014**, *129*, 130-133.

---

## List of conference contributions

**Invited Oral presentation: Dye-Sensitized Downconversion.**

**Poster: Concentration Quenching in Upconversion Nanocrystals.**

5th International Conference on the Physics of Optical Materials and Devices, **2018**, *Igalo*, Montenegro.

**Oral presentation: Dye-Sensitized Downconversion.**

**Oral presentation: Concentration Quenching in Upconversion Nanocrystals.**

**Poster: Photonic Effects for Magnetic Dipole Transitions.**

Material Research Society Spring Meeting, **2018**, *Phoenix*, USA.

Physics@Veldhoven, **2018**, *Veldhoven*, Netherlands.

**Oral presentation: Photonic Effects for Magnetic Dipole Transitions.**

18th International Conference on Luminescence, **2017**, *João Pessoa*, Brazil.

Physics@Veldhoven, **2017**, *Veldhoven*, Netherlands.

**Poster: Photonic Effects for Magnetic Dipole Transitions.**

19th International Conference on Dynamic Processes in Excited States of Solids, **2016**, *Paris*, France.

Physics@FOM, **2016**, *Veldhoven*, Netherlands.

---

## Acknowledgements

I have been in the Netherlands for around three years and the journey is pleasant and unforgettable. I would like to thank many people who are involved in my work and life. First, my sincere gratitude is to my supervisor **Andries**. It is he that provides me an opportunity to fulfill one of my dreams: study aboard and experience differently. Everything proves that I have made a right choice. Hope he has the same feeling. In research, based on his rich experience and profound expertise, he can always dispel my confusion and keep my research in the right track. Every meeting of discussion can enlighten me. Moreover, enough freedom in research lets me seldom feel pressured. I can work at my own pace and cannot agree more with his philosophy that PhD should be self-motivated. Besides his large stock of knowledge, his personality also impresses me. A scenario is still vivid in my mind that he picked me up at the airport. He is good at encouraging people and is willing to offer assists in any aspect. I am deeply grateful and honored to have Andries as my supervisor. There is one thing he may not know. A professor asked some PhDs including me “do you have any suggestion to Andries?” Then we realized that it was difficult to answer than expected. The other thing surprising me is that he works quite efficiently and productively with just a light lunch (several biscuits). Maybe the open secret is the daily seven cups of coffee and a variety of chips. Here, I wish the best to Andries and his lovely family.

Lab is my second home in the Netherlands. The experience in CMI group with four main research subjects raises my horizon and understanding in interdisciplinary research. I would like to thank the supporting staff in our group: **Hans (Ligthart)** and **Peter (van den Beld)** for technical support, and **Stephan** for IT management and TEM measurements, as well as our secretary **Linda**. Without them, our lab would not run so successfully. I am also thankful to **Tim (Senden)**, who is involved in the data analysis for the work of photonic effects on magnetic transitions, **Annelies**, **Jacobine**, **Joep**, **Mathijs** and **Robin** for assisting my experiments and measurements, and **Freddy**, **Pedro** and **Tim (Prins)** for their useful discussion. During the PhD period, I supervised a master student, **Daniele**. It is exciting to work with someone who is diligent. The master project was on sensitization of downconversion emission in nanocrystals, which was realized through dye coupling on nanocrystal surface. In addition, I owe the members of Room 119 in Ornstein building a big thank. The first generation consists of **Chenghui**, **Kunyu**, **Maryam** and me. Chenghui is a social boy and we always make fun with his hair. Kunyu is a little bit quiet and Maryam can be characterized by her unique laughing. Unfortunately, Maryam abandoned us and was replaced by **Ting**. Ting knows lots of stories and we have known each other since we were in Guangzhou. Now his seat belongs to our new member **Markus** who has dual degrees. I also want to thank **Dechao**, who also studied in Guangzhou and has given me valuable advice, and **Annalisa** for her efforts as my paranimfen. Of course, all fellows in CMI group are involved in my enjoyable experience. I would like to thank

---

Anne, Atul, Bas, Carlo, Celso, Christa, Christiaan, Chun Che, Daniël, Elleke, Federico, Giuseppe, Harold, Ingmar, Jaco, Jette, Joost, Kelly, Liudmyla, Maaïke, Marlou, Nadine, Naud, Onno, Pardip, Pascal, Per-Anders, Peter (Jacobse), Pierre, Relinde, Rouhollah, Saoirs é Serena, Shun, Sophia, Thomas (Gardenier), Thomas (van Swieten), Ward, Weiwei, Wenjin and other people I forgot to mention.

On the work of tungstates synthesis, I am thankful for the contributions of **Honghu, Mingmei, Weijie, Yanli** and my master supervisors **Jing** and **Jiuping** in Sun Yat-sen University, who offered huge supports when I prepared for studying abroad and care about my progress all along. The time I went back to my alma mater last year was enjoyable thanks to Jiuping's gracious hospitality. I also would like to express my gratitude to **Dingyong** (Sun Yat-sen University), **Ka-Leung** (Hong Kong Baptist University) and **Ling** (Nanjing University of Technology) for their suggestions on PhD and career planning. Recently, Ling has visited our group and established our collaboration. I did temperature-dependent measurements of photoluminescence spectra and decay dynamics for their samples, and look forward to the wonderful story they are going to write about.

Visiting PhD from Aarhus University, **Jeppe**, is another contributor of my thesis I would like to thank. We worked together and learned from each other during his three-month stay in CMI group. He as a physicist had his first experience as a chemist. Our attempts on  $Mn^{2+}$  and  $Tb^{3+}$  ions unexpectedly did not work and then we moved on to investigate the mechanism in thermal enhancement of upconversion emission in nanocrystals. He played a significant role in temperature-dependent measurements and data analysis. My thanks also go to **Dennie (Wezendonk)** from ICC group for XRD and TG measurements, **Xiaobin** and his supervisors **Alfons** and **Marijn** from SCM group for TEM measurements, and **Thomas (Ran)** from OCC group for EPR measurements. The work could not have completed thoroughly and timely without their efforts.

Electron microscopy is a powerful tool in nanoscience and nanotechnology, and benefits my PhD project profoundly. I would give the credit to **Hans (Meeldijk)** and **Chris** for the TEM training and instructions. One of my projects, devised by Andries and me, focuses on 3D TEM measurements and analyses in luminescent nanocrystals. This project results in our collaboration with **Sara** and **Yang (Zhang)** in Antwerp University. They have examined various systems of nanocrystals. The project is challenging, but its success will make a big difference in research field of lanthanide-doped nanocrystals. Many thanks to them and hope that we can have promising results eventually. Besides, I appreciate **Nick** in AMOLF for choosing my nanocrystals for his cathode-ray related experiments although the conclusion turned out that a more robust nano system is needed. Good luck for his further research.

**Yinhuan** and **Dennis (Wollaars)** couple, has helped a lot in daily life. We two families do enjoy

---

our get-together. Dennis is a big fan of music and has his own album in YouTube. **Yang (Liu)** and **Xueying** couple is my terrific photographer and assistant for wedding photos. We left our footprints in every corner of Utrecht. **Kangming** and **Linli** couple is my neighbor, full of enthusiasm. Coincidentally, their son was born on the same day as mine. For my paranimfen and also neighbor, **Donglong**, his sociability amazes me and we can talk about everything. As he is a PhD in ICC group, we planned to do some interesting research together, but he was too busy. I am very obliged to these friends and **Chonggeng, Da, Fuqiang, Guohua** and **Lihong** couple, **Hongde, Jianye, Kai, Lei, Min, Qian, Siyao, Tian, Wen, Wun Fan, Xiaodan, Xuejie, Yangchun, Yupeng**...Because of you, my life is full of color.

Obsession of **Qiyuan** lets me make an important decision in my life that is to marry her. We attained our marriage certificate in Chinese embassy in the Netherlands on Singles' Day and held the ceremony in China. Three years ago, she gave up her job in Shanghai and came to me without hesitation. This needs tremendous courage and deserves my admiration. Later, she gave birth to our first child **Chuming**. She suffered a lot to bring up a kid in this isolated situation. However, every cloud has a silver lining. At the leisure, we go travelling, meet friends, and visit museums. Every moment with each other should be cherished. I can't tell her how grateful I am for what she has done. As a result, there is an exclusive surprise for her in this thesis. Furthermore, I sincerely appreciate every individual who ever provided assistances in any form, especially our pediatrician **D. A. de Gast-Bakker** in Diakonessenhuis.

Utrecht University is the origin of the nickname UU of my son to commemorate his birthplace and my workplace. I do love everything in the Netherlands except the changeable weather and will miss the land and the people. Last but not the least, I eternally thank and appreciate my parents **Fushou** and **Huorong**, as well as the whole family. To everyone, thank you and best wishes. Bedankt en de beste wensen. 感谢并致以最真挚的祝福。

Zijun

December, 2018

## About the author



Zijun Wang was born in Jiangxi, China, on the 11th of June 1989. He graduated from Yingtan Tianjiabing High School in 2008 and entered Sun Yat-sen University in Guangzhou. After receiving his Bachelor Degree in Chemistry and Honorary Degree of Yat-sen Class aimed at multidisciplinary study in 2012, he continued his master studies in the same university. The master thesis was on “Synthesis and Luminescence Properties of Tungstate Double Salts Micro/Nanocrystals Doping with Rare Earth Ions”, supervised by Jiuping Zhong and Jing Wang. In 2015, he graduated and was awarded the Master Degree in Inorganic Chemistry.

Subsequently, he started his PhD in October 2015 under the supervision of Andries Meijerink in the Condensed Matter and Interfaces group of Debye Institute of Nanomaterials Science, Utrecht University, Netherlands, sponsored by a grant provided by the China Scholarship Council. His PhD project involved lanthanide-doped nanocrystals and multi-photon processes. The results of his PhD research are shown in the thesis and have been published in peer-reviewed scientific journals and presented in international conferences.